

The Pennsylvania State University
The Graduate School
Department of Astronomy and Astrophysics

X-RAY INSIGHTS INTO JETS AND OUTFLOWS
IN RADIO-LOUD QUASARS

A Dissertation in
Astronomy and Astrophysics

by

Brendan P. Miller

© 2010 Brendan P. Miller

Submitted in Partial Fulfillment
of the Requirements
for the Degree of

Doctor of Philosophy

May 2010

The dissertation of Brendan P. Miller was reviewed and approved¹ by the following:

William N. Brandt
Distinguished Professor of Astronomy and Astrophysics
Dissertation Adviser
Chair of Committee

Michael C. Eracleous
Associate Professor of Astronomy and Astrophysics

Donald P. Schneider
Distinguished Professor of Astronomy and Astrophysics

Richard W. Robinett
Professor of Physics

Gordon P. Garmire
Evan Pugh Professor of Astronomy and Astrophysics

Lawrence W. Ramsey
Professor of Astronomy and Astrophysics
Head of the Department of Astronomy and Astrophysics

¹Signatures on file in the Graduate School.

Abstract

This thesis presents X-ray investigations into jets and outflows in radio-loud quasars (RLQs). Deep observations have been conducted of individual objects including a broad absorption line (BAL) RLQ and multiple hybrid morphology radio sources, a survey of BAL RLQs has been performed and supplemented with analysis of archival data, and a large-scale statistical study of X-ray emission in RLQs and radio-intermediate quasars (RIQs) has been carried out. Key findings from these projects include (1) detection of variable X-ray absorption in a BAL RLQ, helping link X-ray absorption with the BAL outflow as in BAL radio-quiet quasars (RQQs); (2) determination that the typical factor of X-ray weakness in BAL RLQs is less than in BAL RQQs, consistent with obscuration of the disk/corona system as in BAL RQQs but with a small-scale (likely partially covered) X-ray jet contributing the majority of the observed X-ray emission; (3) parameterization of the dependence of X-ray luminosity in RLQs upon optical/UV and radio luminosity, measurement of the X-ray brightness of RLQs relative to RQQs as a function of radio loudness and luminosity, and evaluation of the fractional contribution of jet-linked X-ray emission to the nuclear continuum as a function of inclination; (4) conclusive identification of hybrid morphology radio sources as intrinsically powerful objects, in which a dense surrounding environment must disrupt the jet on one side.

Chapter 2 presents an investigation into the X-ray properties of PG 1004+130, a BAL RLQ with a hybrid FR I/FR II radio morphology. The *Chandra* ACIS-S spectrum shows evidence for complex soft X-ray absorption not detected in the data obtained 1.7 yr previously with *XMM-Newton*, with a best-fit intrinsic column density of $N_{\text{H}} = 1.2 \times 10^{22} \text{ cm}^{-2}$ for the preferred partial-covering model. The *Chandra* image also reveals extended X-ray emission $\approx 8''$ (30 kpc) south-east of the nucleus, aligned with the FR I jet but upstream of the 1.4 GHz radio-brightness peak. The multiwavelength characteristics of the PG 1004+130 jet, including its relatively flat X-ray power law and concave spectral energy distribution, are similar to those of powerful FR II jets.

Chapter 3 presents the results of a *Chandra* study of 21 BAL RLQs. We conducted a *Chandra* snapshot survey of 12 bright BAL RLQs selected from SDSS/FIRST data; optical spectra were obtained nearly contemporaneously with the Hobby-Eberly Telescope. We also include in our sample 9 additional BAL RLQs possessing archival *Chandra* coverage. All 12 snapshot and 8/9 archival BAL RLQs are detected, with observed X-ray luminosities less than those of non-BAL RLQs having comparable optical/UV luminosities by typical factors of 4.1–8.5. However, BAL RLQs are not as X-ray weak relative to non-BAL RLQs as are BAL RQQs relative to non-BAL RQQs. While some BAL RLQs have harder X-ray spectra than typical non-BAL RLQs, some have hardness ratios consistent with those of non-BAL RLQs, and there does not appear to be a correlation between X-ray weakness and spectral hardness, in contrast to the situation for BAL RQQs. RLQs are expected to have X-ray continuum contributions from both disk-corona and small-scale jet emission. While the entire X-ray continuum in BAL RLQs cannot be obscured to the same degree as in BAL RQQs, we calculate that the jet is likely partially covered in many BAL RLQs.

Chapter 4 presents the results of an investigation into the optical-to-X-ray properties of RIQs and RLQs. We generate an optically selected sample that includes 177 RIQs and 550 RLQs. This sample is constructed independently of X-ray properties but has a high X-ray detection rate (85%), and it extends to high redshifts (23% of objects have $z = 2 - 5$) and radio-loudness values (33% of objects have $R^* = 3 - 5$, using logarithmic units). We measure the “excess” X-ray luminosity of RIQs and RLQs relative to RQQs as a function of radio loudness and luminosity, and parameterize the X-ray luminosity of RIQs and RLQs as joint function of optical/UV and radio luminosity. The X-ray properties of RIQs are generally similar to those of RQQs, and it is only at high values of radio-loudness ($R^* \gtrsim 3.5$) and luminosity that RLQs become strongly X-ray bright. We find no evidence for evolution in the properties of individual RIQs and RLQs with redshift. We consider a model in which the nuclear X-ray emission contains both disk/corona-linked and jet-linked components and demonstrate that the X-ray jet-linked emission is likely beamed but to a lesser degree than applies to the radio jet.

Chapter 5 presents *Chandra* observations of the hybrid morphology radio sources 3C 433 and 4C 65.15, two members of the rare class of objects possessing an FR I jet on one side of the core and an FR II lobe on the other. The X-ray spectrum of 3C 433 shows intrinsic absorption (with a column density of $N_{\text{H}} \simeq 8 \times 10^{22} \text{ cm}^{-2}$), such as is typical of FR II narrow-line radio galaxies. X-ray emission is detected at the bend in the FR I jet in 4C 65.15; this X-ray jet emission lies above the extrapolation from the high-frequency radio synchrotron emission and has a spectral slope flatter than α_{rx} , indicating that the jet spectral energy distribution is concave as with other FR II quasar jets. Both 3C 433 and 4C 65.15 have unabsorbed X-ray luminosities, radio luminosities, and optical spectra typically seen in comparable sources with FR II morphologies. Presumably the FR I structure seen on one side in these hybrid sources is generated by a powerful jet interacting with a relatively dense environment.

Chapter 6 summarizes key results and discusses future work.

TABLE OF CONTENTS

List of Tables	viii
List of Figures	ix
Acknowledgments	xi
Chapter 1. Introduction	1
1.1 Overview of quasar characteristics	1
1.2 Jets and outflows in RLQs	2
1.3 Thesis outline	3
Chapter 2. X-ray Absorption and an X-ray Jet in the Radio-Loud Broad Absorption Line Quasar PG 1004+130	5
2.1 Introduction	5
2.2 Observations	8
2.3 X-ray Spectral Analysis	12
2.4 Multiwavelength Properties	16
2.4.1 The Nucleus	16
2.4.2 The Jet	22
2.5 Results and Discussion	27
2.6 Acknowledgments	29
Chapter 3. A <i>Chandra</i> Survey of the X-ray Properties of Broad Absorption Line Radio-Loud Quasars	30
3.1 Introduction	30
3.2 Sample properties	32
3.2.1 Selection of snapshot BAL RLQs	32
3.2.2 Selection of archival BAL RLQs	33
3.2.3 Reddening	35
3.2.4 Comparison samples	38
3.3 Observations and Notes	40
3.3.1 <i>HET</i> observations	40
3.3.2 <i>Chandra</i> observations	42
3.3.3 Notes on individual objects	44
3.3.3.1 Snapshot BAL RLQs	44
3.3.3.2 Archival BAL RLQs	47
3.4 Data Analysis	48
3.4.1 Calculation of X-ray hardness ratios and luminosities	48
3.4.2 Relative X-ray luminosities	49
3.4.3 X-ray spectral characteristics	51
3.5 Discussion	56

3.5.1	Physical models	56
3.5.2	BAL RLQ geometries and ages	58
3.6	Conclusions	60
3.7	Acknowledgments	62
Chapter 4.	X-ray Emission from Optically Selected Radio-Intermediate and Radio-Loud Quasars	68
4.1	Introduction	68
4.1.1	Radio-loud and radio-intermediate quasars	68
4.1.2	Aims of this work	70
4.2	Sample selection	71
4.2.1	Primary sample	72
4.2.1.1	Spectroscopic sample	72
4.2.1.2	Photometric sample	77
4.2.2	Supplemental samples	79
4.2.2.1	Einstein sample	80
4.2.2.2	High-redshift sample	80
4.2.2.3	Deep-fields sample	81
4.3	Sample characteristics	83
4.3.1	Optical/UV luminosities	83
4.3.2	Radio luminosities and radio loudness	86
4.3.3	Radio spectral shapes and morphologies	88
4.3.4	X-ray luminosities	89
4.4	Comparison of the X-ray emission in RQQs, RIQs, and RLQs	91
4.5	Parameterizing the X-ray luminosity of RIQs and RLQs	93
4.5.1	$\ell_x(\ell_{uv})$	96
4.5.2	$\ell_x(\ell_{uv}, \ell_r)$	99
4.5.2.1	Inclusion of radio luminosity as a fit parameter	99
4.5.2.2	A “radio-adjusted” $\ell_x(\ell_{uv})$ RLQ relation	100
4.5.3	$\ell_x(\ell_{uv}, \ell_r, z)$	103
4.5.3.1	Inclusion of redshift as a fit parameter	103
4.5.3.2	Dependence of relative X-ray brightness on redshift	107
4.5.4	Additional considerations	108
4.5.4.1	Optical versus radio selection	108
4.5.4.2	Influence of targeted objects	108
4.5.4.3	Log-normality of residuals	110
4.5.4.4	Robustness of luminosity correlations	110
4.6	A physical model for X-ray emission in RIQs and RLQs	113
4.6.1	The model components	114
4.6.1.1	Radio emission: core and lobes	114
4.6.1.2	Disk-dominated optical/UV emission	114
4.6.1.3	Dual X-ray emission components	115
4.6.2	Comparison to observed luminosities	117
4.6.3	Modeling results	119
4.6.4	Alternative model parameters	123

4.7	Conclusions	125
4.8	Acknowledgments	126
4.9	Appendix A: Using GALEX data to improve photometric redshifts .	126
4.10	Appendix B: Notes on individual deep-field objects	127
4.11	Appendix C: Verification of fitting methodology	128
Chapter 5.	<i>Chandra</i> observations of the hybrid morphology radio sources 3C 433 and 4C 65.15: FR IIs with asymmetric environments	140
5.1	Introduction	140
5.2	Observations	142
5.3	3C 433	144
5.4	4C 65.15	150
5.5	Discussion	152
5.5.1	Jet emission	152
5.5.2	Environment	154
5.5.3	Comparison to other radio sources	156
5.6	Conclusions	157
5.7	Acknowledgments	159
Chapter 6.	Conclusions and Future Work	160
6.1	Summary of Results	160
6.1.1	X-ray Absorption and an X-ray Jet in the Radio-Loud Broad Absorption Line Quasar PG 1004+130	160
6.1.2	A <i>Chandra</i> Survey of the X-ray Properties of Broad Absorp- tion Line Radio-Loud Quasars	160
6.1.3	X-ray Emission from Optically Selected Radio-Intermediate and Radio-Loud Quasars	161
6.1.4	<i>Chandra</i> observations of the hybrid morphology radio sources 3C 433 and 4C 65.15: FR IIs with asymmetric environments	161
6.2	Future Work	162
	Bibliography	164

List of Tables

2.1	PG 1004+130 Multiwavelength Luminosity Data	20
3.1	<i>Chandra</i> and <i>HET</i> Observing Log	63
3.2	<i>Chandra</i> Archival Sources	64
3.3	Optical/UV Characteristics	65
3.4	Radio Characteristics	66
3.5	X-ray Counts, Luminosities, and Properties of BAL RLQs	67
4.1	Primary sample RIQs and RLQs	131
4.2	RIQs and RLQs selected from deep surveys	132
4.3	Sample characteristics	133
4.4	RIQ and RLQ properties as a function of ℓ_{uv}	134
4.5	Excess X-ray luminosity as a function of R^* and ℓ_{r}	135
4.6	Correlations with X-ray luminosity	136
4.7	α_{ox} and $\Delta\alpha_{\text{ox}}$ as functions of R^*	137
4.8	Description of model components	138
4.9	Model X-ray luminosities and $\ell_{\text{x}}(\ell_{\text{uv}}, \ell_{\text{r}})$	139
5.1	X-ray spectral fitting	152

List of Figures

2.1	<i>Chandra</i> , <i>HST</i> , and <i>VLA</i> imaging of PG 1004+130	11
2.2	Large-scale diffuse X-ray emission along jet and counterjet	13
2.3	X-ray spectra of PG 1004+130 showing variable complex absorption . .	17
2.4	Spectral energy distribution of PG 1004+130 compared to other RLQs .	21
2.5	Various models applied to the jet spectral energy distribution	26
3.1	Sample selection of SDSS/FIRST/ <i>Chandra</i> BAL RLQs	34
3.2	Radio loudness versus C IV equivalent width for BAL RLQs	36
3.3	SDSS spectra of snapshot sample of BAL RLQs	37
3.4	Relative color $\Delta(g - i)$ of snapshot and archival BAL RLQs	39
3.5	Optical/UV luminosity of BAL RLQs and comparison samples	41
3.6	HET/LRS spectra of selected snapshot BAL RLQs	43
3.7	<i>Chandra</i> images of BAL RLQs with extended radio emission	45
3.8	<i>Chandra</i> spectrum of the BAL RLQ J115944.82+011206.9	46
3.9	X-ray luminosities of BAL quasars compared to non-BAL quasars . . .	52
3.10	Distribution of X-ray weakness in BAL RLQs and BAL RQQs	53
3.11	C IV absorption properties as a function of relative X-ray luminosity . .	54
3.12	X-ray hardness ratios of BAL RLQs as a function of X-ray weakness . .	57
3.13	Jet-linked X-ray emission in BAL RLQs compared to non-BAL RLQs .	59
3.14	Luminosities of GPS and CSS sources compared to those of BAL RLQs	61
4.1	Sky coordinates of full sample of RIQs and RLQs	74
4.2	Color-magnitude plot of RIQs and RLQs	75
4.3	Sample coverage of the $\ell_{\text{uv}} - z$ plane	84
4.4	Sample coverage of the $\ell_{\text{x}} - z$ plane	85
4.5	R^* versus ℓ_{r} for the primary sample of RIQs and RLQs	87
4.6	Optical/UV-to-X-ray spectral slope α_{ox} as a function of ℓ_{uv}	92
4.7	X-ray “excess” in RIQs and RLQs relative to RQQs	94
4.8	Histograms of $\ell_{\text{x}} - \ell_{\text{x,RQQ}}$ plotted in bins of R^* and ℓ_{r}	95
4.9	Fitting $\ell_{\text{x}} = a_0 + b_{\text{uv}} \times \ell_{\text{uv}}$	97
4.10	Parameters for $\ell_{\text{x}} = a_0 + b_{\text{uv}} \times \ell_{\text{uv}}$	98
4.11	Fitting $\ell_{\text{x}} = a_0 + b_{\text{uv}} \times \ell_{\text{uv}} + c_{\text{r}} \times \ell_{\text{r}}$	101
4.12	Parameters for $\ell_{\text{x}} = a_0 + b_{\text{uv}} \times \ell_{\text{uv}} + c_{\text{r}} \times \ell_{\text{r}}$	102
4.13	Residuals versus redshift for $\ell_{\text{x}} = a_0 + b_{\text{uv}} \times \ell_{\text{uv}} + c_{\text{r}} \times \ell_{\text{r}}$	105
4.14	Fitting redshift dependence	106
4.15	Relative X-ray brightness as a function of R^* and redshift	109
4.16	Optical versus radio selection of RIQs and RLQs	111
4.17	Evaluation of normality for residuals	112
4.18	Simulated luminosities of RIQs and RLQs for three models	120
4.19	X-ray properties of simulated RIQs and RLQs for three models	122
4.20	Jet-dominance versus inclination in RIQs and RLQs for three models . .	124

4.21	Fitting methodology for $\ell_x(\ell_{uv})$ applied to RQQs	129
5.1	<i>Chandra</i> , <i>HST</i> , and <i>VLA</i> imaging of 3C 433	143
5.2	Adaptively smoothed 0.5–8 keV <i>Chandra</i> image of 4C 65.15	145
5.3	X-ray spectrum of 3C 433 and radial profile of soft X-ray emission . . .	147
5.4	Maximum likelihood reconstruction of 3C 433 X-ray core region	149
5.5	X-ray spectrum of 4C 65.15 fit with power-law model	151
5.6	Spectral energy distribution for the jet in 4C 65.15	155
5.7	X-ray and radio core luminosity for FR I and FR II sources	158

Acknowledgments

I thank my advisor Niel Brandt for his guidance and support, for his constructive and detailed feedback and advice at all stages of this project, and for his encouragement of my scientific interests. I am indebted to my committee for their counsel and assistance. I am grateful to Mercedes Richards for overseeing my initial research work at Penn State and for her ongoing mentoring. Among the many faculty and staff members in the department whose help I greatly appreciate, I wish particularly to thank Mike Eracleous for numerous productive conversations, Chris Palma for supporting my interest in teaching and outreach, and SherryDawn Jackson and Nina Bumgarner for vital navigational aid in my journey through grad school. I would also like to extend my gratitude to the students, staff, and faculty at the College of Wooster, where I have enjoyed working the past year, and to Herman Marshall, who introduced me to X-ray studies of quasars.

I thank my friends and fellow graduate students, particularly my cohort: Emily Alicea-Munoz, Justin Crepp, Pencheng Guo, Steve Movit, Judy Racusin, Cristian Saez, and Matt Turk. I have enjoyed working alongside a great group of (former or current) post-docs and students, including Jan Budaj, Aaron Steffen, Ohad Shemmer, Rob Gibson, Bret Lehmer, Bin Luo, and Jianfeng Wu.

I thank my family for their constant support and encouragement, especially my grandparents, who sent me so many articles and books about astronomy; my parents, who were always there to help me forward along whatever path I chose; my siblings, whose interest inspires me; and my wonderful wife, Rachel Wannarka, who sustains and uplifts me, and our son Elliot, whose smile lights up his surroundings.

To follow knowledge like a sinking star
—Tennyson

Chapter 1

Introduction

1.1 Overview of quasar characteristics

Quasars were first discovered as bright “quasi-stellar radio sources.” Their optical spectra show strong broad emission lines superposed on a blue continuum, with redshifts corresponding to extragalactic distances and hence mandating large luminosities (e.g., Schmidt 1963). It was soon found that quasars¹ lacking strong radio emission were the numerically dominant population. Radio loudness R^* is typically defined as the ratio of rest-frame monochromatic flux at 5 GHz to that at 2500 Å (e.g., Stocke et al. 1992; sometimes 4400 Å is used instead, as in Kellerman et al. 1989), with radio-loud quasars (RLQs) traditionally satisfying $R^* \geq 10$ and radio-quiet quasars (RQQs) having $R^* < 10$. RLQs with relatively low values of R^* are sometimes described as radio-intermediate quasars (RIQs). The fraction of quasars that are radio-loud is $\sim 10\%$ but appears to vary with both luminosity and redshift (e.g., Jiang et al. 2007).

In the standard model quasars are powered by accretion onto a central supermassive black hole of $\sim 10^{7-9} M_\odot$. For typical RQQs a geometrically thin, optically thick accretion disk (e.g., Shakura & Sunyaev 1973) is believed to generate quasi-thermal optical/UV emission, while the observed X-ray emission is postulated to arise from Compton upscattering of disk photons in a hot “corona.” RLQs are complicated by the additional presence of powerful jets, which have bulk relativistic velocities at least near the nucleus (e.g., Worrall & Birkinshaw 2006 and references therein) and consequent non-isotropic radiation. RLQs generally have more massive central black holes than do RQQs (e.g., Laor 2000; Metcalf & Magliocchetti 2006) and may also have more rapidly spinning black holes (e.g., Wilson & Colbert 1995; Meier 2001).

Quasars are the most luminous members of the class of Active Galactic Nuclei (AGNs), objects characterized by a bright compact source at the center of the host galaxy. There is a plethora of different observational categories of AGNs, but some of the divisions are related to viewing angle rather than intrinsic differences. For example, the optical spectra of AGNs can lack broad emission lines; this is explained as an orientation-dependent effect associated with the presence of an obscuring dusty absorber (often postulated to have a toroidal geometry) that blocks the broad-line region at high inclination angles to the line of sight. The category of radio-loud AGNs includes both narrow-line radio galaxies and broad-line radio galaxies, where again the narrow-line sources are presumed to be viewed closer to edge-on. Radio galaxies can also be classified on the basis of morphology: as defined by Fanaroff & Riley (1974), FR I sources

¹A distinction is sometimes made between “quasi-stellar radio sources” and “quasi-stellar objects” but for simplicity we will use the term “quasar” to refer to luminous broad-line sources independent of their radio properties.

are edge-darkened with initially prominent jets tapering off into dim and diffuse plumes, whereas the more powerful FR II sources are edge-brightened with tightly collimated jets terminating in bright hotspots and complex lobes. In various unification models (e.g., Urry & Padovani 1995; Jackson & Wall 1999), FR II radio galaxies serve as the parent population for lower inclination RLQs. Objects with properties suggestive of extreme beaming (such as BL Lacs and blazars) are believed to be FR I or FR II sources viewed nearly down the jet.

1.2 Jets and outflows in RLQs

A clear understanding of jets and outflows is essential to forming a cohesive picture of the central engine in RLQs and of the relationship between the quasar and its surrounding environment. The influence of jets and outflows stretches from the inner accretion disk to outside the host galaxy; the feedback they provide likely regulates the growth of the supermassive black hole and injects material and energy on scales reaching hundreds of kpc. X-ray observations are particularly useful for studying the energetic emission processes in RLQ jets and for probing absorption linked with outflows.

Jets are believed to be launched along magnetic field lines threading the disk and may also extract energy from a rotating black hole (e.g., Blandford & Znajek 1977; Blandford & Payne 1982; Meier 2005). RLQs are more X-ray luminous than RQQs of comparable optical/UV luminosity (e.g., Zamorani et al. 1981), and the degree of X-ray brightness is linked to their radio properties (e.g., Worrall et al. 1987). This strongly suggests that the small-scale jet provides a significant contribution to the X-ray continuum in RLQs (probably via inverse Compton emission, perhaps of jet synchrotron photons), a conclusion supported by X-ray spectral studies (e.g., Belsole et al. 2006). On larger scales, knots in radio jets are routinely detected in X-rays by the *Chandra* X-ray Observatory. There is ongoing debate as to whether the dominant X-ray emission mechanism in RLQ jet knots is Compton upscattering of cosmic microwave background photons (e.g., Tavecchio et al. 2000) or perhaps instead synchrotron emission from a second population of highly-energetic electrons (e.g., Atoyan & Dermer 2004). A small percentage of radio sources have jets that display differing FR morphologies on opposite sides of the core; this hybrid structure suggests an asymmetric dense surrounding environment may have disrupted an intrinsically powerful jet on one side of the core (e.g., Gopal-Krishna & Wiita 2000).

Outflows such as winds are less narrowly directed than jets, generally act on a smaller scale, and have lower velocities than jets. Perhaps the most extreme manifestation of outflows is the blueshifted broad absorption lines (BALs; e.g., Weymann et al. 1991) seen in the rest-frame UV spectra of $\simeq 18\text{--}26\%$ of RQQs (e.g., Hewett & Foltz 2003). BAL RQQs are usually weaker in X-rays than would be expected from their optical/UV luminosities (e.g., Gallagher et al. 2006). The X-ray spectra of BAL RQQs show clear evidence of X-ray absorption, often complex, with intrinsic column densities $N_{\text{H}} > 10^{22} \text{ cm}^{-2}$ (e.g., Gallagher et al. 2002). Although UV and X-ray absorption are clearly linked (e.g., Brandt, Laor, & Wills 2000), the higher column density of the X-ray absorber (e.g., Arav et al. 2003) suggests the X-ray absorption arises interior to the UV BALs, perhaps in the “shielding gas” postulated by Murray et al. (1995) and generated

naturally in the simulations of Proga et al. (2000). An initial lack of detected BALs in RLQs led to early suggestions that quasars could host either a jet or a BAL wind but not both (e.g., Stocke et al. 1992). This perspective has been overturned by the discovery of a population of BAL RLQs (e.g., Becker et al. 2000), some of which seem to fit more plausibly into an evolutionary (e.g., Gregg et al. 2006) or polar outflow (e.g., Zhou et al. 2006) scenario than the disk-wind model often successfully applied to RQQs. Initial X-ray studies (e.g., Brotherton et al. 2005) indicate BAL RLQs are X-ray weak but likely not strongly absorbed; however, the data admit multiple interpretations and the relationship between the jet and BAL outflow in RLQs remains unclear.

1.3 Thesis outline

This thesis is centered on X-ray observations which are analyzed with the broad aim of improving understanding of jets and outflows in RLQs. The specific goals of this thesis are to (1) determine the degree of intrinsic absorption and the origin of the X-ray continuum in BAL RLQs; (2) quantify the X-ray weakness of BAL RLQs relative to non-BAL RLQs; (3) clarify the relative location of the jet and outflow in BAL RLQs; (4) assess the X-ray brightness of RLQs and RLQs relative to RQQs as a function of radio loudness and radio luminosity; (5) accurately parameterize the X-ray luminosity of RLQs and RLQs as a function of optical/UV luminosity and radio luminosity; (6) determine the degree to which the X-ray continuum of RLQs and RLQs is jet dominated as a function of inclination; (7) ascertain whether hybrid morphology radio sources are intrinsically FR I or FR II; and (8) investigate jet-environment interactions and jet disruption within a dense medium. These goals are realized through the complementary approaches of deep X-ray studies of individual objects and shallower X-ray surveys of larger samples.

Chapter 2 presents a detailed study of the remarkable BAL RLQ PG 1004+130 (Wills et al. 1999), which is also a hybrid morphology radio source (Gopal-Krishna & Wiita 2000). A ~ 20 ks *XMM-Newton* observation and a later ~ 40 ks *Chandra* observation, separated by ~ 500 rest-frame days, are discussed and compared. The high angular resolution of the *Chandra* data also makes it possible to search for an X-ray counterpart to the radio jet. The new X-ray data is placed in context through construction of the spectral energy distribution for the nucleus, and possible models for the origin of the X-ray continuum are discussed. This chapter has been previously published as Miller et al. (2006).

Chapter 3 presents a *Chandra* survey of BAL RLQs, using 12 new snapshot observations and 9 archival observations (some serendipitous). The snapshot sample is selected from the brightest BAL RLQs in the Sloan Digital Sky Survey (SDSS; York et al. 2001) with radio properties taken from the Faint Images of the Radio Sky at Twenty-cm catalog (FIRST; Becker et al. 1995); targets were observed on-axis with the ACIS-S detector for ~ 4 – 7 ks. Most of the snapshot sample also have optical spectra from the Hobby Eberly telescope taken quasi-simultaneously with the *Chandra* observations. The X-ray weakness in BAL RLQs relative to non-BAL RLQs is quantified and compared with that of BAL RQQs relative to non-BAL RQQs. We investigate whether the small-scale X-ray jet in BAL RLQs is partially obscured by the BAL-linked X-ray absorber. This chapter has been previously published as Miller et al. (2009).

Chapter 4 presents a statistical study of X-ray emission from RIQs and RLQs. A large sample of ~ 600 RIQs and RLQs with sensitive archival X-ray coverage by *Chandra*, *XMM-Newton*, or *ROSAT* is constructed. Additional coverage of the luminosity-redshift plane is obtained through inclusion of supplemental samples drawn from previous *Einstein* observations of luminous RLQs (e.g., Worrall et al. 1987) and from *Chandra* observations of high-redshift RLQs (e.g., Bassett et al. 2004; Lopez et al. 2006) and deep field RLQs (e.g., Alexander et al. 2003; Lehmer et al. 2005; Luo et al. 2008; Elvis et al. 2009). The “excess” X-ray luminosity in RIQs and RLQs relative to RQQs is accurately quantified within narrow bins of radio loudness and radio luminosity. X-ray luminosity is modeled as a sole function of optical/UV luminosity and as a joint function of optical/UV and radio luminosity for various groupings of RLQs. Comparison of simulated populations of RIQs and RLQs to the data indicates how the fraction of the X-ray continuum that is jet-linked increases with decreasing inclination. This chapter is being submitted for publication and the interested reader is referred to the published version for the most current results.

Chapter 5 presents deep *Chandra* observations of two hybrid morphology radio sources, the narrow-line radio galaxy 3C 433 and the RLQ 4C 65.15. The ~ 40 ks exposures provide sufficient counts to model accurately the X-ray spectra, permitting classification of the intrinsic X-ray nuclear properties of each source as either FR II or FR I. The innermost radio jet knot in 3C 433 is resolved by *Chandra* with the aid of maximum likelihood image reconstruction. An X-ray jet is discovered in 4C 65.15 and the radio-to-X-ray spectral energy distribution is compared with those of other FR II and FR I jets. The most likely mechanism for the hybrid radio morphology is discussed in light of the new X-ray results. This chapter has been previously published as Miller & Brandt (2009).

Chapter 6 summarizes the main results and conclusions of this work, and discusses promising directions for future research. Extensions of these projects could include monitoring the variable X-ray absorption in PG 1004+130 while looking for short timescale variability to constrain more tightly the location of the absorbing gas, studying BAL variability in RLQs to compare variability properties to those established for BAL RQQs, and determining the optical properties (redshifts, broad or narrow line spectra) and X-ray characteristics (nuclear spectrum, jet fluxes and spectral energy distributions) of newly identified radio-selected hybrid morphology radio sources.

The chapters are intended to be self-contained and consequently there is some repetition of introductory and background information. References to figures and tables within the chapter text are given omitting the chapter number (ie, a reference to “Figure 2” within Chapter 3 corresponds to Figure 3.2). Radio loudness is expressed in logarithmic rather than linear units in Chapter 4 to simplify the presentation of the analysis conducted therein.

Chapter 2

X-ray Absorption and an X-ray Jet in the Radio-Loud Broad Absorption Line Quasar PG 1004+130

2.1 Introduction

Broad absorption line (BAL) quasars show deep and wide blueshifted absorption troughs in their rest-frame UV spectra (e.g., Weymann et al. 1991). The intrinsic fraction of quasars with BALs is $\approx 20\%$ (e.g., Hewett & Foltz 2003); in the most commonly accepted scenario this represents the covering factor of an outflowing BAL wind. While all BAL quasars show absorption from high-ionization transitions, such as Si IV and C IV, some also display absorption from lower ionization transitions, such as Mg II, and such objects tend to be more reddened (e.g., Sprayberry & Foltz 1992; Reichard et al. 2003).

Although BALs were once believed to be confined to radio-quiet sources, optical spectroscopy of the quasars from the Very Large Array (VLA) 1.4 GHz Faint Images of the Radio Sky at Twenty cm (FIRST) survey (Becker et al. 1995), conducted by the FIRST Bright Quasar Survey (White et al. 2000), and the Sloan Digital Sky Survey (SDSS; York et al. 2000) has revealed many radio-loud BAL quasars (e.g., Becker et al. 2000; Menou et al. 2001). Radio loudness is commonly parameterized by the ratio of rest-frame radio-to-optical flux densities, $R^* = f_{5\text{GHz}}/f_{2500\text{\AA}}$ (Sramek & Weedman 1980), for which those quasars with $\log R^* > 1$ are considered radio-loud. As this definition may somewhat exaggerate the radio-loudness of BAL quasars with substantial optical reddening, it is also useful to consider the rest-frame radio luminosity density, where $L_{5\text{GHz}} > 10^{32} \text{ erg s}^{-1} \text{ Hz}^{-1}$ distinguishes radio-loud quasars (e.g., Miller et al. 1993). The majority of radio-loud BAL quasars discovered to date meet both criteria but tend to be of intermediate radio-loudness (fewer than 20% in the combined samples of Becker et al. [2000] and Menou et al. [2001] have $\log R^* > 2$). Becker et al. (2000) found that about one-third of their BAL quasars were flat-spectrum radio sources (some radio loud), suggesting a viewing angle for this subset well above the equatorial region where disk-associated BAL outflows would be visible, and further discovered that most of their BAL quasars were compact (80% unresolved to $0.2''$ at 8 GHz). These results support alternate proposals that BALs may be associated with an evolutionary phase with a large BAL wind-covering fraction, rather than orientation (e.g., Gregg et al. 2000), although the consistency of the sub-millimeter emission of BAL quasars with that of non-BAL quasars is difficult to reconcile with evolutionary scenarios in which BAL quasars are emerging from a dusty “shroud” (Lewis et al. 2003; Willott et al. 2003).

Radio-quiet BAL quasars, particularly those with low-ionization absorption features, are usually weaker in X-rays than would be expected from their optical luminosities (e.g., Green et al. 2001; Gallagher et al. 2006). The X-ray spectra of radio-quiet BAL

quasars show clear evidence of X-ray absorption, often complex, with intrinsic column densities $N_{\text{H}} > 10^{22} \text{ cm}^{-2}$ (e.g., Gallagher et al. 2002). Although UV and X-ray absorption are clearly linked (e.g., Brandt et al. 2000), the higher column density of the X-ray absorber (e.g., Gallagher et al. 2006) suggests that the X-ray absorption arises interior to the UV BALs, perhaps in the “shielding gas” postulated by Murray et al. (1995) and generated naturally in the simulations of Proga et al. (2000). A *Chandra* snapshot survey of five radio-loud BAL quasars confirmed that they are also X-ray weak relative to similar non-BAL quasars, but with fairly soft spectra incompatible with the large column densities necessary to explain this weakness as simple neutral absorption (Brotherton et al. 2005).

Many radio-loud quasars display striking extended emission in the form of jets and lobes. The classification scheme of Fanaroff & Riley (1974) distinguishes the edge-darkened, core-dominated FR I sources from the more luminous edge-brightened, lobe-dominated FR II objects. The multiwavelength properties of FR I and FR II jets are quite distinct: FR I jets have linear or convex spectral energy distributions (SEDs) that can typically be modeled by a synchrotron spectrum extrapolated (with a break if necessary) from the radio through the optical to the X-ray (e.g., Worrall & Birkinshaw 2006), while the SEDs of the prominent knots in FR II jets are concave, frequently possessing only an upper limit at optical wavelengths (e.g., Sambruna et al. 2004; Marshall et al. 2005). The X-ray emission in FR II jets is often interpreted as arising from inverse Compton scattering of cosmic microwave background photons (IC/CMB models; e.g., Tavecchio et al. 2000; Celotti et al. 2001), a process that is increasingly efficient for highly relativistic bulk motions, for jet angles close to the line of sight, and for objects at large redshifts (Schwartz 2002). Some observational and theoretical complications with IC/CMB models have been noted (e.g., Tavecchio et al. 2003; Hardcastle 2006), and high-redshift radio-loud quasars in general do not appear to have extreme jet-to-core X-ray brightness ratios (e.g., Siemiginowska et al. 2003; Bassett et al. 2004; Lopez et al. 2006). Alternative models for the origin of the X-ray emission from FR II jets have been proposed, including synchrotron emission from a population of highly relativistic electrons (e.g., Atoyan & Dermer 2004). X-ray hotspots have been detected by *Chandra* in a number of FR II sources; the most luminous hotspots are consistent with synchrotron self-Compton (SSC) emission but other cases require a second highly energetic synchrotron component to produce the X-ray emission (Hardcastle et al. 2004).

PG 1004+130 (PKS 1004+13, 4C 13.41) is an optically bright ($V = 14.98$; e.g., Garcia et al. 1999), radio-loud ($\log R^* = 2.32$ [Wills et al. 1999] and $L_{5\text{GHz}} = 6.5 \times 10^{32} \text{ ergs s}^{-1} \text{ Hz}^{-1}$), lobe-dominated quasar at a redshift of $z = 0.240$ (Eracleous & Halpern 2004). PG 1004+130 is notably X-ray weak; it was undetected by *Einstein* with a 0.5–4.5 keV flux limit of $1.4 \times 10^{-13} \text{ ergs cm}^{-2} \text{ s}^{-1}$ (Elvis & Fabbiano 1984). Wills et al. (1999) analyzed *International Ultraviolet Explorer* (IUE) and *Hubble Space Telescope* (HST) Goddard High Resolution Spectrograph (GHRS) spectra of PG 1004+130 and found evidence for broad, blueshifted absorption in several UV lines, notably O VI, N V, and C IV. They concluded that PG 1004+130 was likely a BAL quasar with a

BALnicity index¹ (Weymann et al. 1991) of $\approx 850 \text{ km s}^{-1}$. A recent observation with *HST* performed with the Space Telescope Imaging Spectrograph (STIS) to search for BAL variability has confirmed this designation (B. J. Wills, private communication), making PG 1004+130 the only currently known low-redshift ($z < 0.5$) radio-loud BAL quasar. These results suggest that the X-ray weakness of PG 1004+130 is likely related to absorption.

The extended radio structure of PG 1004+130 is also notable: it is one of the prototypical examples discussed by Gopal-Krishna & Wiita (2000) of a hybrid morphology source possessing both an FR I and an FR II lobe. The majority of the radio emission in the FR I south-east (SE) structure is concentrated in a knotted jet that is most prominent close to the nucleus and then fades into a gradually broadening plume, whereas the north-west (NW) structure shows classical FR II edge-brightened morphology. The structure of such hybrid sources is more intuitively explained as arising from the propagation of twin jets into dissimilar large-scale environments rather than by invoking a “lopsided” central engine (Gopal-Krishna & Wiita 2000). Both the extended projected size of PG 1004+130 ($\sim 500 \text{ kpc}$) and the ratio of lobe-to-core flux (we measure this to be ~ 40 at rest-frame 1.7 GHz using FIRST data) suggest that the jet axis is inclined at a relatively large angle to our line of sight, consistent with physical models in which BAL winds flow equatorially from the accretion disk. A quantitative lower limit on the inclination to the line-of-sight, θ , may be estimated from the core radio-to-optical luminosity ratio, $\log R_V = \log(L_{\text{core}}/L_{\text{opt}})$, which Wills & Brotherton (1995) found improves on the commonly used lobe-to-core ratio. PG 1004+130 has $\log R_V \sim 1.1$, suggesting $\theta \gtrsim 45^\circ$ (consistent with Wills et al. 1999). This large inclination angle implies little line-of-sight beaming in the jet and constrains the interpretation of any associated X-ray emission.

We have obtained the first X-ray detections and spectra of PG 1004+130 in order to check for nuclear absorption and determine the quasar’s general X-ray properties. We make use of both *XMM-Newton* and *Chandra*, as they provide complementary information: *XMM-Newton* has high throughput and covers a broader energy range, whereas *Chandra* provides the angular resolution necessary to detect and characterize any extended X-ray emission. The two X-ray observations were conducted $\sim 1.7 \text{ yr}$ apart, allowing investigation of both short and long-term X-ray variability.

In this paper we adopt a standard cosmology with $H_0 = 70 \text{ km s}^{-1} \text{ Mpc}^{-1}$, $\Omega_M = 0.3$, and $\Omega_\Lambda = 0.7$ (Spergel et al. 2003). This choice results in a luminosity distance of 1200 Mpc and an angular distance scale of $3.8 \text{ kpc arcsec}^{-1}$ for PG 1004+130. The Galactic column density toward PG 1004+130 ($\alpha_{2000} = 10 \text{ } 07 \text{ } 26.10$, $\delta_{2000} = +12 \text{ } 48 \text{ } 56.20$) is $3.93 \times 10^{20} \text{ cm}^{-2}$ (Murphy et al. 1996). Unless otherwise noted, errors are given as 90% confidence intervals for one parameter of interest ($\Delta\chi^2 = 2.71$).

¹BALnicity index is calculated from the C IV BAL as the total equivalent width of all associated absorption troughs blueshifted from the emission peak by greater than 3000 km s^{-1} and at least 2000 km s^{-1} wide. Any quasar with a BALnicity index $> 0 \text{ km s}^{-1}$ is formally a BAL quasar according to the criterion of Weymann et al. (1991).

2.2 Observations

PG 1004+130 was observed by *XMM-Newton* (Jansen et al. 2001) on 2003 May 4 (ObsID 0140550601) for an effective exposure time of 22.2 ks, and data were collected by all instruments. There were insufficient counts in the RGS grating spectra for meaningful analysis; we therefore restrict our study of the X-ray spectrum to the EPIC (pn and MOS) imaging spectroscopy data. There was no flaring during the observation in the detector-wide count rate for events with energies greater than 10 keV.

Analysis was performed with the *XMM-Newton* Science Analysis Software (SAS ver. 6.5.0). The nuclear spectrum was extracted from a circular region with a radius of $24.6''$, while background regions were determined separately for the pn (a $533''$ by $82''$ rectangle) and MOS (a $381''$ by $192''$ rectangle) detectors to avoid detector gaps. We generated custom redistribution matrix files (RMFs) and ancillary response files (ARFs), which together describe the instrument response to incident photons and allow forward-fitting of the spectrum. Finally, the extracted nuclear spectrum was binned to contain at least 20 counts per bin using the FTOOLS task *grppha*. There are ~ 1550 counts from 0.5–8 keV in the pn spectrum, and ~ 1100 total counts in the MOS1 and MOS2 spectra; the expected number of background counts is ~ 50 in the pn spectrum and ~ 30 total in the MOS spectra.

The observation included sets of images from the *XMM-Newton* Optical Monitor (OM) for each of the UVW1, UVM2, and UVW2 filters, with central wavelengths of 2910 Å, 2310 Å, and 2120 Å, respectively. We converted background-subtracted OM count rates (automatically calculated during pipeline processing) to flux densities using scaling factors appropriate for active galactic nuclei (AGNs), as determined by the OM Calibration Team. The resulting UVW1, UVM2, and UVW2 observed fluxes for PG 1004+130 are 6.3, 8.2, and 8.1×10^{-15} ergs cm $^{-2}$ s $^{-1}$ Å $^{-1}$, respectively. The standard deviation of the individual flux density measurements in a given filter is $\simeq 0.2 \times 10^{-15}$ ergs cm $^{-2}$ s $^{-1}$ Å $^{-1}$, while the systematic uncertainty in the flux calibration is less than 10%.²

We obtained a subsequent *Chandra* observation to confirm the X-ray spectral properties, to investigate variability, and to examine (at higher angular resolution) any extended X-ray emission. PG 1004+130 was observed by *Chandra* on 2005 January 5 (ObsID 5606) for 41.6 ks with the Advanced CCD Imaging Spectrometer (ACIS; Garmire et al. 2003) S-array in faint mode. These data have been reprocessed (REPRO-III) to incorporate the latest calibration (CALDB ver. 3.2.0) including automatic application of both the ACIS charge-transfer inefficiency correction and the time-dependent gain adjustment. The ACIS-S3 image shows a bright point source at the location of the nucleus of PG 1004+130, jet-associated X-ray emission colinear with but mostly upstream of the SE radio jet, and several additional sources, two of which are coincident with the outer regions of the SE FR I lobe. These two sources have point-source *HST* counterparts; using the methodology and results of Maccacaro et al. (1988), we find that their X-ray-to-optical flux ratios are consistent with those expected for AGNs. We extracted the nuclear and the extended X-ray emission for spectral analysis, using regions

²OM Calibration Team: <http://xmm.vilspa.esa.es/sas/documentation/watchout/uvflux.shtml>

as shown in Figure 1a (a circle with a $4.8''$ radius for the nucleus and a $4.1''$ by $6.3''$ rectangle for the jet) and measuring the background from a large source-free elliptical region (with a $91''$ major axis and a $38''$ minor axis) east of the nucleus. There was no significant background flaring during the observation. Source-specific RMFs and ARFs were generated from the CALDB version 3.2.0 database; the ARFs include the effects of low-energy quantum-efficiency degradation due to contamination build-up on the ACIS optical-blocking filter. The extracted nuclear spectrum was binned to contain at least 20 counts per bin using the FTOOLS task *grppha*. The 0.5–8 keV nuclear spectrum contains ~ 1800 counts (of which only ≈ 5 are expected to be from background), and there are ~ 30 counts in the extended X-ray emission.

We supplement the *XMM-Newton* and *Chandra* data with previously published and archival radio, IR, optical, and UV coverage of PG 1004+130. VLA observations of PG 1004+130 have been performed in several configurations and bands, and we make use of 1.4 GHz, $5.4''$ FWHM catalog images from the FIRST survey (Becker et al. 1995) as well as *C* band (B configuration) data from 1979 taken by E. Fomalont (Fomalont 1981) and *L* band (A configuration) data from 1982 taken by J. Wardle. Images for these latter two observations were constructed using *uv* components between $20k\lambda$ and $160k\lambda$, allowing investigation of the small-scale structure along the jet at a resolution of $1.5''$ while excluding the large-scale structure already apparent in the FIRST image. IR fluxes were obtained from *Infrared Astronomical Satellite* (*IRAS*; 100 – $12\ \mu\text{m}$), ground-based (*N*, *M*, and *L* bands), and Two Micron All-Sky Survey (2MASS; *K*, *H*, and *J* bands) data. An optical spectrum and photometric *ugriz* magnitudes were taken from the SDSS database (PG 1004+130 is SDSS J100726.10+124856.2) and an *HST* Wide Field Planetary Camera 2 (WFPC2) image of PG 1004+130, taken with the F606W filter and analyzed and discussed by Bahcall et al. (1997), was used to search for extended optical emission. PG 1004+130 has been observed spectroscopically in the UV by *HST* (initially with GHRS and later with STIS; Wills et al. 1999), *IUE* (with both the long and short-wavelength spectrographs), and the *Far Ultraviolet Spectroscopic Explorer* (*FUSE*, and portions of these data have been incorporated as well.

X-ray, optical, and radio images of PG 1004+130 are presented in Figure 1. The 0.5–4 keV X-ray image of Figure 1a has been constructed with ACIS pixel randomization removed to increase angular resolution and is shown with overlaid 4.9 GHz VLA contours; the jet-associated X-ray emission commences upstream of the radio jet and extends to the first radio knot. Examination of the optical *HST* image with accompanying radio and smoothed X-ray contours reveals no apparent optical counterpart to the SE FR I jet. A spectral index map of PG 1004+130 generated from 4.9 and 1.5 GHz VLA images of $\sim 1.5''$ resolution is presented in Figure 1c, along with a high-resolution ($0.5''$ FWHM) 5 GHz VLA image of the nuclear region. There does not appear to be any extended kpc-scale inner-jet radio emission from PG 1004+130. The spectral index α_r is -0.41 for the nucleus ($f_\nu \propto \nu^\alpha$) and varies along the jet. The error in the spectral index increases greatly toward the edges of the emission, but the signal-to-noise ratio in both bands is quite high down the spine of the jet; the repeated spectral steepening is genuine. We rebinned the X-ray image to $0.05''$ pixels and extracted the radial profile along the SE radio jet (using concentric annular sectors restricted to a 30° arc) as well as excluding the jet (using annular sectors covering the remaining 330°), subtracting background

as determined from a nearby rectangular region. The background-subtracted surface-brightness profiles are compared with normalized ACIS-S point spread functions (created with *mkpsf*) in Figure 1d. As the nucleus contains ~ 1080 counts from 0.5–2 keV and ~ 730 counts from 2–8 keV, the pre-calculated 1.5 keV response data are sufficient for this analysis. The nucleus appears unresolved, but the jet-associated emission is inconsistent with a point-source profile.

We are confident that the jet-associated X-ray emission arises in a genuine counterpart to the SE FR I radio jet due to the low probability of finding a background source so close to the PG 1004+130 nucleus, the high X-ray-to-optical flux ratio of this feature, and the extended nature of the X-ray emission as well as its position upstream of the peak radio brightness in the jet. From Bauer et al. (2004), the expected sky density of sources (primarily AGNs) with 0.5–2 keV X-ray fluxes comparable to or greater than the $S_{0.5-2} \approx 1.8 \times 10^{-15}$ erg cm $^{-2}$ s $^{-1}$ of the jet is $N(> S) \approx 500$ deg $^{-2}$. Consequently, the probability of finding a background source of appropriate brightness within 10'' and aligned (within 30°) with either the jet or counterjet of PG 1004+130 is only ≈ 0.002 . Further, the lack of any *HST* point sources coincident with the X-ray emission restricts the nature of any such background source; the optical upper limit yields an X-ray-to-optical flux ratio, as defined by Maccacaro et al. (1988), that is more than ~ 20 (~ 8) times greater than the maximum value for AGNs (BL Lac objects) observed by Maccacaro et al. (1988). The X-ray emission is extended along the path of the radio jet, and the peak X-ray brightness in the jet occurs upstream of the peak radio brightness, consistent with the observed trend for the ratio of X-ray-to-radio emission to decrease along jets (e.g., Marshall et al. 2002; Sambruna et al. 2004).

Large-scale diffuse X-ray emission is common within groups and clusters, is sometimes seen in halos around radio-loud quasars (RLQs), and has been observed along radio jets. The intra-group, intra-cluster, and halo X-ray emission is well-established to be thermal radiation from hot gas, but the origin of diffuse X-ray emission along jets is much less certain; IC/CMB scattering has been suggested as a reasonable explanation (e.g., Siemiginowska et al. 2002; Schwartz et al. 2005). We adaptively smoothed the 0.5–4 keV *Chandra* image to search for diffuse extended emission in the vicinity of PG 1004+130; the resulting image is presented in Figure 2a with overlaid 1.4 GHz FIRST contours. The local environment of PG 1004+130 is sparsely populated; McLure & Dunlop (2001) found that PG 1004+130 has the lowest clustering amplitude among the 13 RLQs they surveyed, and the nearest known companion galaxy lies 33.4'' (127 projected kpc) to the south-west, with another associated galaxy 45'' (170 kpc) to the west (Stockton 1978; Bahcall et al. 1997). There does not appear to be any detectable X-ray halo of quasi-spherical, hot, thermally emitting gas around PG 1004+130. The hybrid radio morphology of PG 1004+130 may suggest that the density of the surrounding medium is higher to the SE, where the radio jet is quickly decollimated, than to the NW, where the unseen counterjet powers a distant, edge-brightened lobe, although the lack of any apparent interaction with the few neighboring field galaxies leaves the mechanism for generating such an asymmetrical density distribution unclear. We do not observe any strong gradient in diffuse X-ray emission from the SE to the NW, but naturally this does not prohibit large-scale, asymmetrically distributed, colder gas. However, PG 1004+130 does show intriguing diffuse emission along the path of the SE jet and NW

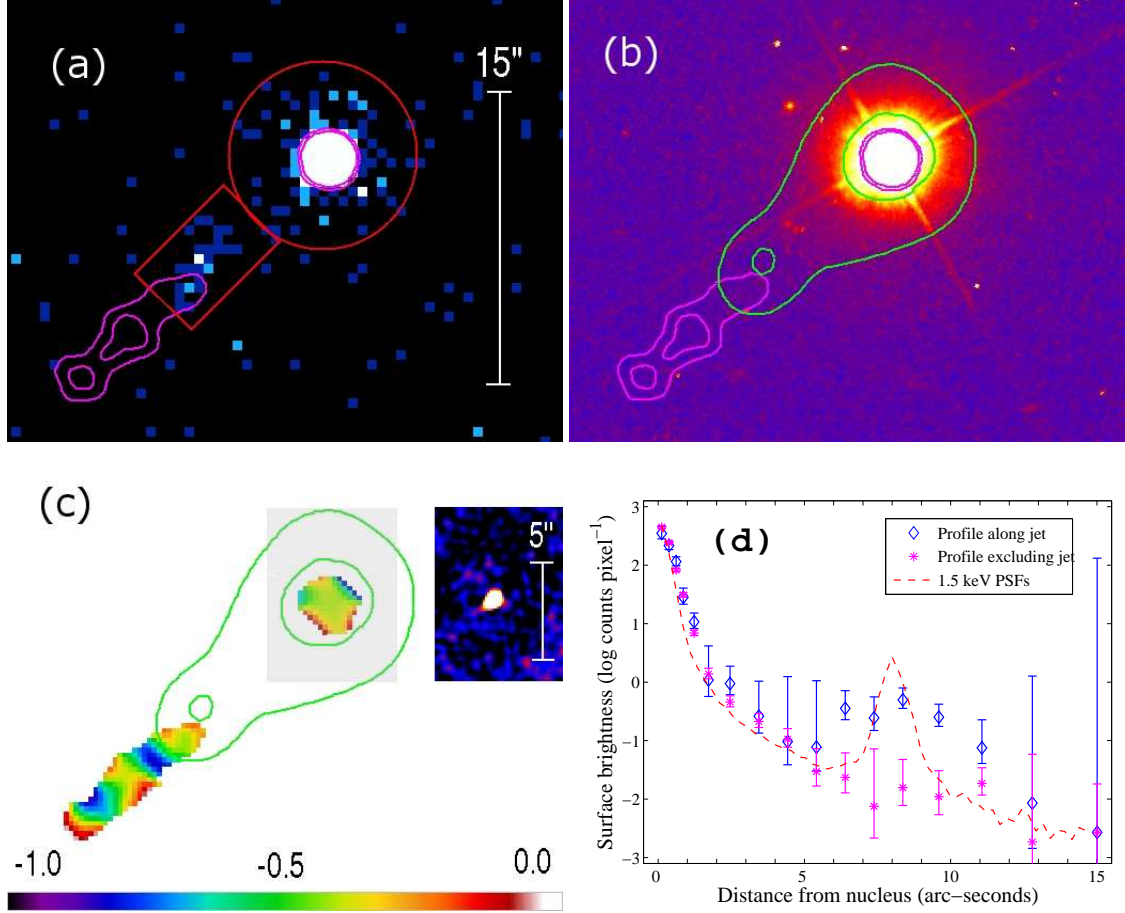


Fig. 2.1 (a) *Chandra* 0.5–4 keV ACIS-S3 image (with pixel randomization removed) of PG 1004+130. There are ~ 30 counts in the jet (box region) and ~ 1600 in the nucleus (circular region) in this band. Overlaid magenta contours show 4.9 GHz emission observed by the *VLA* with 1.5" resolution; the X-ray jet occurs upstream of most of the radio emission. 15" is 57 projected kpc. (b) *Hubble Space Telescope* WFPC2 image of PG 1004+130, taken with the F606W filter, overlaid with green contours from the smoothed *Chandra* image and magenta radio contours duplicated from (a). The scale is identical to (a) and the X-ray contour levels are 0.05 and 0.20 counts pixel⁻¹ (approximately 0.3 and 1.3×10^{-33} ergs cm⁻² s⁻¹ Hz⁻¹ arcsec⁻²). (c) Spectral-index map of the FR I jet (linear color scale given at bottom), generated from 4.9 and 1.5 GHz *VLA* images of $\sim 1.5''$ resolution. Inset shows a 0.5" resolution 5 GHz image. (d) Background-subtracted X-ray radial profiles of the nucleus and jet compared with normalized 1.5 keV point spread functions located at the nucleus and jet centroids. The nucleus is unresolved, but the jet is extended.

counterjet. We verified that this emission was not an artifact of the smoothing process by extracting radial profiles from the rebinned image as with the PSF analysis described previously; here we use the regions indicated in Figure 2a to obtain surface-brightness profiles along the jet, counterjet, and non-jet background (excluding all point sources). Figure 2b shows that beyond $\sim 16''$ (past the SE X-ray jet emission), the diffuse emission in the jet and counterjet is similar and clearly surpasses the emission from the non-jet background region; we calculate ~ 29.3 counts above background in the 0.5–4 keV diffuse emission from $16''$ to $63''$ to the SE, and ~ 27.4 to the NW. Note that the ACIS readout streak cannot contribute significantly to the diffuse emission, as it should contain less than 6 total counts over the jet/counterjet region, is offset by $\sim 15^\circ$ from the jet position angle, and would extend the entire length of the chip. Extended X-ray emission around RLQs has occasionally been noted to follow the direction of the radio lobes (e.g., Croston et al. 2004, 2005) but detection of an X-ray counterjet component is somewhat unusual (cf. Schwartz et al. 2005). We briefly consider the nature of this large-scale emission in §4.2.

The X-ray light curves of PG 1004+130 do not reveal significant rapid variability within either the *XMM-Newton* or the *Chandra* observations. The cumulative photon arrival times are consistent with a constant count rate, with Kolmogorov-Smirnov probabilities of 0.64 and 0.61 for *XMM-Newton* (pn detector) and *Chandra*, respectively. The 1σ upper limit to the 0.5–8 keV count-rate variability on 1 ks timescales is $<12\%$ over the *XMM-Newton* observation, and $<15\%$ over the *Chandra* observation. After accounting for the relative number of soft (0.5–2 keV) and hard (2–8 keV) band counts, the 1σ upper limit to hard band variability is somewhat greater than that for the soft band.

2.3 X-ray Spectral Analysis

We analyzed the X-ray spectra using the most recent (v12.2.1) XSPEC (Arnaud 1996) software package. Data associated with energies below 0.4 keV or above 8.0 keV were discarded for the purposes of fitting; these cutoffs were imposed due to increasing calibration uncertainties at low energies and declining source counts (due to decreasing instrumental effective area and the spectral shape) as well as increasing background at high energies. All fits include Galactic absorption fixed at $3.93 \times 10^{20} \text{ cm}^{-2}$ (Murphy et al. 1996). Joint fitting of the spectra from the *XMM-Newton* pn, MOS1, and MOS2 detectors increases the signal-to-noise ratio and is consequently preferred in the absence of significant cross-calibration uncertainties. Fitting a simple power-law model gives consistent results (the 90% confidence intervals for both photon index and normalization overlap for the pn, MOS1, and MOS2 detectors); therefore, all model parameters with the exception of normalization have been fit jointly throughout the remainder of the analysis. Unless otherwise noted we quote the outcome of fitting various models to the binned spectra with χ^2 minimization, but the following results agree with those obtained by fitting the ungroupped spectra with the XSPEC *C*-statistic (after Cash 1979).

Given the BALs observed in the UV by Wills et al. (1999) and the correlation between BALs and X-ray absorption (e.g., Gallagher et al. 2002), we anticipated potential X-ray absorption at low energies. In an effort to disentangle the underlying power law from any intrinsic absorption, we initially fit only the data in the 2–8 keV range with

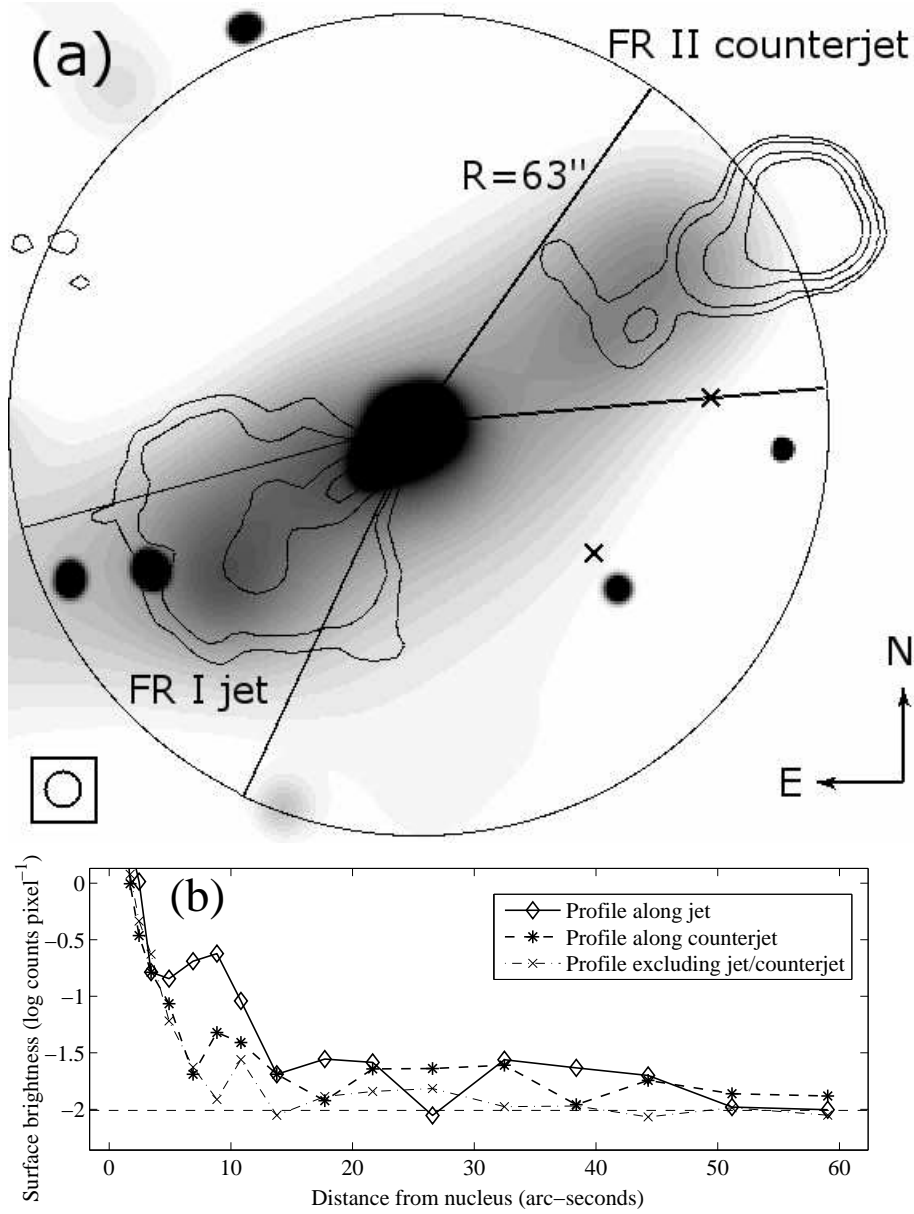


Fig. 2.2 (a) Adaptively smoothed 0.5–4 keV *Chandra* image overlaid with 1.4 GHz radio contours from the FIRST survey. Levels are 1.5, 3, 8, and 15 mJy beam⁻¹; the 5.4'' FWHM beam is shown at lower left. There are two unrelated background X-ray sources located near the end of the SE radio jet, and the positions of the two galaxies believed to be associated with PG 1004+130 are indicated with crosses. Diffuse X-ray emission is observed along both the SE jet and the NW counterjet. (b) Surface brightness radial profiles along the jet, counterjet, and non-jet regions as indicated in (a); contaminating point sources have been removed for this analysis, and the local background is indicated with a dashed line. Past the inner 16'' where the X-ray jet is found, the surface brightness of the diffuse emission is similar to the SE and the NW, and in both the jet and counterjet regions the diffuse emission is significantly higher than the background out to $\approx 50''$.

a power-law model. The photon index obtained by jointly fitting the pn, MOS1, and MOS2 data from *XMM-Newton* is $\Gamma = 1.57^{+0.13}_{-0.19}$, consistent with the *Chandra* result of $\Gamma = 1.52^{+0.16}_{-0.26}$. This photon index is typical for the high-energy spectra of RLQs; e.g., Reeves & Turner (2000) found $\langle\Gamma\rangle = 1.66$ with $\sigma = 0.22$ for an *Advanced Satellite for Cosmology and Astrophysics* (*ASCA*) sample of 35 RLQs, while Page et al. (2005) determined $\langle\Gamma\rangle = 1.55$ with $\sigma = 0.29$ for an *XMM-Newton* sample of 16 RLQs at $z > 2$. The 2–8 keV *XMM-Newton* pn model flux is $2.57^{+0.35}_{-0.66} \times 10^{-13}$ ergs cm $^{-2}$ s $^{-1}$, 23% lower than the *Chandra* result of $3.32^{+0.87}_{-1.05} \times 10^{-13}$ ergs cm $^{-2}$ s $^{-1}$; this flux difference exceeds cross-calibration uncertainties, which are on the order of 12% (S. Snowden 2005, private communication).

Many AGNs with significant X-ray absorption also have strong Fe K α emission lines (e.g., see the *ASCA* observations of Seyfert 2 galaxies by Turner et al. 1997). This was predicted by Krolik & Kallman (1987), who argued that the prominence of iron features produced in the scattering and reflection regions increases as the observed X-ray continuum becomes dominated by reprocessed radiation. Examination of the residuals from the power-law fit described above did not show any obvious emission features in the X-ray spectrum of PG 1004+130. We tested for Fe K α emission by adding an unresolved ($\sigma = 0.01$ keV) redshifted Gaussian emission line to the 2–8 keV power-law model. Here we fit the ungrouped data (with the XSPEC *C*-statistic), as the large energy bins at high energy would tend to smooth out any narrow line in the binned spectra. The *XMM-Newton* pn and MOS spectra show no evidence for neutral or ionized Fe K α emission and an upper limit of 105 eV (90% confidence) can be placed on the rest-frame equivalent width of a narrow line at a fixed rest-frame energy of 6.4 keV from the pn spectrum. Modeling the *Chandra* spectrum by adding a narrow line at rest-frame 6.4 keV imposes an upper limit of 121 eV on the intrinsic equivalent width. If the line energy is allowed to vary, there is marginal evidence for emission at $6.57^{+0.15}_{-0.11}$ keV; the rest-frame equivalent width of the line is only 105^{+109}_{-88} eV. Since this line energy does not match the transition energy for Fe K α emission from either neutral/low ionization (6.4 keV), He-like (6.7 keV), or H-like (6.9 keV) iron, if the marginal detection is assumed to be indicative of physical conditions then there must be a range of ionization states in the scattering material. Overall, the lack of strong Fe K α emission argues against a scenario in which the nucleus of PG 1004+130 is heavily absorbed and the weak continuum arises chiefly from scattering or reflection.

We extrapolated the 2–8 keV power-law fits to lower energies to search for X-ray absorption, as illustrated in Figures 3a and 3b. Many quasars, including radio-loud objects, show enhanced flux above a power-law model below ~ 2 keV (Porquet et al. 2004; Brocksopp et al. 2006); no such soft excess is observed from PG 1004+130. While there is only minimal evidence for intrinsic absorption in the *XMM-Newton* spectra, the large systematic negative residuals in the *Chandra* spectrum indicate substantial absorption. This significant change in the absorption properties of PG 1004+130 occurred over only 494 rest-frame days. We characterized this absorption by adding a redshifted neutral absorber to our model and expanding the range of the fit to 0.4–8 keV. The *XMM-Newton* spectra do not require any intrinsic absorption (the 90% confidence upper limit is $N_{\text{H}} < 1.6 \times 10^{20}$ cm $^{-2}$) and the modest negative residuals in Figure 3a disappear in

Figure 3d (top plot) when the photon index is adjusted to $\Gamma = 1.37_{-0.05}^{+0.07}$. Applying this procedure to the *Chandra* data does indeed indicate the presence of intrinsic absorption, but the negative residuals in the *Chandra* spectrum of Figure 3b are accommodated primarily through an extreme flattening of the photon index to $\Gamma = 1.13_{-0.09}^{+0.10}$. This model is physically implausible in light of the inconsistency with the best-fit high-energy photon index, and it is also not a particularly good fit ($\chi^2/\nu = 85/76$). A lower limit to the intrinsic absorption indicated by the *Chandra* spectrum may be obtained by constraining Γ to lie within the 90% errors from the high-energy fit; the resulting column density is $N_{\text{H}} < 9.29 \times 10^{20} \text{ cm}^{-2}$, with Γ fixed at 1.26. The residuals for this fit (shown in Figure 3d, middle plot) suggest that further refinements to the absorption model are required.

Complex absorption is common in BAL quasars, of both the radio-quiet (e.g., Gallagher et al. 2002) and the radio-loud (Brotherton et al. 2005) types, and thus it is perhaps not surprising that the simple intrinsic-absorption model is insufficient to fit the *Chandra* spectrum for PG 1004+130. A partial-covering absorber model gives a better representation (χ^2/ν decreases from 85/76 to 79/75, an improvement with an *F*-test probability of only 0.02 of occurring by chance; see Figure 3d, bottom plot), with parameters $N_{\text{H}} = 1.20_{-0.84}^{+0.83} \times 10^{22} \text{ cm}^{-2}$, $f_c = 0.49_{-0.26}^{+0.14}$, and $\Gamma = 1.37_{-0.22}^{+0.18}$. Here f_c is the fraction of the source emission that passes through an intrinsic redshifted absorber with column density given by the fitted N_{H} , while the remaining $1 - f_c$ of the source emission experiences only Galactic absorption. Given our photon statistics, we cannot constrain the nature of the absorption complexity in detail, but the physical significance of this result is discussed further in §5.

While variable absorption appears to be required in PG 1004+130, a brief consideration of possible alternative explanations for the discrepancy between the *XMM-Newton* and *Chandra* soft-band spectra is warranted. The small-scale jet seen in the *Chandra* image and unresolved by *XMM-Newton* is much too weak to explain the differences in the soft X-ray spectra: when the larger *XMM-Newton* extraction region, which includes the jet, is used to extract a *Chandra* spectrum, the resulting parameters for the partial-covering absorber model are similar to those found above, with $N_{\text{H}} = 0.95_{-0.97}^{+0.81} \times 10^{22} \text{ cm}^{-2}$, $f_c = 0.42_{-0.28}^{+0.17}$, and $\Gamma = 1.30_{-0.21}^{+0.20}$. Another possibility is that the change in the low-energy X-ray spectrum may be due to variable soft-band emission rather than variable absorption. It has been suggested that the “soft excess” in FR II objects may be related to jet emission (e.g., Evans et al. 2006), and so perhaps a variable unresolved jet might explain the discrepancy between the *XMM-Newton* and *Chandra* spectra. The *XMM-Newton* spectra can also be adequately fitted with a partial-covering absorber with parameters fixed (except for normalization) to the best-fit *Chandra* values, and an additional “unresolved jet” power-law component with a likely photon index fixed at $\Gamma = 1.8$. The unresolved jet would then have had to decrease in brightness by a factor of ~ 15 by the *Chandra* observation; flaring on that order has been observed in the inner jet knot of M87 (Harris et al. 2006), so it is possible (albeit somewhat contrived) that the *XMM-Newton* observation occurred during a flaring episode. However, the unresolved jet must contribute approximately one-fourth of the total *XMM-Newton* 2–8 keV flux to avoid worsening the fit, and as the *XMM-Newton* hard-band flux is already observed to be lower than that measured by *Chandra*, additional variability of the nuclear X-ray emission would be required. The coincidental

brightening of the unresolved jet during the presumed flare episode to the level necessary to mimic the unbroken, continuous power-law seen in the *XMM-Newton* spectra further suggests that variable absorption is a more logical explanation than such conspiratorial combinations of variable emission components. Note that disfavoring an additional variable unresolved jet component does not impact interpretation of the underlying origin of the entire 0.5–8 keV nuclear X-ray emission, a topic considered further in §5.

The 0.5–2 keV observed fluxes for the best-fit models as described above are 1.07×10^{-13} ergs cm $^{-2}$ s $^{-1}$ for *XMM-Newton* and 9.35×10^{-14} ergs cm $^{-2}$ s $^{-1}$ for *Chandra*, with 2–8 keV fluxes of 2.60×10^{-13} ergs cm $^{-2}$ s $^{-1}$ and 3.56×10^{-13} ergs cm $^{-2}$ s $^{-1}$, respectively. The observed 1980 *Einstein* 0.5–4.5 keV soft-band limit would predict (for a $\Gamma = 1.5$ power-law model with Galactic absorption) 0.5–2 keV and 2–8 keV fluxes of 6.7×10^{-14} ergs cm $^{-2}$ s $^{-1}$ and 1.5×10^{-13} ergs cm $^{-2}$ s $^{-1}$, respectively, with a greater uncertainty applying to the high-energy extrapolation; both the *XMM-Newton* and the *Chandra* soft and hard-band fluxes are higher than suggested by the *Einstein* non-detection. The *Einstein* non-detection cannot be explained by simply increasing the covering factor while holding the column density fixed to the value measured in the *Chandra* spectrum, as even with $f_c=1$ the predicted 0.5–4 keV flux is higher than the limit measured by *Einstein*. If the *Einstein* non-detection results from variable absorption (rather than emission), then N_H must have been a factor of ~ 3 higher (for $f_c=1$) to account for the lack of soft-band X-ray flux relative to the *Chandra* observation. The unabsorbed 0.5–2 keV (rest-frame 0.6–2.5 keV) luminosities are 2.08×10^{43} ergs s $^{-1}$ for *XMM-Newton* and 2.98×10^{43} ergs s $^{-1}$ for *Chandra*, with 2–8 keV (rest-frame 2.5–9.9 keV) luminosities of 4.52×10^{43} ergs s $^{-1}$ and 6.44×10^{43} ergs s $^{-1}$.

There are sufficient counts to fit the *Chandra* X-ray jet spectrum with a simple power-law model (assuming fixed Galactic absorption), although the small number of counts necessitates use of the XSPEC *C*-statistic rather than χ^2 . The best-fit photon index is $\Gamma = 1.71^{+0.51}_{-0.47}$. A power-law model is almost universally appropriate for the X-ray spectra of jets (e.g., Worrall & Birkinshaw 2006), but with the limited counts available here other possibilities cannot be excluded. For example, a thermal bremsstrahlung model also yields an acceptable fit (the *C*-statistic value is essentially unchanged) with $kT \sim 5$ keV, although the temperature is poorly constrained. The 0.5–2 and 2–8 keV fluxes associated with the power-law model are 1.8 and 3.1×10^{-15} ergs cm $^{-2}$ s $^{-1}$, respectively, corresponding to unabsorbed luminosities of 3.6 and 5.3×10^{41} ergs s $^{-1}$ (quoted for isotropic, unbeamed emission; see §4.2).

2.4 Multiwavelength Properties

2.4.1 The Nucleus

The optical/UV-to-X-ray spectral slope, α_{ox} , describes the ratio of rest-frame luminosity density at 2500 Å to that at 2 keV as $\alpha_{\text{ox}} = 0.384 \times \log(l_x/l_{\text{uv}})$; we take l_{uv} and l_x to have units of erg s $^{-1}$ Hz $^{-1}$ throughout. The optical/UV and X-ray luminosities of radio-quiet quasars (RQQs) are correlated ($l_x \propto l_{\text{uv}}^\alpha$), although not directly proportional (e.g., Strateva et al. 2005; Steffen et al. 2006). This relationship likely reflects a connection between optical/UV emission from the inner accretion disk and X-ray emission

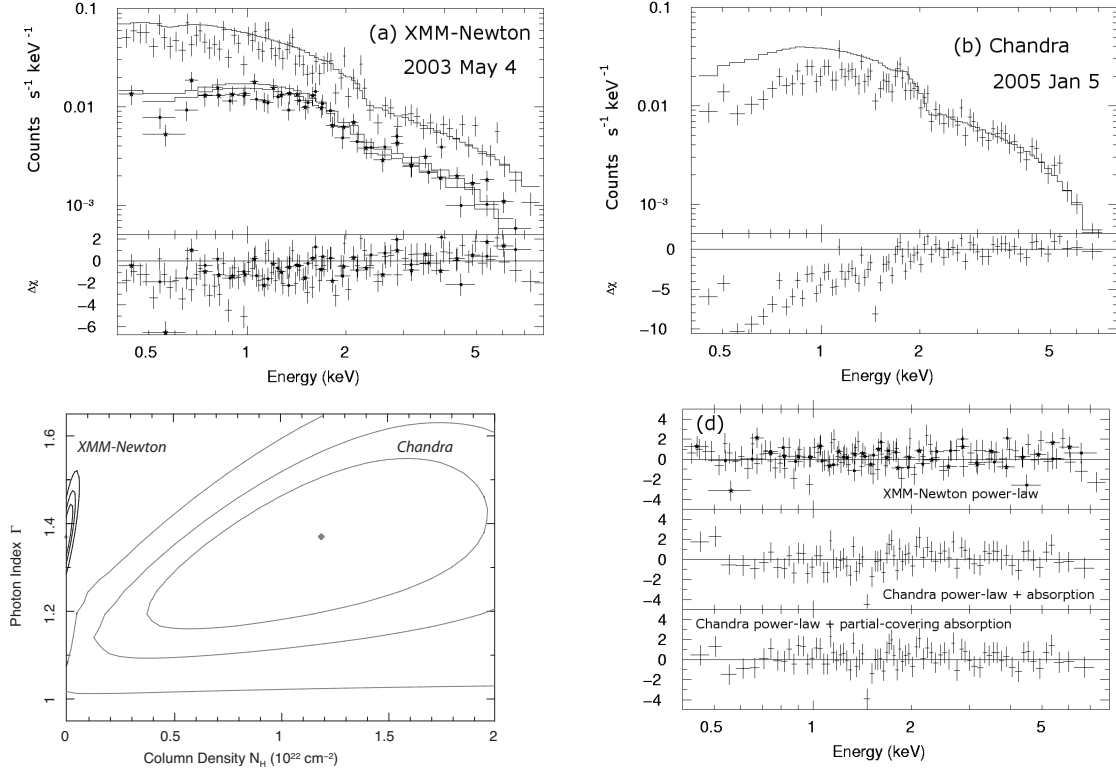


Fig. 2.3 (a) *XMM-Newton* pn (plain crosses) and MOS (dots and stars) spectra of PG 1004+130, shown with a model consisting of fixed Galactic absorption and a power-law component; the power-law fit was performed over the 2–8 keV range and then extrapolated to lower energies. The residuals indicate the deviation of the data from the model in units of σ , and reveal only minimal evidence for intrinsic absorption. (b) *Chandra* ACIS-S3 spectra analyzed as above. It is apparent that the 2–8 keV fit does not satisfactorily extend to the soft X-ray band, indicating significant absorption. The photon index ($\Gamma \approx 1.5$) is consistent with that of the *XMM-Newton* fit. (c) $N_H - \Gamma$ contours (at 68%, 90%, and 99% confidence) for the best-fit models illustrating that the tight constraints on any intrinsic neutral absorption in the *XMM-Newton* spectrum (black contours) conflict with the column density of the partial-covering absorber in the *Chandra* spectrum (gray contours). The photon indices are again similar but slightly flatter ($\Gamma \approx 1.4$) than for 2–8 keV power-law models. (d) Residuals from the fits, showing the *XMM-Newton* power-law model (top plot), the *Chandra* power-law model with intrinsic neutral absorption (middle plot), and the *Chandra* partial-covering absorption model (bottom plot).

arising from Compton upscattering of disk photons in a hot corona. In RLQs this picture is complicated by additional jet emission, and in both RQQs and RLQs absorption can significantly depress X-ray flux. The ratio of optical/UV to X-ray luminosity increases with increasing optical/UV luminosity, which may be expressed as an anti-correlation between α_{ox} and l_{uv} ; Steffen et al. (2006) found $\alpha_{\text{ox}} = -0.139 \times \log l_{\text{uv}} + 2.680$ for their sample of unabsorbed RQQs. We compare the α_{ox} value for PG 1004+130 with those of other quasars with $M_B < -23$ and $z < 0.5$ in the Palomar-Green (PG; Schmidt & Green 1983) survey.

We make use of data from Steffen et al. (2006) for the PG α_{ox} values. They determined monochromatic UV luminosities by extrapolating known 3000 Å values to 2500 Å assuming $\alpha_o = -0.5$, and used *ROSAT* pointed and All-Sky Survey PSPC count rates with an assumed $\Gamma = 2$ power-law to calculate monochromatic X-ray luminosities. The parameterization of the luminosity dependence of α_{ox} for RLQs is not as accurately known as it is for RQQs. Worrall et al. (1987) found that RLQs with flat radio spectra also have somewhat flatter optical/UV-to-X-ray spectra than steep-spectrum RLQs (which they attribute to stronger jet X-ray emission in the flat-spectrum sources), but both flat-spectrum and steep-spectrum RLQs have $l_x \propto l_{\text{uv}}^\alpha$ correlations with slopes consistent (within the 90% error range) with those of RQQs. We therefore remove the luminosity dependence of α_{ox} using the Steffen et al. (2006) relation for RQQs discussed previously, which we find also orders RLQs adequately for purposes of comparison. The resulting $\alpha_{\text{ox}} - \alpha_{\text{ox}}(l_{\text{uv}})$ histograms are shown in Figure 4a. While there are some quasars in the negative α_{ox} tail of the RQQ distribution that lack evidence of intrinsic UV or X-ray absorption, those quasars with strong UV absorption all have anomalously steep optical/UV-to-X-ray spectral slopes. The two RLQs with confirmed intrinsic absorption (PG 1309+355 and 2251+113 both show UV and X-ray absorption) similarly have more negative values of luminosity-corrected α_{ox} than most of the unabsorbed RLQs.

The monochromatic UV luminosity for PG 1004+130 was determined from the *XMM-Newton* OM fluxes and SDSS spectroscopy, as the dates of these measurements are most nearly coincident with those of the X-ray observations. The SDSS spectrum was scaled by SDSS photometric measurements to correct for fiber inefficiencies. Extrapolation to rest-frame 2500 Å was performed by renormalizing a standard (Elvis et al. 1994) RLQ SED to fit the dereddened (Cardelli et al. 1989) optical/UV data; the scaled RLQ SED was matched to the OM UVW1 and UVM1 fluxes and is then only slightly below the continuum of the SDSS spectrum, giving a luminosity density of $\log l_{\text{uv}} = 30.51$. The monochromatic X-ray luminosity was calculated from the *Chandra* data for two different best-fit models (see §3 for details), the first a simple power-law fit over the observed 2–8 keV band (yielding a “hard” $\alpha_{\text{ox}} = -1.83$ determined by the high-energy X-ray spectrum) and the second a partial-covering neutral absorption model fit over the observed 0.5–8 keV band (yielding a “soft” $\alpha_{\text{ox}} = -1.88$ primarily influenced by the low-energy X-ray spectrum). The model flux densities were measured at rest-frame 2 keV (observed 1.6 keV) and converted to bandpass-corrected luminosity densities. The results of this analysis are plotted in Figure 3, along with the *Einstein* $\alpha_{\text{ox}} < -2.01$ limit from Elvis & Fabbiano (1984). We note that our l_{uv} is ≈ 2.5 times less than that used by Elvis & Fabbiano (1984) to determine α_{ox} , and the *Einstein* X-ray flux limit with our l_{uv} measurement would give $\alpha_{\text{ox}} < -1.97$. The 1973–1990 photographic monitoring

of Smith et al. (1993) indicates that PG 1004+130 fluctuates in optical brightness by ≈ 0.5 mag on timescales of 6–10 yr. More recently, Garcia et al. (1999; 2006, private communication) found that PG 1004+130 brightened and then dimmed over a magnitude range of $V = 14.7$ – 15.2 from 1993–1999 (the SDSS 2003 photometry corresponds to $V = 15.3$), and Stalin et al. (2004) found that PG 1004+130 dimmed in R by 0.09 magnitudes from 1999 March to 2000 April. The *Einstein* versus *Chandra* discrepancy in α_{ox} values arises from a combination of measurement uncertainties and genuine variability at both optical/UV and X-ray frequencies. The optical/UV-to-X-ray spectral slope is indeed steeper for PG 1004+130 than for other PG RLQs, even if calculated from the hard-band emission, and it is steeper than almost all of the non-absorbed RQQs as well. To differentiate conclusively between excess “big blue bump” emission (see Elvis & Fabbiano 1984) and X-ray weakness as the cause of the low value of α_{ox} , it is helpful to compare the broad-band SED of PG 1004+130 with those of other quasars.

The SED of PG 1004+130 presented in Figure 4b was constructed with radio and IR fluxes, optical and UV spectra and photometry, and the X-ray best-fit models. There are two sets of radio measurements shown: the Parkes data include the extended radio emission, while the *VLA* data are for the nucleus alone. The optical (SDSS) and UV (*HST* GHRS and *IUE*) spectra were smoothed to reduce noise, and the geocoronal Ly α region has been excluded. The SDSS spectrum was scaled to match SDSS photometric measurements, as described previously. Data were corrected for Galactic extinction [with $E(B - V) = 0.038$ mag] following Cardelli et al. (1989). We have included the best-fit *XMM-Newton* power-law model and the *Chandra* partial-covering absorber model with parameters as given in §3 (in both cases correcting for Galactic absorption), as well as the 2 keV flux density corresponding to the 0.5–4.5 keV *Einstein* limit. Bandpass-corrected luminosity densities at radio-to-X-ray rest-frame frequencies for PG 1004+130 are given in Table 1.

Comparing the standard quasar SEDs compiled by Elvis et al. (1994) to that of PG 1004+130 in Figure 4b, there is excellent agreement in the shapes of the SEDs at radio-to-optical/UV frequencies. There does not appear to be evidence for enhanced UV emission (relative to the radio, IR, and optical data), but PG 1004+130 is distinctly X-ray weak relative to RLQs with comparable optical/UV luminosities. Removing the intrinsic absorption apparent in the *Chandra* spectrum partially accounts for the weakness of the X-ray emission, but the unabsorbed *Chandra* and *XMM-Newton* power-law spectra remain below the standard RLQ X-ray emission. Some of this apparent X-ray weakness may be a consequence of the chosen method of comparison, as the Elvis et al. (1994) composite SEDs are biased toward X-ray-bright objects due to selection criteria requiring an *Einstein* detection. Indeed, the average α_{ox} of the RLQs used to construct the standard SED plotted in Figure 4b is $\langle \alpha_{\text{ox}} \rangle = -1.31$, corresponding to relatively greater X-ray luminosities than the $\langle \alpha_{\text{ox}} \rangle = -1.54$ average of the PG RLQs. However, the “hard” $\alpha_{\text{ox}} = -1.83$ for PG 1004+130 is still 1.2σ below the average α_{ox} of the PG RLQs; the corresponding ratio by which PG 1004+130 is X-ray weak relative to other PG RLQs is ~ 5.4 (for similar optical/UV luminosities).

The black-hole mass for PG 1004+130 was found by Vestergaard & Peterson (2006) to be $1.87^{+0.40}_{-0.40} \times 10^9 M_{\odot}$ (from the FWHM of the H β line and the monochromatic optical luminosity at 5100 Å), while Falomo et al. (2003) estimate a mass of $1.35 \times 10^9 M_{\odot}$ (from

Table 2.1 PG 1004+130 Multiwavelength Luminosity Data

Band	Frequency ^a	Luminosity ^b	Date ^c	Source
Radio ^d	8.00	34.26	...	PKS 80 MHz
	8.34	33.85	...	PKS 178 MHz
	8.70	33.58	...	PKS 408 MHz
	9.24	33.26 (31.92)	...	PKS (VLA) 1.4 GHz
	9.53	33.05	...	PKS 2.7 GHz
	9.79	32.77 (31.70)	...	PKS (VLA) 5 GHz
IR	12.57	32.85	1983	IRAS 100 μm
	12.79	32.40	1983	IRAS 60 μm
	13.17	32.24	1983	IRAS 25 μm
	13.49	31.98	1983	IRAS 12 μm
	13.55	31.56	1986/01	N (BJW ^e)
	13.89	31.40	1986/01	M (BJW ^e)
	13.98	31.23	1986/01	L' (BJW ^e)
	14.03	31.17	1986/01	L (BJW ^e)
	14.23	30.83	2000/04/06	2MASS K
	14.35	30.69	2000/04/06	2MASS H
	14.47	30.67	2000/04/06	2MASS J
Optical	14.62	30.64	2003/01/28	SDSS z
	14.70	30.66	2003/01/28	SDSS i
	14.78	30.61	2003/01/28	SDSS r
	14.90	30.61	2003/01/28	SDSS g
	15.02	30.61	2003/01/28	SDSS u
UV	15.11	30.48	2003/05/04	OM UVW1
	15.21	30.44	2003/05/04	OM UVM1
	15.24	30.38	2003/05/04	OM UVW2
	15.59	29.48	2000/12/17	FUSE
X-ray	17.68	25.36	1980/05/09	<i>Einstein</i>
	17.68	25.59	2005/01/05	<i>Chandra</i>
	17.68	25.56	2003/05/04	<i>XMM-Newton</i>

^aLog of rest-frame frequency in units of Hz.^bLog of bandpass-corrected luminosity density in units of $\text{ergs s}^{-1} \text{Hz}^{-1}$, after correcting for Galactic extinction.^cDate is UT yyyy/mm/dd^dParkes catalog data from Wright & Otrupcek 1990; note that due to limited resolution the luminosity densities from the Parkes survey quoted here are dominated by the extended emission. Luminosities for the nucleus alone measured from *VLA* data are given in parentheses.^eData obtained by author B.J. Wills

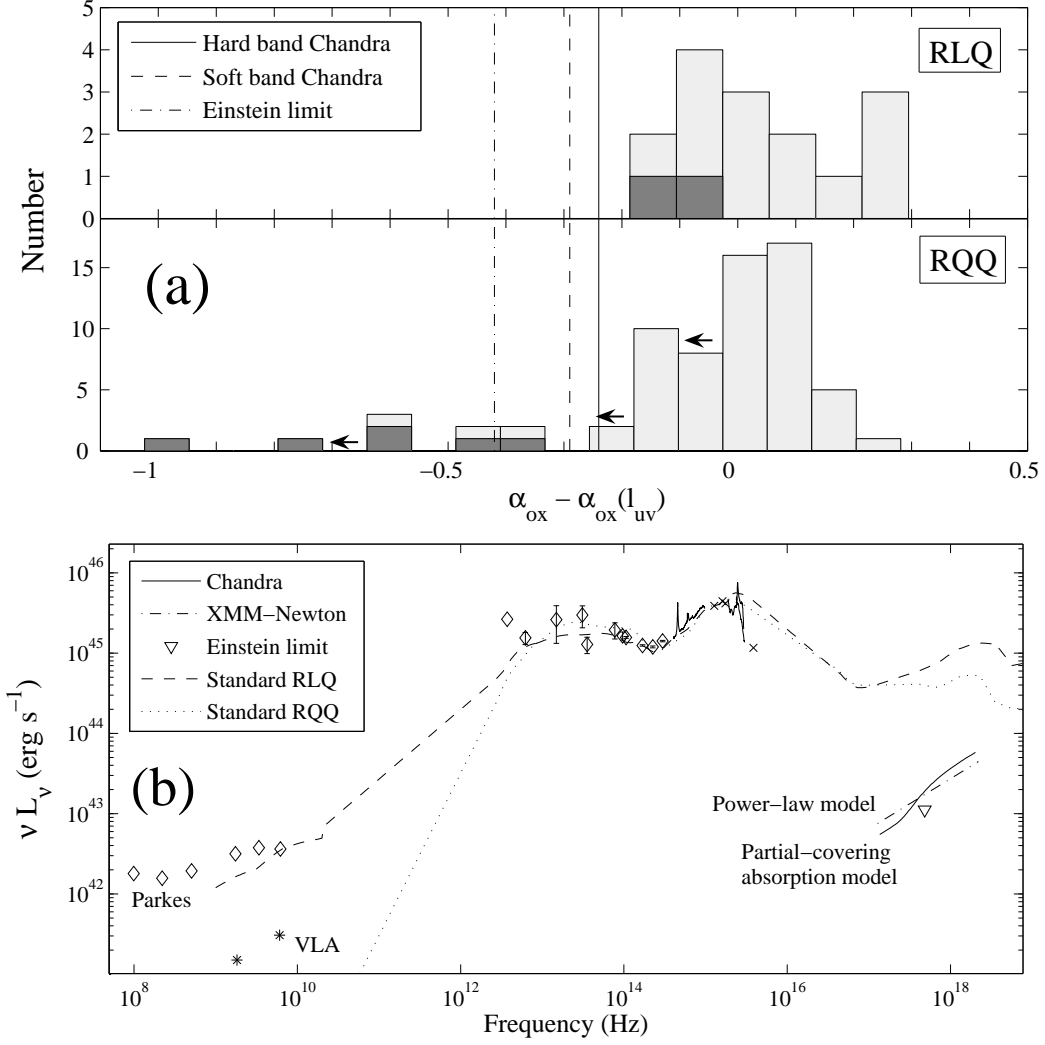


Fig. 2.4 (a) Comparison of the optical/UV-to-X-ray spectral slope, α_{ox} , of PG 1004+130 (corrected for luminosity dependence following Steffen et al. 2006) with radio-loud (top plot) and radio-quiet (bottom plot) quasars from the Palomar-Green survey. The subset of quasars with intrinsic absorption is shaded dark, and limits are indicated with arrows. Three values of α_{ox} are given for PG 1004+130, one from the *Einstein* limit (dot-dashed line) and two from the *Chandra* spectrum, the first based on the partial-covering absorber model (“soft band”, dashed line) and the next based on the 2–8 keV power-law model (“hard band”, solid line). PG 1004+130 shows an anomalously steep decline in intensity from optical/UV-to-X-ray wavelengths, an effect that is reduced for the hard band. (b) Rest-frame SED for PG 1004+130, with standard RLQ and RQQ SEDs from Elvis et al. (1994) overplotted for reference. The Parkes data include the extended radio emission, while the *VLA* data are given for the nucleus alone. The best-fit “unfolded” models for the *XMM-Newton* and *Chandra* spectra are shown. PG 1004+130 is X-ray weak relative to other RLQs. SED data and references are listed in Table 1.

the $M_{\text{BH}}-L_{\text{bulge}}$ relation). The black hole masses calculated for PG 1004+130 using these different methods are in general agreement and correspond to an Eddington luminosity of $\sim 2 \times 10^{47}$ ergs s $^{-1}$. We measure the bolometric luminosity for PG 1004+130 by integrating the scaled standard SED up to X-ray frequencies, then integrating the best-fit power-law model from rest-frame 0.5–10 keV, and obtain $L_{\text{Bol}} = 2.0 \times 10^{46}$ ergs s $^{-1}$. The observed X-ray emission may not be representative of the true X-ray power of the source (see §5); if instead the scaled standard SED is integrated to 10 keV, the bolometric luminosity is slightly higher, $L_{\text{Bol}} = 2.3 \times 10^{46}$ ergs s $^{-1}$. Both calculations suggest that PG 1004+130 is radiating at $L_{\text{Bol}} \sim 10^{-1} L_{\text{Edd}}$.

2.4.2 The Jet

The SE radio jet is made up of a string of emission peaks (knots), presumably indicating distinct shock sites where particle acceleration takes place. The spectral index α_{r} steepens downstream of each knot (see Figure 1c), perhaps reflecting an evolution in the underlying electron distribution. The observed-frame lifetimes for synchrotron cooling for plausible magnetic-field strengths are quite long, corresponding to scales orders of magnitude longer than these projected distances, so if spectral aging is the dominant factor behind this effect the electrons must remain trapped within the shock region for long periods before diffusing downstream. The X-ray emission begins upstream of the first bright radio knot, and there does not appear to be any jet-associated optical emission. Radio fluxes were extracted from the region encompassing the first knot, overlapping with the end of the X-ray jet extraction region indicated in Figure 1a and extending a short distance beyond it. A 5σ optical upper limit was determined from the noise in the *HST* image within the X-ray jet extraction region. The 2 keV νS_{ν} taken from the power-law fit to the jet X-ray spectrum and the error bars on α_{x} are plotted in Figure 5 along with the *HST* limit and the *VLA* fluxes. The power-law fit for the jet is consistent with the $\Gamma \sim 1.5$ photon indices found by Sambruna et al. (2004) for the brightest X-ray knots in their *Chandra* and *HST* survey of core-dominated FR II quasars with known radio jets; however, the X-ray spectra of prominent knots in FR I jets are generally steeper, with $\Gamma \sim 2.3$ (e.g., 3C 66B: Hardcastle et al. 2001; 3C 31: Hardcastle et al. 2002; M 87: Marshall et al. 2002; Cen A: Hardcastle et al. 2003; B2 0755+37: Parma et al. 2003). The $\alpha_{\text{rx}} = -0.87$ value for PG 1004+130 is similar to those seen for both FR I (FR I jet references as above) and FR II (Sambruna et al. 2004; Marshall et al. 2005) jets. The PG 1004+130 jet optical limit falls well below the power law connecting the radio and X-ray data, ruling out simple single-component synchrotron models. The broad-band spectral indices are constrained to be $\alpha_{\text{ro}} < -1.1$, $\alpha_{\text{ox}} > -0.46$, and consequently $\alpha_{\text{ro}}/\alpha_{\text{ox}} > 2.3$. These values are similar to those found for FR II jets (Sambruna et al. 2004) but are inconsistent with those of FR I jets, which tend to have $\alpha_{\text{ro}} \sim -0.7$, $\alpha_{\text{ox}} \sim -1.2$, and thus $\alpha_{\text{ro}}/\alpha_{\text{ox}} \sim 0.6$ (FR I jet references as above). Despite its standard FR I radio structure, the SE PG 1004+130 jet shares many of the characteristics of well-known FR II jets.

While the agreement between the multiwavelength characteristics of the SE FR I jet and powerful FR II jets initially appears somewhat surprising, this result might have been anticipated based on the radio luminosity and hybrid morphology of PG 1004+130.

The radio luminosity density at rest-frame 178 MHz of PG 1004+130 is $\sim 7.1 \times 10^{33}$ ergs s⁻¹ Hz⁻¹ (from the flux measurement of Wright & Otrupcek 1990), more than an order of magnitude above the 2×10^{32} ergs s⁻¹ Hz⁻¹ luminosity density found by Fanaroff & Riley (1974) to divide empirically the lower power FR I population from the higher power FR II sources. More recently, the radio power separating FR I from FR II sources has been observed to be an increasing function of the host galaxy optical luminosity (e.g., Ledlow & Owen 1996), and the optical magnitude ($M_R = -24.26$; Falomo et al. 2003) of its elliptical host (Bahcall et al. 1997) places PG 1004+130 somewhat closer to the observed transition line.³ Further, the NW lobe of PG 1004+130 has standard edge-brightened FR II structure. If hybrid morphology sources are reflective of dissimilar environments rather than dissimilar jets, as suggested by Gopal-Krishna & Wiita (2000), then the SE FR I jet should be as intrinsically powerful as the NW FR II jet.

We have applied various models to the multiwavelength jet emission with the goal of determining the most plausible origin for the X-ray emission. The results of this analysis are described below and representative models are shown in Figure 5. The radio-to-optical emission in jets is well-established as synchrotron radiation, with the principle observational support coming from polarization measurements. The radio data and optical limit allow determination of the magnetic field, assuming equipartition. Based on the *VLA* images we estimate the emission region to be roughly circular with a radius of around $1.75''$, corresponding to a spherical volume of 3.6×10^{67} cm³. As is standard practice, we assume a power-law electron energy distribution, with index $p=2$ to match the spectral slope of the *VLA* radio data (see Figure 1c). The low energy cutoff for the electron spectrum is observationally unconstrained, and we choose $\gamma_{\min}=50$, similar to values typically assumed for FR II jets. The high energy cutoff is limited by the *HST* non-detection, and we use $\gamma_{\max}=10^6$. In the case of PG 1004+130, the large angular size, the high lobe-to-core ratio, and the optical-to-radio core luminosity ratio suggest that the jet is inclined to the line of sight by $\theta \gtrsim 45^\circ$, which would limit the allowed beaming to $\delta \lesssim 1.4$. We consider here the $\delta=1$ case. We use standard synchrotron formulae (e.g., Worrall & Birkinshaw 2006) for a single-injection model with pitch-angle isotropization (Jaffe & Perola 1973). A continuous-injection model, in which the spectral slope steepens by 0.5 above a critical frequency (e.g., Carilli et al. 1991), would still require an exponential cutoff at frequencies below the optical limit, but a Kardashev-Pacholczyk (Kardashev 1962; Pacholczyk 1970) model with no pitch-angle scattering would allow a synchrotron cutoff at higher frequencies. The precise slope of the synchrotron spectrum above the turnover frequency does not greatly affect the X-ray emission, so a Kardashev-Pacholczyk or continuous-injection model would lead to similar qualitative conclusions. We derive a magnetic field strength $B_1 = 14 \mu\text{G}$, and note that in general $B_{eq} = B_1/\delta$ (e.g., Harris & Krawczynski 2002).

A natural explanation for the origin of the X-ray emission would be Compton upscattering by the synchrotron electrons. We consider two sources of seed photons: the synchrotron radiation itself (SSC; e.g., Hardcastle et al. 1998) or the cosmic microwave

³As noted by Scarpa & Urry (2001), the underlying radio and optical luminosity functions lead naturally to an anti-correlation of radio power with host luminosity, and hence host luminosity need not be physically indicative of radio characteristics.

background (IC/CMB; e.g. Tavecchio et al. 2000; Celotti et al. 2001). At the distance of the X-ray jet, the photon flux from the AGN or from the host galaxy is comparatively insignificant. The X-ray emission expected from the SSC process with the above parameters is more than three orders of magnitude less than the observed X-ray flux. The X-ray SSC emission increases relative to the synchrotron emission if the magnetic-field strength decreases, but radically sub-equipartition fields are required to attribute the observed X-ray flux to SSC emission. A representative model of this type is included in Figure 5. Both the high and low electron-energy cutoffs have been adjusted to accommodate the optical limit ($10^{3.2} < \gamma < 10^{7.5}$), but given the $p = 2$ power-law distribution and the consistent span of 4.3 decades in energy, the equipartition magnetic field remains $14 \mu\text{G}$. The actual magnetic field required to fit the X-ray flux is then $0.021 \mu\text{G}$, several hundred times less than the equipartition value. IC/CMB is often put forward as an explanation for the concave SEDs of powerful FR II jets, and this process is particularly efficient for high-redshift, relativistic jets inclined close to the line of sight. Unlike SSC, which is actually depressed by beaming, X-ray IC/CMB emission is boosted by an additional factor of $1+\alpha$ relative to synchrotron emission (Dermer 1995). In the case of PG 1004+130, the expected IC/CMB emission is still several hundred times less than the observed X-ray emission; the enhanced beaming required to match the X-ray flux, $\delta=3.0$, would place an upper limit (where $\delta = \Gamma$) on the jet angle of $\theta < \arcsin \delta^{-1} < 19^\circ$, smaller than the $\theta \gtrsim 45^\circ$ suggested from the optical and radio luminosities, as well as the radio morphology (see §1). Further, the lifetime of the low-energy electrons ($\gamma \sim 10^2$) responsible for the X-ray emission in IC/CMB models greatly surpasses the length of the jet, and so X-ray emission would be expected to persist along the jet (absent deceleration; e.g., Georganopoulos & Kazanas 2004). Despite the similarities in PG 1004+130 to the SEDs and X-ray spectra of the core-dominated, highly beamed FR II jets that dominate the surveys of both Sambruna et al. (2004) and Marshall et al. (2005), the IC/CMB model commonly applied to such FR II jets does not appear to be appropriate for PG 1004+130. For both SSC and IC/CMB models, the location of the X-ray emission largely upstream of the parent synchrotron electrons is difficult to explain, and the predicted X-ray spectral slope is flatter than observed. We consider it unlikely that the X-ray emission arises from either SSC or IC/CMB emission.

If the X-ray jet emission does not arise as a consequence of the low-energy synchrotron radiation (as in the SSC and IC/CMB cases), then various other emission mechanisms may be considered, such as thermal bremsstrahlung or synchrotron emission from a secondary population of high-energy electrons (e.g., Atoyan & Dermer 2004). The offset of the X-ray and radio emission is perhaps more easily accommodated by such models. The X-ray emission occupies a rectangular region of approximately $5''$ by $2.4''$; for an edge-on cylinder this again corresponds to a volume of $3.6 \times 10^{67} \text{ cm}^3$. The best-fit temperature for a bremsstrahlung model is $kT \sim 5 \text{ keV}$, but this is only poorly constrained. Neglecting line emission (which contributes significantly to the soft X-ray emission at lower temperatures), a gas cloud with an average ion charge of $Z \sim 1$ would be required to have a density of $n = 0.05 \text{ cm}^{-3}$ to account for the observed X-ray flux. This corresponds to a total mass of $1.5 \times 10^9 M_\odot$ and an ideal-gas pressure of $4.6 \times 10^{-10} \text{ dynes cm}^{-2}$. Such a large quantity of concentrated hot gas at so great a distance from the host galaxy seems unlikely, and as this gas cloud would be overpressured with respect

to the surrounding intergalactic medium (IGM) we would have to be observing it at a favorable time before it dispersed. If instead the X-ray emission from PG 1004+130 arises from a second synchrotron component generated by a population of highly relativistic electrons, the low-energy cutoff must be high enough to avoid over-predicting the optical flux. Taking the magnetic field to be $14 \mu\text{G}$ and setting the electron energy index to be $p=2.4$ as indicated by the X-ray photon index, this model provides an acceptable explanation of the X-ray emission with $\gamma_{\text{min}}=1.6 \times 10^7$, as shown in Figure 5. As the lifetime of the X-ray synchrotron electrons is quite short (electrons initially associated with 1 keV emission would have half lives of ~ 600 years), multiple acceleration or injection sites are required along the extent of the X-ray jet. Electrons with these injection parameters would lose sufficient energy within $\sim 30,000$ years to produce fluxes at optical frequencies in excess of the observed *HST* limit, suggesting that the energetic electrons escape the shock region before cooling to energies below $\gamma \sim 3 \times 10^6$.

The diffuse emission extends $40\text{--}50''$ ($150\text{--}190$ projected kpc) from the nucleus to both the SE and the NW, tracing the path of the FR I radio jet and providing supporting evidence for the presence of the hidden FR II counterjet. There are insufficient counts for spectral analysis, but with an assumed $\Gamma=1.8$ power law, the $0.5\text{--}8$ keV X-ray flux of the SE component is $4.5 \times 10^{-15} \text{ ergs cm}^{-2} \text{ s}^{-1}$, while that of the NW component is $4.2 \times 10^{-15} \text{ ergs cm}^{-2} \text{ s}^{-1}$. Most radio jets are one-sided, with the absence of a detectable counterjet generally attributed to Doppler boosting and hence yielding a constraint on the line-of-sight angle. As the line-of-sight angle for PG 1004+130 is likely $\theta \gtrsim 45^\circ$, the jet/counterjet flux ratio for twin jets is expected to be less than ~ 15 (using $R_j = [(1 - \beta \cos \theta)/(1 + \beta \cos \theta)]^{\alpha-2}$ and $\Gamma = \delta_{\text{max}} = 1/\sin \theta = 1.4$; e.g., Worrall & Birkinshaw 2006). However, the observed ratio of radio emission in the SE jet to that in the undetected NW counterjet exceeds 100, indicating that Doppler boosting alone cannot explain the lack of a radio counterjet in PG 1004+130. The diffuse X-ray emission precludes the possibility of an intrinsically one-sided jet, leading us to hypothesize that the entraining environment is indeed less dense to the NW, as suggested by the hybrid radio morphology.

If the diffuse X-ray emission is thermal radiation, then the required gas density is $\sim 4.5 \times 10^{-4} \text{ cm}^{-3}$, with a total mass of $2.3 \times 10^{11} M_\odot$ and a pressure of $1.5 \times 10^{-12} \text{ dynes cm}^{-2}$; while these parameters are not as restrictive as those for the thermal jet models, similar concerns apply. The mechanism for heating the gas along the jet is unclear, and a non-thermal origin seems somewhat more plausible. SSC emission alone is not a viable explanation for the diffuse X-ray emission, as the absence of a detectable radio counterjet to the NW imposes a stringent limit to the available synchrotron photon density above 1 GHz, and the concurrent lack of energetic electrons makes boosting to X-ray frequencies difficult. The diffuse X-ray emission could result from unbeamed IC/CMB emission, and indeed its apparently smooth extent along the entire jet suggests an association with long-lived electrons. The paucity of radio emission in the NW counterjet region does not greatly affect the IC/CMB X-ray yield, which is driven by low-energy electrons associated with sub-GHz synchrotron radiation. Diffuse X-ray emission unaccompanied by detectable radio emission has been observed in a handful of additional sources and can be successfully attributed to IC/CMB processes in those cases as well (e.g., Siemiginowska et al. 2002; Schwartz et al. 2005). The *VLA* C band limit on radio emission in

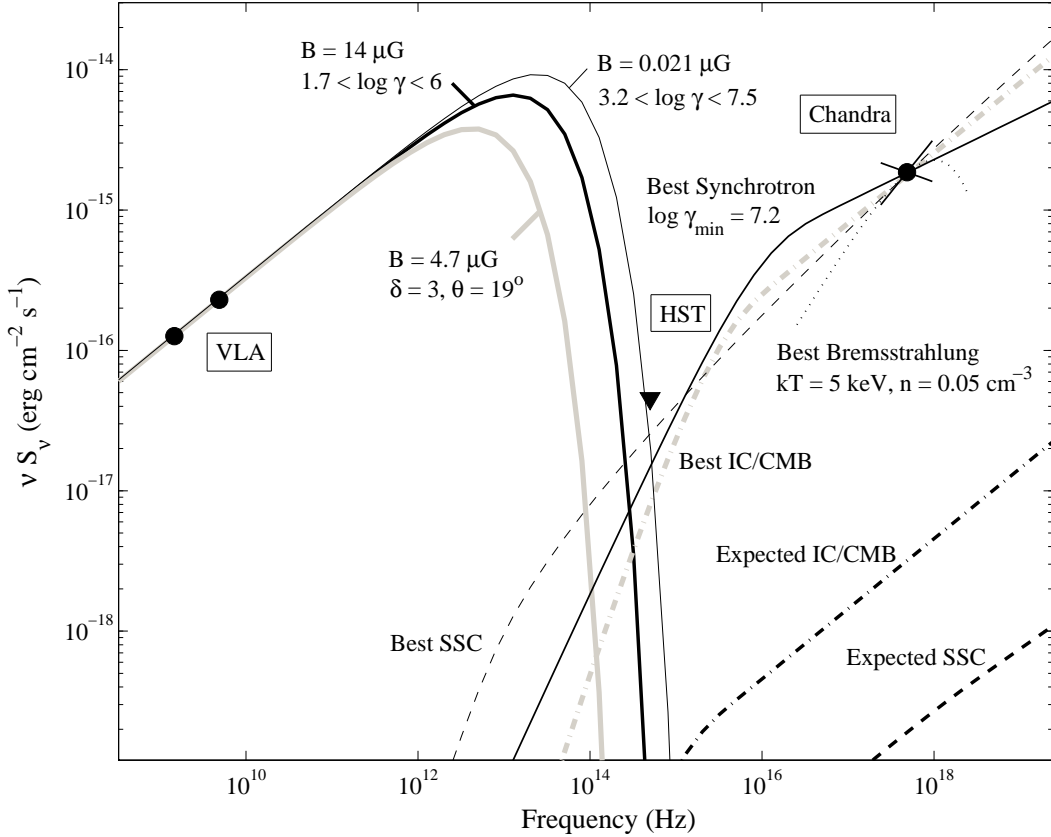


Fig. 2.5 Application of various models to the multiwavelength SED of the PG 1004+130 jet. Solid lines show synchrotron components, dashed lines show associated SSC emission, dot-dashed lines show associated IC/CMB emission, and the dotted line shows a bremsstrahlung model. The thickest black lines correspond to unbeamed models with an equipartition magnetic field of $B_{eq}=14 \mu\text{G}$, the thin black lines illustrate the “best-case” SSC model, with a highly sub-equipartition magnetic field of $B=0.021 \mu\text{G}$, and the thick gray lines illustrate the “best-case” IC/CMB model, in which the line-of-sight angle is constrained to be less than 19° for the required Doppler boosting of $\delta=3$. The X-ray photon index predicted by the SSC and IC/CMB models is flatter than observed and the presence of the X-ray emission largely upstream of the parent synchrotron electrons is difficult to explain. We consider the two-component synchrotron model to provide the most likely explanation of the multiwavelength jet emission.

the NW counterjet allows for considerable leeway in determining the high-energy cutoff and magnetic field required to generate sufficient diffuse X-ray emission via the IC/CMB process. For $\gamma_{min} = 50$ and $\gamma_{max} = 10^{3.5}$, the magnetic field is required to be lower ($\sim 2 \mu\text{G}$) than in the jet region, with equipartition electron densities ~ 30 times less than in the knots.

2.5 Results and Discussion

The primary results from our analysis of the first X-ray detections and spectra of PG 1004+130 are the following:

1. Variable complex absorption: Although the *XMM-Newton* observation of PG 1004+130 shows only minimal intrinsic absorption, the *Chandra* spectrum reveals significant soft X-ray absorption that cannot be modeled by a simple redshifted neutral absorber. The best-fit parameters for the preferred partial-covering model are $N_{\text{H}} = 1.20^{+0.83}_{-0.84} \times 10^{22} \text{ cm}^{-2}$, $f_c = 0.49^{+0.14}_{-0.26}$, and $\Gamma = 1.37^{+0.18}_{-0.22}$. The 2–8 keV *XMM-Newton* flux is 23% lower than the 2–8 keV *Chandra* flux.

2. X-ray weakness: PG 1004+130 has the lowest luminosity-corrected value of α_{ox} among the PG RLQs, and after correcting for intrinsic absorption it is ~ 5.4 times weaker in X-rays than the other PG RLQs, when normalizing to similar optical/UV luminosities. Examination of the SED of PG 1004+130 confirms that the anomalous value of α_{ox} is due to X-ray weakness rather than optical/UV brightness.

3. X-ray jet: The *Chandra* image reveals an X-ray counterpart to the SE radio FR I jet. The jet is undetected by *HST*, ruling out simple single-component synchrotron emission models, and both the X-ray spectrum and the multiwavelength SED shape are similar to those observed for prominent knots in FR II jets. Diffuse X-ray emission is observed along the path of the jet and counterjet.

Complex X-ray absorption is common in radio-quiet BAL quasars (e.g., Gallagher et al. 2002, 2006) and may be inferred by X-ray weakness coupled with relatively soft X-ray spectra for radio-loud BAL quasars as well (Brotherton et al. 2005). There is precedent for variable X-ray absorption such as that seen in PG 1004+130; Gallagher et al. (2004) found that PG 2112+059 showed a factor of ~ 7 increase in intrinsic N_{H} over three years (483 rest-frame days). The more absorbed *Chandra* spectrum for PG 2112+059 required either an ionized or partially covering absorber to fit the flat soft X-ray region and also revealed Fe K α emission undetectable against the higher continuum of the earlier *ASCA* observation, with a rest-frame equivalent width of $1050^{+520}_{-471} \text{ eV}$. The best-fit N_{H} for PG 1004+130 is relatively low compared with that of most radio-quiet BAL quasars, as is the covering fraction (cf. Green et al. 2001). Together these results suggest that the nature of the X-ray absorber is broadly similar in radio-quiet and radio-loud BAL quasars, but that the column density associated with the observed X-ray absorption is lower in radio-loud BAL quasars, somewhat analogous to the trend for UV absorption to be stronger in radio-quiet BAL quasars than in radio-loud BAL quasars (Becker et al. 2000).

Although notably X-ray weak relative to non-BAL RLQs, PG 1004+130 is not as X-ray weak as the BAL RLQs examined by Brotherton et al. (2005), and it is possible that PG 1004+130 is simply an intrinsically X-ray weak RLQ that also shows

variable absorption. Alternative hypotheses as to the cause of the X-ray weakness of PG 1004+130 are constrained by the characteristics of the *XMM-Newton* and *Chandra* spectra. The X-ray weakness cannot be attributed solely to attenuation by simple intrinsic neutral absorption, as the required high column densities would result in X-ray spectra significantly harder than observed. If much of the intrinsic X-ray emission is hidden by heavy absorption of significantly higher column density ($N_{\text{H}} > 5 \times 10^{23} \text{ cm}^{-2}$) than that indicated by the flat spectral shape, the observed X-ray spectrum could result from photons leaking through “holes” in the absorber or scattering off a “torus” or electron-cloud mirror into the line of sight. However, the absence of strong Fe $K\alpha$ emission is somewhat surprising if the latter scenario is correct, and PG 1004+130 is actually brighter in X-rays than expected for a reflection-dominated continuum. If the nucleus is obscured for photon energies up to $\approx 8 \text{ keV}$ (or extremely weak in X-rays), it is also possible that we are viewing X-ray emission from a subparsec-scale jet; this may provide a natural explanation for the absence of prominent Fe $K\alpha$ emission, as well as the observed lack of excess low-energy emission that distinguishes the X-ray spectra of PG 1004+130 from those of other quasars.

Motivated by the observed correlation between radio and optical luminosity for narrow-line radio galaxies, Chiaberge et al. (2000) suggested a synchrotron origin for the nuclear optical emission from these sources. This correlation has been extended to the X-ray band by Evans et al. (2006), who argued that FR I RLQs derive a significant fraction of their (generally unabsorbed) nuclear X-ray emission from an unresolved jet, while FR II RLQs are dominated by (absorbed) accretion-powered X-ray emission but also contain a jet spectral component. In the particular case of PG 1004+130, the complexity and intermediate column density of the absorption in the observed *Chandra* X-ray spectrum could plausibly be attributed to viewing the jet through progressively diminishing BAL-wind column densities with increasing distance from the nucleus. X-ray spectra with improved photon statistics and resolution are required to constrain better the physical nature of the nuclear X-ray emission, or it may also be possible to detect direct X-rays in the $\approx 8\text{--}200 \text{ keV}$ band if the putative absorption does not exceed $N_{\text{H}} \simeq 2 \times 10^{24} \text{ cm}^{-2}$ (e.g., Matt 2002). Detection of rapid X-ray variability would restrict the size of the emission region and limit the degree to which reprocessed radiation could contribute to the observed continuum, but neither the *XMM-Newton* nor the *Chandra* observation shows such variability.

Identification of the X-ray emission mechanism in the PG 1004+130 jet would be aided by an optical detection of the jet and determination of the frequency and nature of the break in the SED between radio and X-ray wavelengths. However, we consider it unlikely that the X-ray jet is dominated by IC/CMB emission, and instead favor the X-ray emission arising from a second synchrotron component. As with other X-ray jets (e.g., Marshall et al. 2002; Sambruna et al. 2004), the X-ray jet of PG 1004+130 peaks in brightness upstream of the brightest radio knot. This suggests that X-ray synchrotron emission may be more prominent in the inner jet, because of either stronger magnetic fields or a supply of highly energetic electrons (e.g., Sambruna et al. 2004). The agreement in the multiwavelength properties of the PG 1004+130 jet with those of other FR II jets indicates that the FR I radio morphology is likely due to propagation into a dense environment rather than intrinsically lower power, as suggested by Gopal-Krishna

& Wiita (2000). The orientation of the jet axis demonstrates that concave jet SEDs can arise without substantial beaming. The diffuse X-ray emission traces the path of the jet and hidden counterjet and suggests that low-energy electrons inhabit the entire length from nucleus to lobes, more consistent with continuous jet emission from the central engine than with sporadic activity (e.g., Stawarz et al. 2004).

2.6 Acknowledgments

We gratefully acknowledge the financial support of NASA grant SAO SV4-74018 (PI: GPG), NASA LTSA grant NAG5-13035 (BPM, WNB, DPS), *XMM-Newton* grant NAG5-13541 (BPM, WNB), the *Spitzer* Fellowship Program, under award 1256317 (SCG), and NASA grant GO-09432 from the Space Telescope Science Institute, which is operated by the Association of Universities for Research in Astronomy, Inc., under NASA contract NAS5-26555 (BJW). Ed Fomalont kindly reduced and analyzed the *VLA* data used in this paper, and we appreciate his generous assistance with this project. We thank George Chartas for helpful discussions, and we thank an anonymous referee for many constructive suggestions. This work includes observations obtained with *XMM-Newton*, an ESA science mission with instruments and contributions directly funded by ESA Member States and NASA. Funding for the SDSS and SDSS-II has been provided by the Alfred P. Sloan Foundation, the Participating Institutions, the National Science Foundation, the U.S. Department of Energy, the National Aeronautics and Space Administration, the Japanese Monbukagakusho, the Max Planck Society, and the Higher Education Funding Council for England. The SDSS Web Site is <http://www.sdss.org/>.

Chapter 3

A *Chandra* Survey of the X-ray Properties of Broad Absorption Line Radio-Loud Quasars

3.1 Introduction

Quasar outflows help regulate the accretion structure about the central supermassive black hole and propagate kinetic energy into the surrounding environment. Apparently the most extreme manifestation of outflows observed in radio-quiet quasars (RQQs) is the blueshifted broad absorption lines (BALs) present in the rest-frame UV spectra of $\simeq 18\%$ – 26% of RQQs (e.g., Hewett & Foltz 2003). In an orientation-based unification model, this fraction represents the covering factor of the BAL wind that is common to RQQs. The high polarization within BAL troughs (e.g., Ogle et al. 1999) supports orientation models, while the general IR similarity of BAL and non-BAL RQQs (e.g., Willott et al. 2003; Gallagher et al. 2007) argues against competing “dust-shroud” evolutionary models. BAL RQQs are usually weaker in X-rays than would be expected from their optical luminosities (e.g., Gallagher et al. 2006; Gibson et al. 2009). The X-ray spectra of BAL RQQs show clear evidence of X-ray absorption, often complex, with intrinsic column densities $N_{\text{H}} > 10^{22} \text{ cm}^{-2}$ (e.g., Gallagher et al. 2002). Although UV and X-ray absorption are clearly linked (e.g., Brandt, Laor, & Wills 2000), the higher column density of the X-ray absorber (e.g., Arav et al. 2003) suggests that the X-ray absorption arises interior to the UV BALs, perhaps in the “shielding gas” postulated by Murray et al. (1995) and generated naturally in the simulations of Proga et al. (2000).

A lack of detected BALs in radio-loud¹ quasars (RLQs) led to early suggestions that quasars could possess either a jet, or a BAL wind, but not both simultaneously (e.g., Stocke et al. 1992). However, an increasing number of individual BAL RLQs began to be discovered (e.g., Becker et al. 1997; Brotherton et al. 1998; Wills et al. 1999; Gregg et al. 2000; Ma 2002; Benn et al. 2005), and systematic optical spectroscopic coverage of quasars detected in the Very Large Array (VLA) 1.4 GHz Faint Images of the Radio Sky at Twenty-Centimeters (FIRST) survey (Becker et al. 1995) obtained by the FIRST Bright Quasar Survey (FBQS; White et al. 2000) and the Sloan Digital Sky Survey (SDSS; York et al. 2000) has increased the number of known radio-loud BAL quasars to $\gtrsim 100$ (e.g., Becker et al. 2000, 2001; Menou et al. 2001; Shankar et al. 2008). The fraction of quasars with BALs does decrease with increasing radio luminosity (e.g., Shankar et

¹We follow the convention that “radio-loudness” (R^*) is defined by the ratio of monochromatic luminosities at rest-frame 5 GHz and 2500 Å (e.g., Stocke et al. 1992), where optical/UV luminosities have been corrected for any strong intrinsic reddening. RQQs have $R^* < 10$ while RLQs require at least $R^* > 10$; we consider objects with $10 < R^* < 50$ to be radio-intermediate and those with $R^* > 50 - 100$ to be definitively radio-loud.

al. 2008). Several of the discovered BAL RLQs have flat or convex radio spectra and/or compact morphologies (e.g., Becker et al. 2000; Liu et al. 2008; Montenegro-Montes et al. 2008), similar to the radio properties of compact steep spectrum (CSS) or GHz peaked spectrum (GPS) radio sources (e.g., O’Dea 1998). The association of BAL RLQs with GPS/CSS radio sources, commonly presumed to be young (e.g., Stawarz et al. 2008 and references therein), has revived evolutionary scenarios (e.g., Gregg et al. 2006), as has the prevalence of objects with low-ionization BALs among dust-reddened quasars (Urrutia et al. 2009) which are plausibly newly active (e.g., Urrutia et al. 2008). Further, Zhou et al. (2006) identify six BAL RLQs (at least four of which show low-ionization BALs) with high brightness temperatures, suggesting that the nucleus is observed from a polar perspective. The presence of BALs in low-inclination RLQs would seem inconsistent with the quasi-equatorial disk-wind model often applied to RQQs.

X-ray observations of BAL RLQs can provide insight into the nature of the BAL outflow, through quantifying any X-ray weakness or spectral hardening associated with BAL-linked absorption. Unfortunately, there have been only a handful of X-ray studies of BAL RLQs to date. Brotherton et al. (2005) conducted a *Chandra* study of five BAL RLQs and found that they were X-ray weak but had relatively soft spectra, consistent with complex absorption or a jet-dominated continuum. None of these sources has a dereddened $R^* > 100$, and three of the five were in the minority population of low-ionization BAL quasars, which in RQQs display particularly strong X-ray absorption (e.g., Green et al. 2001; Gibson et al. 2009). Wang et al. (2008) present *XMM-Newton* observations of four BAL RLQs believed to be viewed at low inclinations (three of which have low-ionization BALs and only one of which has $R^* > 100$), finding the two detected BAL RLQs to lack intrinsic X-ray absorption and to possess normal X-ray luminosities. X-ray studies of individual BAL RLQs include the work of Schaefer et al. (2006), who find J101614.25+520915.4 to be X-ray weak with significant soft X-ray emission, and Miller et al. (2006), who detect variable X-ray absorption in the BAL RLQ PG 1004+130 (but with an observed column density less than that of most BAL RQQs) and suggest the power-law form and X-ray weakness of the unabsorbed X-ray spectrum may indicate a jet-dominated X-ray nuclear continuum. Statistical efforts to understand the X-ray properties of BAL RLQs require a larger sample covering a wide range of BAL and radio properties.

We here present results from a *Chandra* snapshot survey of a well-defined sample of 12 BAL RLQs primarily selected from the SDSS Data Release 3 (DR3) BAL quasar catalog of Trump et al. (2006). The objects were selected to be distinctly radio-loud ($R^* \gtrsim 100$) with strong C IV absorption spanning a range of equivalent widths (EW²) and velocities; both core-dominated and lobe-dominated radio sources are included in the sample. For most of these objects we were able to obtain optical spectra and photometry with the Hobby-Eberly Telescope (*HET*) within ~ 1 – 3 rest-frame weeks of the *Chandra* pointing, to check for BAL and continuum variability. We also make use of *Chandra* archival data for an additional 9 BAL RLQs (including those observed by the SDSS in DR4 and DR5), all of which have C IV EW > 5 Å and $R^* \gtrsim 50$. Even taking redshift

²We use positive values throughout for C IV absorption equivalent widths; emission line properties are not considered in this work. All EW values are rest-frame.

censoring into account, our sample is dominated by high-ionization BAL quasars, which represent the majority of SDSS-selected BAL quasars (e.g., Trump et al. 2006). We have carefully constructed comparison samples of non-BAL RLQs, BAL RQQs, and non-BAL RQQs observed with SDSS/FIRST/*Chandra* in order to provide proper context for our results and to enable interpretation of the physical nature of BAL outflows in RLQs. Such comparisons are necessitated by the presence of a radio-linked component in the X-ray emission of RLQs, apparent both through increased X-ray luminosity (e.g., Worrall et al. 1987) and X-ray spectral flattening (e.g., Wilkes & Elvis 1987) with increasing radio loudness, and commonly presumed to arise in a small-scale jet.

This paper is organized as follows: §2 describes the selection of the snapshot and archival BAL RLQ samples and the construction of comparison samples, §3 presents the *HET* optical and *Chandra* X-ray observations and provides notes on individual objects, §4 quantifies X-ray luminosities and spectral properties relative to the comparison samples, §5 discusses physical interpretations of BAL RLQs, and §6 summarizes the main conclusions. A standard cosmology with $H_0 = 70 \text{ km s}^{-1} \text{ Mpc}^{-1}$, $\Omega_M = 0.3$, and $\Omega_\Lambda = 0.7$ is assumed throughout. Unless otherwise noted, errors are given as 90% confidence intervals for one parameter of interest ($\Delta\chi^2 = 2.71$). Radio, optical/UV, and X-ray monochromatic luminosities l_r , l_{uv} , and l_x have units of $\log \text{ ergs s}^{-1} \text{ Hz}^{-1}$, at rest-frame frequencies of 5 GHz, 2500 Å, and 2 keV, respectively. Object names are typically given as SDSS J2000.

3.2 Sample properties

Our sample of BAL RLQs consists of 21 objects, greatly increasing the number of BAL RLQs with high-quality X-ray coverage. 12 of these BAL RLQs have X-ray data from a *Chandra* snapshot survey (PI Garmire) and 9 have archival *Chandra* coverage. 20/21 BAL RLQs are detected in the 0.5–8 keV band. We also make use of comparison samples of RLQs, BAL RQQs, and RQQs with *Chandra* coverage.

3.2.1 Selection of snapshot BAL RLQs

The targets for the *Chandra* snapshot survey were selected from the Trump et al. (2006) BAL quasar catalog, which includes SDSS quasars with spectra as of DR3. To ensure consistent consideration of BAL properties, only C IV absorption measurements were used. The Absorption Index (*AI*; Hall et al. 2002) was required to exceed 1500 km s^{-1} to remove borderline BALs from further consideration. Note that *AI* is defined from zero velocity with a minimum velocity width of 1000 km s^{-1} , and is consequently less restrictive than the traditional Balnicity Index (*BI*; Weymann et al. 1991); several objects in our sample have $BI = 0 \text{ km s}^{-1}$. Optical/UV luminosities were determined from SDSS photometry (corrected for Galactic extinction) through redshifting the composite quasar spectrum of Vanden Berk et al. (2001), convolving it with the SDSS filters, and then using the nearest magnitude (or nearest two magnitudes) to $2500 \times (1 + z) \text{ Å}$ to determine the continuum flux (assuming an optical/UV power-law continuum slope of $\alpha_\nu = -0.5$, which is reasonable at these wavelengths). We verified

that alternative methods of calculating luminosities (e.g., the spectral-fitting method of Gibson et al. 2009) yield similar results.

These BAL quasars were then checked against the FIRST radio catalog to generate a list of BAL RLQs. Because FIRST has angular resolution sufficient to detect extended radio emission (when present) as distinct sources in many cases, it is necessary to consider the nearby environment to include all components (which could be some combination of core, lobes, and jet) and determine the full radio flux. Candidate matches were considered from all fields in which there was either a FIRST source within $2''$ of the SDSS optical position, or two or more FIRST sources within $90''$. All candidate fields were then examined to exclude intruding background sources (often identifiable due to an optical counterpart seen in the Digitized Sky Survey image). Radio luminosities were calculated at rest-frame 5 GHz, assuming radio power-law continuum slopes of $\alpha_\nu = -0.5$ for core components and $\alpha_\nu = -1.0$ for extended components, when present. Candidates for inclusion in the list of *Chandra* snapshot targets were required to be distinctly radio-loud, defined as having $R^* \gtrsim 100$ and $l_r > 33$. The optical spectra were checked for obvious signs of intrinsic reddening (see §2.3) to ensure that the radio-loudness values were not significantly artificially elevated.

The target list for the snapshot *Chandra* survey was then constructed from the brightest (in SDSS m_i) BAL RLQs. As can be seen in Figure 1, the survey is substantially complete within DR3 BAL RLQs to $m_i < 18.6$. (The single DR3 object near $m_i = 17.5$ lacking *Chandra* coverage is J144707.41+520340.0, which was considered for inclusion in the target list but dropped as lowest priority due to having the lowest absorption index, $AI = 1517 \text{ km s}^{-1}$.) One BAL RLQ (J112506.95–001647.6) with a fainter $m_i \simeq 18.9$ was included based on showing extended radio structure. One BAL RLQ (J102258.41+123429.7) with a post-DR3 SDSS spectrum (hence not listed in Trump et al. 2006) was selected from the quasar catalog of Schneider et al. (2007) based on showing extended radio structure along with BAL absorption. The full snapshot sample of BAL RLQs is listed in Table 1.

Gibson et al. (2009) provide an SDSS BAL quasar catalog that covers through DR5, and we make use of this to search for BAL RLQs with archival *Chandra* coverage (see §2.2) and to characterize the BAL properties of the snapshot and archival samples (this catalog was not available at the time of our *Chandra* target selection). All but one (J074610.50+230710.8) of the snapshot BAL RLQs are listed in Gibson et al. (2009), and the listed BAL RLQs targeted in the snapshot survey all have C IV EW $> 5 \text{ \AA}$. Since the spectral fitting method and BAL definition in the catalog of Gibson et al. (2009) differ slightly from those used by Trump et al. (2006), minor inconsistencies in absorption properties and object inclusion are to be expected.

3.2.2 Selection of archival BAL RLQs

Two lists of BAL RLQs were checked for archival *Chandra* Advanced CCD Imaging Spectrometer (ACIS; Garmire et al. 2003) non-grating coverage; the first (134 BAL RLQs) was generated by cross-matching quasars with C IV absorption measurements from the BAL catalog of Gibson et al. (2009) with the FIRST catalog, in a manner analogous to that outlined in §2.1, while the second (~ 50 BAL RLQs) was drawn from

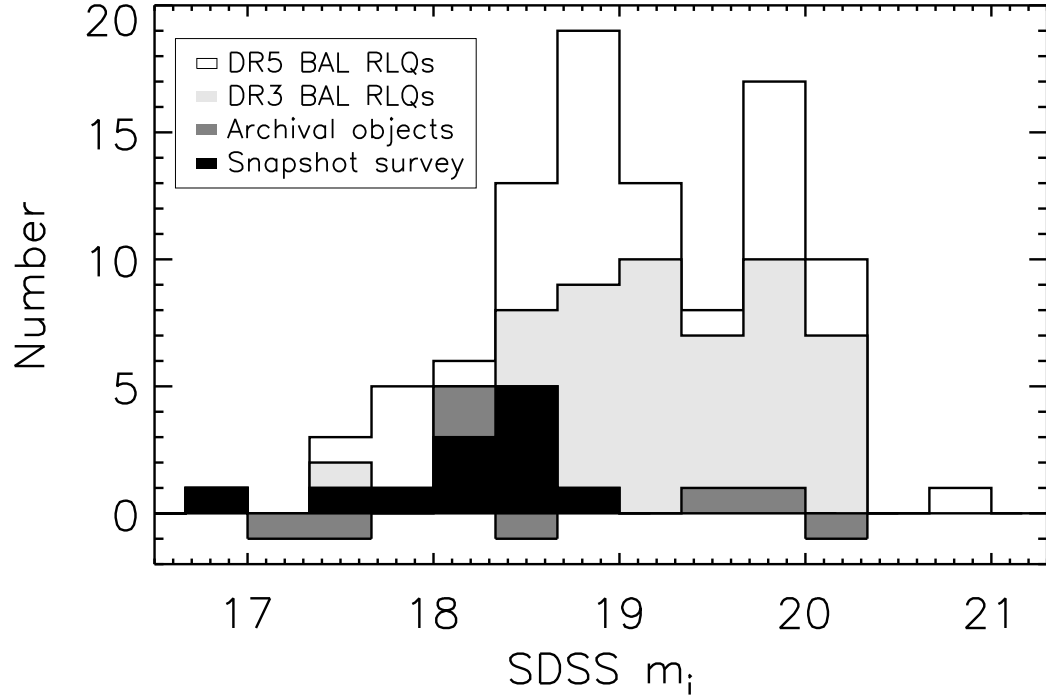


Fig. 3.1 Histogram showing the SDSS m_i distribution for radio-loud broad absorption line quasars satisfying $R^* \gtrsim 100$ and $\text{EW}_{\text{CIV}} > 5\text{\AA}$. The light gray shaded area indicates the subset of BAL RLQs that had spectra available in SDSS DR3 or earlier, and the filled area shows those objects selected for the snapshot survey (black, 12 objects) or possessing archival *Chandra* coverage (dark gray, 8 objects shown; PG 1004+130 has $m_i = 15.2$). Archival objects selected from the literature are plotted on a negative scale.

mentions of individual BAL RLQs in the literature.³ Naturally, BAL RLQs can appear in both of these lists. Candidates were required to be definitively radio-loud ($R^* \gtrsim 50$ and $l_r > 32$) with strong C IV absorption ($EW > 5 \text{ \AA}$). These radio criteria are slightly less stringent than those required of objects in the snapshot BAL RLQ sample, so as to include potentially interesting BAL RLQs with existing X-ray coverage, but still select objects comfortably on the radio-loud side of the canonical $R^* = 10$ border.

Other X-ray telescopes cannot match the angular resolution of *Chandra*, important for minimizing background contamination with faint sources, and many also have lower sensitivities and/or cover a significantly different energy range. We searched the *XMM-Newton* archives for observations pointed to within $15'$ of any of the BAL RLQs described above, and find coverage of only three objects that would meet our selection criteria: J081102.91+500724.5 (Wang et al. 2008), J101614.25+520915.4 (Schaefer et al. 2006), and J151630.30–005625.5 (PI Boehringer). Adding archival BAL RLQs observed with other X-ray telescopes would not notably increase our sample size or alter our conclusions.

The archival BAL RLQ sample is listed in Table 2. The snapshot and archival BAL RLQs together span a wide range of absorption and radio properties, and constitute a reasonably representative sample of definitively radio-loud BAL RLQs (Figure 2). As mentioned by previous authors (e.g., Shankar et al. 2008), it is rare for quasars to be simultaneously strongly absorbed and strongly radio-loud, but our sample includes a few such objects. The SDSS spectra of the BAL RLQs (Figure 3) display a variety of BAL structures. The majority of the sample BAL RLQs have compact morphologies at arc-second scales, but 4/21 show double-lobed structure and are dominated by extended radio emission.

3.2.3 Reddening

Some BAL RLQs targeted by *Chandra* or mentioned in the literature have unusual and extreme characteristics, and caution is warranted before including such objects in a statistical study. In particular, objects with heavy intrinsic reddening may have artificially elevated apparent radio-loudness values. The BAL RLQs J100424.88+122922.2 (Lacy et al. 2002; Urrutia et al. 2005) and J155633.77+351757.3 (Becker et al. 1997; Brotherton et al. 2005) have radio-loudness values below our selection criteria after correcting for intrinsic reddening (J100424.88+122922.2 is also gravitationally lensed), and are therefore excluded from the archival sample. Both these objects have low-ionization BALs, as do two additional BAL RLQs presented in Brotherton et al. (2005) which are also strongly reddened (such that their corrected radio loudness values are below our selection threshold, although both were already excluded from consideration here due to their low redshifts precluding observation of their C IV absorption properties); this is

³BAL RLQs identified in the following references were checked for archival *Chandra* coverage: Becker et al. (1997, 2000, 2001); Brotherton et al. (1998, 2002, 2005, 2006); Wills et al. (1999); Gregg et al. (2000, 2006); Menou et al. (2001); Lacy et al. (2002); Ma (2002); Willott et al. (2002); Jiang & Wang (2003); Benn et al. (2005); Gallagher et al. (2005, 2006); Urrutia et al. (2005); Miller et al. (2006); Schaefer et al. (2006); Zhou et al. (2006); Just et al. (2007); Kunert-Bajraszewska & Marecki (2007); Liu et al. (2008); Montenegro-Montes et al. (2008).

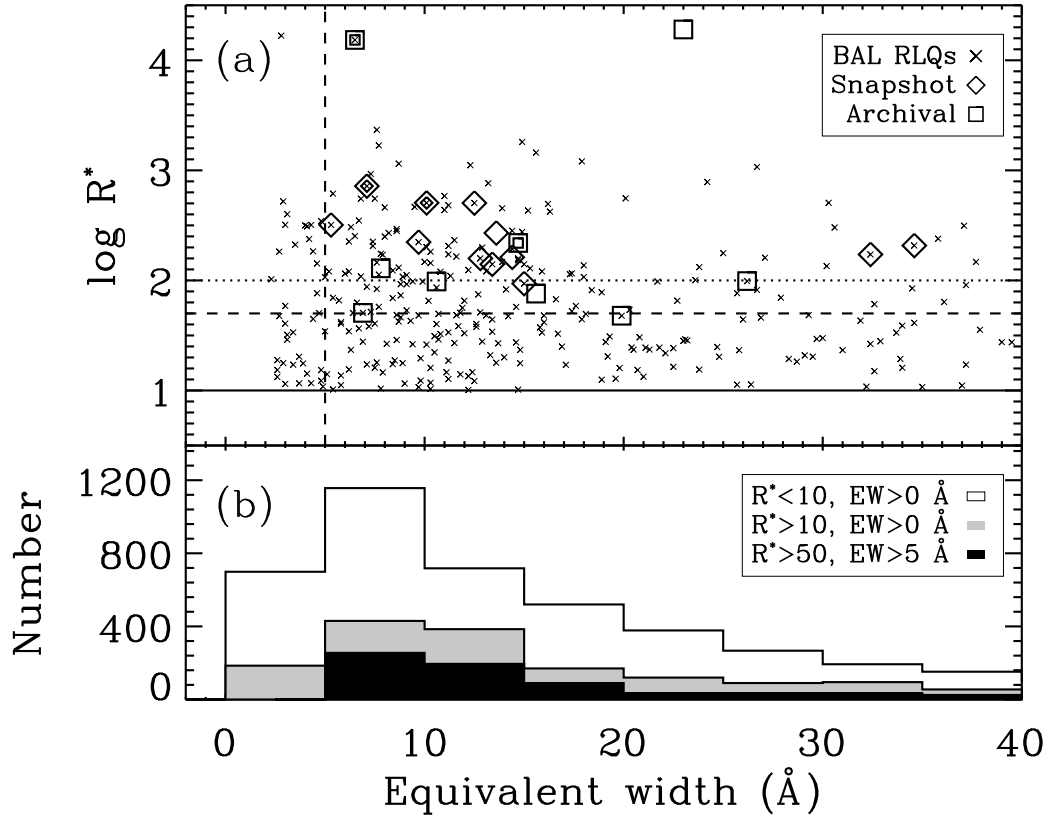


Fig. 3.2 (a) Radio loudness plotted versus broad absorption line strength (parameterized by C IV equivalent width). The *Chandra* snapshot BAL RLQs are shown as diamonds and the archival BAL RLQs as squares (nested symbols are lobe-dominated BAL RLQs). The solid line marks the $R^* > 10$ ($\log R^* > 1$) boundary, below which quasars are defined to be radio-quiet. The dashed lines show the selection criteria for the archival sample of BAL RLQs, which were required to be definitively radio-loud ($R^* \gtrsim 50$) and show strong broad absorption lines ($\text{EW} > 5$ Å). The dotted line shows the more restrictive criteria of $R^* \gtrsim 100$ that was used to select the snapshot sample. As reported by previous authors it is rare for quasars to be simultaneously strongly absorbed and strongly radio-loud. (b) Plot of the distribution of C IV equivalent width for objects with $R^* < 10$ (open histogram), objects with $R^* > 10$ (gray histogram), and objects with $R^* > 50$ and $\text{EW} > 5$ Å (black histogram). Numbers for objects with $R^* > 10$ (the gray and black histograms) have been multiplied by 5 for clarity.

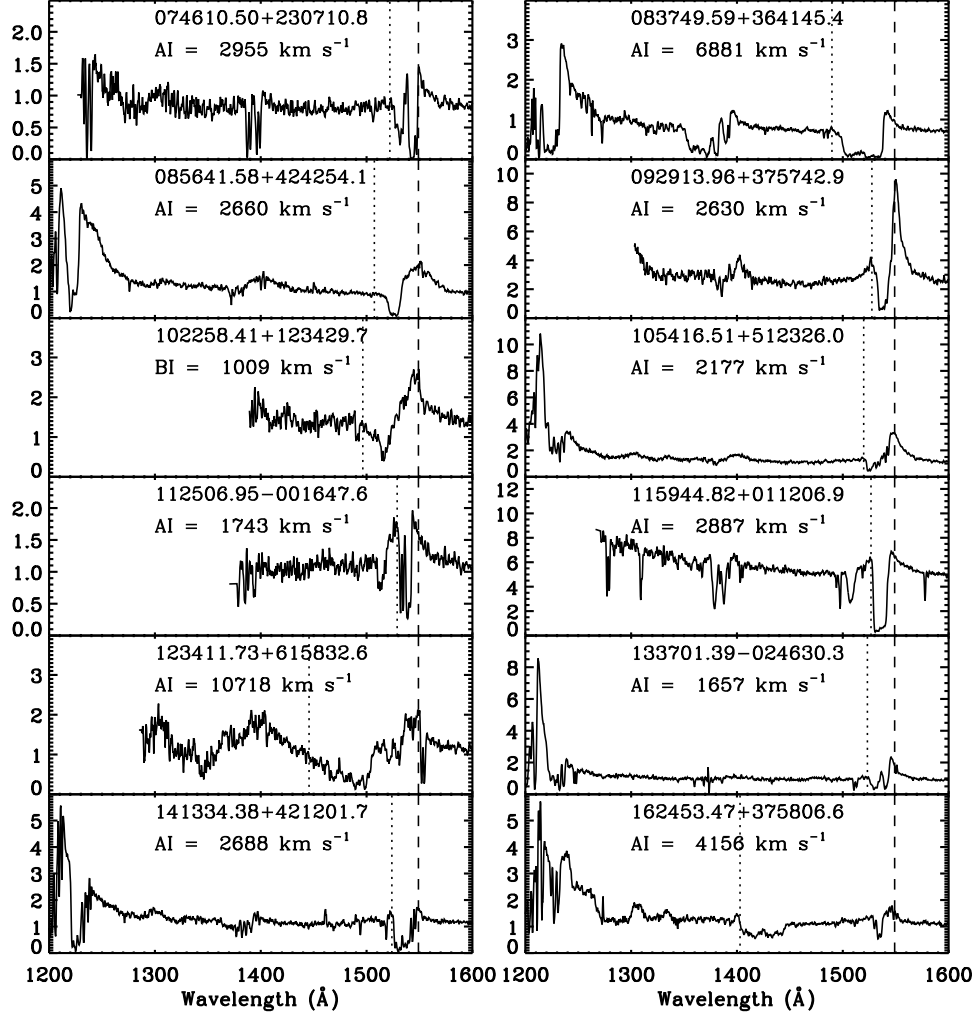


Fig. 3.3 SDSS spectra for the snapshot sample, plotted with rest-frame wavelengths and showing the $\text{Ly}\alpha$ to C IV BAL region. The dashed line in each panel is at 1549 Å, or zero velocity. The dotted line indicates the maximum outflow velocity, primarily taken from Gibson et al. (2009). Flux is given in units of $10^{-16} \text{ erg cm}^{-2} \text{ s}^{-1} \text{ Å}^{-1}$. The sample includes objects covering a range of BAL absorption strengths and outflow velocities. Each panel is labeled with the SDSS DR5 name as well as the absorption index (a measure of BAL strength), primarily taken from Trump et al. (2006).

not unexpected, as low-ionization BAL quasars are known to be generally redder than high-ionization BAL quasars (e.g., Reichard et al. 2003).

We use the relative color indicator $\Delta(g-i)$ (calculated by subtracting the median quasar color at a given redshift) to check for large intrinsic reddening (e.g., Hall et al. 2006), keeping in mind that RLQs generally show slightly redder colors than do RQQs (e.g., Ivezić et al. 2002). The snapshot and archival BAL RLQs have relative colors that are on average redder than those of SDSS quasars (although most of our BAL RLQs do have relative colors within the range spanned by 90% of SDSS quasars) but consistent with those of BAL RLQs in general⁴ (Figure 4). They do not appear to have strongly distorted radio-loudness values.

The only established low-ionization BAL RLQ in our sample is the archival object J081426.45+364713.5, and although it does have a notably red relative color, its $\Delta(g-i)$ value is within the tail of the BAL RLQ distribution and is significantly less than that of the strongly reddened J155633.77+351757.3 (Figure 4). The CSS BAL RLQ J104834.24+345724.9 suffers from intrinsic reddening (Willott et al. 2002), but its corrected radio-loudness is still quite high, so it is retained in our archival sample but with a dereddened optical luminosity.

3.2.4 Comparison samples

In order to interpret the X-ray properties of BAL RLQs, it is also necessary to analyze comparison samples of non-BAL RLQs (e.g., to gauge the expected X-ray luminosities, including the contribution from an unresolved jet to the X-ray nuclear emission), of BAL RQQs (e.g., to provide context for X-ray absorption relative to UV properties), and of non-BAL RQQs (e.g., to give a baseline for measuring X-ray weakness in BAL RQQs). We caution that the comparison samples we use are specifically chosen to permit comparative investigation of our samples of BAL RLQs and should not necessarily be used to infer general properties of non-BAL RLQs, BAL RQQs, or non-BAL RQQs, particularly those having luminosities outside of the ranges studied here. The optical/UV luminosities and redshifts of the BAL RLQs observed with *Chandra* and of the comparison samples are shown in Figure 5.

We constructed a comparison sample of RLQs by matching the SDSS DR5 Quasar Catalog (Schneider et al. 2007) to FIRST in a manner analogous to that described in §2.1, and then retaining RLQs with *Chandra* coverage with constraints of off-axis angle less than $12'$, exposure greater than 1 ks, ACIS-S or ACIS-I used as the detector, and no grating. This list was then filtered to include only RLQs with $R^* > 50$ and $l_r > 32$ so as to match the selection criteria for the BAL RLQ archival sample. X-ray luminosities were determined from *Chandra* count rates using the method described in §3.2. There are 68 RLQs selected in this manner, of which 67 (99%) are detected in X-rays. Additional luminous RLQs were added from the sample of Worrall et al. (1987)

⁴A Kolmogorov-Smirnov (KS) test comparing the BAL RLQs observed with *Chandra* to SDSS/FIRST BAL RLQs with $R^* > 50$ and $EW > 5\text{\AA}$ gives $p = 0.29$ (comparing to BAL RLQs with $R^* > 10$ and $EW > 0\text{\AA}$ gives $p = 0.12$), indicating that the distribution of colors for the snapshot and archival BAL RLQs is not significantly different from that of BAL RLQs in general. Comparing the snapshot and archival BAL RLQs to BAL RQQs gives $p = 0.03$.

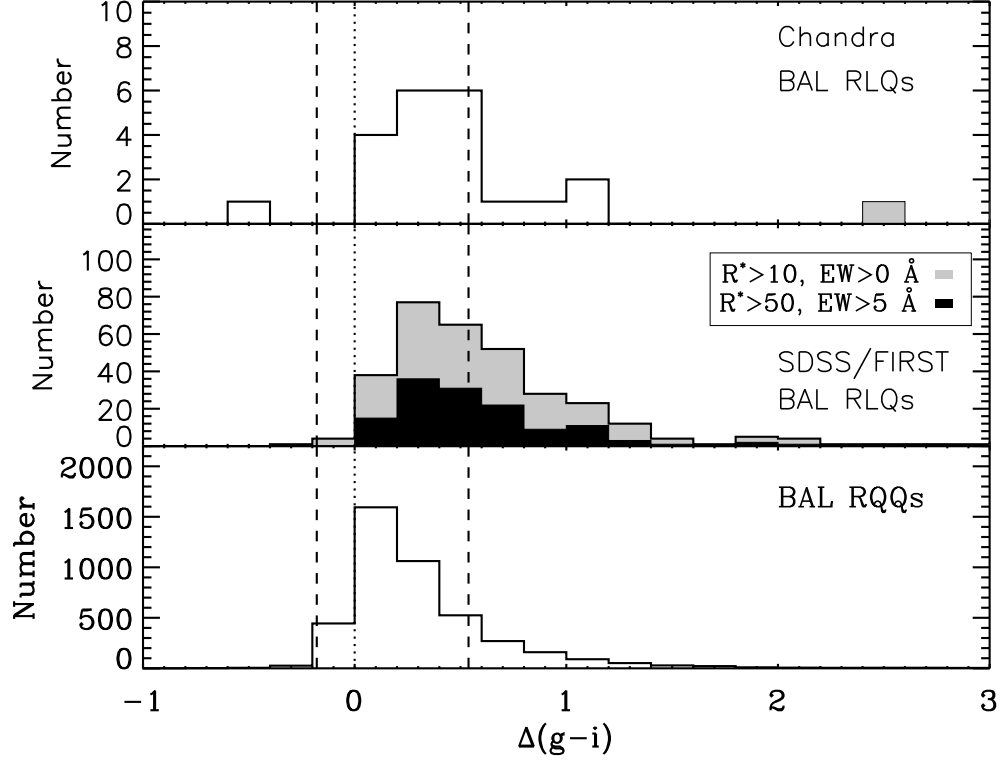


Fig. 3.4 Relative color $\Delta(g-i)$, calculated by taking the measured $(g-i)$ for a given object and subtracting the $(g-i)$ that is typical for quasars at that redshift (positive values correspond to redder objects). The top panel shows the snapshot and archival sample of BAL RLQs with *Chandra* coverage (the object shaded in gray is the strongly reddened object FBQS J1556+3517, marked for comparison but not included in the archival sample). The middle panel shows SDSS/FIRST BAL RLQs, and the bottom panel shows BAL RQQs. The dashed lines enclose 90% of SDSS DR5 quasars. While BAL quasars tend to be redder than non-BAL quasars, the BAL RLQs studied with *Chandra* are representative of BAL RLQs in general and do not show excessive intrinsic reddening that could significantly elevate radio-loudness values.

based on *Einstein* observations; after correcting to our chosen cosmology, we select those RLQs with $l_{\text{uv}} > 31.3$, which yields a further 36 RLQs, 32 (89%) with X-ray detections. The total RLQ comparison sample comprises 104 RLQs, 99 (95%) with X-ray detections. Although some of the RLQs have redshifts too low to permit ready observation of the C IV region, the fraction of BAL RLQs is small enough (see references in §1) that any contamination of the comparison sample is minor and does not impact later analysis; we often refer to the RLQ comparison sample as “non-BAL RLQs” throughout.

A comparison sample of BAL RQQs is taken from the BAL catalog of Gibson et al. (2009), combining their Table 1 (absorption properties) with their Table 5 (X-ray data). All high-ionization BAL RQQs with *Chandra* coverage were selected, a total of 37 objects of which 28 (76%) have X-ray detections. We also include those high-ionization BAL RQQs lacking SDSS spectra (i.e., not available for inclusion in the Gibson et al. 2009 catalog) from the Large Bright Quasar Survey (LBQS; e.g., Foltz et al. 1987) observed with *Chandra* by Gallagher et al. (2006), an additional 15 objects, 13 (87%) detected by *Chandra*. The total BAL RQQ comparison sample comprises 52 BAL RQQs, 41 (79%) with X-ray detections.

A comparison sample of non-BAL RQQs is taken from Gibson et al. (2008a); this sample has an excellent combination of size, high-quality X-ray coverage, and well-characterized UV properties. It is composed of the 139 non-BAL RQQs in their sample B, which is made up of optically-selected quasars (SDSS objects targeted exclusively based on FIRST or ROSAT properties excluded) with serendipitous (off-axis angle constrained to be $1' < \theta < 10'$) *Chandra* coverage having exposure > 2.5 ks. These objects span a redshift range of $1.7 < z < 2.7$, with the lower limit set to permit the detection of C IV absorption if present (and thereby exclude BAL RQQs) and the upper limit set to permit the direct measurement of the 2500 Å continuum flux. We also include 21 highly luminous non-BAL RQQs from Just et al. (2007), taking all objects in their “clean” sample with SDSS and *Chandra* data, to match better the luminosity range of the BAL RLQs. The total RQQ comparison sample comprises 160 RQQs, all of which have X-ray detections.

3.3 Observations and Notes

3.3.1 *HET* observations

We obtained optical photometry and spectroscopy of 10/12 of the snapshot BAL RLQs near-contemporaneously with the *Chandra* observations, using the queue-scheduled HET (Ramsey et al. 1998). The Low-Resolution Spectrograph (LRS; Hill et al. 1998) was used for the spectroscopic observations, generally with a $1.5''$ slit and the g2 grating, providing a resolution of $R \simeq 867$ (sufficient for productive comparison to SDSS spectra, which have a typical resolution of $R \simeq 1800$). The HET data were reduced with the Image Reduction and Analysis Facility⁵ (IRAF) using standard techniques, and the resulting spectra are presented in Figure 6. (The *HET* spectrum for J102258.41+123429.7 is not shown; unfortunately the BAL region fell too close to the edge of the chip to

⁵<http://iraf.noao.edu/iraf/web/>

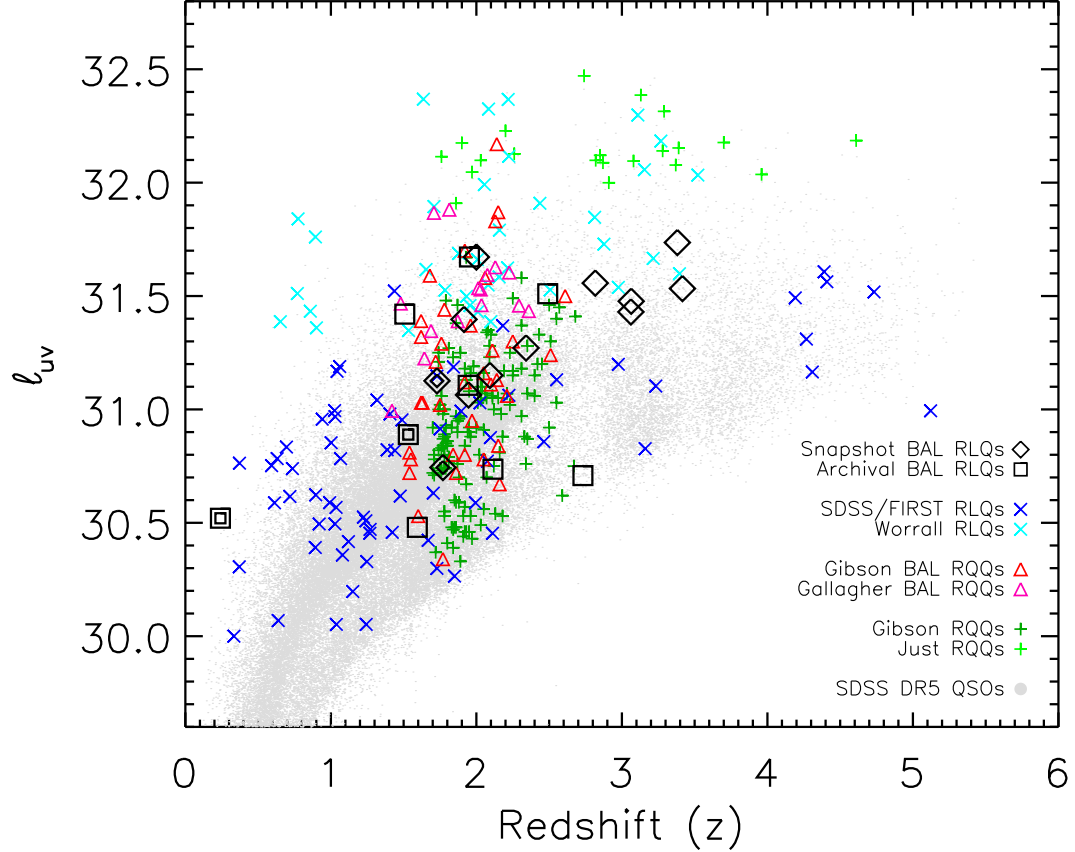


Fig. 3.5 Optical luminosity l_{uv} in units of $\log \text{ergs s}^{-1} \text{Hz}^{-1}$ calculated at rest-frame 2500 \AA for our sample of BAL RLQs (nested symbols are lobe-dominated BAL RLQs) and for comparison samples of non-BAL RLQs, BAL RQQs, and non-BAL RQQs, plotted versus redshift. The RLQ comparison sample is constructed from SDSS/FIRST/*Chandra* data, supplemented with some particularly luminous RLQs observed by *Einstein* (Worrall et al. 1987). The BAL RQQ comparison sample is taken from Gibson et al. (2009) and is supplemented with non-SDSS objects from Gallagher et al. (2006). The RQQ comparison sample is taken from Gibson et al. (2008a) and is supplemented with luminous RQQs from Just et al. (2007). Quasars from the DR5 Quasar Catalog of Schneider et al. (2007) are shown as gray points. Our *Chandra* snapshot sample is biased toward luminous quasars as a consequence of the magnitude-limited selection method. The comparison samples have been constructed to overlap and bracket the BAL RLQs in optical luminosity and redshift.

provide a useful comparison to the SDSS data.) None of the objects displays strong absorption-line variability, although a few objects show minor changes in their BAL structure (see §3.3.1); a more detailed discussion of BAL variability in RLQs is deferred to a later work. We also obtained *R*-band images and looked for any flux variability via comparison to field stars and galaxies; none of the observed objects showed large (> 0.5 magnitudes) variability. The *HET* observing log is provided in Table 1.

3.3.2 *Chandra* observations

All snapshot BAL RLQ *Chandra* observations were carried out using ACIS with exposure times of 4–7 ks. The targets were positioned at the aim point of the S3 chip, and data were collected in Very Faint mode. The pipeline processing includes automatic application of both the ACIS charge-transfer inefficiency correction and the time-dependent gain adjustment, and it is carried out using the calibration database version CALDB v3.4.2. The data were analyzed using CIAO version 4.0.2.

The archival BAL RLQ J081426.45+364713.5 has two *Chandra* observations of comparable quality. These were stacked for the purposes of determining source detection and extracting counts, and the resulting increase in signal-to-noise ratio is helpful for more accurately determining the X-ray properties of this faint off-axis source.

Source extraction for the BAL RLQ snapshot and archival objects and for the non-BAL RLQ comparison sample (see §2.2) *Chandra* sources was performed using 90% encircled-energy radii, using nearby source-free regions for background determination. We evaluate source detection through comparison of the observed aperture counts to the 95% confidence upper limit for background alone. Where the number of background counts is less than 10 (as applies in almost all cases) we use the Bayesian formalism of Kraft et al. (1991) to determine the limit; else, we use equation 9 from Gehrels (1986). If the aperture counts exceed the 95% confidence upper limit we consider the source detected and calculate the net counts by subtracting the background from the aperture counts and then dividing by the encircled-energy fraction; else, the source is considered undetected and the upper limit is used. All snapshot BAL RLQs are detected, with net 0.5–8 keV counts ranging from 17 to ~ 170 (Table 1), and 8/9 archival BAL RLQs are detected (Table 2). We confirmed source detections for the BAL RLQs by running the CIAO *wavdetect* routine on 200×200 square pixel images centered at the SDSS object coordinates, with wavelet scales of 1, 1.41, 2, 2.83, 4, and 5.66 pixels; most sources are detected using a significance threshold of 10^{-6} , while J081426.45+364713.5 is detected (in the stacked image only) using a significance threshold of 10^{-5} .

All BAL RLQs were examined for variability within the *Chandra* observation using the Gregory-Loredo algorithm implemented by CIAO⁶. This method filters by relevant good time intervals and accounts for any dither near chip edges for off-axis sources. The probability that a source is variable can be indicated with a variability index, ranging from 0 to 10; most BAL RLQs had values of 0 (“definitely not variable”) with only 3 objects having variability indices as high as 2 (“probably not variable”).

⁶<http://cxc.harvard.edu/ciao/ahelp/glvary.html>

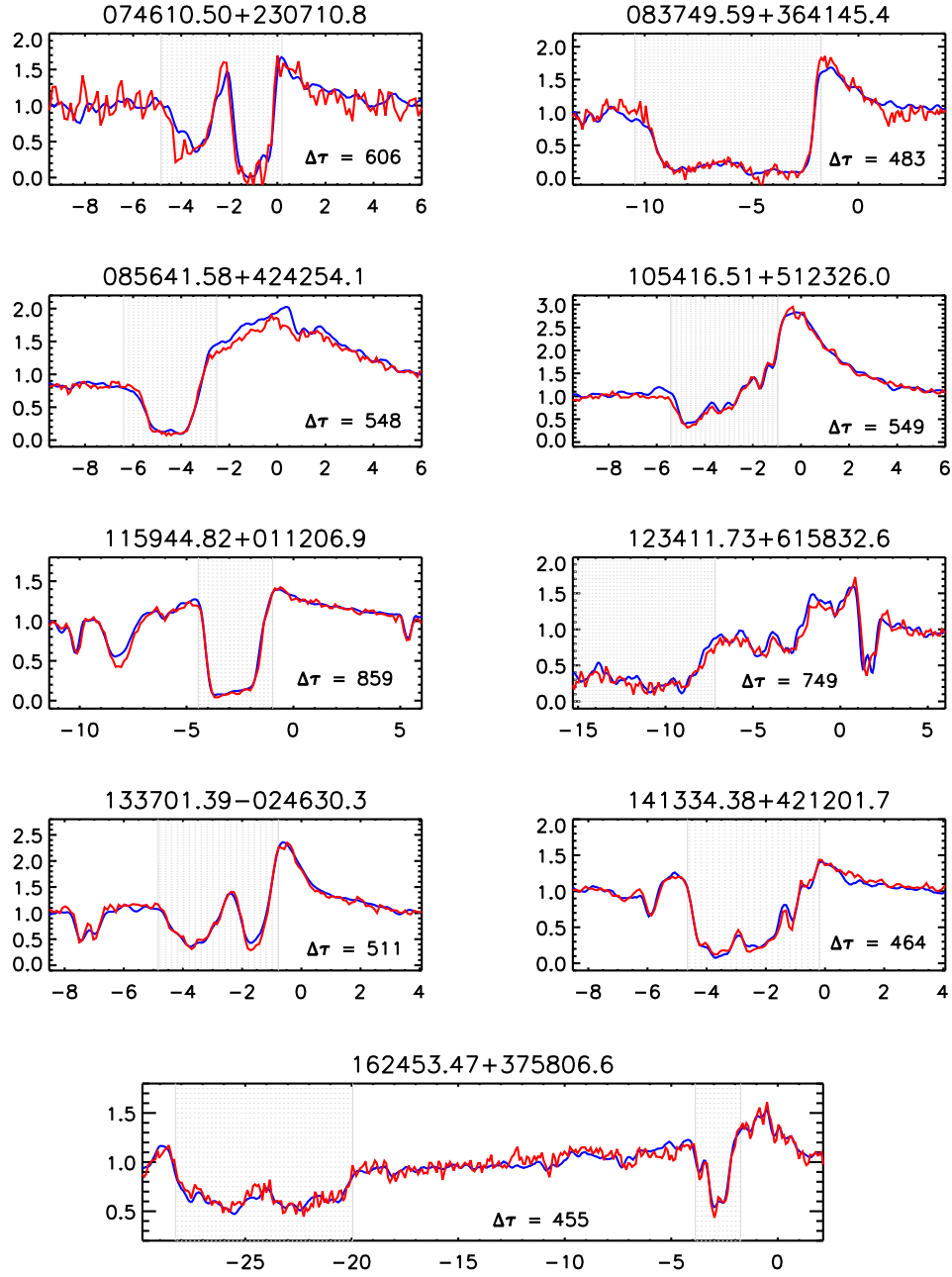


Fig. 3.6 HET/LRS spectra (red lines) taken near the times of the *Chandra* snapshot observations, shown compared to the earlier epoch SDSS spectra (blue lines) matched to HET/LRS resolution. Each panel is labeled with the SDSS DR5 name as well as the rest-frame interval between observations (in days). The horizontal axis is velocity in 1000 km s^{-1} and the vertical axis is normalized flux. The C IV absorption regions are shaded gray. There is only minor BAL variability seen in these objects, indicating that variability does not significantly complicate a comparison of UV absorption properties to X-ray weakness.

Longer exposures could more tightly constrain variability on ks timescales, while repeat observations could assess variability between epochs.

3.3.3 Notes on individual objects

Optical/UV properties (including absorption characteristics) of the BAL RLQs are listed in Table 3, while radio fluxes and spectral indices are given in Table 4. Below, we briefly comment on interesting aspects of the BAL RLQs.

3.3.3.1 Snapshot BAL RLQs

J074610.50+230710.8 has a relatively large C IV absorption index of $AI = 2955 \text{ km s}^{-1}$ (Trump et al. 2006), and has a wide and deep BAL-like absorption structure (Figures 3 and 6) despite being the only snapshot BAL RLQ not included in the Gibson et al. (2009) BAL quasar catalog. The HET spectrum shows enhanced absorption in the higher-velocity BAL (Figure 6), perhaps qualitatively consistent with the tendency of BAL RQQs to vary within narrow discrete regions (Gibson et al. 2008b). It is the reddest snapshot BAL RLQ with $\Delta(g - i) \simeq 1.1$ (the next reddest snapshot BAL RLQ has $\Delta(g - i) \simeq 0.6$). An archival *VLA* X-band image (program AB862, observation date 1998-05-04) suggests that the radio spectrum of this compact-morphology source peaks near 5 GHz.

J083749.59+364145.4 has particularly strong C IV, Si IV, Ly α , and O VI BALs. The C IV equivalent width of 34.6 \AA is the largest in the snapshot or archival BAL RLQ sample. It appears to have a GHz-peaked (possibly variable) radio spectral shape and is unresolved at milliarcsecond scales (Montenegro-Montes et al. 2008, 2009).

J085641.58+424254.1 displays strong N V absorption. The HET spectrum suggests the C IV emission line might be slightly variable.

J092913.96+375742.9 (also FBQS J092913.9+375742) appears to be resolved in an X-band *VLA* image (program AG0574, observation date 1999-07-12). There is a jet-like feature with a flux of 2.1 mJy located $0.5''$ West of the core.

J102258.41+123429.7 is resolved into a double-lobed morphology by FIRST (see Figure 7), and the southern lobe shows extended diffuse emission past the primary hotspot. The *Chandra* image does not show any extended X-ray emission, but there are only ~ 20 X-ray source counts.

J105416.51+512326.0 has a flat radio spectrum that steepens to $\alpha_r = -0.35$ above 1.4 GHz.

J112506.95-001647.6 is resolved into a double-lobed morphology by FIRST (de Vries et al. 2006; see Figure 7). The *Chandra* image does not show any extended X-ray emission; there are ~ 80 X-ray source counts. The primary C IV absorption trough is at low velocity and splits the emission line.

J115944.82+011206.9 (also B1157+014) was identified as a BAL RLQ by Menou et al. (2001), who noted that in addition to the primary low-velocity BAL there is an additional absorption trough near 8000 km s^{-1} . The depth of this secondary absorption may have increased slightly between the SDSS and HET observations. The radio spectrum appears to be double-peaked (Montenegro-Montes et al. 2008). The source shows symmetric jet-like extended emission on milliarcsecond scales and a one-sided

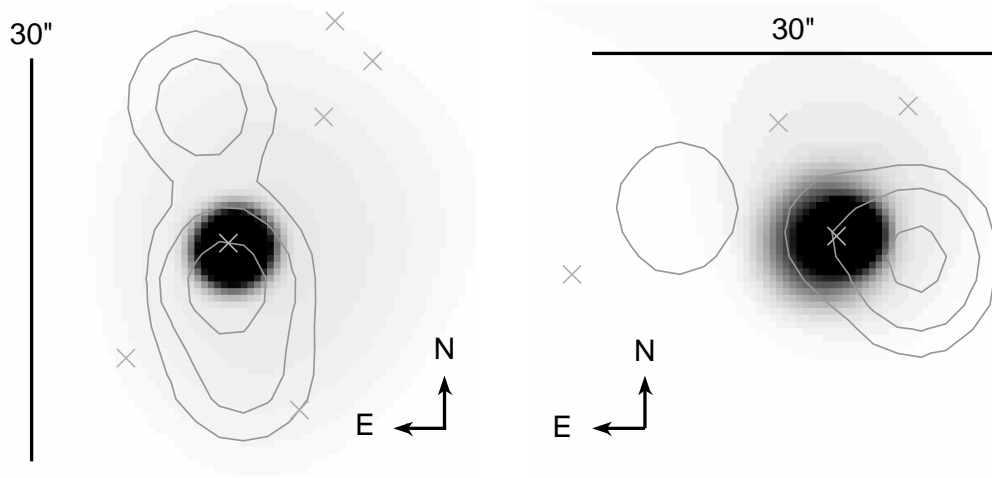


Fig. 3.7 *Chandra* images of the two BAL RLQs in the snapshot survey possessing extended radio emission. The left panel shows J102258.41+123429.7; the right panel shows J112506.95-001647.6. For both objects 30'' is $\simeq 250$ kpc. Adaptively smoothed 0.5–8 keV images are plotted in grayscale with logarithmic scaling, overlaid with contours from the 5 GHz FIRST survey at levels of 2, 8, and 32 mJy beam $^{-1}$. Peak fluxes for the radio sources are $< 85\%$ of the integrated fluxes and the deconvolved major axes are $\sim 3 - 5''$; FIRST apparently resolves these components. The crosses mark SDSS photometric sources within the field; none of these aligns with the apparent extended radio emission, further indicating that these are lobes rather than unrelated sources.

misaligned sequence of faint knots stretching to ~ 100 milliarcseconds (Montenegro-Montes et al. 2009). J115944.82+011206.9 has the lowest m_i in the snapshot sample and has sufficient X-ray counts (~ 170 from 0.5–8 keV) for basic spectral analysis (Figure 8). The relatively hard X-ray spectrum suggests intrinsic absorption; a neutral absorber has a best-fit column density of $N_H = 3.2^{+2.9}_{-2.1} \times 10^{22}$ cm $^{-2}$ with an unusual flat photon index of $\Gamma = 1.06^{+0.35}_{-0.33}$ required.

J123411.73+615832.6 has an atypical BAL structure, with a deep and wide trough that decreases gradually in depth until smoothly meeting the base of the Si IV emission line. Narrow redshifted C IV absorption is also present. A C-band VLA image (program AP450, observation date 2003-02-27) indicates that the radio spectral index is $\alpha_r \simeq -0.5$.

J133701.39-024630.3 has the highest measured X-ray hardness ratio in the snapshot or archival BAL RLQ sample. A C-band VLA image (program AG400, observation date 1994-01-08) suggests that this is a flat-spectrum RLQ with $\alpha_r \simeq -0.1$.

J141334.38+421201.7 (also FBQS J141334.4+421201) was identified as a BAL RLQ by Becker et al. (2000). The radio spectrum is complex (Montenegro-Montes et al. 2008) while the morphology is compact with a one-sided jet on milliarcsecond scales (Liu et al. 2008).

J162453.47+375806.6 is described in detail by Benn et al. (2005), and we use their value of $BI = 2990$ km s $^{-1}$ and estimate $V_{\max} = 28300$ km s $^{-1}$ rather than taking measurements from Gibson et al. (2009) (for which BAL absorption was integrated to

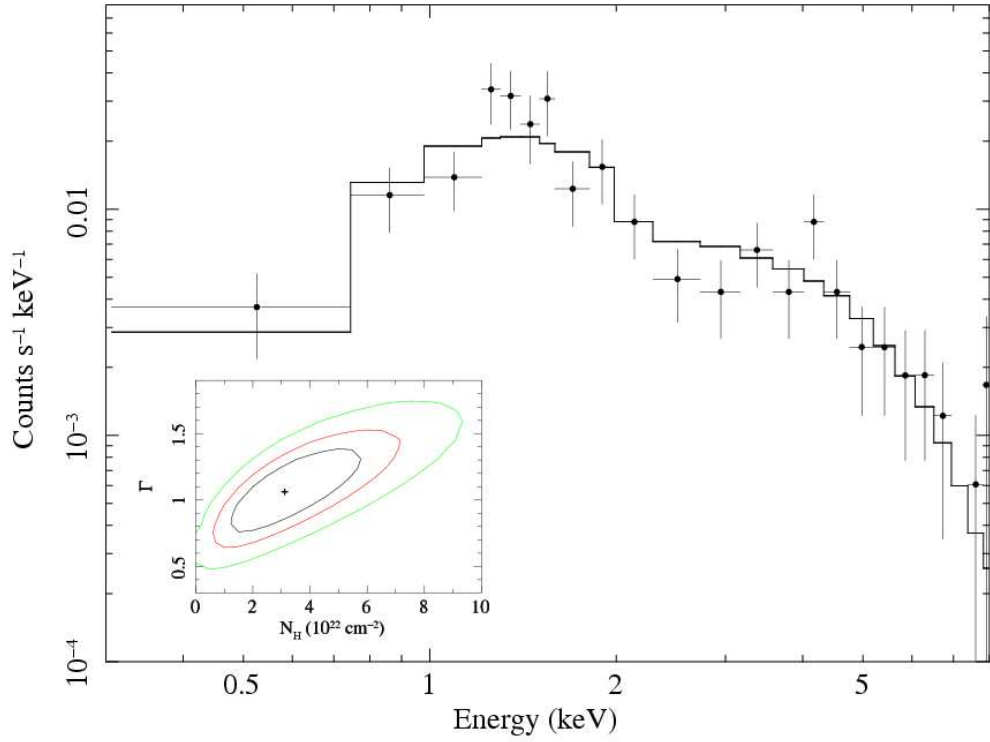


Fig. 3.8 *Chandra* spectrum of J115944.82+011206.9, the X-ray brightest source in our snapshot sample with $\simeq 170$ counts from 0.3–8 keV ($\sim 2\times$ that of the next-brightest snapshot BAL RLQ). The plotted model has intrinsic absorption with column density $N_{\text{H}} = 3.2^{+2.9}_{-2.1} \times 10^{22} \text{ cm}^{-2}$ and a power-law photon index of $\Gamma = 1.06^{+0.35}_{-0.33}$. The fit was performed using the *cstat* statistic and the cosmetic binning is based on a minimum significance of 3σ within a maximum of 30 bins. The inset shows the 68%, 90%, and 99% confidence contours (for two parameters of interest) for the photon index Γ and intrinsic column density N_{H} .

25000 km s⁻¹). The large minimum ($V_{\min} = 20560$ km s⁻¹) and maximum velocities of the C IV BAL in this source are unusual for BAL RLQs and unique within our snapshot and archival samples. There is also low-velocity absorption, described by Benn et al. (2005) as a mini-BAL (defined as total velocity range < 2000 km s⁻¹; the mini-BAL is shaded gray along with the primary BAL in Figure 6 for identification). The radio spectrum is GHz-peaked (steep at high frequencies) and milliarcsecond imaging reveals a one-sided jet (Benn et al. 2005; Montenegro-Montes et al. 2008, 2009).

3.3.3.2 Archival BAL RLQs

J020022.01–084512.0 (also FBQS J0200–0845) was identified as a BAL RLQ by Becker et al. (2001). It was observed serendipitously in an ~18 ks ACIS-I image (ObsID 3265; PI Ebeling) and is discussed by Gallagher et al. (2005). The source has a radio-loudness value of $R^* = 48$, on the border for inclusion in the archival sample.

FBQS J0256–0119 was identified as a BAL RLQ by Becker et al. (2001). Flux measurements by Montenegro-Montes et al. (2008) indicate a steep radio spectrum; those authors also note that the increased flux measured by FIRST relative to NVSS may be due to variability. The ~5 ks ACIS-S observation shows FBQS J0256–0119 to be X-ray weak but with a soft spectrum (Brotherton et al. 2005). We do not have access to photometric magnitudes for this object, so we take the lack of intrinsic reddening noted by Brotherton et al. (2005) as justification to set the relative color $\Delta(g - i) = 0$.

J081426.45+364713.5 has a low radio luminosity ($l_r = 32.7$) and the reddest relative color [$\Delta(g - i) = 1.1$] in the snapshot or archival BAL RLQ sample. The optical spectrum shows deep and wide BALs in both high- and low-ionization lines (Trump et al. 2006 categorize it as an FeLoBAL) and only weak emission lines. It was observed serendipitously in two ~10 ks ACIS-I exposures (ObsID 3436, 3437; PI Fox) and is X-ray weak.

J091951.29+005854.9 has a non-zero $BI = 673.1$ km s⁻¹ and a C IV equivalent width of 6.9 Å, but the BAL is relatively narrow and the absorption index is low ($AI = 1268$ km s⁻¹). The radio loudness is also borderline for our sample ($R^* = 51$). It was observed serendipitously in a ~5 ks ACIS-S image (ObsID 7056; PI Murray) but is not detected.

J100726.10+124856.2 (also PG 1004+130) is a low-redshift ($z = 0.24$) RLQ in which BALs were discovered by Wills et al. (1999); we use their values of $BI = 850$ km s⁻¹ and $V_{\max} = 10000$ km s⁻¹ since the SDSS spectrum does not cover the C IV region. It is also a hybrid-morphology radio source (Gopal-Krishna & Wiita 2000), with an edge-brightened lobe opposite a broadening edge-darkened jet. It is perhaps the best-studied BAL RLQ at X-ray frequencies: deep *XMM-Newton* and *Chandra* observations show X-ray absorption variability and also reveal X-ray jet emission (Miller et al. 2006). PG 1004+130 is X-ray weak relative to comparable non-BAL RLQs.

J104834.24+345724.9 (also 4C +35.23) is a CSS RLQ with a C IV BAL identified by Willott et al. (2002). It is radio luminous, and even after correcting for some intrinsic reddening it remains notably radio-loud (Kunert-Bajraszewska et al. 2007). It was targeted by *Chandra* in a ~5 ks ACIS-S observation (ObsID 9320; PI Kunert-Bajraszewska) and is detected with a hard X-ray spectral shape.

J122033.87+334312.0 (also 3C 270.1) is a double-lobed steep-spectrum RLQ with the second-highest radio loudness ($\log R^* = 4.2$) in the snapshot or archival BAL RLQ sample. Low-velocity C IV absorption has been known to be present in this object for some time (e.g., Anderson et al. 1987) although it has not necessarily been described as a BAL quasar; however, the balnicity index measured from the SDSS data is non-zero ($BI = 52.5$; Gibson et al. 2009). *J122033.87+334312.0* was observed serendipitously in a ~ 3 ks ACIS-S exposure (ObsID 2118; PI Cagnoni).

J131213.57+231958.6 (also FBQS J131213.5+231958) was identified as a BAL RLQ by Becker et al. (2000) and shows a wide and deep C IV absorption trough that extends to 25000 km s^{-1} (from FBQS data; the DR7 SDSS spectrum does not have sufficient short wavelength coverage to see the BAL). It shows two-sided extended radio emission on milliarcsecond scales but is core dominated (Jiang & Wang 2003) and likely variable (Montenegro-Montes et al. 2008); these radio characteristics do not provide a self-consistent orientation measure. Liu et al. (2008) suggest this object is similar in some respect to CSS sources. The ~ 5 ks ACIS-S observation (Brotherton et al. 2005) shows it to be X-ray weak but with an X-ray spectrum actually somewhat softer than is typical of non-BAL RLQs.

LBQS 2211–1915 was identified as a “marginal” BAL quasar by Weymann et al. (1991), with a non-zero but low $BI = 27 \text{ km s}^{-1}$, and is radio-loud based on an NVSS flux measurement. The ~ 6 ks ACIS-S observation (Gallagher et al. 2006) shows it to be X-ray weak relative to non-BAL RLQs. We estimate the relative color to be $\Delta(g - i) = 0.32$ based on data from Gallagher et al. (2007).

3.4 Data Analysis

Because RLQs are generally more X-ray luminous than comparable RQQs (e.g., Worrall et al. 1987), a direct comparison of the X-ray properties of BAL RLQs to those of BAL RQQs is of limited value. To gain additional insight, we quantify the degree to which BAL RLQs are X-ray weak relative to non-BAL RLQs, then compare this to the X-ray decrement for BAL RQQs relative to non-BAL RQQs. Much of the X-ray weakness of BAL RQQs may be explained by low-energy X-ray absorption (e.g., Gallagher et al. 2006), which can produce X-ray spectra that are harder than typical; examination of the X-ray spectral properties of BAL RLQs compared with those of non-BAL RLQs can clarify whether a similar effect typically applies to BAL RLQs.

3.4.1 Calculation of X-ray hardness ratios and luminosities

When insufficient counts are available for productive spectral modeling, as is unfortunately the case for the majority of our data, the relative contributions of hard and soft X-ray emission to the overall spectrum can be assessed from the hardness ratio $HR = (H - S)/(H + S)$, where H and S are the net hard-band (2–8 keV) and soft-band (0.5–2 keV) counts, respectively. Large values of the hardness ratio can indicate intrinsic absorption, or alternatively an unusually flat power law (or both effects together). Since all our data are taken from *Chandra* (including the non-BAL RLQ, BAL RQQ, and non-BAL RQQ comparison samples), we can compare hardness ratios without concern

for instrumental cross-calibration effects. Hardness ratios for objects observed with one of the front-illuminated CCDs have been adjusted by subtracting 0.14 to enable direct comparison to the hardness ratios for the back-illuminated CCDs (such as S3, which covers the ACIS-S aim point).

The probability distribution for the hardness ratio can be calculated using the Bayesian formalism detailed in Jin et al. (2006), using a uniform prior (i.e., their equation 13). The maximum-likelihood hardness ratio is simply $(H - S)/(H + S)$. We use this method to calculate 1σ errors on the value of HR , defined such that 68% of the area above (below) the maximum likelihood hardness ratio is enclosed within the range of the upper (lower) bound (e.g., Wu et al. 2007). Where the total number of counts exceeds 100 symmetric errors are calculated from Equation 8 of Jin et al. (2006).

X-ray luminosities are calculated from the 0.5–8 keV count rates, which are converted to observed-frame 2 keV flux densities with PIMMS⁷, in all cases assuming Galactic absorption and a power-law spectrum with $\Gamma=1.5$. This model is typical of RLQs: for example, Reeves & Turner (2000) found $\langle\Gamma\rangle = 1.66$ with $\sigma = 0.22$ for an *ASCA* sample of 35 RLQs, while Page et al. (2005) determined $\langle\Gamma\rangle = 1.55$ with $\sigma = 0.29$ for an *XMM-Newton* sample of 16 RLQs at $z > 2$. However, reasonable alternate choices for Γ have only a few percent impact upon the calculated X-ray fluxes. Count rates for archival observations were converted to flux densities using the calibration appropriate to that cycle, in order to account for the temporal changes in ACIS sensitivity. The ACIS-I model in PIMMS was used for all front-illuminated chips.

The bandpass-corrected X-ray luminosities l_x are given in units of $\log \text{ ergs s}^{-1} \text{ Hz}^{-1}$ at rest-frame 2 keV in Table 5. We also calculate X-ray luminosities $l_{x,S}$ and $l_{x,H}$ at rest-frame 2 keV determined from the soft and hard-band count rates, respectively, in order to investigate the influence of spectral shape (and intrinsic absorption) on the X-ray luminosity.

3.4.2 Relative X-ray luminosities

X-ray and optical/UV luminosities are correlated in quasars, and so to evaluate the degree of X-ray weakness in BAL quasars it is necessary to compare to non-BAL quasars of similar optical/UV luminosity. Extensive studies (e.g., Avni & Tananbaum 1986; Strateva et al. 2005; Steffen et al. 2006; Just et al. 2007; Kelly et al. 2007) have demonstrated that X-ray luminosity in non-BAL RQQs may be parameterized as $l_x \propto \beta \times l_{uv}$, where $\beta \simeq 0.6-0.8$ (i.e., the linear ratio of monochromatic optical/UV luminosity to monochromatic X-ray luminosity increases with increasing l_{uv}). There is continuing debate (e.g., Just et al. 2007; Kelly et al. 2007) as to whether the optical/UV-to-X-ray properties of individual RQQs are also significantly dependent upon redshift, but for our purposes the $l_x(l_{uv})$ parameterization is fully satisfactory to explore the large deviations from predicted X-ray luminosity that are seen in BAL quasars. We make use of the relation $l_x = 0.636 \times l_{uv} + 7.055$ (a linear fit to \log luminosities) found by Just et al. (2007) taking l_x as the dependent variable and fitting their large sample of non-BAL RQQs using the Astronomy Survival Analysis Package (ASURV; Lavelley et al. 1992).

⁷<http://cxc.harvard.edu/toolkit/pimms.jsp>

Using the Bayesian maximum-likelihood method of Kelly (2007), which accounts for both upper limits and errors (we presume uncertainties are dominated by typical quasar variability; see, e.g., §3.5 of Gibson et al. 2008), and fitting our comparison sample of RQQs yields a similar relation⁸ of $l_x = (0.574 \pm 0.057) \times l_{uv} + (8.995 \pm 1.772)$.

As an initial step toward understanding the X-ray luminosities of BAL RLQs, we fit $l_x(l_{uv})$ for non-BAL RLQs as for non-BAL RQQs, finding a best-fit correlation of $l_x = (0.905 \pm 0.079) \times l_{uv} - (0.813 \pm 2.459)$, with significant scatter (Figure 9a). The majority of snapshot and archival BAL RLQs have X-ray luminosities less than those of non-BAL RLQs with comparable optical/UV luminosities, typically by a factor of 4.1–8.5 (median 6.6). However, the difference between observed and predicted X-ray luminosity in BAL RLQs is not as extreme as that for BAL RQQs relative to non-BAL RQQs (Figure 9b); here the difference is typically a factor of 2.8–34.0 (median 11.4) but exceeds 40 for $\sim 15\%$ of BAL RQQs. The sample BAL RLQs also tend to be X-ray weaker than non-BAL RQQs at low optical/UV luminosities.

The X-ray luminosities of non-BAL RLQs can also be parameterized as a function of radio luminosity, with a best-fit result for the comparison non-BAL RLQ sample of $l_x = (0.617 \pm 0.043) \times l_r + (6.328 \pm 1.480)$ (Figure 9c). Some BAL RLQs again tend to fall below the non-BAL RLQ correlation, although to a lesser degree, while some are matched in radio and X-ray properties to comparable non-BAL RLQs. Possibly the reduced offset in $l_x(l_r)$ for BAL RLQs reflects not only X-ray weakness but also lower radio-loudness values for BAL RLQs than for the comparison non-BAL RLQs; the median value of $\log R^*$ is 2.2 for the BAL RLQs and 3.0 for the RLQs. The outlier with high radio luminosity and low X-ray luminosity is the CSS source J104834.24+345724.9 (see also §5.2). Fitting X-ray luminosity as a joint function of optical/UV *and* radio luminosity yields a relation with reduced scatter: $l_x = (0.472 \pm 0.085) \times l_{uv} + (0.413 \pm 0.054) \times l_r - (1.392 \pm 1.192)$ (Figure 9d). Due to the similar coefficients BAL RLQs have essentially averaged offsets from $l_x(l_{uv})$ and $l_x(l_r)$ for $l_x(l_{uv}, l_r)$. Obviously more sophisticated models are possible, but this provides a useful quantitative measure of X-ray luminosity in BAL RLQs relative to RLQs taking into account both optical/UV and radio properties.

The difference between the observed X-ray luminosity in BAL RLQs and that predicted from non-BAL RLQs with comparable optical/UV luminosities, $\Delta l_{x,uv} = l_x - l_x(l_{uv})$, is plotted as a histogram in Figure 10a. The scatter for non-BAL RLQs (Figure 10b) is smaller than the degree to which BAL RLQs are X-ray weak. However, BAL RLQs do not extend to extreme values of X-ray weakness (log offsets of < -1), as do some BAL RQQs [Figure 10c; here $\Delta l_{x,uv}$ is calculated from the Just et al. (2007) relation for non-BAL RQQs] relative to non-BAL RQQs (Figure 10d). Note that the underlying distribution of $\Delta l_{x,uv}$ for BAL RQQs is even X-ray weaker than the histogram in Figure 10c suggests, as there are a large number of X-ray upper limits. There appears to be a limit to how X-ray weak BAL RLQs can become. The Kaplan–Meier estimates of the median $\Delta l_{x,uv}$ values are -0.82 , -0.03 , and -1.06 for BAL RLQs, non-BAL RLQs, and BAL RQQs, respectively. A Peto–Prentice two-sample test indicates that

⁸Here and for subsequent model fits the quoted parameter values are the median of draws from the posterior distribution and the errors are 1σ .

the distribution of $\Delta l_{x,uv}$ values for BAL RLQs is significantly different from that of non-BAL RLQs (test statistic 6.621, $p < 5 \times 10^{-5}$) and BAL RQQs (test statistic 2.249, $p = 0.02$). Figure 10e shows a histogram of the difference between the observed X-ray luminosity in BAL RLQs and that predicted from non-BAL RLQs with comparable optical/UV *and* radio luminosities, $\Delta l_x = l_x - l_x(l_{uv}, l_r)$. BAL RLQs are a factor of 2.0–4.5 (median 3.2) weaker in X-rays than comparable non-BAL RLQs. The results are similar if the relative X-ray luminosity is instead calculated from the soft- or hard-band luminosities, $l_{x,S}$ and $l_{x,H}$ (Figures 10f and 10g).

There is a general trend in quasars relating C IV absorption to X-ray weakness (e.g., Brandt, Laor, & Wills 2000; Laor & Brandt 2002; Gallagher et al. 2006). We plot the relative X-ray luminosity for BAL RLQs [presented as $\Delta\alpha_{ox}$ for ease of comparison to previous work, where $\alpha_{ox} = 0.384 \times (l_x - l_{uv})$ and $\Delta\alpha_{ox} = \alpha_{ox} - \alpha_{ox}(l_{uv})$ with $\alpha_{ox}(l_{uv})$ calculated from the $l_x(l_{uv})$ relations given above] versus C IV equivalent width (Figure 11a) and maximum outflow velocity (Figure 11b). It is apparent that even BAL RLQs with large C IV equivalent widths (10–40 Å) do not have $\Delta\alpha_{ox} < -0.5$, as do many strongly absorbed BAL RQQs. BAL RLQs appear to follow the correlation between maximum outflow velocity and relative X-ray luminosity that holds for BAL RQQs, but only to a limiting value of $\Delta\alpha_{ox}$, near which BAL RLQs are observed with a wide range of outflow velocities.

Additional context for interpreting the relative X-ray luminosities of some BAL RLQs is provided by their radio morphologies or spectral properties, which can constrain source inclination (e.g., Wills & Brotherton 1995) or age (e.g., Stawarz et al. 2008). Lobe-dominated BAL RLQs (nested symbols in Figures 9 and 11), which presumably lie at larger angles to the line of sight than do core-dominated BAL RLQs, show a range of behavior: J112506.95–001647.6 and J122033.87+334312.0 are X-ray bright relative to non-BAL RLQs with similar optical/UV luminosities, whereas J102258.41+123429.7 and particularly J100726.10+124856.2 (PG 1004+130) are X-ray weak. J122033.87+334312.0 becomes X-ray weak when radio luminosity is also taken into account, and perhaps the X-ray brightness of J112506.95–001647.6 reflects its relatively weak C IV BAL (low absorption index and maximum velocity). Plausibly young objects [including the GPS sources J083749.59+364145.4 and J162453.47+375806.6 as well as the CSS source J104834.24+345724.9 (4C+35.23)] seem to have strong BALs and to be X-ray weak, but additional data are required to investigate such trends in detail.

3.4.3 X-ray spectral characteristics

Most of the quasars in the snapshot and archival BAL RLQ samples and in the non-BAL RLQ, BAL RQQ, and non-BAL RQQ comparison samples lack sufficient counts for productive spectral fitting, so we investigate basic X-ray spectral properties using hardness ratios (see §4.1). We are primarily interested in whether BAL RLQs show evidence for intrinsic X-ray absorption. Absorption by a neutral column will preferentially remove soft X-ray emission and lead to greater values of HR , although this effect can be diluted by complex (partial covering or ionized) absorption, such as is established to occur in BAL RQQs (e.g., Gallagher et al. 2002, 2006) and has been suggested for

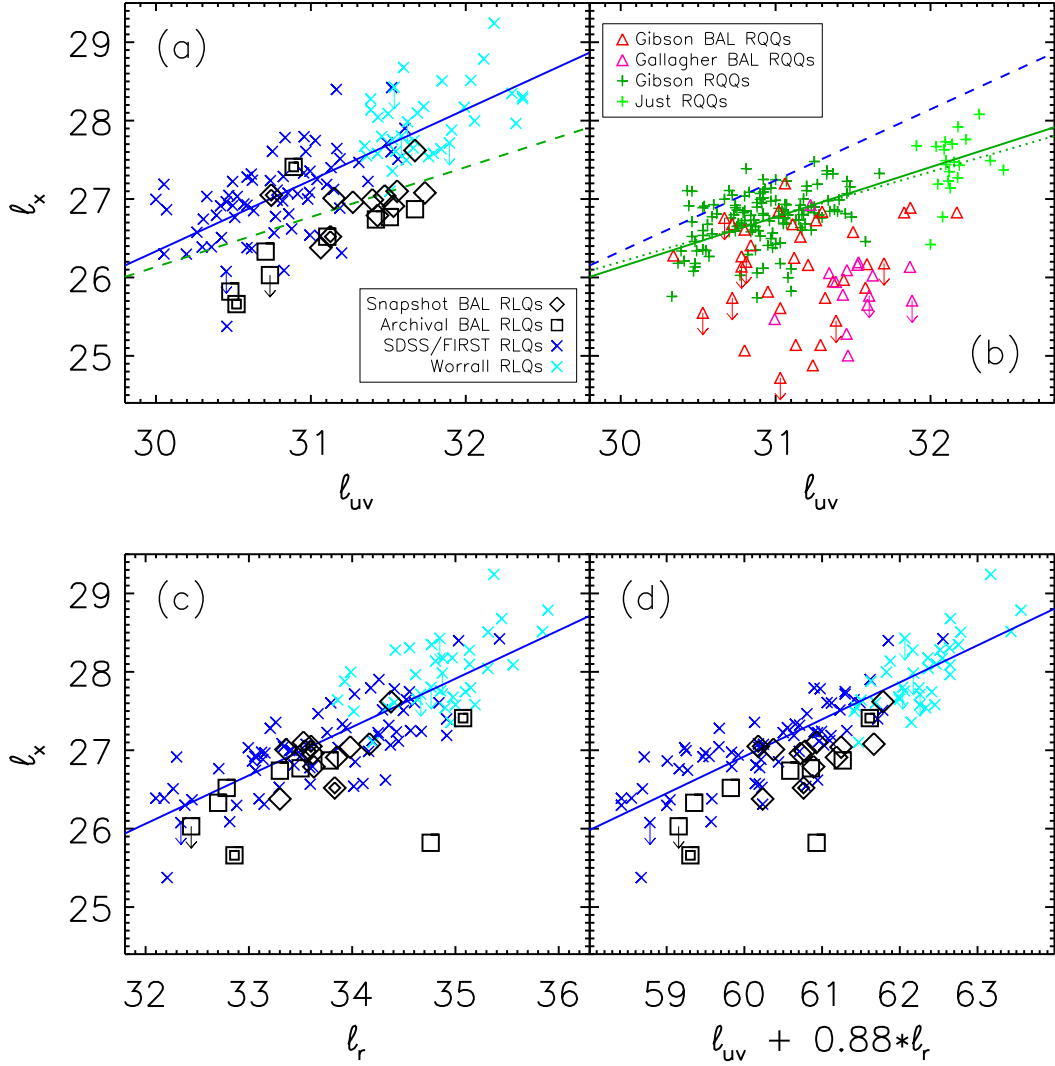


Fig. 3.9 X-ray luminosities of BAL quasars compared to similar non-BAL quasars. Luminosities have units of $\log \text{ergs s}^{-1} \text{Hz}^{-1}$, at rest-frame frequencies of 5 GHz, 2500 Å, and 2 keV for l_r , l_{uv} , and l_x , respectively. Arrows indicate X-ray upper limits, and nested symbols are lobe-dominated BAL RLQs. Blue lines are best-fit correlations for non-BAL RLQs (taking l_x as the dependent variable) calculated using the Bayesian maximum-likelihood method of Kelly (2007). The solid green line shows the best-fit correlation for non-BAL RQQs that Just et al. (2007) calculated with ASURV for a large sample of RQQs; fitting our comparison sample of RQQs yields a similar result (dotted green line). The $l_x(l_{uv})$ relation for RLQs/RQQs is also plotted as a dashed line in (b)/(a), illustrating the well-known tendency for RLQs to be X-ray brighter than comparable RQQs. BAL RLQs are X-ray weak relative to non-BAL RLQs with similar optical/UV luminosities (a) but not to the same degree as are BAL RQQs relative to non-BAL RQQs (b). BAL RLQs are also modestly X-ray weak relative to non-BAL RLQs with similar radio luminosities (c) and to non-BAL RLQs with similar optical/UV and radio luminosities (d).

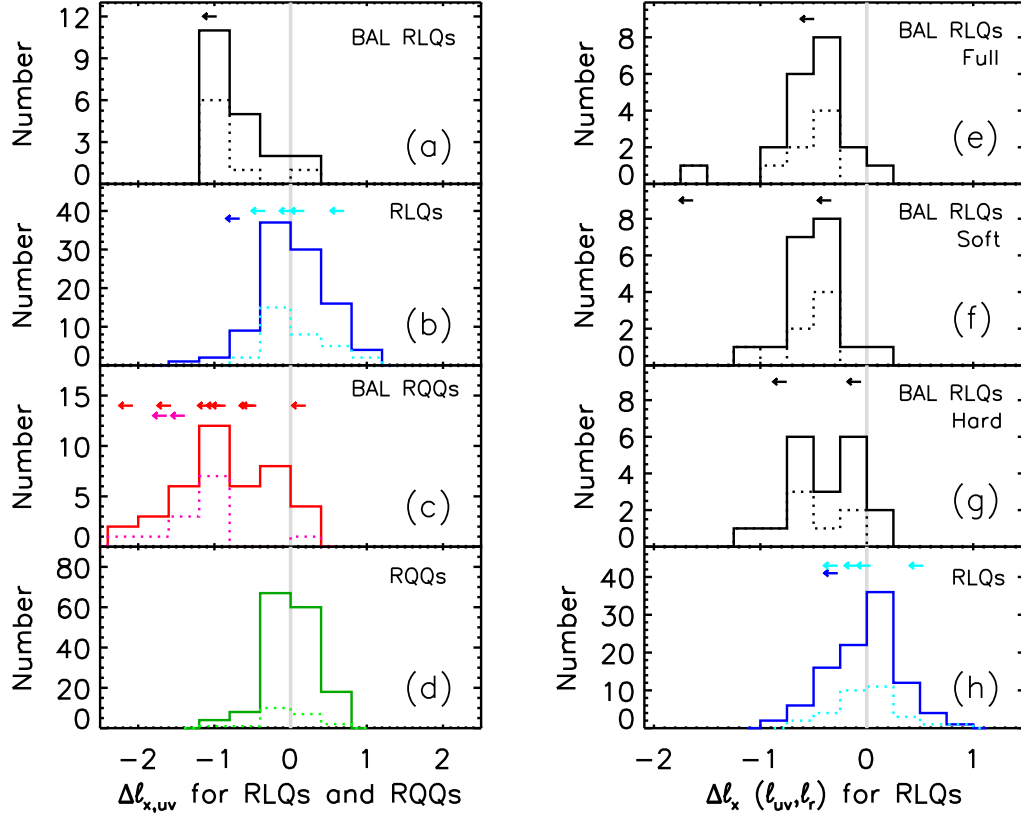


Fig. 3.10 Histograms showing the distribution of the difference between actual and anticipated X-ray luminosity. Arrows indicate X-ray limits. Dotted histograms show subsamples: archival BAL RLQs (black), Worrall et al. (1987) RLQs (cyan), Gallagher et al. (2006) BAL RLQs (magenta), and Just et al. (2007) RQQs (light green). The left column (a, b, c, d) shows $\Delta l_{x,uv}$ calculated from optical/UV luminosities using the relations shown in Figures 9a and 9b. BAL RQQs reach more extreme values of X-ray weakness relative to non-BAL RQQs than do BAL RLQs relative to non-BAL RLQs with similar optical/UV luminosities. The right column (e, f, g, h) shows Δl_x calculated from both optical/UV and radio luminosities for RLQs, using the relation shown in Figure 9d. X-ray luminosity is calculated using the full (0.5–8 keV), soft (0.5–2 keV), and hard (2–8 keV) counts. BAL RLQs are typically X-ray weaker than comparable non-BAL RLQs by a factor of 2.0–4.5. The similarity of results derived using full, soft, and hard X-ray luminosities suggests simple absorption of the entire X-ray continuum source cannot provide a universal explanation for the X-ray weakness in BAL RLQs.

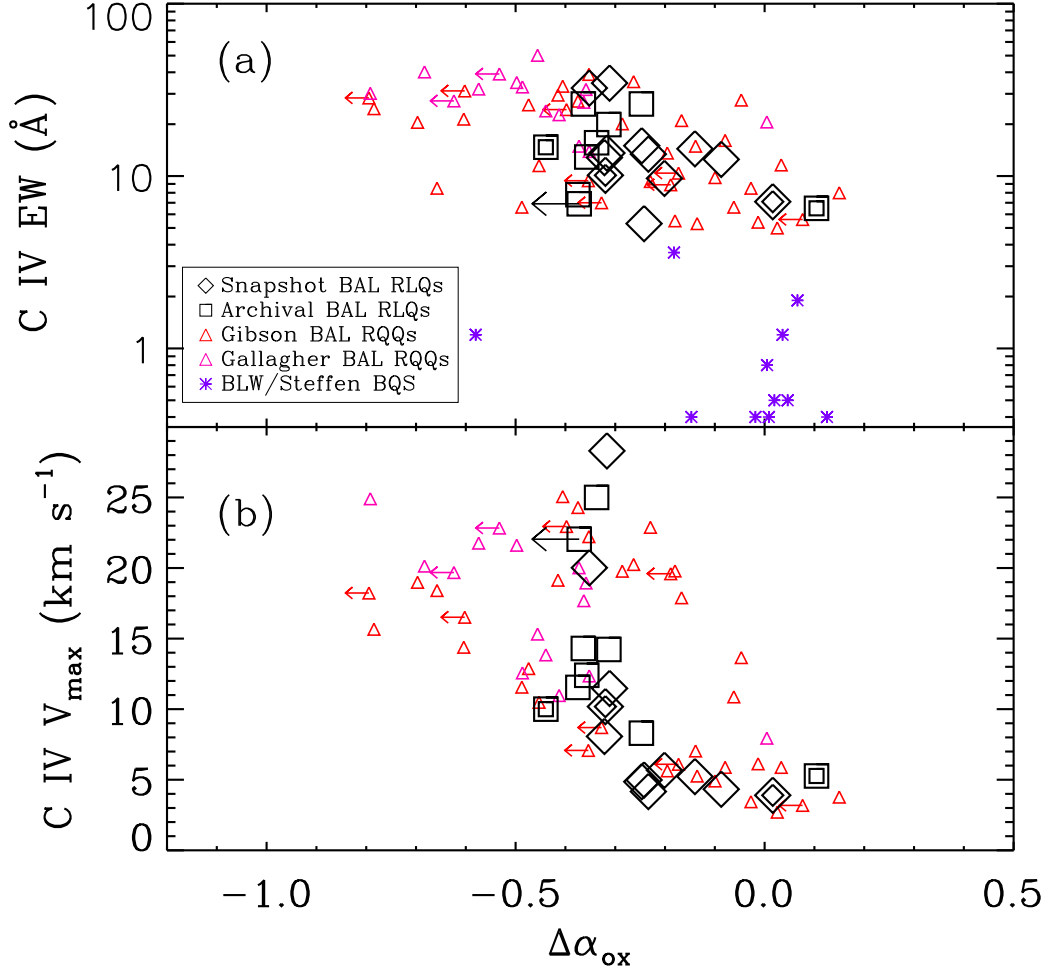


Fig. 3.11 C IV absorption properties as a function of relative X-ray luminosity, calculated using the relations shown in Figures 9a and 9b and expressed in terms of $\Delta\alpha_{\text{ox}}(l_{\text{uv}})$, where $\alpha_{\text{ox}} = 0.384 \times (l_{\text{x}} - l_{\text{uv}})$, for ease of comparison with previous work. Panel (a) shows C IV equivalent width and (b) shows maximum outflow velocity. Nested symbols are lobe-dominated BAL RLQs. The purple points in (a) are non-BAL RQQs from the BQS, with C IV absorption values from Brandt, Laor, & Wills (2000) and optical and X-ray luminosities from Steffen et al. (2006). X-ray weakness appears more closely linked to absorption strength in BAL RQQs than in BAL RLQs; even BAL RLQs with extreme C IV absorption properties do not have $\Delta\alpha_{\text{ox}} < -0.5$, as do many strongly absorbed BAL RQQs.

BAL RLQs (e.g., Brotherton et al. 2005). Absorption spectral effects are also diluted by increasing redshift pushing the rest-frame soft band to lower observed-frame energies.

The non-BAL RLQs in our comparison sample have relatively uniform hardness ratios that do not appear strongly dependent upon redshift (Figure 12a), suggesting that the spectra for these RLQs are generally dominated by a simple power-law component with a standard photon index and insignificant intrinsic absorption. Many BAL RLQs have hardness ratios similar to those of non-BAL RLQs, but there are several BAL RLQs with harder X-ray spectra, although none with measured $HR > 0.2$. A Peto-Prentice two-sample test indicates that the distribution of HR values for BAL RLQs is significantly different from that of non-BAL RLQs (test statistic 3.704, $p = 2 \times 10^{-4}$). BAL RQQs typically have harder X-ray spectra than non-BAL RQQs (the distributions are statistically different, with $p < 5 \times 10^{-5}$) and can have extreme hardness ratios (Figure 12b). The distribution of hardness ratios for the snapshot and archival sample of BAL RLQs is not statistically inconsistent with that of BAL RQQs (test statistic 1.396, $p = 0.16$). The Kaplan-Meier estimates of the median/mean HR values for the BAL RLQs, non-BAL RLQs, BAL RQQs, and non-BAL RQQs in our samples are -0.40 , -0.52 , -0.26 , and -0.57 , respectively; the distribution for BAL RLQs is skewed, with a Kaplan-Meier estimate of the mean HR of -0.34 . The slightly higher median HR for non-BAL RLQs relative to non-BAL RQQs might be expected from prior X-ray spectral studies, but the distributions for our comparison samples of non-BAL RLQs and non-BAL RQQs are not statistically inconsistent ($p = 0.23$; possibly the more radio-luminous RLQs observed by *Einstein* would have slightly larger *Chandra* hardness ratios than the RLQs plotted here). For reference, a photon index of $\Gamma = 2$ approximately corresponds to $HR = -0.6$ and $\Gamma = 1.7$ to $HR = -0.5$.

Five BAL RLQs have particularly hard X-ray spectral shapes (with $HR > -0.2$) relative to both RLQs and other BAL RLQs; these objects include J092913.96+375742.9 and J115944.82+011206.9 (both of which apparently have small-scale radio jet emission), J133701.39-024630.3, J100726.10+124856.2 (PG 1004+130, for which the *XMM-Newton* spectrum is softer), and J104834.24+345724.9 (the CSS source 4C+35.23). Although this study is not designed to investigate the X-ray spectral properties of various subcategories of BAL RLQs, we note briefly that the GPS sources J083749.59+364145.4 and J162453.47+375806.6 have soft X-ray spectral shapes, and the FeLoBAL object J081426.45+364713.5 has an intermediate $HR = -0.29$, slightly harder than the median for the BAL RLQs studied here.

The correlation between X-ray weakness and hardness ratio in BAL RQQs (Figure 12d) is reflective of (often complex) absorption reducing the soft-band X-ray flux in BAL RQQs (e.g., Gallagher et al. 2006). A similar trend is not obviously apparent for BAL RLQs (Figure 12c), for which there are several X-ray weak objects with low hardness ratios (or soft X-ray spectra), and essentially no BAL RLQs with $\Delta l_x(l_{uv}) \lesssim -1$. Note that our observations are sensitive to low values of $\Delta l_x(l_{uv})$ (only one undetected BAL RLQ is not plotted, and many of the rest could be detected if they were even X-ray weaker by a linear factor of 5–10; see net counts in Tables 1 and 2); the sample simply lacks notably X-ray weak BAL RLQs. It does not appear possible to ascribe X-ray weakness in BAL RLQs to intrinsic absorption (with properties as in BAL RQQs) obscuring the

entire nuclear X-ray continuum source, although such an interpretation could hold for some particular BAL RLQs.

3.5 Discussion

3.5.1 Physical models

The above results suggest a picture in which BAL RLQs are in some sense intermediate between BAL RQQs and non-BAL RLQs: BAL RLQs are X-ray weak, but not to the same relative degree as are BAL RQQs, and they can have harder X-ray spectra, but often have hardness ratios consistent with those of non-BAL RLQs. A simple physical model could also portray BAL RLQs as having X-ray characteristics of both BAL RQQs (an outflowing BAL wind that is associated with an X-ray absorber) and non-BAL RLQs (an unresolved X-ray emitting jet that contributes to the total continuum). There are too many free parameters to constrain such a model in detail, but some insight can be gained by making the simplifying assumptions that the disk-corona emission in RLQs has the same optical/UV-to-X-ray properties as are observed in RQQs [i.e., that any systematic differences in the accretion structure of RLQs compared to RQQs do not produce dramatic changes in the $l_x(l_{uv})$ relation], and that the optical luminosity in RLQs is dominated by disk-related emission with only a minimal jet-linked contribution (certainly plausible for these broad-line RLQs, and often inferred for even RLQs in which the radio emission and the X-ray emission are established as jet-dominated; e.g., Sambruna et al. 2006). Then the disk-corona X-ray luminosity in RLQs may be calculated using the $l_x(l_{uv})$ relation for RQQs, and any additional X-ray luminosity may be ascribed to jet-linked emission.

The ratio of total RLQ X-ray luminosity to equivalent RQQ (disk-corona) X-ray luminosity increases with increasing radio luminosity (Figure 13a); this presumably reflects increasing jet luminosity at both radio and X-ray frequencies with decreasing inclination. The precise nature of the X-ray jet emission in RLQs (and its dependence upon inclination) remains a matter of debate, although it seems likely that two-zone models are required (e.g., Jester et al. 2006), in which beamed jet-linked X-ray emission from the fast spine dominates for objects viewed at low inclinations while a slower (and less beamed) sheath could generate jet-linked X-ray emission radiated in a more isotropic manner. We refrain from imposing a particular jet model upon the data but quantify the observed increase in the X-ray luminosity of RLQs relative to RQQs with increasing radio luminosity through the trendline shown in Figure 13a. Non-BAL RLQs with optical/UV and radio luminosities similar to those of the BAL RLQs in our sample would have total X-ray luminosities greater than the non-BAL RQQ equivalent by a typical multiplicative factor of 1.8–2.7, suggesting roughly equal contributions from disk-corona and jet-linked X-ray emission.

If we further presume that the X-ray absorber in BAL RLQs has characteristics similar to those found for BAL RQQs, then based on Figure 10c the disk-corona emission ought to be reduced by a factor of ~ 10 in BAL RLQs relative to non-BAL RLQs. If the jet-linked X-ray emission were also absorbed to a similar degree, the entire X-ray continuum in BAL RLQs would be veiled as in BAL RQQs and the relative X-ray

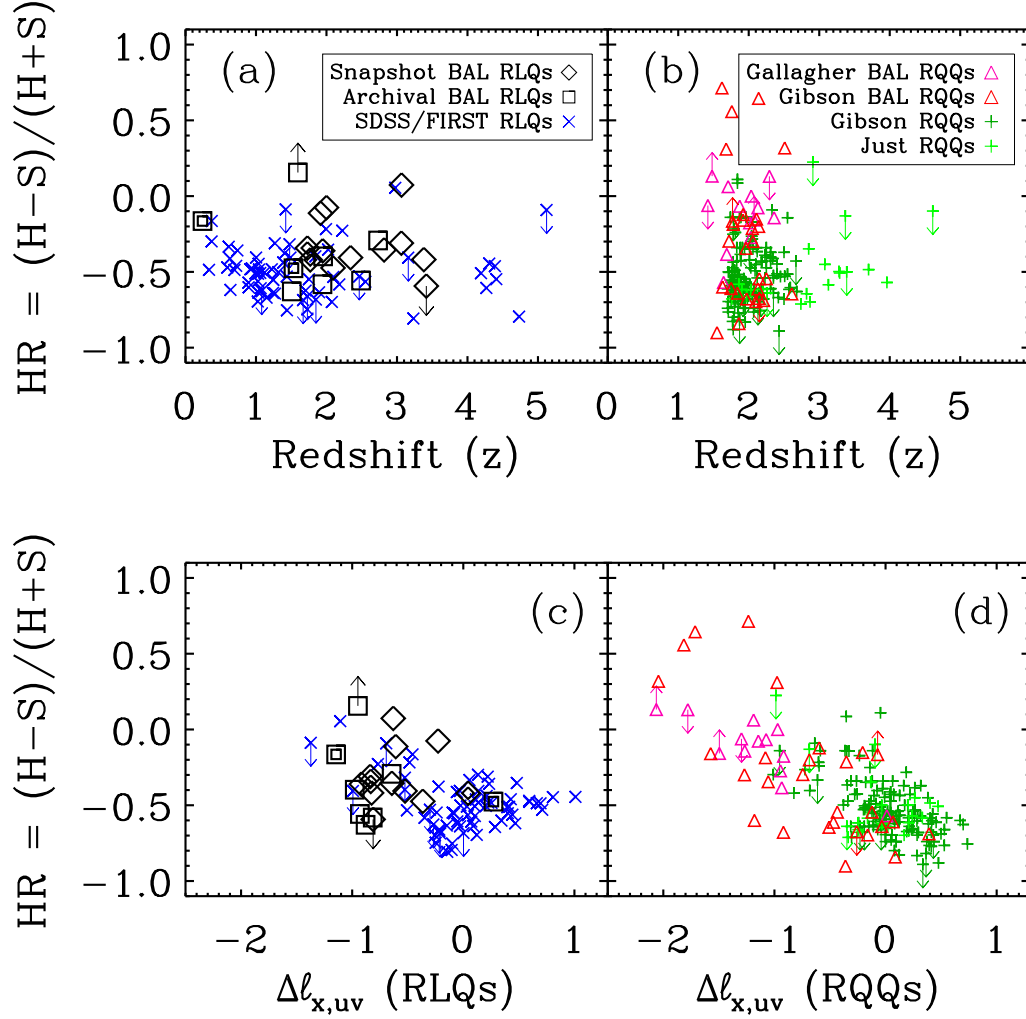


Fig. 3.12 Hardness ratio plotted versus redshift for the sample of BAL RLQs (nested symbols are lobe-dominated BAL RLQs) and for comparison samples of RLQs (a) and for BAL RQQs and RQQs (b). The X-ray spectra of BAL RLQs are sometimes harder than those of typical non-BAL RLQs, but are often consistent. The X-ray spectra of BAL RQQs are often harder than for typical non-BAL RQQs, reaching extreme hardness ratios in some cases, and the distribution of hardness ratios for BAL RQQs is not statistically consistent with that of RQQs. Panels (c) and (d) show hardness ratio plotted versus $\Delta l_{x,uv}$ calculated using the relations shown in Figures 9a and 9b; the X-ray weakness of BAL RQQs is linked to increasing intrinsic absorption of the continuum (illustrated via harder X-ray spectra), while many X-ray weak BAL RLQs do not have extremely hard X-ray spectra.

luminosities and hardness ratios of BAL RLQs would agree better with those of BAL RQQs, in contrast to observation. However, it seems that the jet must be partially covered by the BAL-linked X-ray absorber in order to explain the difference between predicted and observed jet-linked X-ray emission in BAL RLQs. Specifically, we find that many BAL RLQs have jet-linked X-ray emission only 20%–80% of that expected, and further those BAL RLQs with hardness ratios harder than 90% of RLQs tend to have less jet-linked X-ray emission than predicted (Figure 13b). We postulate that the BAL-linked X-ray absorber is of sufficient size to cover some fraction of the X-ray emitting jet in many BAL RLQs.

Alternative scenarios are possible; while we cannot rule them out, they are difficult to motivate either physically or from the data. It might be surmised that BAL RLQs are intrinsically X-ray weak relative to RLQs and are also (typically) unabsorbed. The X-ray absorber is thought to shield the BAL wind from overionization in disk-wind models (e.g., Murray et al. 1995), so such a postulated lack of an X-ray absorber could require BAL formation and acceleration to occur in a manner distinct from that in BAL RQQs. One mechanism by which BAL RLQs could be intrinsically X-ray weak would be if the presence of a BAL outflow inhibited the production of small-scale jet-linked X-ray emission. If the disk/corona system were relatively similar to that of RQQs, then BAL RLQs should follow the non-BAL RQQ luminosity correlations; however, BAL RLQs with lower radio luminosities have X-ray luminosities less than those of non-BAL RQQs with comparable optical/UV luminosities (Figures 9a and 13a). Another mechanism by which BAL RLQs could be intrinsically X-ray weak would be for the disk/corona system to be an inefficient emitter of X-rays. If the small-scale X-ray emitting jet were relatively similar to that in RLQs, then as the fractional contribution in RLQs from the disk/corona would be expected to decrease at high radio luminosities, the difference in X-ray luminosity between BAL RLQs and RLQs should likewise decrease; however, the offset between BAL RLQs and RLQs appears roughly constant (Figures 9c and 9d) across the two orders of magnitude in radio luminosity spanned by our sample. In any event, it seems most straight-forward to retain those fundamental features firmly established as present in BAL RQQs or RLQs when interpreting BAL RLQs, and the simple model associated with Figure 13 and described above suffices to explain the current data naturally.

3.5.2 BAL RLQ geometries and ages

There have been suggestions that BAL outflows occur at low inclinations (e.g., Brotherton et al. 2006; Zhou et al. 2006), something difficult to explain from simple disk-wind models. Some of the BAL RLQs in our sample have radio properties consistent with the jet being pointed close to the line of sight, including compact morphologies and flat radio spectra, although GPS sources with sparsely sampled radio spectra can mimic such characteristics at a range of inclinations. It does not seem likely that outflows in BAL RLQs must always be polar, since some of the BAL RLQs in our sample are steep-spectrum objects dominated by extended radio emission, arguing against low inclinations for these objects. We can estimate the inclinations of the core-dominated BAL RLQs using the core-radio-to-optical luminosity ratio (essentially the radio loudness, excluding

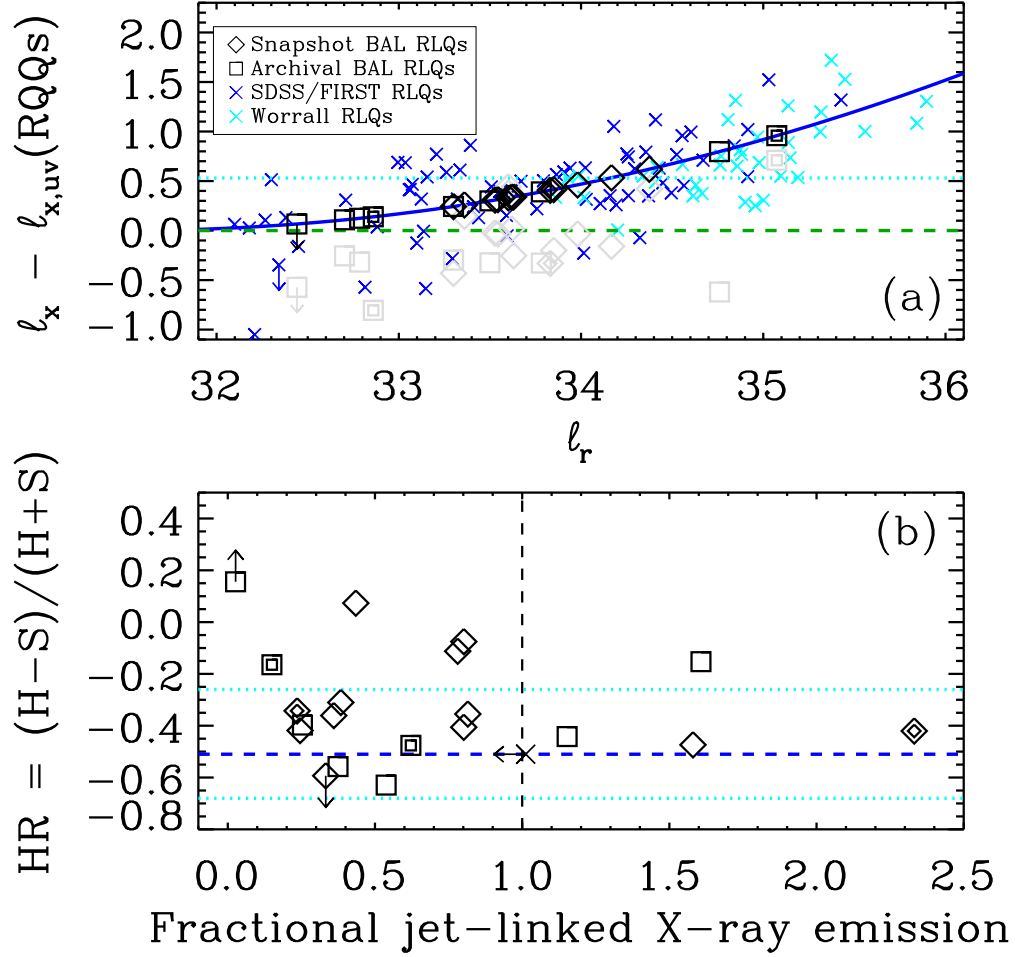


Fig. 3.13 The top panel (a) shows the ratio of X-ray luminosity in RLQs to that of RQQs with comparable optical/UV luminosities, expressed in log units, as a function of radio luminosity. The median factor by which the comparison sample of RLQs are X-ray brighter than the comparison sample of RQQs is 3.4 (cyan dashed line); there is a trend (illustrated with the solid blue line) toward increasing X-ray brightness with increasing radio luminosity that likely reflects increasing jet dominance. BAL RLQs are plotted at their predicted (black) and observed (gray) X-ray luminosity ratios (nested symbols are lobe-dominated BAL RLQs). The bottom panel (b) shows the fraction of jet-linked X-ray emission in BAL RLQs relative to that expected for non-BAL RLQs with similar optical/UV and radio luminosities, assuming the disk/corona X-ray emission (predicted from the optical/UV luminosity using the RQQ relation) is reduced by a factor of 10, as is typical for BAL RQQs. Values for the fractional jet-linked emission near (or above) 1 would suggest the jet is unobscured, while values near 0.1 would indicate the jet is covered and reduced in intensity to a similar degree as is the disk/corona emission. The median, 10th, and 90th percentile values of hardness ratio for RLQs are also plotted (blue dashed and cyan dotted lines, respectively).

lobe emission; Wills & Brotherton 1995), and find probable inclinations of $\sim 20^\circ$ to $> 40^\circ$, but this method is insensitive to larger inclinations and may not apply to BAL RLQs. The sample BAL RLQs do not tend to have large values of R^* ($\gtrsim 500$ – 1000), with the two exceptions being a lobe-dominated and a CSS RLQ, suggesting most are not low inclination sources (cf. Figure 1 of Wills & Brotherton 1995).

The discovery of BALs in RLQs which are compact and have radio spectra similar to those of presumed young GPS or CSS sources has led to suggestions that BALs are associated with a quasar evolutionary phase.⁹ Not all GPS or CSS sources display BALs, and not all BAL RLQs are associated with young sources;¹⁰ if there is no inclination dependence to BALs then (as assessed by Shankar et al. 2008) strictly evolutionary models require problematic fine tuning of the various phases to match observations. It is possible to compare directly the X-ray properties of GPS and CSS sources to those of BAL RLQs to search for similarities. We plot data from *Chandra* observations of GPS and CSS radio galaxies and RLQs carried out by Siemiginowska et al. (2008) on the $l_x(l_{uv})$ and $l_x(l_r)$ relations shown earlier (Figure 14). GPS/CSS sources are often X-ray weak relative to RLQs of similar optical/UV luminosity, but they are also often extremely radio-loud (see also the spectral energy distribution plots from Siemiginowska et al. 2008) in a manner that the (non-GPS, non-CSS) BAL RLQs are not. The CSS BAL RLQ J104834.24+345724.9 is both radio luminous and X-ray weak, with a hard X-ray spectrum atypical of GPS/CSS sources, as might be expected for an object in both classes.

3.6 Conclusions

This work presents and discusses the X-ray properties of 21 BAL RLQs observed with *Chandra*. The sample of BAL RLQs spans a wide range of C IV absorption properties, is dominated by high-ionization BAL quasars, is restricted to definitively radio-loud quasars with $R^* \gtrsim 50$, and includes objects with both core-dominated and lobe-dominated radio morphologies. We find the following results:

1. BAL RLQs are X-ray weak relative to non-BAL RLQs of similar optical/UV luminosity, but not to as extreme a degree as are BAL RQQs relative to comparable non-BAL RQQs. BAL RLQs are also X-ray weak, to a lesser extent, relative to non-BAL RLQs of similar radio luminosity or of both similar optical/UV and radio luminosities.
2. BAL RLQs do not show a strong correlation between X-ray spectral hardness and X-ray weakness, as is observed in BAL RQQs, and do not tend to have as extreme hardness ratios as can BAL RQQs.
3. The simplest model to explain our results is that the X-ray continuum in BAL RLQs consists of both disk/corona and jet-linked X-ray emission; absorption of the

⁹The relatively high fraction of low-ionization BAL quasars among dust-reddened quasars has also motivated the association of (at least low-ionization) BALs with young quasars (e.g., Urrutia et al. 2009).

¹⁰As in our sample, BAL RLQs can be found in FR IIs with large projected sizes, although the rarity of such objects is interpreted by Gregg et al. (2006) as support for an evolutionary scenario.

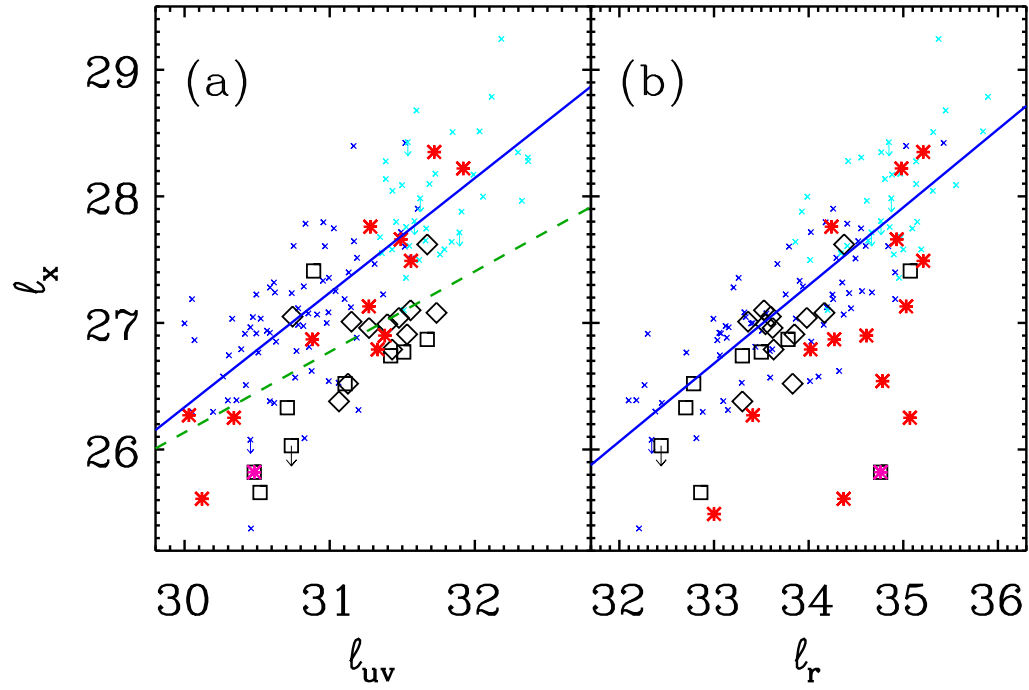


Fig. 3.14 Comparison of the luminosities of GPS and CSS sources to those of BAL RLQs and non-BAL RLQs. Data for GPS and CSS sources (red stars) are from Siemiginowska et al. (2008). The legend and caption for BAL RLQs and non-BAL RLQs are identical to Figures 9a and 9c for (a) and (b), respectively. The $l_x(l_{uv})$ relation for non-BAL RLQs from Figure 9b is shown as a dotted green line in (a). The CSS BAL RLQ J104834.24+345724.9 is indicated with a magenta star.

disk/corona emission alone typically will neither reduce the observed X-ray luminosity nor harden the X-ray spectrum of BAL RLQs to the same degree as in BAL RQQs.

4. Although jet-linked X-ray emission in BAL RLQs does not generally appear to be absorbed to the same degree as is the X-ray continuum in BAL RQQs, it does seem likely that the X-ray emitting small-scale jet is partially covered in many BAL RLQs.

Microquasar observations have been interpreted to show that in the soft state a radiatively-driven disk wind develops and becomes the dominant channel for outflow of accreting material, quenching the jet (Neilsen & Lee 2009). Although the dearth of BALs in strongly radio-loud objects suggests that a similar mechanism may apply to quasars, it is clear that jets and winds can coexist in at least some RLQs. Further X-ray studies can help clarify the relationship between jets and outflows in RLQs: snapshot *Chandra* observations of additional BAL RLQs could permit more quantitative consideration of various physical models, while deep *XMM-Newton* spectral observations of the brightest BAL RLQs would help elucidate the properties of the X-ray absorber and perhaps differentiate them from those in BAL RQQs.

3.7 Acknowledgments

We gratefully acknowledge the financial support of NASA grant SAO SV4-74018 (G. P. G., Principal Investigator) and NASA LTSA grant NAG5-13035 (B. P. M., W. N. B.). We thank the referee for useful comments, Mike Eracleous for helpful discussions as well as assistance with HET/LRS data reduction and analysis, Jianfeng Wu for technical advice, and Chris Willot and Bob Becker/Rick White for providing us with electronic spectra of 4C +35.23 and FBQS 0256–0119, respectively.

Funding for the SDSS and SDSS-II has been provided by the Alfred P. Sloan Foundation, the Participating Institutions, the National Science Foundation, the U.S. Department of Energy, the National Aeronautics and Space Administration, the Japanese Monbukagakusho, the Max Planck Society, and the Higher Education Funding Council for England. The SDSS Web Site is <http://www.sdss.org/>.

The Hobby-Eberly Telescope (HET) is a joint project of the University of Texas at Austin, the Pennsylvania State University, Stanford University, Ludwig-Maximilians-Universität München, and Georg-August-Universität Göttingen. The HET is named in honor of its principal benefactors, William P. Hobby and Robert E. Eberly. The Marcario Low-Resolution Spectrograph is named for Mike Marcario of High Lonesome Optics, who fabricated several optics for the instrument but died before its completion; it is a joint project of the Hobby-Eberly Telescope partnership and the Instituto de Astronomía de la Universidad Nacional Autónoma de México.

Table 3.1. *Chandra* and *HET* Observing Log

Name (SDSS)	ObsID	<i>Chandra</i> Observations			<i>HET</i> Observations			
		Date	Exp (s)	Counts ^a	Date	Exp (s)	$\lambda/\Delta\lambda^b$	S/N ^c
074610.50+230710.8..	9160	2007 Dec 12	6954	67.9 ^{+9.3} _{-8.2}	2007 Dec 18	1200	867	10
083749.59+364145.4..	9153	2007 Dec 23	6101	17.7 ^{+5.3} _{-4.2}	2007 Dec 18	1800	867	20
085641.58+424254.1..	9156	2008 Feb 10	5968	17.0 ^{+5.2} _{-4.1}	2008 Feb 24	1500	867	18
092913.96+375742.9..	9162	2007 Dec 28	3987	47.6 ^{+7.9} _{-6.9}
102258.41+123429.7..	9154	2008 Apr 04	4976	24.1 ^{+6.0} _{-4.9}	2008 May 03	900	300	26
105416.51+512326.0..	9163	2008 Jan 20	4979	36.7 ^{+7.1} _{-6.0}	2008 Feb 08	1500	867	19
112506.95-001647.6..	9157	2008 Apr 29	5112	80.1 ^{+10.0} _{-8.9}
115944.82+011206.9..	9158	2007 Feb 28	3706	171.1 ^{+14.1} _{-13.1}	2008 Feb 13	900	867	37
123411.73+615832.6..	9152	2008 Feb 22	6142	17.4 ^{+5.2} _{-4.1}	2008 Apr 23	1500	867	29
133701.39-024630.3..	9159	2007 Dec 10	4692	23.3 ^{+5.9} _{-4.8}	2008 Feb 08	1500	867	17
141334.38+421201.7..	9161	2008 Apr 03	6954	48.6 ^{+8.0} _{-6.9}	2008 May 08	1200	650	36
162453.47+375806.6..	9155	2007 Nov 25	3994	18.3 ^{+5.4} _{-4.2}	2008 Feb 08	1300	867	15

Note. — All targets were observed with *Chandra* on-axis with the ACIS-S array, using Very Faint mode. *HET* spectra were obtained with the Low Resolution Spectrograph; 10/12 targets were able to be observed.

^aBackground-subtracted and aperture-corrected counts in the 0.5–8 keV band. Errors are 1σ (Poisson errors; Gehrels 1986). All snapshot targets are detected.

^bMost observations were conducted using the g2 grism with a $1.5''$ slit, providing a resolving power of 867.

^cSignal-to-noise of the continuum near observed-frame 6000 Å.

Table 3.2. *Chandra* Archival Sources

Name (SDSS)	Name (Other)	ObsID	Date	Exp (s)	θ (') ^a	Counts ^b	Sel ^c	Ref
020022.01−084512.0	FBQS J0200−0845	3265	2002 Oct 02	17901	9.4	55.3 ^{+8.5} _{−7.4}	S	1
...	FBQS J0256−0119	850	1999 Dec 09	4456	0.0	18.8 ^{+5.4} _{−4.3}	L	2
081426.45+364713.5	3436	2002 Jan 31	9839	8.3	8.8 ^{+4.1} _{−2.9}	S	...
081426.45+364713.5 ^d	3437	2002 Feb 11	9933	8.3	9.5 ^{+4.2} _{−3.0}	S	...
091951.29+005854.9	7056	2006 Jun 28	5080	4.3	< 3.6	S	...
100726.10+124856.2	PG 1004+130	5606	2005 Jan 05	41064	0.0	1851.4 ^{+44.0} _{−43.0}	L	3
104834.24+345724.9	4C +35.23	9320	2008 Jan 20	4658	0.0	5.5 ^{+3.5} _{−2.3}	L	4
122033.87+334312.0	3C 270.1	2118	2002 Apr 03	3087	4.3	177.4 ^{+14.3} _{−13.3}	S	...
131213.57+231958.6	FBQS J1312+2319	852	2000 May 19	4686	0.0	58.8 ^{+8.7} _{−7.6}	L	2
...	LBQS 2211−1915	4836	2003 Nov 19	5889	0.0	53.8 ^{+8.4} _{−7.3}	L	5

^aOff-axis angle in arc-minutes; a value of 0.0 indicates an observation targeting that BAL RLQ.

^bBackground-subtracted and aperture-corrected counts in the 0.5–8 keV band. Errors are 1σ (Poisson errors; Gehrels 1986), while limits for non-detections are at the 95% confidence level (Bayesian statistics; Kraft et al. 1991).

^cSelection method: S = BAL RLQ identified from SDSS/FIRST data with serendipitous *Chandra* archival coverage, while L = BAL RLQ identified from literature with targeted *Chandra* archival coverage.

^dSince the two observations of 081426.45+364713.5 are of comparable quality, both are shown; these observations are stacked for later analysis. There are 18.3^{+5.4}_{−4.2} net 0.5–8 keV counts in the combined 19.8 ks exposure.

References. — Prior analysis of *Chandra* data: (1) Gallagher et al. (2005); (2) Brotherton et al. (2005); Miller et al. (2006); (4) PI Kunert-Bajraszewska; (5) Gallagher et al. (2006).

Table 3.3. Optical/UV Characteristics

Name (SDSS)	z	m_i	M_i	$\Delta(g-i)$	BI	AI	EW	V_{\max}	Type ^a	Ref ^b
074610.50+230710.8.....	2.093	18.27	-27.19	1.057	...	2955	14.4 ^c	5225	Hi	1
083749.59+364145.4.....	3.416	18.55	-28.01	0.614	4243.0	6881	34.6	11472	HL	2
085641.58+424254.1.....	3.062	18.41	-27.91	0.106	820.6	2660	12.8	8071	H	2
092913.96+375742.9.....	1.915	17.51	-27.76	0.562	0.0	2630	13.4	4166	Hi	2
102258.41+123429.7.....	1.729	17.86	-27.16	0.562	1008.7	...	10.1	10180	Hi	2
105416.51+512326.0.....	2.341	18.48	-27.24	0.352	337.5	2177	9.7	5669	H	2
112506.95-001647.6.....	1.770	18.86	-26.22	0.264	0.0	1743	7.1	3897	Hi	2
115944.82+011206.9.....	2.000	16.96	-28.40	0.412	0.0	2887	12.5	4331	Hi	2
123411.73+615832.6.....	1.946	18.39	-26.90	0.442	4907.9	10718	32.4	20020	Hi	2
133701.39-024630.3.....	3.064	18.41	-27.91	0.242	0.0	1657	5.3	4983	H	2
141334.38+421201.7.....	2.817	18.24	-27.89	0.516	0.0	2688	15.0	4861	H	2
162453.47+375806.6.....	3.381	18.15	-28.38	0.281	2990.0	4156	13.6 ^c	28300	H	3
020022.01-084512.0.....	1.943	18.28	-27.01	0.484	2788.2	4135	19.9	14231	Hi	2
FBQS J0256-0119.....	2.490	18.40	-27.46	0	250.0	...	12.9 ^c	12400 ^c	H	4
081426.45+364713.5.....	2.732	19.81	-26.26	1.104	2438.40	5289	26.2	8300	HLF	2
091951.29+005854.9.....	2.114	19.45	-26.04	0.130	673.1	1268	6.9	22041	nHi	2
100726.10+124856.2.....	0.241	15.20	-25.09	-0.45	850.0	...	14.7 ^c	10000	Hi	5
104834.24+345724.9.....	1.594	20.17	-24.66	0.88	26.2 ^c	14300 ^c	Hi	6
122033.87+334312.0.....	1.532	18.10	-26.64	0.398	52.5	...	6.5	5266	HL	2
131213.57+231958.6.....	1.508	17.11	-27.59	0.084	1400.0	...	15.6 ^c	25000	Hi	7
LBQS 2211-1915.....	1.952	17.34	-27.96	0.32	27.0	...	7.8	11544	Hi	8,9

Note. — The k -correction for M_i assumes a power-law continuum with spectral index $\alpha_\nu = -0.5$. The absorption properties refer to C IV measurements. BI, EW, and V_{\max} values are primarily from the listed reference, chiefly Gibson et al. (2009), while AI values are taken from Trump et al. (2006) where available. The units for BI, AI, and V_{\max} are km s^{-1} ; EW is in Å.

^aBAL type following Trump et al. (2006): Hi = HiBAL (no Mg II absorption in spectrum); HLF = FeLoBAL (C IV BAL, Fe II or Fe III absorption in spectrum); HL = HiBAL with some low-ionization absorption; H = HiBAL lacking spectral coverage of Mg II; n = relatively narrow absorption. Type is taken from Trump et al. (2006) for all quasars with reported AI measurements; the remainder are classified based on our examination of the SDSS spectrum where available or else by the listed reference.

^bReferences.— (1) Trump et al. (2006); (2) Gibson et al. (2009); Benn et al. (2005); (4) Becker et al. (2001); (5) Wills et al. (1999); (6) Willott et al. (2002); (7) Becker et al. (2000); (8) Weymann et al. (1991); (9) Gallagher et al. (2006).

^cEW or V_{\max} value measured by us.

Table 3.4. Radio Characteristics

Name (SDSS)	Type ^c	Flux-Density Measurements ^a				Spectral Indices ^b	
		≤ 365 MHz	1.4 GHz (F)	1.4 GHz (N)	4.85 GHz	α_{low}	α_{high}
074610.50+230710.8	P	...	23.68	22.3 \pm 0.8	27 \pm 4 G	...	+0.11
083749.59+364145.4	P	...	27.10	-0.43
085641.58+424254.1	P	...	19.99	20.2 \pm 0.7	29 \pm 4 G	...	+0.30
092913.96+375742.9	P	94 W	43.43	42.9 \pm 1.3	24 \pm 4 G	-0.53	-0.48
102258.41+123429.7	D	448 \pm 51 T	118.65 ^d	126.1 \pm 3.8	44 \pm 6 G	-0.99	-0.80
105416.51+512326.0	P	44 W	33.88	35.6 \pm 1.1	22 \pm 4 G	-0.18	-0.35
112506.95-001647.6	D	890 \pm 130 V	65.47 ^d	74.0 \pm 2.7	...	-0.89	...
115944.82+011206.9	P	887 \pm 30 T	268.48	275.6 \pm 8.3	137.8 \pm 1.7 M	-0.89	-0.54
123411.73+615832.6	P	...	23.96	22.7 \pm 0.8	13.2 C	...	-0.48
133701.39-024630.3	P	...	44.82	45.1 \pm 1.4	39.4 C	...	-0.10
141334.38+421201.7	P	22 W	18.74	16.8 \pm 0.6	8.8 \pm 0.7 M	-0.11	-0.61
162453.47+375806.6	P	72 W	56.44	55.6 \pm 1.7	23.3 \pm 1.1 B	-0.17	-0.71
020022.01-084512.0	P	...	7.34	8.0 \pm 0.5
FBQS J0256-0119	P	...	27.56	22.3 \pm 0.8	12.0 \pm 0.5 M	...	-0.67
081426.45+364713.5	P	...	2.98	3.8 \pm 0.4
091951.29+005854.9	P	...	2.78	2.6 \pm 0.5
100726.10+124856.2	D	2740 P	...	1216.1 \pm 29.6 ^d	415 \pm 37 G	-0.66	-0.87
104834.24+345724.9	P	2437 \pm 29 T	1050.97	1034.4 \pm 31.0	439 \pm 39 G	-0.63	-0.70
122033.87+334312.0	D	9742 \pm 134 T	2819.00 ^d	2845.9 \pm 85.4	842 \pm 75 G	-0.92	-0.97
131213.57+231958.6	P	...	44.12	46.5 \pm 1.4	25.7 \pm 0.6 M	...	-0.43
LBQS 2211-1915	P	64.0 \pm 2.0

^a All flux density measurements are in mJy, taken from the following sources: B = Benn et al. (2005); C = archival VLA C-band imaging; F = FIRST: Faint Images of the Radio Sky at Twenty cm, integrated flux, RMS errors are $\simeq 0.15$ mJy beam⁻¹ (White et al. 1997); G = Green Bank 6-cm survey (Gregory et al. 1996); M = Montenegro-Montes et al. (2008); N = NVSS: NRAO VLA Sky Survey (Condon et al. 1998); P = Parkes Catalogue 1990, 408 MHz; T = Texas Survey of Radio Sources at 365 MHz (Douglas et al. 1996); V = VLA Low-Frequency Sky Survey, 74 MHz (Perley et al. 2006); W = Westerbork Northern Sky Survey, 326 MHz, RMS errors are $\simeq 4$ mJy beam⁻¹ (Rengelink et al. 1997).

^b Radio spectral indices include extended emission components, are given as $S_{\nu} \propto \nu^{\alpha_{\text{r}}}$, and use FIRST measurements where available (else NVSS measurements); the quantities α_{low} and α_{high} are calculated from the flux densities presented in the columns labeled ≤ 365 MHz and 4.85 GHz, respectively, in addition to the 1.4 GHz data. J083749.59+364145.4 has a bright unrelated radio source $\sim 50''$ North of the core that contaminates low-resolution maps; the spectral index is from a high-resolution 8.45 GHz flux density measurement from Montenegro-Montes et al. (2008).

^c Radio morphology: P = point source, D = double (lobes summed for flux measurements). See §3.3 for comments.

^d Extended emission: J102258.41+123429.7 has two FIRST components offset from the SDSS position by 0.058' and 0.174', with integrated fluxes of 93.98 and 24.67 mJy, respectively; J112506.95-001647.6 has two FIRST components offset from the SDSS position by 0.099' and 0.201', with integrated fluxes of 55.36 and 10.11 mJy, respectively; J100726.10+124856.2 (PG 1004+130) is over-resolved by FIRST, but has two NVSS components offset from the SDSS position by 0.434' and 1.010', with fluxes of 656.4 and 559.7 mJy, respectively; J122033.87+334312.0 (3C 270.1) has two FIRST components offset from the SDSS position by 0.067' and 0.073', with integrated fluxes of 2096.61 and 722.39 mJy, respectively.

Table 3.5. X-ray Counts, Luminosities, and Properties of BAL RLQs

Name (SDSS)	Soft	X-ray Counts		Rate	Luminosities			Derived Properties				
		Hard	HR		l_r	l_{uv}	l_x	R^*	α_{ox}	$\Delta l_{x,uv}$	$\Delta l_{x,S}$	$\Delta l_{x,H}$
074610.50+230710.8	$49.4^{+8.1}_{-7.0}$	$17.6^{+5.3}_{-4.2}$	$-0.47^{+0.11}_{-0.10}$	$9.8^{+1.3}_{-1.2}$	33.36	31.15	27.01	2.21	-1.59	-0.37	-0.06	-0.15
083749.59+364145.4	$13.6^{+4.8}_{-3.6}$	< 3.5	< -0.59	$2.9^{+0.9}_{-0.7}$	33.85	31.53	26.91	2.32	-1.77	-0.81	-0.52	< -0.7
085641.58+424254.1	$11.5^{+4.5}_{-3.3}$	$6.1^{+3.6}_{-2.4}$	$-0.31^{+0.24}_{-0.19}$	$2.8^{+0.9}_{-0.7}$	33.63	31.43	26.79	2.20	-1.78	-0.84	-0.55	-0.45
092913.96+375742.9	$26.3^{+6.2}_{-5.1}$	$21.0^{+5.6}_{-4.5}$	$-0.11^{+0.14}_{-0.14}$	$11.9^{+2.0}_{-1.7}$	33.54	31.40	26.99	2.15	-1.69	-0.61	-0.40	-0.11
102258.41+123429.7	$15.8^{+5.1}_{-3.9}$	$7.7^{+3.9}_{-2.7}$	$-0.34^{+0.20}_{-0.17}$	$4.9^{+1.2}_{-1.0}$	33.83	31.13	26.52	2.71	-1.77	-0.84	-0.78	-0.72
105416.51+512326.0	$26.0^{+6.2}_{-5.1}$	$11.0^{+4.4}_{-3.3}$	$-0.41^{+0.16}_{-0.13}$	$7.4^{+1.4}_{-1.2}$	33.62	31.27	26.96	2.35	-1.65	-0.53	-0.29	-0.27
112506.95-001647.6	$59.5^{+8.8}_{-7.7}$	$24.3^{+6.0}_{-4.9}$	$-0.42^{+0.10}_{-0.09}$	$15.7^{+2.0}_{-1.7}$	33.60	30.74	27.05	2.86	-1.42	+0.04	+0.08	+0.05
115944.82+011206.9	$93.1^{+10.7}_{-9.6}$	$80.1^{+10.0}_{-8.9}$	$-0.08^{+0.08}_{-0.08}$	$46.2^{+3.8}_{-3.5}$	34.38	31.67	27.62	2.70	-1.56	-0.23	-0.24	+0.07
123411.73+615832.6	$11.6^{+4.5}_{-3.3}$	$5.4^{+3.5}_{-2.3}$	$-0.36^{+0.24}_{-0.19}$	$2.8^{+0.9}_{-0.7}$	33.30	31.06	26.38	2.24	-1.80	-0.92	-0.67	-0.61
133701.39-024630.3	$10.5^{+4.3}_{-3.2}$	$12.2^{+4.6}_{-3.4}$	$0.07^{+0.20}_{-0.20}$	$5.0^{+1.3}_{-1.0}$	33.98	31.48	27.04	2.50	-1.70	-0.63	-0.65	-0.21
141334.38+421201.7	$34.7^{+6.9}_{-5.9}$	$16.5^{+5.1}_{-4.0}$	$-0.35^{+0.14}_{-0.12}$	$7.0^{+1.2}_{-1.0}$	33.53	31.56	27.10	1.97	-1.71	-0.65	-0.24	-0.18
162453.47+375806.6	$13.4^{+4.7}_{-3.6}$	$5.5^{+3.5}_{-2.3}$	$-0.42^{+0.23}_{-0.17}$	$4.6^{+1.3}_{-1.1}$	34.17	31.74	27.08	2.43	-1.79	-0.83	-0.61	-0.60
020022.01-084512.0	$38.4^{+7.2}_{-6.2}$	$14.9^{+4.9}_{-3.8}$	$-0.58^{+0.13}_{-0.11}$	$3.1^{+0.5}_{-0.4}$	32.79	31.11	26.52	1.68	-1.76	-0.82	-0.31	-0.36
FBQS J0256-0119	$15.4^{+5.0}_{-3.9}$	$4.4^{+3.2}_{-2.0}$	$-0.56^{+0.21}_{-0.15}$	$4.2^{+1.2}_{-1.0}$	33.50	31.51	26.77	1.99	-1.82	-0.93	-0.51	-0.59
081426.45+364713.5	$10.2^{+4.3}_{-3.1}$	$7.5^{+3.8}_{-2.7}$	$-0.29^{+0.23}_{-0.21}$	$0.9^{+0.3}_{-0.2}$	32.70	30.71	26.33	1.99	-1.68	-0.65	-0.38	-0.17
091951.29+005854.9	< 3.3	< 3.5	...	< 0.7	32.44	30.74	< 26.0	1.71	< -1.8	< -1.0	< -0.3	< -0.0
100726.10+124856.2	$1107^{+34.3}_{-33.3}$	$794^{+29.2}_{-28.2}$	$-0.16^{+0.02}_{-0.02}$	$45.1^{+1.1}_{-1.0}$	32.86	30.52	25.66	2.34	-1.87	-1.15	-0.99	-0.77
104834.24+345724.9	< 3.2	$4.4^{+3.2}_{-2.0}$	> 0.16	$1.2^{+0.7}_{-0.5}$	34.76	30.48	25.82	4.28	-1.79	-0.95	< -1.6	-1.10
122033.87+334312.0	$134.1^{+12.6}_{-11.6}$	$47.6^{+7.9}_{-6.9}$	$-0.48^{+0.10}_{-0.10}$	$57.5^{+4.6}_{-4.3}$	35.07	30.89	27.41	4.19	-1.34	+0.27	-0.26	-0.20
131213.57+231958.6	$48.4^{+8.0}_{-6.9}$	$11.0^{+4.4}_{-3.3}$	$-0.63^{+0.11}_{-0.09}$	$12.5^{+1.9}_{-1.6}$	33.30	31.42	26.74	1.88	-1.80	-0.88	-0.42	-0.55
LBQS 2211-1915	$38.4^{+7.2}_{-6.2}$	$16.6^{+5.1}_{-4.0}$	$-0.40^{+0.13}_{-0.11}$	$9.1^{+1.4}_{-1.2}$	33.78	31.67	26.87	2.11	-1.84	-0.98	-0.66	-0.54

Note. — The soft and hard bands are 0.5–2 keV and 2–8 keV, respectively; the hardness ratio is $HR = (H - S)/(H + S)$; rate is counts ks^{-1} in the 0.5–8 keV band. The radio loudness (in log units) is $R^* = l_r - l_{uv}$ and the optical/UV-to-X-ray spectral slope is $\alpha_{ox} = 0.3838 \times (l_x - l_{uv})$. The relative X-ray luminosities are $\Delta l_{x,uv} = l_x - (0.905 \times l_{uv} - 0.813)$ and $\Delta l_{x,S/H} = l_{x,S/H} - (0.472 \times l_{uv} + 0.413 \times l_r - 1.392)$, where $l_{x,S/H}$ is calculated at 2 keV from soft/hard band count rates.

Chapter 4

X-ray Emission from Optically Selected Radio-Intermediate and Radio-Loud Quasars

4.1 Introduction

4.1.1 Radio-loud and radio-intermediate quasars

Quasar emission is believed to result largely from accretion onto a supermassive black hole (e.g., Lynden-Bell 1969). The bulk of the optical/UV continuum in radio-quiet quasars (RQQs) is associated with quasi-thermal emission originating in the accretion disk, while the X-ray emission is postulated to arise from Compton upscattering of disk photons occurring in a hot “corona.” This scenario leads naturally to a correlation between optical/UV and X-ray luminosity. Extensive studies of RQQs (e.g., Avni & Tananbaum 1986; Strateva et al. 2005; Steffen et al. 2006; Just et al. 2007; Kelly et al. 2007; Green et al. 2009) have found that the optical/UV-to-X-ray spectral slope steepens (in the sense that objects become relatively less X-ray luminous) with increasing optical/UV luminosity. Intriguingly, most studies (see above references) find that there does not appear to be significant evolution with redshift in the spectral energy distributions of RQQs; despite the strong evolution in the space density of quasars, these studies generally find that RQQs in the early universe appear to have similar optical/UV-to-X-ray spectral slopes to their local analogs.

Radio-loud quasars (RLQs) are often defined to be the subset of quasars with a radio-loudness parameter satisfying $R^* \geq 1$, where R^* is the logarithmic ratio of monochromatic luminosities (with units of $\text{erg s}^{-1} \text{Hz}^{-1}$) measured at (rest-frame) 5 GHz and 2500 Å (e.g., Stocke et al. 1992)¹; RQQs must minimally satisfy $R^* < 1$ and often are found to have $R^* < 0$. RLQs comprise $\sim 10\%$ of quasars, with this fraction apparently varying with both luminosity and redshift (e.g., Jiang et al. 2007 and references therein). The definitive physical trigger for radio-loudness remains elusive, but RLQs generally have more massive central black holes than RQQs (e.g., Laor 2000; Metcalf & Magliocchetti 2006), and it has also been suggested that RLQs host more rapidly spinning black holes than do RQQs (e.g., Wilson & Colbert 1995; Meier 2001). RLQs and RQQs are typically treated as distinct populations, in part due to the apparent relative scarcity of objects with $R^* \approx 1$. The appropriateness of this canonical separation has been questioned due to the discovery of numerous quasars of intermediate radio-loudness (e.g., White et al. 2000; Cirasuolo et al. 2003), which may outnumber RLQs

¹Some authors measure at 4400 Å instead, following Kellerman et al. (1989); this method results in only a minor change (~ 0.1) in calculated R^* values. Note that many authors prefer to define R^* in linear units.

(e.g., White et al. 2007), but there does appear to be a genuine bimodality of R^* allowing fairly objective distinction between RQQs and RLQs (e.g., Ivezić et al. 2004; Zamfir et al. 2008). It should be noted that RQQs are not necessarily radio-silent; for example, Miller et al. (1993) found the radio emission from radio-detected RQQs to be dominated by a starburst-linked component,² and interpreted radio-intermediate quasars (RIQs) as being RQQs in which a low-power and mildly relativistic jet is viewed at low inclinations (see also, e.g., Falcke et al. 1996; Zamfir et al. 2008).

The observed properties of RLQs and their likely parent population of radio galaxies are dependent upon orientation to the observer’s line of sight (e.g., Urry & Padovani 1995). As with RQQs, there is believed to be an obscuring “torus” present in RLQs that blocks the broad-line region from view at large inclinations, but RLQs are further complicated by significant non-isotropic jet emission (e.g., Urry & Padovani 1995). Radio jets have been measured to have relativistic bulk velocities on parsec scales from multi-epoch high-resolution radio imaging of moving knots in the inner jet, and the frequent lack of a detectable counterjet is consistent with Doppler beaming (e.g., Worrall & Birkinshaw 2006 and references therein). RLQ jets terminate in hotspots within lobes, for which the velocities are typically non-relativistic (e.g., Scheuer 1995) and so this emission is relatively isotropic. Both the ratio of radio core-to-lobe flux and the ratio of core radio-to-optical luminosities are observed to depend upon orientation, and these results suggest that both the lobe emission³ and the optical continuum in RLQs are correlated with intrinsic unbeamed jet power (e.g., Wills & Brotherton 1995). The luminosities of narrow emission lines appear to correlate directly with jet power, with the link plausibly coming from a mutual underlying dependence upon accretion rate and/or black-hole spin (e.g., Rawlings & Saunders 1991; Willott et al. 1999). Various unification models (e.g., Urry & Padovani 1995; Jackson & Wall 1999) link narrow-line radio galaxies, broad-line radio galaxies, RLQs, and blazars by decreasing inclination. Our focus in the present study is restricted to broad-line quasars, but our results are of potential relevance to radio galaxies and blazars in the context of such unification schemes.

X-ray studies of RLQs strongly suggest that the nuclear X-ray emission contains a significant jet-linked component. Zamorani et al. (1981) discovered that RLQs are more X-ray luminous than are RQQs with comparable optical/UV luminosities, by a typical factor of about three. Worrall et al. (1987) used *Einstein* data to show that the relative X-ray brightness is greater for RLQs that are more radio-luminous or have flatter radio spectra, and found no evidence for redshift evolution out to $z \sim 3.5$ in the properties of RLQs. Wilkes & Elvis (1987) and Shastri et al. (1993) uncovered X-ray spectral flattening with increasing radio loudness and radio core dominance in samples of quasars observed with *Einstein*. Brinkmann et al. (1997) investigated a large sample of *ROSAT*-detected RLQs and found that both lobe-dominated and core-dominated RLQs show X-ray luminosity correlated with core radio luminosity, with the X-ray luminosity

²Weak radio emission from RQQs has also been suggested to be generated within magnetically heated coronae (Laor & Behar 2008) or slow and dense disk winds (Blundell & Kuncic 2007).

³The scatter within the correlation of core-to-lobe flux ratio to inclination is a factor of $\simeq 5 - 10$ for a given inclination, from Figure 1a of Wills & Brotherton 1995; this scatter may reflect environmental effects, which can be of sufficient scale to induce lobe asymmetries (e.g., Mackay et al. 1971; Gopal-Krishna & Wiita 2000).

of core-dominated RLQs increasing more rapidly with increasing core radio luminosity (e.g., their Figure 15). It is also noteworthy in the context of unification schemes that FR II (see Fanaroff & Riley 1974 for description of the FR I and FR II classes) radio-galaxy X-ray spectra typically show both a dominant absorbed and a weaker unabsorbed component, apparently linked with the disk/corona and jet, respectively (e.g., Evans et al. 2006; Hardcastle et al. 2009).

4.1.2 Aims of this work

Recent wide-angle, overlapping surveys in the radio (e.g., Faint Images of the Radio Sky at Twenty-cm, or FIRST; Becker et al. 1995) and optical (e.g., the Sloan Digital Sky Survey, or SDSS; York et al. 2000) may be matched (e.g., Ivezić et al. 2002) to enable the selection of large, well-defined samples of RLQs, for which X-ray properties may be investigated. For example, Suchkov et al. (2006) present a catalog of SDSS Data Release Four (DR4) quasars matched to FIRST sources as well as X-ray sources from pointed *ROSAT* PSPC observations. Jester et al. (2006a) matched a subset of SDSS DR5 quasars to FIRST sources and X-ray sources from the *ROSAT* All Sky Survey, finding radio loudness to be dependent upon both optical and X-ray luminosity. The improved capabilities of modern X-ray observatories such as *Chandra* and *XMM-Newton* have substantially advanced understanding of RLQs. For example, the high angular resolution and low background of *Chandra* enable the routine detection of X-ray emission from the knots of large-scale RLQ jets (e.g., Worrall 2009 and references therein), while the broad bandpass and high throughput of *XMM-Newton* generate high signal-to-noise X-ray spectra useful for quantifying differences between RQQs and RLQs (e.g., Page et al. 2005; Young et al. 2009) or radio galaxies and RLQs (e.g., Belsole et al. 2006). Samples of SDSS quasars with X-ray coverage by *Chandra* or *XMM-Newton* that include subsamples matched to FIRST sources are presented and discussed by Green et al. (2009) and Young et al. (2009).

Guided by the results described in §1.1 (and taking advantage of our large sample size, which permits finer categorization), we consider three categories of quasars in this work: RQQs, RIQs, and RLQs (rather than just RQQs and RLQs), where we define RIQs to consist of objects with $1 \leq R^* < 2$; consequently, the objects we classify as RLQs satisfy $R^* \geq 2$. The goal of this study is to quantify the optical-to-X-ray properties of RIQs and RLQs and to investigate the physical origin of their X-ray emission. Such an effort requires (1) consistent selection criteria that are unbiased with respect to the X-ray properties we wish to investigate; (2) a large sample of quasars spanning a broad range of radio properties and possessing sensitive X-ray coverage; (3) radio imaging capable of resolving extended sources (multifrequency radio coverage to calculate or constrain spectral indices is also useful); (4) a high fraction of X-ray detections along with proper statistical consideration of X-ray limits; and (5) effective coverage of the luminosity-redshift plane to avoid degeneracies in regression analysis and other biases. We generate a large sample of RIQs and RLQs with archival X-ray coverage by matching the SDSS DR5 quasar catalog of Schneider et al. (2007) and the photometrically selected quasars from Richards et al. (2009) to FIRST and to high-quality observations from *Chandra*, *XMM-Newton*, or *ROSAT*. We supplement this primary sample with additional RLQs

observed by *Einstein*, high-redshift RLQs, and low-luminosity RLQs detected in deep multiwavelength surveys. The full sample enables accurate parameterization of X-ray luminosity correlations across a wide range of radio properties, notably including the previously sparsely probed but well-populated RIQ regime. We are also able to take advantage of recent advances in statistical methods (e.g., Kelly 2007) in our analysis and of newly established constraints on jet properties (e.g., Mullin & Hardcastle 2009) in our modeling. In addition, our use of modern accurate cosmological parameters eliminates a source of systematic error present in some earlier analyses of luminosity correlations.

The outline of this paper is as follows: in §2 we describe the selection methods used to generate our sample, in §3 we discuss characteristics of the RIQs and RLQs studied here, in §4 we compare the X-ray properties of RIQs and RLQs to those of RQQs, in §5 we parameterize X-ray luminosity in RIQs and RLQs as a joint function of optical/UV and radio properties, in §6 we determine a plausible physical model for the spectral energy distributions of RLQs, and in §7 we summarize our results. We adopt a standard cosmology with $H_0 = 70 \text{ km s}^{-1} \text{ Mpc}^{-1}$, $\Omega_M = 0.3$, and $\Omega_\Lambda = 0.7$ (e.g., Spergel et al. 2007) throughout. Radio, optical/UV, and X-ray monochromatic luminosities ℓ_r , ℓ_{uv} , and ℓ_x are expressed as logarithmic quantities with units of $\text{ergs s}^{-1} \text{ Hz}^{-1}$ (suppressed hereafter), at rest-frame 5 GHz, 2500 Å, and 2 keV, respectively. In these units the radio loudness is $R^* = \ell_r - \ell_{\text{uv}}$ and the useful quantity α_{ox} , the optical/UV-to-X-ray spectral slope (e.g., Avni & Tananbaum 1986), is $\alpha_{\text{ox}} = 0.384 \times (\ell_x - \ell_{\text{uv}})$. Object names are typically taken from the SDSS DR5 spectroscopic quasar catalog of Schneider et al. (2007) or from the SDSS DR6 photometric quasar catalog of Richards et al. (2009) and are J2000 throughout.

4.2 Sample selection

Our primary sample consists of 575 optically selected RIQs and RLQs with SDSS/FIRST observations and high-quality X-ray coverage from *Chandra*, *XMM-Newton*, or *ROSAT*. The X-ray detection fraction for the primary sample is 83%; the detection fraction for those objects with *Chandra* or *XMM-Newton* coverage exceeds 90% (typical *ROSAT* observations are comparatively less sensitive and have higher background, so the detection fraction is lower). The primary sample is split nearly evenly between spectroscopic (274) and high-confidence photometric (301) quasars. We also include several supplemental samples to increase coverage of the $\ell - z$ plane: 105 luminous RLQs with *Einstein* coverage from Worrall et al. (1987), 15 high-redshift RLQs studied by Bassett et al. (2004) and Lopez et al. (2006), and 32 low-luminosity RLQs selected from deep multiwavelength surveys (see §2.2.3 for details and references) including the Cosmic Evolution Survey (COSMOS), the Extended *Chandra* Deep Field–South (E-CDF-S) and the *Chandra* Deep Field–South (CDF-S), and the *Chandra* Deep Field–North (CDF-N). These supplemental samples are combined with the primary sample to produce the full sample.

The full sample consists of 727 quasars with $R^* \geq 1$ (with an X-ray detection fraction of 85%), of which 177 are RIQs with $R^* < 2$ and 550 are RLQs with $R^* \geq 2$. The sky coverage of the full sample is shown in Figure 1. Properties for objects in the primary sample are provided in Table 1, properties for objects in the deep-fields sample

are provided in Table 2, and characteristics of the various samples are provided in Table 3.

4.2.1 Primary sample

4.2.1.1 Spectroscopic sample

The spectroscopic sample is drawn from the SDSS DR5 Quasar Catalog of Schneider et al. (2007). The sky area covered by DR5 spectroscopic observations is 5740 deg^2 near the north Galactic cap (Adelman-McCarthy et al. 2007). The Schneider et al. (2007) quasar catalog includes quasars targeted for matching a variety of (often overlapping) criteria (see Schneider et al. 2007 and Richards et al. 2002 for details). Of the 77429 objects in the quasar catalog, 51577 were targeted based on quasar-like optical colors and have BEST target flags of “QSO” or “HIZ” set (see Schneider et al. 2007 for description of these parameters). Most of the remaining quasars were targeted as “serendipitous” objects based on possessing non-stellar optical colors. A smaller number of quasars were targeted based on their radio (FIRST) or X-ray (RASS) emission and/or photometrically categorized as stars or galaxies. Matching objects targeted as quasars or serendipitous objects to the FIRST radio survey and then to archival high-quality X-ray coverage provides an initial list of 311 RIQs and RLQs. As described below, we remove from this list 21 BAL quasars, 8 highly reddened quasars, and 8 GHz-peaked spectrum sources; the remaining 274 objects constitute our spectroscopic sample of optically-selected RIQs and RLQs. We also construct and separately analyze a slightly smaller sample of 178 “QSO/HIZ” targeted RIQs and RLQs.

The SDSS quasar survey is $\sim 95\%$ complete for unresolved sources (for objects categorized as quasars on the basis of optical spectra) and $\sim 89\%$ complete overall (Vanden Berk et al. 2005); the catalog consists of quasars with strong broad emission lines (of width $> 1000 \text{ km s}^{-1}$) and by design does not include BL Lacs with featureless spectra (e.g., Plotkin et al. 2008, 2010). It does, however, include broad-absorption line (BAL) quasars, and it is now clear (e.g., Becker et al. 2000, 2001; Menou et al. 2001) that a small fraction ($\lesssim 8\%$ at high radio luminosities; e.g., Shankar et al. 2008) of RLQs have BALs and are, like BAL RQQs, relatively X-ray weak due to intrinsic absorption (e.g., Brotherton et al. 2005; Gibson et al. 2008; Miller et al. 2009); since we are interested in intrinsic emission and not absorption, we exclude from our sample any objects included in the SDSS BAL catalog of Gibson et al. (2009) and also any RLQs we are aware of as possessing BALs not observable in the SDSS spectrum (e.g., J100726.10+124856.2, the $z = 0.24$ object PG 1004+130 identified as a BAL RLQ by Wills et al. 1999). Through this process 21 BAL quasars are identified and dropped from further consideration. (Note that the X-ray coverage of BAL RIQs and RLQs is non-random, as several were specifically targeted for observation.) Contamination from low-redshift ($z < 1.7$) RLQs not identifiable as having BALs due to SDSS bandpass limitations (i.e., spectroscopic quasars

lacking coverage of the 1400–1550 Å region, which includes the strong C IV BAL transition) should be $\sim 2\%$ of the entire sample⁴, and a small number of X-ray weak outliers would not materially impact our results below. Objects with apparent heavy intrinsic reddening are sometimes also associated with X-ray absorption (e.g., Hall et al. 2006). The quantity $\Delta(g-i)$ (plotted in Figure 2) is the $g-i$ color of an object (corrected for Galactic extinction) less the median $g-i$ quasar color at the redshift of that object; negative $\Delta(g-i)$ values correspond to objects bluer than the norm and positive $\Delta(g-i)$ values indicate redder colors (e.g., Richards et al. 2001). Almost all non-reddened objects have $\Delta(g-i) < 1$ while intrinsically reddened objects form a tail in the distribution that extends past this value (e.g., Hall et al. 2006), so objects with $\Delta(g-i) > 1$ are culled from the sample. This cut removes 8 objects that would otherwise be included (an additional 4 of the already excluded BAL quasars also have $\Delta(g-i) > 1$). Finally, 8 objects possess radio spectra (described in §3.3) indicating they are GHz-peaked spectrum (GPS; e.g., O’Dea 1998) sources, which are generally considered to be young sources and have X-ray properties that are not necessarily representative of RLQs in general (e.g., Siemiginowska et al. 2008); these GPS sources are therefore culled and not considered further.

The radio properties of these quasars are determined from the 1.4 GHz FIRST survey, which has a resolution of $\sim 5''$, a 5σ limiting flux density of ~ 1 mJy, and 9030 deg² of sky coverage, much of which overlaps the SDSS area (Becker et al. 1995). Objects were retained as RIQs or RLQs if the summed luminosity of their constituent components satisfied $\ell_r > 31.0$ (motivated by, e.g., Zamfir et al. 2008) along with $R^* > 1.0$. Although the requirements of optical selection and a joint SDSS/FIRST detection necessarily limit the completeness of our sample, the depths of the SDSS and FIRST surveys are well matched for detecting RLQs. An $m_i=19.1$ quasar (the limit for $z < 3$ candidate “QSO” SDSS spectroscopic targeting) with $R^* = 1$ and a typical spectral slope would have a 1.4 GHz flux density of $\simeq 1.2$ mJy, near the ~ 1 mJy 5σ FIRST point-source detection limit.

Extended radio sources (with jets or lobes) may have separate entries in the FIRST source catalog for each detected component, and lobe-dominated sources do not always possess a detected core component. It is therefore necessary to match to the entire environment surrounding each quasar to recover all associated emission (e.g., Best et al. 2005; Lu et al. 2007). Very few radio sources that lack a core component have lobe-to-lobe angular sizes greater than $90''$ (e.g., de Vries et al. 2006), so we search for radio emission within $90''$ of each optically-selected quasar. We considered as candidates for radio-detected quasars those objects with a radio source within $2''$, referred to hereafter as the core, or two or more radio sources within $2'' < \theta < 90''$ of which at least one pair has component angular orientations relative to the core differing by more than 90° (where a 180° separation would indicate components on directly opposite sides of the core), classified as potential lobes pending additional review. The potential lobes were then matched to the SDSS photometric catalog, and if they had an optical counterpart (unless that apparent counterpart was a spectroscopically-classified star) they were

⁴This estimate assumes $\sim 8\%$ (e.g., Shankar et al. 2008) of the 196 spectroscopic RIQs and RLQs with $z < 1.7$ are BAL quasars, out of a total sample of 727 objects; BAL contamination within the photometric sample is addressed separately in §2.1.2.

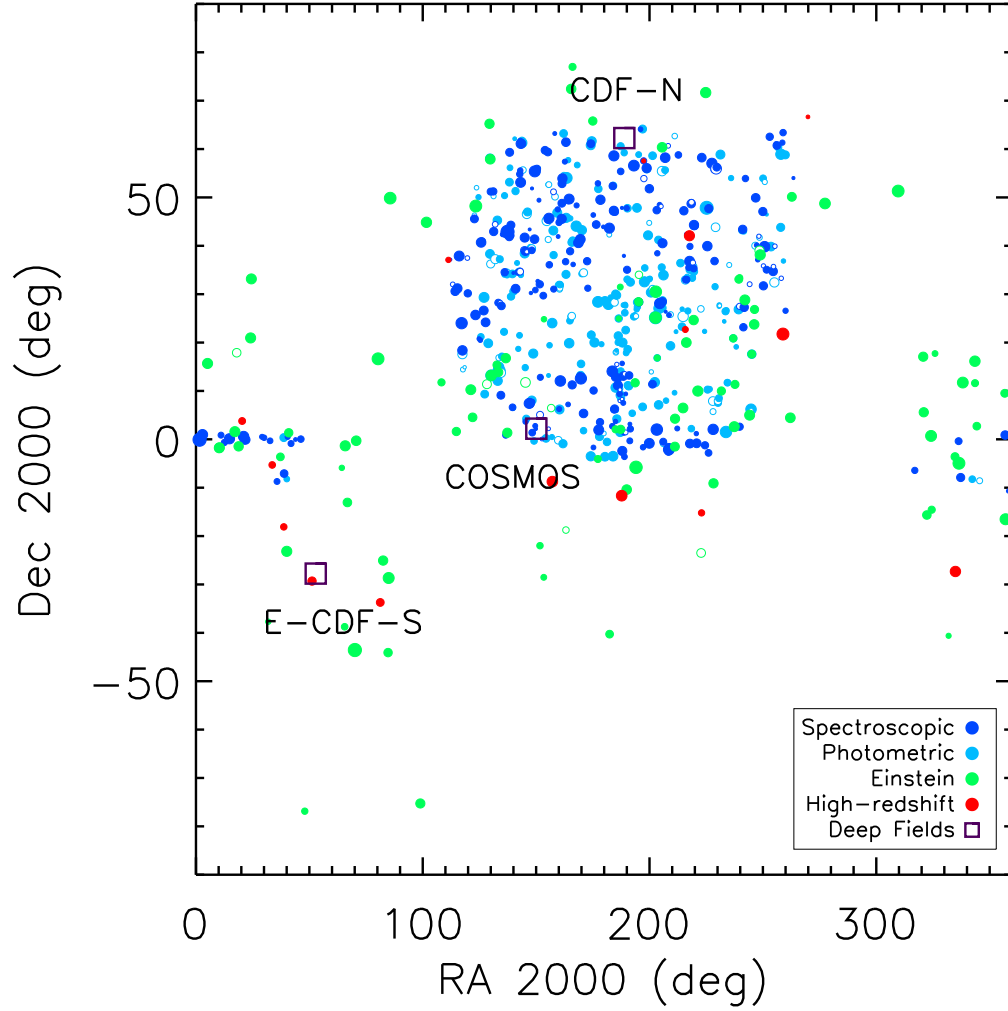


Fig. 4.1 The sky coordinates of objects in the full sample of 727 RIQs and RLQs. The filled symbols are X-ray detections, and the open symbols are X-ray upper limits. The symbol size is proportional to R^* ; larger symbols correspond to quasars with greater radio loudness values. Primary sample SDSS spectroscopic/photometric quasars ($n = 575$) are plotted in blue/cyan, and the supplemental samples of *Einstein* ($n = 105$) and high-redshift ($n = 15$) RLQs are plotted in green and red, respectively. The deep-field sample ($n = 32$) is indicated by the locations of the COSMOS, E-CDF-S, and CDF-N surveys (marked with purple squares and labels; the square size does not indicate the solid-angle coverage of these surveys).

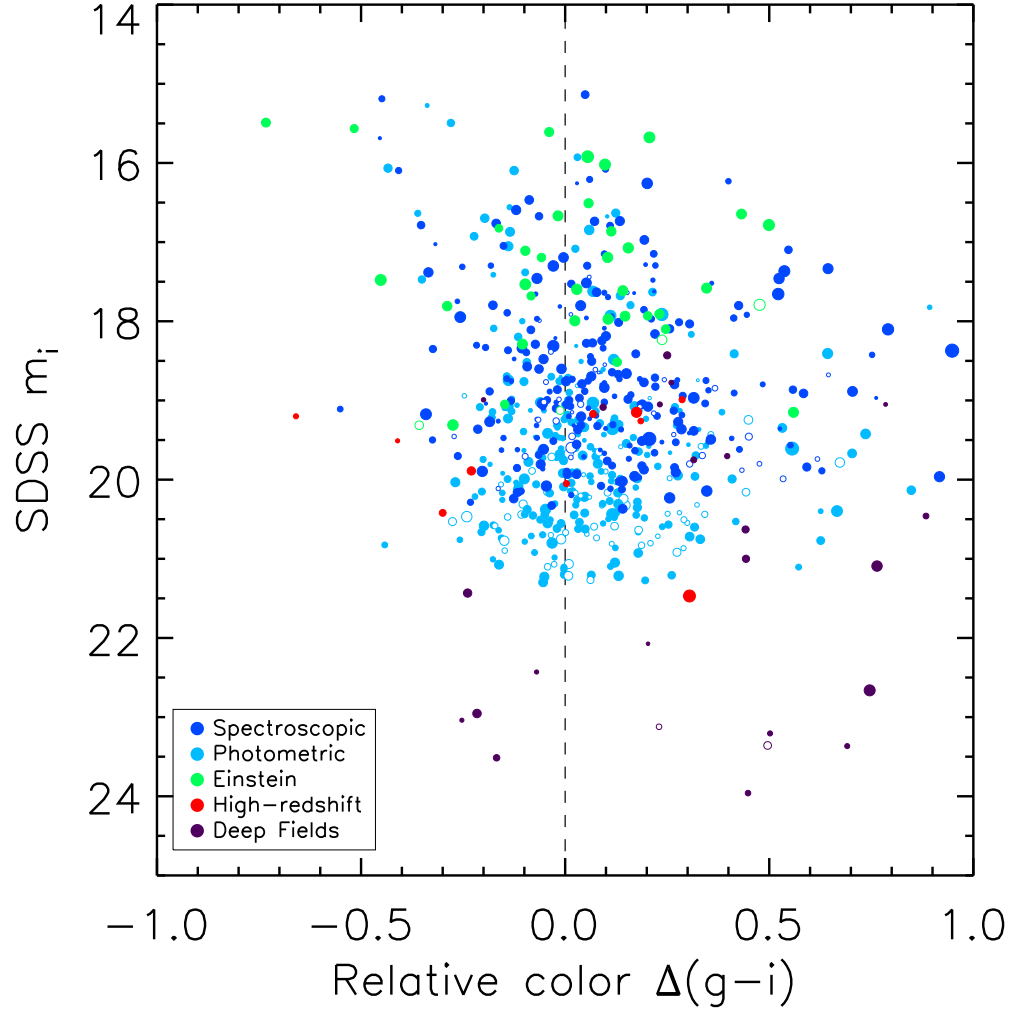


Fig. 4.2 Color-magnitude plot of RIQs and RLQs, where the relative color $\Delta(g-i)$ is the $g-i$ color (corrected for Galactic extinction) for a given object less the median quasar color at that redshift. Bluer/redder objects have negative/positive values of $\Delta(g-i)$. The filled symbols are X-ray detections and the open symbols are X-ray upper limits. Larger symbols correspond to more radio-loud quasars. Primary sample SDSS spectroscopic/photometric quasars are plotted in blue/cyan, and the supplemental samples of *Einstein*, high-redshift, and deep-field RLQs are plotted in green, red, and purple, respectively. The $\Delta(g-i)$ and m_i values for the deep field RLQs have been calculated by transforming *UBVRI* magnitudes to *ugriz* equivalents.

flagged as intruding background sources and not considered further in determining the radio characteristics of that quasar; if this process left only one potential lobe and no core then the object was eliminated as not radio-detected. All objects with remaining potential lobes were then examined visually to screen further for misclassifications (for example, unrelated background double-lobed radio sources are readily identifiable by eye as intruding but are difficult to categorize correctly automatically). A few cases in which an obviously-associated extended component had been mistakenly flagged as background due to a randomly coincident SDSS optical source were also corrected. Visual screening also identified four objects with likely associated radio components outside the $90''$ consideration radius (J093200.08+553347.4, J112956.53+364919.2, J094745.14+072520.6, and J142735.60+263214.5, with maximal lobe offset from the core of $93''$, $99''$, $117''$, and $148''$, respectively); since we wish to take into account all lobe emission from objects already included in the sample, these components were added to the total radio fluxes for these objects. Visual screening also confirmed that the FIRST catalog contains entries for all obvious components in all sources included in the sample [with only one exception: we added a core component to J170441.37+604430.5 (3C 351) based on examination of the FIRST and other radio maps]. The FIRST survey is not particularly sensitive to large-scale regions of low surface brightness, so diffuse lobes may not be detected or may have their fluxes underestimated. The NRAO VLA Sky Survey (NVSS; Condon et al. 1998) provides lower angular resolution coverage that complements the high angular resolution imaging of FIRST; 1.4 GHz fluxes from the NVSS catalog were used for a handful of obviously extended FIRST sources.

The 274 RIQs and RLQs in the spectroscopic sample all possess sensitive X-ray coverage from *Chandra*, *XMM-Newton*, or *ROSAT*. For *Chandra*, we checked all public non-grating ACIS-S or ACIS-I observations with exposures longer than 1 ks and off-axis angles of less than $12'$ (note that each one of the ACIS CCDs covers an area of approximately $8'$ by $8'$). For *XMM-Newton*, we considered only those observations with exposure times greater than 1 ks and off-axis angles of less than $15'$. For *ROSAT*, we initially considered unfiltered PSPC observations with exposure times greater than 2 ks and off-axis angles less than $40'$. All X-ray observations were examined to screen out cases in which the quasar did not fall on the detector, was too close to another bright source, was located within an instrumental artifact, or was otherwise unsuitable for further analysis. Due to their greater X-ray sensitivity, *Chandra* or *XMM-Newton* observations were prioritized over *ROSAT* data. In cases where both *Chandra* and *XMM-Newton* provide coverage, the observation with the greatest predicted X-ray signal-to-noise ratio (estimated based on exposure time, off-axis angle, detector efficiency, and average background) was used. *ROSAT* observations were ranked by predicted X-ray signal-to-noise ratio and lower-quality observations were discarded. The threshold value for discarding *ROSAT* observations was chosen so as to provide a large sample size while maintaining a relatively high detection fraction. In cases where multiple *ROSAT* observations were available, the observation with the greatest predicted X-ray signal-to-noise ratio was used. Despite their lower sensitivity, the *ROSAT* observations are essential for this project, as they provide a large area of sky coverage beyond that available solely from *Chandra* and *XMM-Newton* observations. Note that this method is unbiased with respect to intrinsic quasar properties (including X-ray brightness) as it

is based only on the expected quality of the X-ray observations, so it should not lead to any biases or systematic errors in our analyses.

In addition to the optically-selected (“QSO/HIZ” or serendipitous) spectroscopic sample of 274 RIQs and RLQs and the subsample of 178 “QSO/HIZ” quasars, we generate a sample of 155 quasi-radio-selected objects through selecting quasars for which the “FIRST” target flag is set. Such objects were targeted by the SDSS on the (not necessarily exclusive) basis of being likely optical counterparts to FIRST radio sources. This does not constitute a true radio-selected sample because the SDSS retains optical magnitude limits for FIRST sources and because lobe-dominated radio sources without a FIRST core component will not be targeted by SDSS as FIRST sources, but this approach provides a useful basis for broad comparison to RIQs and RLQs targeted on the basis of their optical colors. There is considerable overlap between the categories of “QSO/HIZ” and “FIRST” targeted objects; 138 of the 155 objects with the “FIRST” flag set also have either the “QSO” or “HIZ” flags set. The median properties of these subsamples are similar, with median $\Delta(g-i) = 0.06/0.09$, median $\ell_r = 33.15/33.15$, median $R^* = 2.50/2.39$, and median $\alpha_{\text{ox}} = -1.40/-1.42$ for the objects selected (as “QSO/HIZ”)/(as “FIRST”). These results do not mandate that a complete radio-selected sample of RIQs and RLQs would have properties consistent with those of color-selected SDSS RIQs and RLQs, but they do suggest that there is substantial overlap in these selection methods and that discrepancies in the median properties of a radio-selected sample as compared to an optically-selected sample of RIQs and RLQs are probably not large.

4.2.1.2 Photometric sample

The photometric sample is constructed from a parent population of over 1,000,000 photometric SDSS sources identified as potential quasars through the nonparametric Bayesian classification conducted by Richards et al. (2009) on unresolved SDSS DR6 objects. The efficiency of the photometric catalog at excluding non-quasar contaminants within the list of candidates is high (for example, it is estimated at 97% within a subsample of $\sim 500,000$ robust UV-excess candidates; it is lower for high-redshift candidates). We consider only the most likely quasar candidates by requiring the *good* flag to be ≥ 1 (this measure is determined based on several metrics; see Richards et al. 2009 for details). Our analysis requires reliable redshifts and luminosities, so we discard those sources with more uncertain photometric redshifts (probability < 0.5 of lying within the given range). Our minimum radio loudness and radio luminosity requirements improve efficiency still further, as only a small fraction of the non-quasars in the photometric sample would be expected to display sufficient radio emission to pass these cuts; we expect that non-quasar contamination in the matched photometric SDSS/FIRST sample is negligible. By utilizing photometrically selected quasars, it is possible to expand the luminosity coverage of the primary sample. Over half of the Richards et al. (2009) catalog consists of objects fainter than $m_i = 20.1$, which is already a full magnitude fainter than the SDSS limit for spectroscopic targeting of $z < 3$ “QSO” candidates (SDSS spectroscopic targeting of “HIZ” candidates is limited to objects with $m_i \leq 20.2$). The classification scheme is calibrated with spectroscopically confirmed SDSS quasars, and consequently the optical properties of these photometrically identified quasars are expected to be consistent with

those selected from the DR5 Quasar Catalog. This can be verified from Figure 2, which shows that the relative colors of the photometric RIQs and RLQs are distributed similarly to those of the spectroscopic sample, but that the photometric sample extends to fainter magnitudes.

The matching to radio sources and determination of X-ray coverage for the photometric quasars is identical to the procedure described for the spectroscopic quasars in Section 2.1.1. This process produces a candidate list of 359 photometric RIQs and RLQs. However, 13 of these objects have SDSS spectroscopic redshifts obtained on an MJD of less than 53535; these objects were available for inclusion in the Schneider et al. (2007) DR5 quasar catalog but were deliberately not included therein, and are therefore not appropriate for our sample.⁵ (Recall that no known DR5 spectroscopic quasars are permitted in our photometric sample, since spectroscopic data are preferred.) After excluding objects rejected from the DR5 Schneider et al. (2007) quasar catalog, the updated candidate list of photometric RIQs and RLQs contains 346 objects.

We perform an additional check for those RIQs and RLQs with photometric redshifts of $z_{\text{phot}} \geq 1.9$ in order to improve further sample fidelity. To our knowledge, the only significant set of systematically erroneous photometric redshifts within the Richards et al. (2009) catalog, as established via cross-checking with SDSS spectroscopic data, consists of a small fraction of low-redshift ($z_{\text{spec}} \leq 1$) quasars assigned photometric redshifts of $z_{\text{phot}} \sim 2$. (The additional and unavoidable effect of increasing redshift uncertainty at very faint magnitudes is difficult to quantify in the absence of spectroscopic coverage and we do not consider it here.) While such inaccuracies are atypical, it is possible to identify many of the low-redshift quasars with $z_{\text{phot}} \sim 2$ through matching to UV observations carried out by the Galaxy Evolution Explorer (GALEX; Martin et al. 2005). We make use of both redshift-dependent color-color separation (D. W. Hogg 2009, personal communication) and FUV/NUV (far/near UV) band SDSS detection rates (Trammell et al. 2007) to find and discard 27 RIQs and RLQs for which the $z_{\text{phot}} \sim 2$ photometric redshift is likely inaccurate and conservatively also discard a further 15 objects with $z_{\text{phot}} > 1.9$ that lack GALEX coverage; see Appendix A for details. The updated candidate list of photometric RIQs and RLQs contains 304 ($= 346 - 27 - 15$) objects, within which the remaining fraction with this type of redshift misidentification is only $\sim 1.5\%$.

We found 61 (out of 304) photometric RIQs or RLQs with SDSS spectroscopic redshifts obtained on an MJD of greater than 53535; these objects were not available for inclusion in the Schneider et al. (2007) DR5 quasar catalog, and thus provide a “blind test” of our selection methodology above. After examination of the SDSS spectra, only one object (133818.26+222156.4) did not show obvious broad lines (with an SDSS pipeline spectral type of “Unknown”); it seems possible that the photometric

⁵We verified that these objects were properly excluded from the Schneider et al. (2007) catalog and from our study by examining the SDSS spectra. Of these 13 objects, 7 objects (100656.46+345445.1, 101858.54+591127.8, 105829.60+013358.8, 110021.06+401928.0, 124141.38+344031.0, 131106.47+003510.0, 162625.85+351341.4) display BL Lac type spectra, and are therefore presumably highly beamed with consequent extreme X-ray properties. The remaining 6 objects (030055.97−002206.5, 082324.75+222303.2, 112211.80+431649.7, 123251.42+123110.9, 132833.56+114520.5, 133925.47−002705.5) display non-quasar spectra, with no broad emission lines apparent, and were classified by the SDSS pipeline as spectral type “Galaxy” or “Unknown”, and presumably have non-quasar X-ray properties.

classification is correct and that the photometric redshift ($z = 2.035$) is much closer to correct than the pipeline spectroscopic redshift ($z = 0.392$); however, we take a conservative view and exclude this object as not matching our optical selection criteria. We note for completeness that this object is X-ray detected, with an X-ray luminosity a factor of $\sim 3 - 5$ lower than typical RLQs of comparable optical/UV luminosity (calculated from the photometric redshift). One non-quasar object from 61 photometric candidate RIQs and RLQs with SDSS spectra corresponds to 1.6%, suggesting that non-quasar contamination of our optical/radio matched sample is quite low, at least for brighter objects.

Of the remaining 60 objects, two (080447.96+101523.7 and 155259.18+203107.9) show BAL features, with the absorption in 155259.18+203107.9 being particularly prominent; since as discussed in §2.1.1 BAL quasars are typically X-ray absorbed, these two objects are excluded from our sample. Two BAL quasars from 60 photometric RIQs and RLQs with SDSS spectra corresponds to 3.3%, suggesting that BAL contamination of our optical/radio matched sample is quite low, at least for brighter objects. This fraction is slightly lower than the typical fraction of RIQs and RLQs with BALs (e.g., Shankar et al. 2008), perhaps because the photometric color-selection is less efficient for BAL quasars with redder colors (with such a tendency reinforced by the requirement that $\Delta(g - i) < 1$).

The photometric redshifts for the remaining 58 photometric RIQs and RLQs with SDSS spectra were replaced with their spectroscopic redshifts. The ratio of the absolute value of the difference between photometric and spectroscopic redshifts to the spectroscopic redshift was checked to assess redshift accuracy. There are no sources for which this ratio exceeds 0.8, as the prior process of matching to GALEX data has already removed any spectroscopic quasars with substantially inaccurate photometric redshifts. For only 4/12 objects does this ratio exceed 0.2/0.1, and these remaining modest/tiny redshift errors are relatively random (the mean/median/standard-deviation of $z_{\text{phot}} - z_{\text{spec}} = -0.39/-0.14/0.59$ for the 12 objects with $|z_{\text{phot}} - z_{\text{spec}}|/z_{\text{spec}} > 0.1$). These 4/12 objects correspond to percentages of 6.9%/20.7% for objects with modest/tiny redshift errors out of the 58 available for checking. Applying these percentages to the 243 photometric objects lacking spectroscopic coverage suggests percentages of 5.6%/16.7% for the full photometric sample. Not only are the percentages of errors small and relatively random, but the impact on the luminosities for objects with modestly incorrect photometric redshifts is only ~ 0.2 (expressed in logarithmic units), less than the intrinsic scatter; this should have no appreciable impact on our analysis. The luminosities for the 58 photometric RIQs and RLQs with SDSS spectra are recalculated using the spectroscopic redshifts. In no case did this cause the radio luminosity of a previously accepted RIQ or RLQ to drop below the minimum selection cutoff values of $\ell_r = 31$. The final photometric sample consists of 301 ($= 304 - 1 - 2$) RIQs or RLQs, with properties as given in Table 3.

4.2.2 Supplemental samples

We supplement the primary sample with additional RLQs chosen to increase coverage of the $\ell - z$ plane. The selection methods for these additional RLQs are by

necessity not identical to those employed to obtain our primary sample, but the optical colors of the supplemental sample RLQs are reasonably consistent with those of the primary sample, as can be seen in Figure 2. The additional $\ell - z$ coverage provided by the supplemental samples considerably reduces the $\ell - z$ degeneracy when performing statistical analyses below, but we conduct most fitting on both the full and primary-only samples.

4.2.2.1 Einstein sample

To increase population of the high-luminosity region of the $\ell - z$ plane, we include the RLQs with *Einstein* observations analyzed by Worrall et al. (1987), as this sample includes many luminous RLQs that even today do not have high-quality X-ray coverage from other telescopes. Their sample of 114 RLQs includes objects from both the North and South celestial hemispheres and has an X-ray detection rate of 89%. Their sample was primarily radio-selected at both high and low frequencies and consequently includes a mix of compact and extended radio sources, and their RLQs tend to have higher radio, optical, and X-ray luminosities (and also radio-loudness values) than the objects in our primary sample. We take the radio, optical, and X-ray luminosities from Worrall et al. (1987) but translate their values to our adopted cosmology. Some of the Worrall et al. (1987) RLQs lie within the SDSS/FIRST sky coverage, and we independently find 9 duplicate objects in our primary sample; for these objects we use our more recent data and discard the older measurements. Of their remaining 105 RLQs, 11 were undetected by *Einstein* (although three of these are detected in shallow *ROSAT* observations; we use these ℓ_x values rather than the *Einstein* limits). The relative colors of the 52 of the 114 RLQs that have measured SDSS magnitudes (of which 31 also have SDSS spectra) are plotted on Figure 2 and are consistent with but perhaps slightly bluer than the relative colors of the primary sample. Note that 3C 273 is too bright to fit on this plot, and also too bright to be targeted for spectroscopy by the SDSS. Almost all of the Worrall et al. RLQs within the SDSS area are identified as quasars or quasar candidates by the SDSS pipeline, and so they would appear in our sample if they had recent high-quality X-ray coverage.

4.2.2.2 High-redshift sample

To increase population of the high-redshift region of the $\ell - z$ plane, we include the 15 high-redshift RIQs and RLQs tabulated by Bassett et al. (2004) and the 6 high-redshift RLQs observed by Lopez et al. (2006). Three of the Bassett et al. (2004) objects have $R^* < 2$ and meet our definition of RIQs. These high-redshift objects were selected based on radio flux as well as redshift and targeted by *Chandra*, typically in “snapshot” observations of ~ 5 ks; all are X-ray detected. The Lopez et al. (2006) objects have Southern declinations and are therefore unavailable to the SDSS/FIRST surveys. Most (11/15) of the Bassett et al. (2004) objects have SDSS coverage, and most (7/11) of these have SDSS spectra and are identified as SDSS quasars. The relative colors of the Bassett et al. (2004) RLQs for which we have SDSS magnitudes are plotted in Figure 2; there is one object with $\Delta(g - i) > 1$ not shown. We independently find 6 of the 15

objects from Bassett et al. (2004) in our primary sample and for consistency we use our measurements in our analysis of these objects.

Some of the high-redshift RLQs have particularly large radio-loudness values, with five having $R^* > 3.5$. These objects are referred to as “blazars” by Bassett et al. (2004) and Lopez et al. (2006) and are likely viewed at lower inclinations than most of our full-sample objects (though all are broad-line quasars and not BL Lacs). The relatively large fraction of objects with extreme radio-loudness values within the high-redshift sample should not be taken to be representative of high-redshift RLQs.

4.2.2.3 Deep-fields sample

To increase population of the low-luminosity region of the $\ell - z$ plane, we include RIQs and RLQs identified from deep-field surveys; properties of these objects are given in Table 2. We select 16 objects by optical color (of which 14 have X-ray detections) and include a further 16 X-ray detected objects known to possess broad-line optical spectra.

We attempt to mimic the optical color selection process of the primary sample when searching for lower luminosity RIQs and RLQs in deep surveys. Our general procedure is to utilize the Vanden Berk et al. (2000) color-color selection method to identify potential quasars from large catalogs of objects with *UBVRI* photometry. This set of color cuts primarily selects for $z < 2$ UV-excess objects, but also includes additional color cuts designed to identify potential quasars at higher redshift ($z = 2 - 4$). Optical catalogs for the COSMOS region are described in Ilbert et al. (2008); for the E-CDF-S they include COMBO-17 (Wolf et al. 2004) and MUSYC (Gawiser et al. 2006); for the CDF-N they include the Hawaii survey (Capak et al. 2007). We converted *UBVRI* to SDSS *ugriz* magnitudes following the transformations given by Jester et al. (2005; see their Table 1) as calculated for $z \leq 2.1$ quasars and use the *ugriz* magnitudes to calculate $\Delta(g - i)$ (discarding any heavily reddened objects with $\Delta(g - i) \gtrsim 1$) and ℓ_{uv} . Accurate photometry is important for calculating colors, luminosities, and photometric redshifts, and so we additionally require $m_i < 24$ within the *Chandra* Deep Fields; since COSMOS has shallower X-ray coverage, we require $m_i < 22.5$ for this survey to maintain a reasonable X-ray detection fraction. These magnitude limits are factors of ~ 90 and ~ 20 deeper than the $m_i < 19.1$ limit for SDSS targeting of $z < 3$ “QSO” objects. These optical selection criteria are unbiased with respect to X-ray properties. The majority of the selected deep-field RIQs and RLQs have spectroscopic redshifts (see Table 2 for references), and the remainder have accurate photometric redshifts that have been derived including UV or IR data where available.

The resulting optically-selected quasar candidates are then matched to radio catalogs, and non-radio-loud objects are removed from further consideration. This step significantly improves the efficiency of the candidate list at excluding non-quasar contaminants. The COSMOS, E-CDF-S, and CDF-N surveys have highly sensitive radio coverage, with detection limits better than $\sim 50 \mu\text{Jy}$ at 1.4 GHz. The VLA 1.4 GHz radio catalogs used for the COSMOS, E-CDF-S and CDF-S, and CDF-N fields are presented in Schinnerer et al. (2007), Miller et al. (2008) [which includes many objects also given in Kellerman et al. (2008)], and Biggs & Ivison (2006), respectively. Luminous starburst galaxies make up an increasing fraction of the radio-source population at low radio fluxes

and luminosities (e.g., Windhorst et al. 1985; Barger et al. 2007), and so we also impose radio-selection criteria designed to screen out starbursts (erring on the conservative side of also omitting some genuine RIQs or RLQs). We require $\ell_r > 31.0$ as for the primary sample and further impose a more stringent requirement of $R^* > 1.3$ upon deep-field candidates, thereby decreasing potential starburst contamination of the sample with the tradeoff of bypassing some radio-intermediate deep-field quasars.

We next match to X-ray catalogs, with any X-ray limits determined from sensitivity maps. We make use of X-ray point-source catalogs based on *Chandra* observations of the COSMOS, E-CDF-S, CDF-S, and CDF-N as presented in Elvis et al. (2009), Lehmer et al. (2005), Luo et al. (2008), and Alexander et al. (2003), respectively. Maximum *Chandra* effective exposure times are ~ 160 ks for COSMOS, ~ 250 ks for the E-CDF-S, and ~ 2 Ms for the CDF-S and the CDF-N. We use a matching radius around the optical position of $2.5''$, which is large enough to account for joint uncertainties in position (see above references) but sufficiently small that no spurious matches are expected.

As we are interested in characterizing the fundamental X-ray emission properties of RIQs and RLQs, it is helpful to identify and remove objects with heavy intrinsic X-ray absorption. This is important for the low-luminosity deep-field sample, since the fraction of obscured AGNs is large at low X-ray luminosities and decreases to high X-ray luminosities (from $\approx 80\%$ for a 2–10 keV luminosity of 10^{42} erg s $^{-1}$ to $\approx 20\%$ at 10^{45} erg s $^{-1}$; e.g., Hasinger 2008, and see also discussion in Brandt & Alexander 2010). Removing objects with strong optical reddening (as we do for both the primary and the deep-field samples) can also remove many objects with X-ray absorption, but for the deep-field sample we take the additional step of considering X-ray spectral shape (but not X-ray luminosity) as a selection criterion, as measured using the X-ray hardness ratio [defined as $HR = (H - S)/(H + S)$, where H and S are the 2–8 keV and 0.5–2 keV counts, respectively]. We screen out sources that are likely absorbed by requiring that the hardness ratio satisfy $HR < 0$; this would correspond to a power-law slope of $\Gamma \simeq 1$ for no intrinsic absorption, $\simeq 2\sigma$ from a typical RLQ $\Gamma \simeq 1.55$ (e.g., Page et al. 2005). After application of the hardness-ratio cut, this color-selection method yields 16 deep-field RIQs and RLQs, of which 14 have X-ray detections; 9 are from the E-CDF-S, 4 from the CDF-N, and 3 from COSMOS. In Appendix B, we briefly comment on interesting aspects of some of these RIQs and RLQs. Most (12/16) of the deep-field quasars selected in this manner are RLQs with $R^* > 2$.

To maximize our use of available information, we also employ optical spectra for selection, accepting RIQs or RLQs which are known to have broad emission-line spectra. Optical spectroscopy specifically targeting X-ray sources is available in COSMOS (based on *XMM-Newton* detections; Cappelluti et al. 2009), the CDF-S (based on 1 Ms sources; Giacconi et al. 2002), and the CDF-N (based on 2 Ms sources; Alexander et al. 2003) and is presented in Trump et al. (2009), Szokoly et al. (2004), and Barger et al. (2003) as well as Trouille et al. (2008), respectively. We include 16 RIQs and RLQs selected based on broad-line emission. Of these, one is from the CDF-N and two are from the E-CDF-S; these three objects have radio luminosities of $\ell_r < 31$ and so were not available for consideration as color-selected objects, but they do satisfy the Vanden Berk et al. (2000) color-color selection method for quasar candidates, as well as the hardness ratio cut, and so would otherwise have been expected to have been selected through this process. The

remaining 13 RIQs and RLQs are from the *XMM-Newton* COSMOS survey, which is shallower than the *Chandra* COSMOS survey but covers a wider area; many of these broad-line objects do not fall within the *Chandra* coverage and/or have radio luminosities of $\ell_r < 31$, and so were not considered for color selection. Again, all of these broad-line objects would have been identified as quasar candidates based on their optical colors, and all but one object passes the hardness ratio cut; that one object (J095835.06+022316.9) has blue colors (in addition to its broad-line spectrum) and is relatively X-ray bright ($\alpha_{\text{ox}} = -1.19$) and is therefore likely unabsorbed and does not need to be discarded.

In principle this manner of selecting broad-line objects known to be X-ray sources might introduce a bias toward X-ray bright sources, were similarly optically-bright broad-line objects with X-ray limits not also considered. However, we are unaware of any broad-line objects within the extensively surveyed E-CDF-S or CDF-N which lack X-ray detections, and in any event the RIQs and RLQs selected based on optical spectroscopy could generally have had lower X-ray counts by factors of ~ 10 and still been detected, suggesting that their relative X-ray brightness is not atypical for their optical/UV luminosities. This is supported by the observation that the α_{ox} values of the broad-line selected objects are similar to those of the color-selected objects. The complete deep-field sample then consists of 32 RIQs and RLQs, of which 30 are X-ray detected.

4.3 Sample characteristics

Characteristics of the various samples are presented in Tables 3 and 4 and illustrated in Figures 1–6. The sky coverage of the full sample is indicated in Figure 1, a color-magnitude diagram is provided as Figure 2, optical/UV luminosities are plotted versus redshift in Figure 3 and X-ray luminosities in Figure 4, the radio characteristics of the primary sample are given in Figure 5, and the optical/UV-to-X-ray spectral slope as a function of optical/UV luminosity is shown in Figure 6.

4.3.1 Optical/UV luminosities

Optical/UV monochromatic luminosities for all primary sample objects are calculated at rest-frame 2500 Å from SDSS photometric *ugriz* PSF magnitudes (corrected for Galactic extinction) via comparison to a redshifted composite quasar spectrum taken from Vanden Berk et al. (2001). This method accounts (in a statistical sense) for the flux from emission lines as well as typical breaks in the continuum slope. It can be inaccurate for individual quasars with strong absorption features or heavy intrinsic reddening, but objects known to possess such spectral characteristics are already excluded from our sample. The error in this method due to differences in emission-line strength or spectral shape in a particular object is expected to be less than the inherent uncertainty ($\sim 30\%$; e.g., Kaspi et al. 2007; see also Vanden Berk et al. 2004) due to typical quasar optical variability. Only the AGN power-law component is included in the luminosity; a typical iron-emission “bump” near 2500 Å is subtracted, as is the contribution from a typical RLQ host galaxy ($\ell_{\text{uv}} = 28.2$ based on an old stellar population as in, e.g., Coleman et al. 1980). We verify the accuracy of this approach through comparison to ~ 100 RQQs for which Strateva et al. (2005) calculated luminosities by fitting SDSS spectra (after

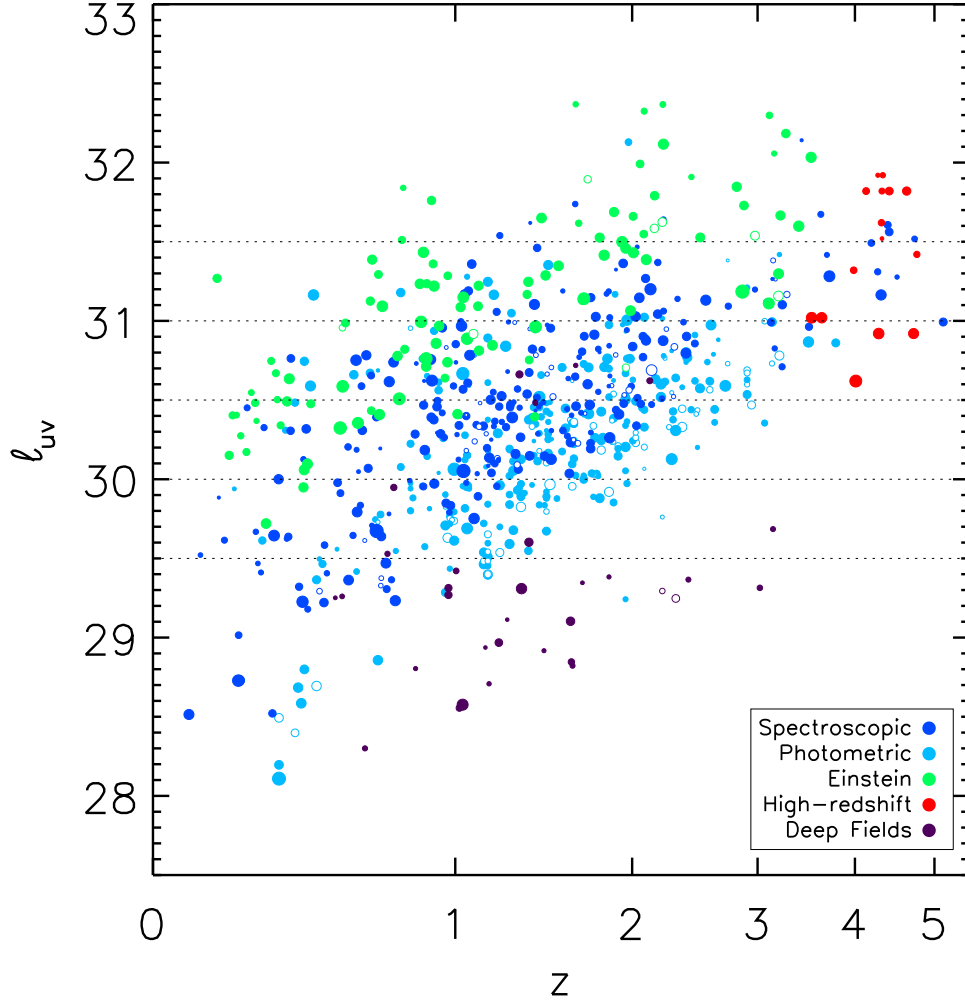


Fig. 4.3 Sample coverage of the $\ell_{\text{uv}} - z$ plane, with optical/UV luminosity as measured at rest-frame 2500 \AA . The filled symbols are X-ray detections, and the open symbols are X-ray upper limits. Larger symbols correspond to more radio-loud quasars. Primary sample SDSS spectroscopic/photometric quasars are plotted in blue/cyan, and supplemental sample *Einstein*/high-redshift/deep fields RLQs are plotted in green/red/purple. The dotted lines define luminosity bins within which various properties are summarized in Table 4.

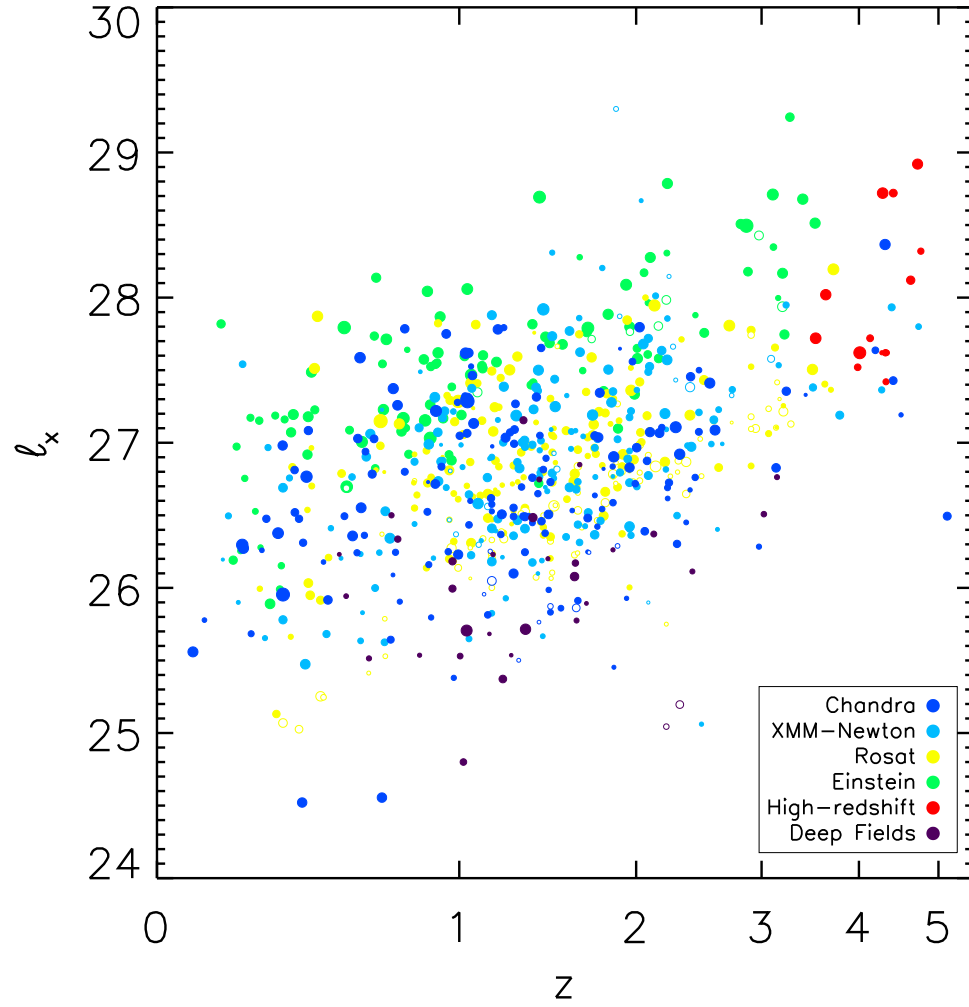


Fig. 4.4 Sample coverage of the $\ell_x - z$ plane, with X-ray luminosity as measured at rest-frame 2 keV. The filled symbols are X-ray detections, and the open symbols are X-ray upper limits. Larger symbols correspond to more radio-loud quasars.

dereddening and correcting for fiber inefficiencies, and also subtracting host-galaxy emission) and find close agreement. By using photometric rather than spectroscopic data to compute optical/UV luminosities, we can treat the SDSS spectroscopic and photometric samples in a fully consistent fashion.

Optical/UV luminosities for the *Einstein* RLQs are taken from Worrall et al. (1987), corrected to our adopted cosmology. Optical/UV luminosities for the high-redshift RLQs are taken from Bassett et al. (2004) and Lopez et al. (2006). Optical/UV luminosities for COSMOS objects are calculated from SDSS photometry, and for the CDF-N and E-CDF-S regions are calculated from synthetic SDSS photometry based on transforming *UBVRI* magnitudes to SDSS *ugriz* equivalents. The full sample (Figure 3) achieves dense coverage of the $\ell - z$ plane, a wide span (almost five decades) in luminosity coverage (~ 2.5 decades at a given redshift even without considering deep-field RIQs and RLQs, and ~ 3.5 including deep-field objects), and coverage to $z \approx 5$, all of which help eliminate unphysical correlations in the analysis of §5.

4.3.2 Radio luminosities and radio loudness

Radio monochromatic luminosities are calculated at rest-frame 5 GHz through extrapolation of the observed 1.4 GHz flux densities. It is desirable to treat the entire sample in a uniform fashion, but many sources lack multi-frequency radio measurements, or are multi-component sources with multi-frequency radio flux densities obtained at an angular resolution insufficient to distinguish α_r for the core from any extended emission. Therefore, we do not use individual α_r values calculated for a particular source (see §3.3) to determine the radio luminosity of that source, but instead assume a radio spectral index of $\alpha_r = -1$ for lobe emission and $\alpha_r = -0.5$ for core emission. In any event, alternative choices of α_r produce only small changes in ℓ_r since it is only necessary to extrapolate over a small frequency range. The radio monochromatic luminosities within the full sample span over four decades, with a median $\ell_r = 32.99$; the median radio monochromatic luminosity within the primary sample is slightly lower, with $\ell_r = 32.81$. This difference chiefly reflects the high radio luminosities of the supplemental *Einstein* RLQ sample, which may be due to some targets being radio selected. The radio luminosities within the deep-field sample are lower, with a median $\ell_r = 31.50$ (recall that we permit $\ell_r < 31$ for broad-line selected deep-field objects).

Radio loudness in our sample is correlated with radio luminosity (Figure 5), signifying the influence of beamed jet emission that comes to dominate the radio emission measured by FIRST for objects at low inclinations (or with intrinsically powerful jets) but apparently does not similarly dominate the optical/UV luminosity (as is also suggested by the SDSS broad emission-line equivalent widths, which do not suggest significant dilution by a featureless jet-linked continuum for these sources). The median radio loudness for the full sample is $R^* = 2.62$; it is notably higher for the *Einstein* sample (median $R^* = 3.42$) and lower for the deep-field objects (median $R^* = 2.06$, with the lowest permitted value being $R^* = 1.3$). Because the photometric sample extends to somewhat fainter magnitudes than the spectroscopic sample, the photometric sample has a slightly lower median optical/UV luminosity (along with a slightly higher median radio-loudness value).

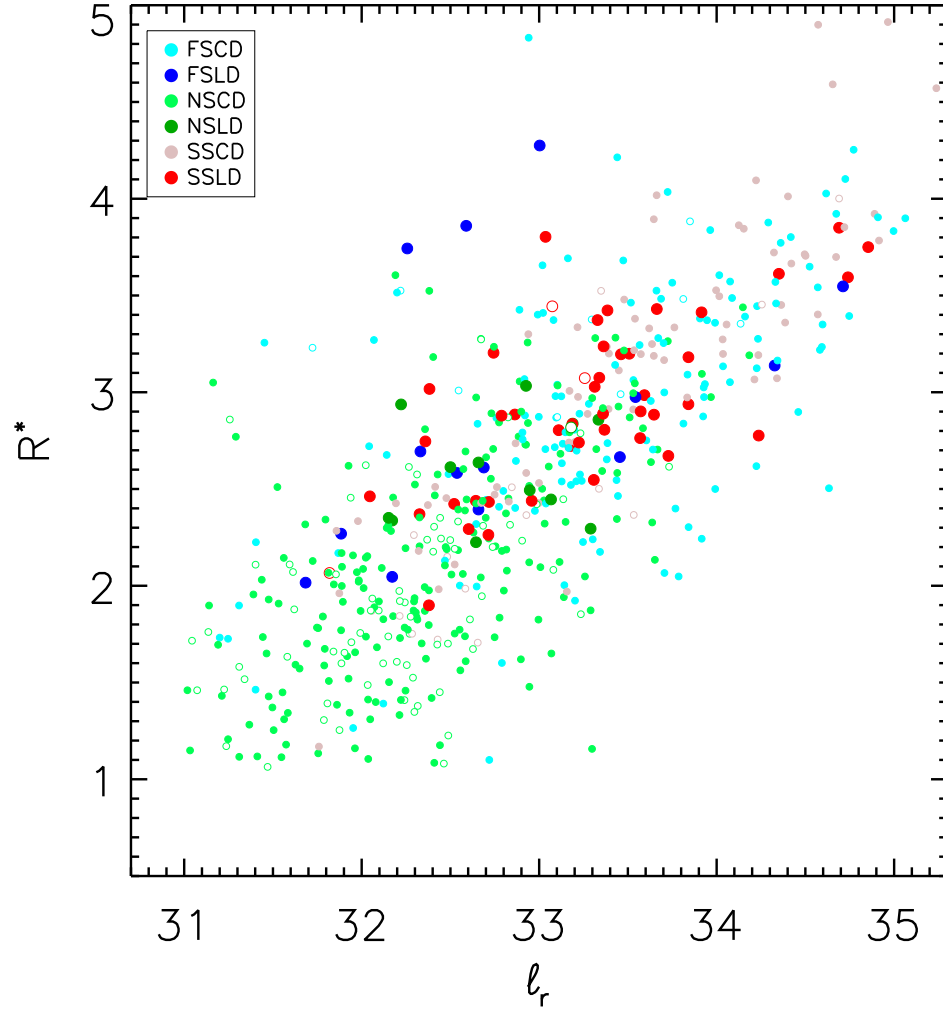


Fig. 4.5 Radio loudness (R^*) versus radio luminosity for the 575 RIQs and RLQs in the SDSS primary sample, where ℓ_r is $\log \text{erg s}^{-1} \text{Hz}^{-1}$ and $R^* = \ell_r - \ell_{\text{uv}}$. Symbol color identifies objects as flat-spectrum core-dominated (FSCD; cyan), flat-spectrum lobe-dominated (FSLD; blue), unmeasured radio spectrum core-dominated (NSCD; light green), unmeasured radio spectrum lobe-dominated (NSLD; dark green), steep-spectrum core-dominated (SSCD; pink), and steep-spectrum lobe-dominated (SSLD; red). Radio loudness and luminosity are correlated within this sample, albeit with large scatter. The most radio-loud objects tend to be core-dominated and not steep-spectrum. Lobe-dominated objects tend to be steep-spectrum. See discussion in §3.2 and §3.3.

4.3.3 Radio spectral shapes and morphologies

Although we do not use radio spectral slope to calculate luminosity, we do distinguish between flat-spectrum and steep-spectrum radio sources when radio spectral information is available. Flat-spectrum RLQs are X-ray brighter than their steep-spectrum counterparts (e.g., Worrall et al. 1987), so we also conduct analyses of X-ray luminosity correlations on separate subsamples of flat-spectrum and steep-spectrum RLQs. In light of the difficulties inherent in comparing fluxes obtained at widely differing angular resolutions, spectral indices are computed in the observed frame from the source flux densities (summed over all components for cases of resolved extended radio emission). The 168 objects with $\alpha_r < -0.5$ are classified as steep spectrum, while the 206 objects with $\alpha_r \geq -0.5$ are classified as flat spectrum.

To find α_r for objects with multifrequency radio coverage, counterparts for all primary sample objects were sought in the Green Bank 6 cm (5 GHz) catalog (Gregory et al. 1996), which has a flux-density limit of ~ 18 mJy and covers $0^\circ < \delta < 75^\circ$, in the Texas 82 cm (365 MHz) catalog (Douglas et al. 1996), which has a flux-density limit of ~ 250 mJy and covers $-35^\circ < \delta < 70^\circ$, and in the Westerbork 92 cm (325 MHz) Northern Sky Survey (Rengelink et al. 1997), which has a flux-density limit of ~ 18 mJy and covers $\delta > +30^\circ$. All of these surveys have significantly lower angular resolution than does the FIRST survey, so components resolved by FIRST may be blended in these catalogs. Any sources within $90''$ of the optical position are presumed to be associated with the quasar, unless a FIRST background source is known to be present within the field; for such instances the relative positions and fluxes have been evaluated on a case-by-case basis and the multi-frequency radio data discarded if deemed background contaminated. The false-match probability is low: artificially shifting the declination by one degree and rematching returns 5.6% as many matches within $90''$, but most of these matches lie outside of $30''$ of the quasar position and could be caught by the screening of potential background objects as gauged by FIRST data, and only 0.5% as many objects lying within $30''$ of the quasar position are returned when matching with shifted declination.

Green Bank data are prioritized when calculating α_r since we are most interested in assessing the relationship of X-ray emission to the radio core (rather than extended) emission. The uncertainty on α_r is then often dominated by the error in the Green Bank flux measurements, which is generally $\sim 10\%$. A quasar with a typical FIRST radio flux and a borderline $\alpha_r = -0.5$ radio spectral slope would have an uncertainty on α_r of ± 0.08 . There are 34 objects with $-0.58 \leq \alpha_r \leq -0.42$, which is 9% of the total number of objects with measured α_r values, so for most objects the classification as flat or steep spectrum is secure. Objects with both Green Bank and low-frequency measurements were considered more closely; sources with concave spectra are presumed to arise from the emerging dominance of a flat-spectrum core, but (as described in §2.1.1) all 8 objects with convex spectra were identified as possible GPS sources, which have properties not shared by RLQs in general and are thus not included in the primary sample.

All primary sample objects are also classified as either core-dominated or lobe-dominated, with core-dominated objects having a core radio monochromatic luminosity (at 5 GHz) greater than half the total radio luminosity. As a consequence of performing radio selection at an observed frequency of 1.4 GHz (rather than at, for example, a lower

frequency such as 159 MHz or 178 MHz, at which the 3C and 4C surveys, respectively, were carried out), core-dominated, likely low-inclination sources are over-represented relative to their presumed parent radio population. (Recall, however, that extremely beamed objects are mostly excluded from our sample by the optical selection criteria; for example, objects with featureless optical spectra are not included in the SDSS DR5 quasar catalog.) The primary sample lobe-dominated RIQs and RLQs are more likely to have steep radio spectra, whereas the core-dominated objects are more likely to have flat radio spectra (Figure 5). The primary sample RLQs with particularly large radio-loudness values ($R^* > 3.5$) tend to be core-dominated and have flat radio spectra. These trends are likely in large part a consequence of core small-scale jet emission gradually overwhelming (steep-spectrum) lobe emission as inclination decreases (see also §6).

4.3.4 X-ray luminosities

X-ray counts were measured for all primary sample objects using the IDL *aper* task. X-ray images for objects observed with *ROSAT* or *XMM-Newton* were downloaded from HEASARC⁶ along with exposure maps and, for *ROSAT*, background images. For objects observed with *Chandra*, the CIAO task *dmcop*y was used to produce full-band images from the pipeline-processed level 2 event files. Source counts were extracted from $\sim 90\%$ encircled-energy apertures. The energy coverage of the utilized images is 0.4–2.4 keV for *ROSAT*, 0.5–8 keV for *Chandra*, and 0.2–12 keV for *XMM-Newton*. Background counts were determined from the provided background image for *ROSAT* observations and as the median of 8 nearby non-overlapping apertures for *Chandra* and *XMM-Newton* observations.

Source detection is evaluated by comparison of the observed aperture counts to the 95% confidence upper limit for background alone. Where the number of background counts is less than 10 we use the Bayesian formalism of Kraft et al. (1991) to determine the limit; else, we use equation 9 from Gehrels (1986). If the aperture counts exceed the 95% confidence upper limit we consider the source detected and calculate the net counts by subtracting the background from the aperture counts and then dividing by the encircled-energy fraction; else, the source is undetected and the 95% confidence upper limit is used. Counts were converted to count rates using the furnished or generated exposure maps. Count rates were converted to observed-frame 2 keV flux densities with PIMMS⁷, in all cases assuming Galactic absorption and a power-law spectrum with $\Gamma = 1.5$ (alternate reasonable choices for Γ have only a few percent impact upon the calculated X-ray fluxes), which were then used to determine bandpass-corrected rest-frame 2 keV monochromatic luminosities.

Where available, data from the *Chandra* Source Catalog (Evans et al. 2008) or the *XMM-Newton* Serendipitous Source Catalog (Watson et al. 2009) were used in preference to our own measurements (with X-ray luminosities calculated from catalog broad-band fluxes as given at 0.5–7 keV for *Chandra* and 0.5–4 keV for *XMM-Newton*). It is not possible for this project to rely exclusively on catalogs, however, as large “blind search”

⁶High Energy Astrophysics Science Archive Research Center: <http://heasarc.gsfc.nasa.gov/>

⁷<http://cxc.harvard.edu/toolkit/pimms.jsp>

source catalogs must utilize more conservative detection thresholds. In addition, it would be difficult to determine accurate upper limits based on a catalog non-detection. Our calculated luminosities are in good agreement with those derived from catalog data, indicating that our measurements (detections or upper limits) for those objects not included in catalogs should also be accurate.

The X-ray data for the primary sample of 575 RIQs and RLQs are based for 159 objects on *Chandra* observations, for 184 objects on *XMM-Newton* observations, and for 232 objects on *ROSAT* observations. The X-ray detection rates for *Chandra*, *XMM-Newton*, and *ROSAT* are 93%, 90%, and 68%, respectively. X-ray data for 104 objects detected with *Chandra* were taken from the *Chandra* Source Catalog, and X-ray data for 132 objects detected with *XMM-Newton* were taken from the *XMM-Newton* Serendipitous Source Catalog (the match radii were 3'' and 10'', respectively). In a few cases the source catalogs provide total X-ray coverage deeper than our single-observation photometry, and our sample is improved by making use of these additional data. No objects are discarded based on non-inclusion in source catalogs. Many of the sources which are not included in the utilized source catalogs but are detected by our photometry are associated with observations not included in the source catalogs, either due to the observation date falling outside of the range covered by the source catalogs or some observation parameter (e.g., subarray type) not satisfying the requirements for inclusion in the catalogs.

Almost all of the *ROSAT* coverage is serendipitous; only 6/232 (2.6%) sources are found within 3' of the aimpoint of the best *ROSAT* observation. The SDSS and FIRST surveys served as a source of targets for many *XMM-Newton* and *Chandra* observations; 31/184 (16.8%) sources are found within 2' of the aimpoint of the best *XMM-Newton* observation, and 62/159 (39.0%) sources are found within 1' of the aimpoint of the best *Chandra* observation. Some of these targeted objects also have serendipitous coverage and would be in our sample even absent the targeted observations: four of the objects targeted by *XMM-Newton* have off-axis *Chandra* coverage, one of the objects targeted by *Chandra* has off-axis *XMM-Newton* coverage, and three of the objects targeted by *Chandra* have off-axis *ROSAT* coverage, although one of these three also has *XMM-Newton* coverage. In total, then, 92/575 (16.0%) of the RIQs and RLQs in our primary sample were targeted for X-ray observations. The analysis of luminosity correlations below was carried out including targeted objects to increase the size of the primary sample, but results are also provided for an “Off-axis” sample of sources with only serendipitous X-ray coverage and for the “Targeted” sample exclusively, and discussed in §5.4.2.

There may be cases in which the extraction region used to calculate the X-ray luminosity includes both nuclear and X-ray jet emission. Many X-ray jets have been discovered by *Chandra* (e.g., Sambruna et al. 2004; Marshall et al. 2005), and some would not be resolvable with *ROSAT* or even *XMM-Newton*. Additionally, in some instances the inner knot(s) of an X-ray jet might lie inside the *Chandra* extraction region. Generally even the inner knots of RLQs with X-ray jets are observed to be only

a few percent as bright as the X-ray core⁸ (e.g., Marshall et al. 2005), which would not significantly change the calculated ℓ_x values. The XJET catalog⁹ provides a useful listing of ~ 100 objects with known extended X-ray emission. Out of the primary sample of 575 RIQs and RLQs, only 15 are listed in the XJET catalog. We examined X-ray images of all 15 objects and in no case did it appear likely that the extended X-ray emission could significantly increase the measured X-ray luminosity.

4.4 Comparison of the X-ray emission in RQQs, RIQs, and RLQs

Several previous studies have noted the tendency for RLQs to be more X-ray bright than RQQs of comparable optical/UV luminosity (e.g., Zamorani et al. 1981; see also discussion and references in §1). We confirm that general result, and also quantify the degree to which RIQs and RLQs differ in X-ray brightness from RQQs as a function of radio loudness and luminosity. Our large, representative, and comprehensive sample permits relatively fine-grained binning for such measurements.

The necessity of controlling for optical/UV luminosity when comparing RIQs and RLQs to RQQs is driven by the well-known steepening in RQQs of optical/UV-to-X-ray spectral slope with increasing optical/UV luminosity (e.g., $\alpha_{\text{ox}} = -0.137 \times \ell_{\text{uv}} + 2.638$ as given in Equation 2 of Steffen et al. 2006; other studies typically find similar results). As RLQs are X-ray brighter than RQQs at a given ℓ_{uv} , they have smaller values of α_{ox} . The median optical/UV-to-X-ray spectral slope for the full sample of RIQs and RLQs is $\alpha_{\text{ox}} = -1.35$, whereas RIQs have a median $\alpha_{\text{ox}} = -1.42$, closer than is the median $\alpha_{\text{ox}} = -1.34$ of RLQs to the typical value for RQQs (the sample of RQQs we use for comparison, from Steffen et al. 2006, has a median $\alpha_{\text{ox}} = -1.51$).

The α_{ox} and ℓ_{uv} values for the complete sample of RIQs and RLQs are plotted in Figure 6, along with the RQQ $\alpha_{\text{ox}}(\ell_{\text{uv}})$ relation and the 25th and 75th percentiles for α_{ox} for RQQs within each ℓ_{uv} decade (from Table 5 of Steffen et al. 2006). The flattening of the RQQ relation at low luminosities appears to be genuine (e.g., Steffen et al. 2006; Maoz et al. 2007) and Figure 6 suggests a qualitatively similar effect may apply to RIQs and RLQs, although a larger sample is required to confirm this. Like RQQs, RIQs and RLQs also appear to show an anti-correlation between α_{ox} and ℓ_{uv} (a Spearman test gives $\rho = -0.282$, with a probability less than $p = 5 \times 10^{-5}$ that no correlation is present), albeit with a systematic offset toward less negative values of α_{ox} , and there is greater scatter about this trend for RIQs and RLQs than is observed for RQQs. Figure 6 also demonstrates that the degree to which RIQs and RLQs are brighter in X-rays than comparable RQQs is dependent upon radio loudness (the larger points, representing more radio-loud objects, are generally further above the RQQ $\alpha_{\text{ox}}(\ell_{\text{uv}})$ relation).

The “excess” X-ray luminosity from RLQs may be defined as $\ell_x - \ell_{x,\text{RQQ}}$, where we take the expected X-ray luminosity for RQQs to be $\ell_{x,\text{RQQ}} = 0.721 \times \ell_{\text{uv}} + 4.531$

⁸The X-ray core itself may contain an unresolved component of X-ray emission linked to the pc-scale radio jet, of course, but we desire such a component be included for our analysis and in any case it would be impossible to exclude from simple photometry.

⁹<http://hea-www.harvard.edu/XJET/>

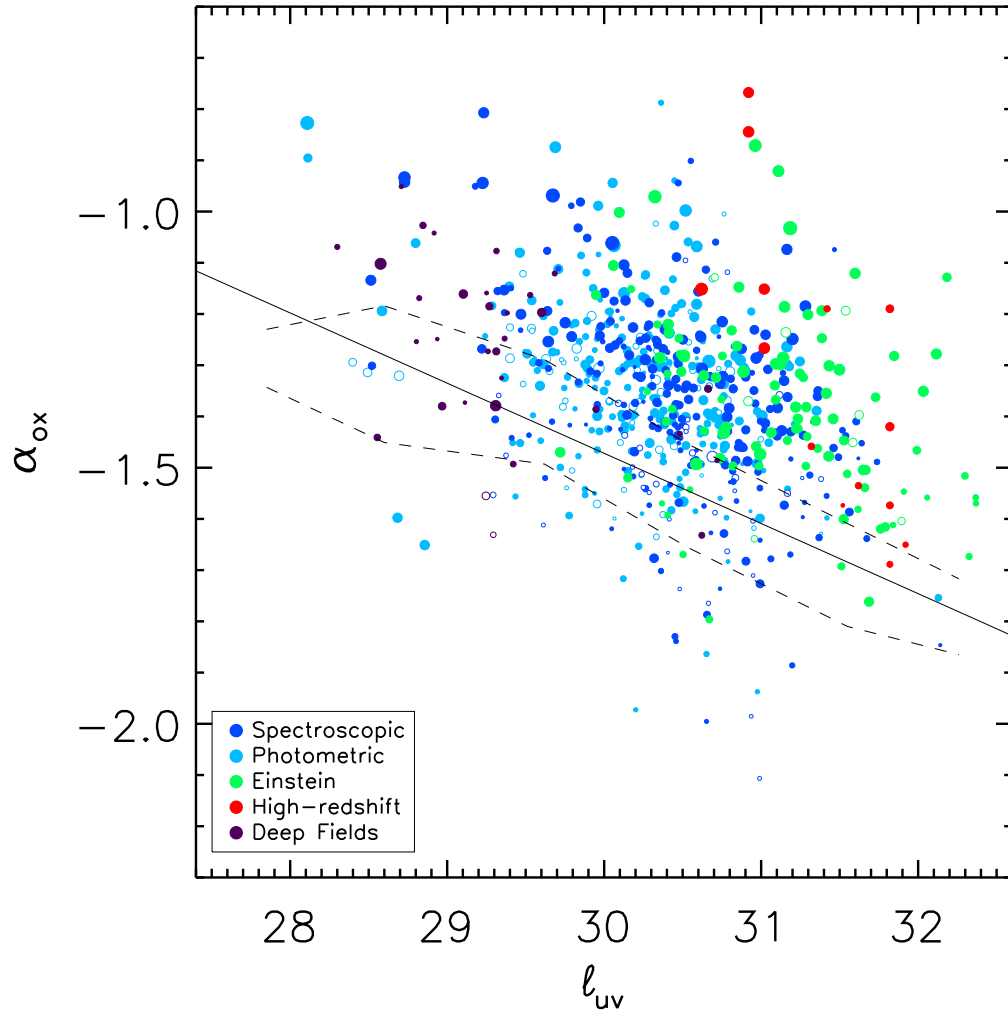


Fig. 4.6 Optical/UV-to-X-ray spectral slope α_{ox} as a function of ℓ_{uv} ; symbols are coded as in Figure 3. The solid line is the best-fit linear relation for RQQs from Steffen et al. (2006), while the dashed lines show the 25th and 75th percentiles from their sample of RQQs. RLQs are X-ray bright relative to RQQs of comparable optical/UV luminosities.

(Equation 1c from Steffen et al. 2006) and use ℓ_{uv} as measured for RIQs and RLQs¹⁰. Figure 7 shows excess X-ray luminosity for the complete sample of RIQs and RLQs as a function of radio loudness and of radio luminosity, along with median values and the 25th–75th percentile range within bins of R^* and ℓ_r . The median values and 25th and 75th percentiles plotted in Figure 7 are listed in Table 5. When expressed in linear units, the multiplicative factor by which the X-ray luminosity for RIQs and RLQs exceeds that of RQQs ranges (25th–75th percentiles) from 0.9–3.2 for RIQs through the canonical ~ 3 for RLQs to 3.5–10.2 for extremely radio-loud ($R^* > 3.5$) RLQs, with a similar increase in excess X-ray luminosity with increasing radio luminosity. Figure 8 shows the distribution of $\ell_x - \ell_{\text{x,RQQ}}$ (the shaded histogram is detected objects and the open histogram includes X-ray upper limits) within the same bins of R^* (left) and ℓ_r (right) as used to construct Table 5. The distribution of excess X-ray luminosity is reasonably well-characterized as log-normal (see overplotted Gaussians) but there is a tail to brighter X-ray luminosity that is particularly prominent within the highest radio-loudness and luminosity bins.

The excess X-ray luminosity may also be fit directly as a function of radio loudness or luminosity, for example as $\ell_x - \ell_{\text{x,RQQ}} = a + b \times R^*$ or $\ell_x - \ell_{\text{x,RQQ}} = a + b \times \ell_r$, where a and b are fitting constants. We carry out such a fit using the IDL code of Kelly (2007), which utilizes Bayesian techniques that incorporate both uncertainties and upper limits. The best-fit models for the full sample are $\ell_x - \ell_{\text{x,RQQ}} = (-0.375 \pm 0.061) + (0.281 \pm 0.021) \times R^*$ and $\ell_x - \ell_{\text{x,RQQ}} = (0.401 \pm 0.018) + (0.154 \pm 0.016) \times (\ell_r - 33.3)$. Flat-spectrum RLQs appear to have excess X-ray luminosity more strongly correlated with radio properties than do steep-spectrum RLQs, with flat/steep spectrum RLQs having coefficients of $(0.334 \pm 0.046)/(0.276 \pm 0.041) \times R^*$ and $(0.137 \pm 0.032)/(0.101 \pm 0.031) \times (\ell_r - 33.3)$. The large amount of scatter in these relations prevents productive consideration of more complex models, but Figures 7 and 8 do suggest that these linear fits (to log quantities) may not adequately capture the apparent slow rise in X-ray excess at low radio-loudness or luminosity and the more rapid increase at higher R^* or ℓ_r values.

4.5 Parameterizing the X-ray luminosity of RIQs and RLQs

We parameterize X-ray luminosity as a sole function of optical/UV luminosity and as a joint function of optical/UV and radio luminosity for various groupings of RIQs and RLQs, and also consider whether an additional dependence upon redshift is required. All fitting is carried out with the IDL code of Kelly (2007), which utilizes Bayesian techniques that incorporate both uncertainties and upper limits. The potential measurement errors in optical magnitudes and radio fluxes are generally small, and most objects have sufficient X-ray counts that the uncertainties may be assumed to be dominated by intrinsic random flux variability (e.g., see §3.5 of Gibson et al. 2008). The luminosities are normalized prior to fitting to median values for RLQs, as $\ell_r - 33.3$, $\ell_{\text{uv}} - 30.5$, $\ell_x - 27.0$. Results are given in Tables 6 and 7 and illustrated in Figures 9–17.

¹⁰Such an analysis is easiest to interpret in the case that the optical/UV luminosity in broad-line RIQs and RLQs is disk-dominated (generally consistent with Figure 5, and supported by the apparently undiluted equivalent widths of the broad emission lines) and if the disk/corona in RIQs and RLQs has the same basic X-ray efficiency as in RQQs, as seems a reasonable initial assumption; see §6 for further discussion of these points.

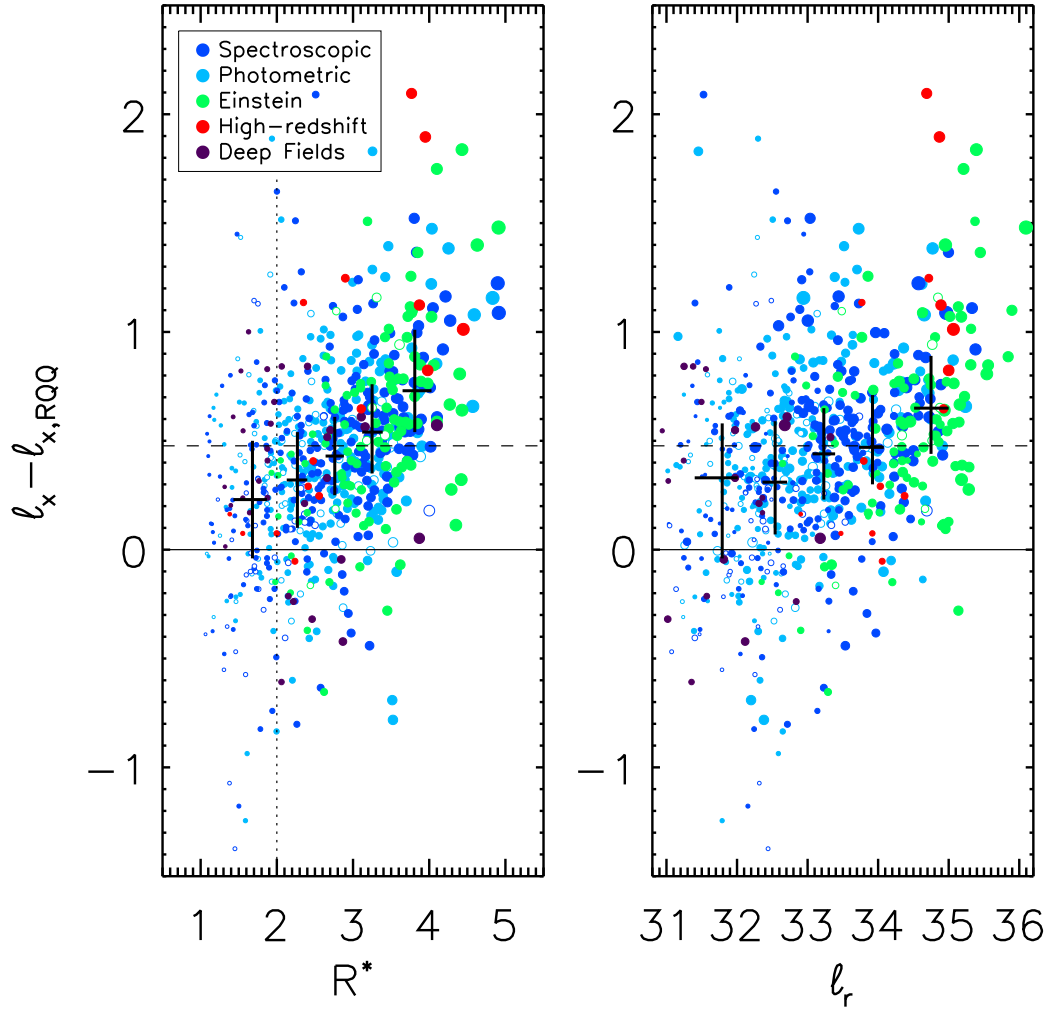


Fig. 4.7 X-ray “excess” in RIQs and RLQs relative to comparable RQQs plotted as a function of radio loudness (left) and radio luminosity (right). The solid line corresponds to a ratio of one and the dashed line to a ratio of three. The black crosses show median values within bins; the arms show the 25th–75th percentile range in each bin. Symbols are coded as in Figure 3.

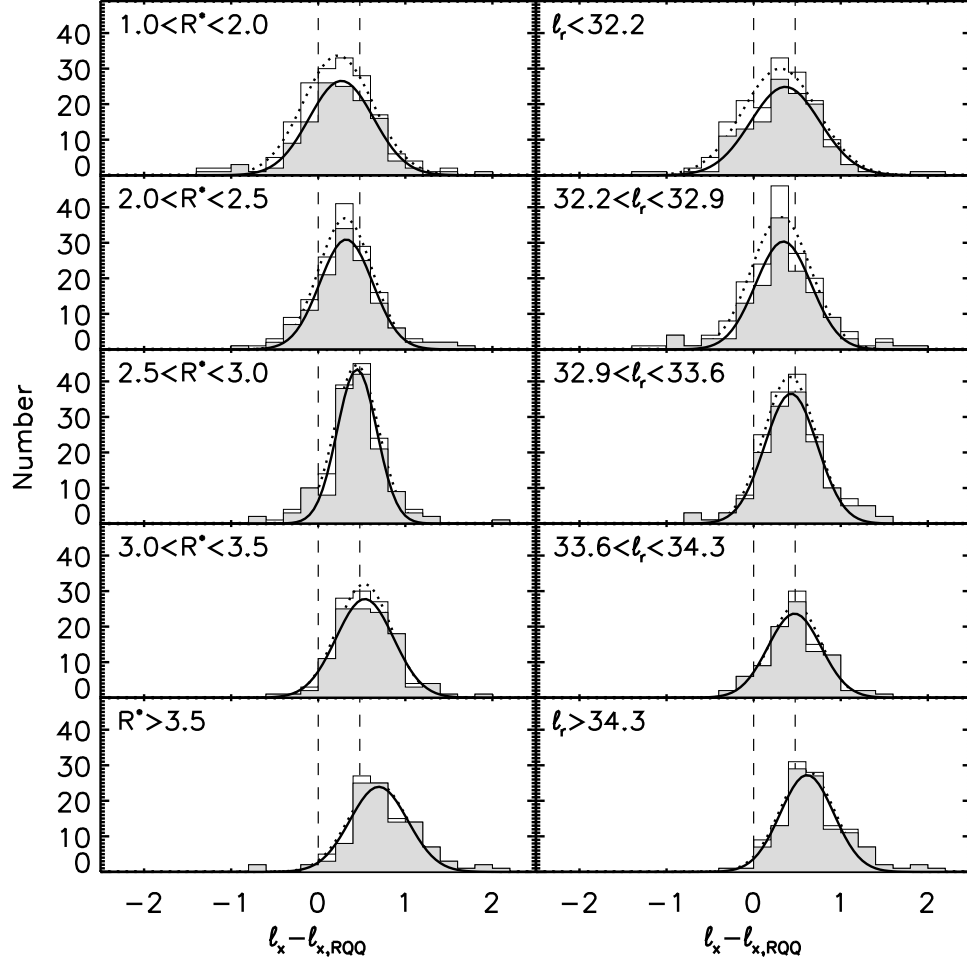


Fig. 4.8 Histograms of $\ell_x - \ell_{x,RQQ}$ (defined as in §4) plotted in (increasing downward) bins of radio-loudness (left) and radio luminosity (right); the bins are identical to those in Table 5. The filled histograms contain X-ray-detected objects and the open histograms include upper limits. The vertical dashed lines correspond to linear multiplicative factors of 1 and 3 for the ratio of the X-ray luminosity of RIQs and RLQs to comparable RQQs. The solid/dotted curves are Gaussians fit to detected/all objects to investigate log-normality; there appears to be a tail of objects with high X-ray luminosities, particularly in the maximum radio-loudness and luminosity bins.

For any given model fit the quoted parameter values are the median of draws from the posterior distribution and the errors are credible intervals corresponding to 1σ . See Appendix C for additional discussion of fitting methodology.

4.5.1 $\ell_x(\ell_{uv})$

The first model we consider is X-ray luminosity as a sole function of optical/UV luminosity, such as is typically applied to RQQs: $\ell_x = a_0 + b_{uv} \times \ell_{uv}$. It is most convenient to treat ℓ_x as the dependent variable for the purposes of fitting, given the X-ray limits (and perhaps also most appropriate for our predominantly optically-selected sample of RIQs and RLQs, whose X-ray properties were not considered in selection); since our analysis is comparative in nature, it suffices to maintain consistency and so we do not also calculate coefficients treating ℓ_{uv} as the dependent variable, nor do we calculate a bisector fit. This approach also simplifies analysis when additional variables are considered. We first re-fit the RQQs from Steffen et al. (2006) using the same procedure we adopt for analyzing the RIQs and RLQs, to demonstrate the consistency of this method with previous work. Our results agree with those of Steffen et al. (2006) for their Equation 1a (see also Appendix C). We also re-fit the luminous *Einstein* RLQs from Worrall et al. (1987) separately, to assess the influence this subsample exerts upon the full sample. Finally, we fit the full sample and then also fit various groupings of RIQs and RLQs. Results for this model are given on the left side of Table 6 and plotted in Figure 9.

The general tendencies revealed by Figure 9 are (9a) RIQs have X-ray luminosities similar to those of RQQs of comparable optical/UV luminosities (perhaps particularly so at high optical/UV luminosities), whereas RLQs become increasingly X-ray bright relative to comparable RQQs as ℓ_{uv} increases; (9b) when RLQs are subdivided by radio loudness, RLQs with $R^* > 3$ are more X-ray bright than those with $R^* < 3$, with this difference roughly constant with increasing ℓ_{uv} ; (9c) when RLQs are subdivided by radio luminosity, RLQs with $\ell_r > 33.3$ are more X-ray bright than those with $\ell_r < 33.3$, with this difference roughly constant with increasing ℓ_{uv} (although there is minimal overlap in ℓ_{uv} for these two categories of RLQs); (9d) RLQs with flat radio spectra are more X-ray luminous than those with steep radio spectra, with this difference perhaps increasing over the ℓ_{uv} range studied, and in particular almost all of the most X-ray luminous RLQs (with $\ell_x > 28$) have flat radio spectra. There does not appear to be any grouping of RIQs or RLQs that contains objects with X-ray luminosities less than those of comparable RQQs at any optical/UV luminosities; this is broadly consistent with RIQs and RLQs being similar to RQQs but with an “extra” source of X-ray emission whose strength depends upon radio properties. Over all groupings and models, there is a general tendency for the RLQs at the highest optical/UV luminosities to lie above their best-fit models (to a degree exceeding any possible slight systematic flattening of the slope due to the fit method; see Appendix C), and this structure in the residuals suggests that a linear fit (to logarithmic quantities) of X-ray luminosity as a sole function of optical/UV luminosity is not an adequate model even when applied within subgroups of RLQs, at least for particularly radio-loud, luminous, or flat-spectrum RLQs.

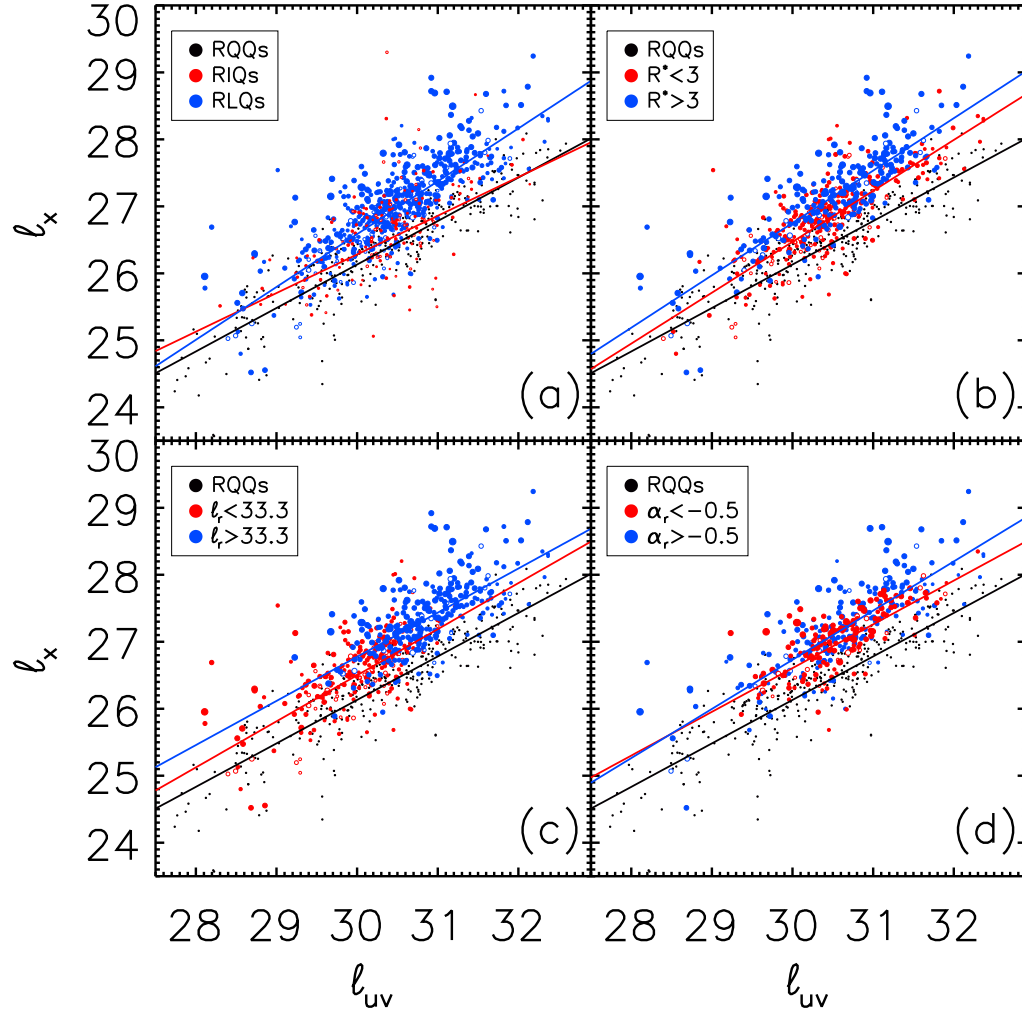


Fig. 4.9 X-ray luminosity as a function of optical/UV luminosity for RIQs and RLQs (a) and for various sub-samples of RLQs (b, c, d). The model considered is $\ell_x = a_0 + b_{uv} \times \ell_{uv}$ (where ℓ_x and ℓ_{uv} have been normalized prior to fitting as described in §5). Filled symbols are X-ray detections and larger symbols are more radio-loud throughout. Solid lines show best-fit linear models.

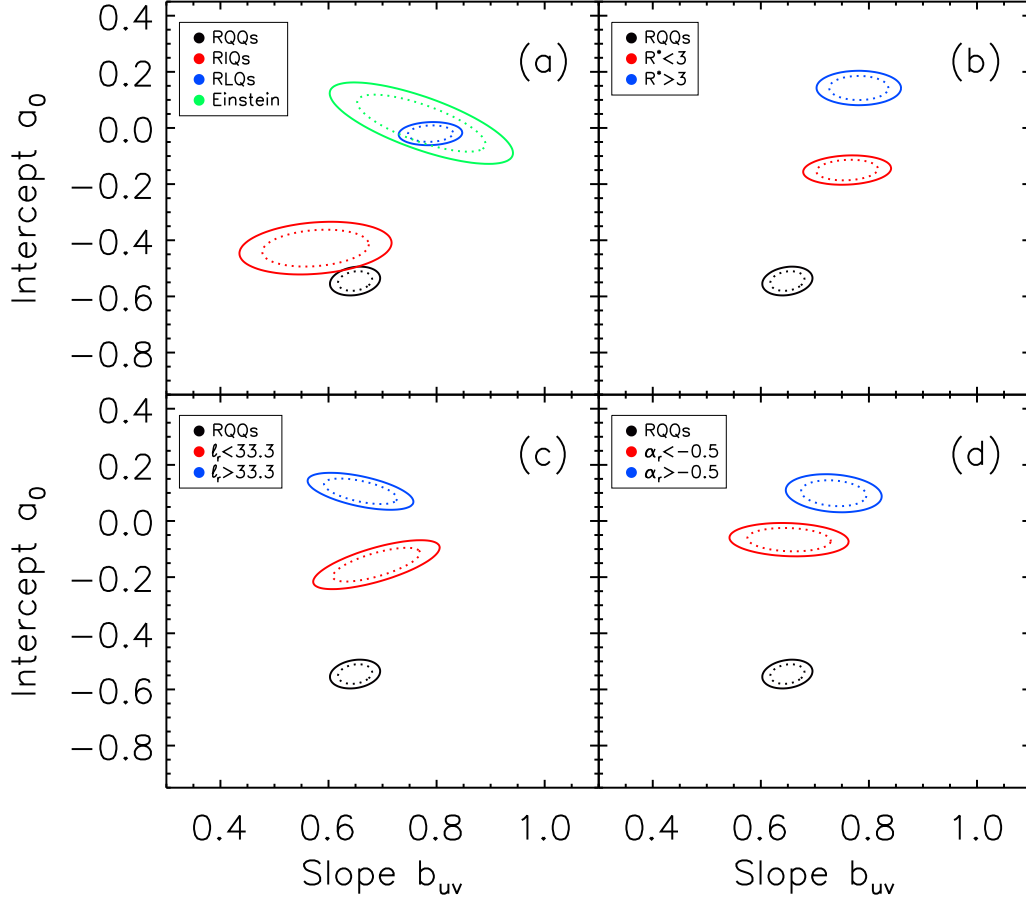


Fig. 4.10 Joint 90% (solid) and 68% (dotted) confidence contours for fitting X-ray luminosity as a (sole) function of optical/UV luminosity for various subsamples of RLQs. The model considered is $\ell_x = a_0 + b_{uv} \times \ell_{uv}$ (where ℓ_x and ℓ_{uv} have been normalized prior to fitting as described in §5). RLQs with larger values of radio-loudness or luminosity or with flat radio spectra are more X-ray bright than those with smaller values of radio-loudness or luminosity or with steep radio spectra.

Joint 90% and 68% confidence ellipses for the various fits to this model are plotted in Figure 10. In all panels the RQQ result is plotted as a black ellipse for comparison. It can be seen in (10a) that the confidence region for RQQs is near to and (for the 90% ellipse) even slightly overlaps that of RIQs; the modest radio loudness and radio luminosity of RIQs generally do not appear to enhance substantially their X-ray emission. In contrast, the confidence region for RLQs is well separated from that of RQQs, with both a greater model intercept and slope. It can also be seen that our sample substantially increases the precision with which the model parameters can be assessed over that provided by previous studies, such as that of Worrall et al. (1987) for their *Einstein* sample of RLQs. In (10b), (10c), and (10d) the confidence regions for each subgroup of RLQs are fully distinct from the other subgroup and from RQQs. Splitting RLQs by radio loudness, radio luminosity, or radio spectral index yields subgroups with significantly differing X-ray emission properties. It is only for RLQs with flat radio spectra versus those with steep radio spectra that a difference in slope between two subgroups of RLQs is plausible, although both the 90% and the 68% confidence regions still overlap in projection onto the slope variable; the increased X-ray brightness for $R^* > 3$ or $\ell_r > 33.3$ RLQs is exclusively reflective of a larger intercept in the modeled relation.

4.5.2 $\ell_x(\ell_{uv}, \ell_r)$

4.5.2.1 Inclusion of radio luminosity as a fit parameter

The second parameterization we consider is X-ray luminosity as a joint function of optical/UV luminosity and radio luminosity: $\ell_x = a_0 + b_{uv} \times \ell_{uv} + c_r \times \ell_r$. The resulting coefficients obtained from fitting various groupings of RIQs and RLQs are listed on the right side of Table 6. The optical/UV luminosity coefficient is now $b_{uv} < 0.6$ for RLQs and $b_{uv} < 0.5$ for highly radio-loud or luminous RLQs, compared to the $b_{uv} \simeq 0.65$ for RQQs; this suggests that the apparently stronger dependence of RLQ X-ray luminosity upon ℓ_{uv} indicated in the previous model of $\ell_x(\ell_{uv})$ was actually reflecting the influence of radio luminosity, which is now explicitly considered. The best-fit model for RIQs has b_{uv} consistent with that for RQQs and c_r consistent with zero, indicating that radio properties do not significantly influence the X-ray luminosities of RIQs in general. The intercept is perhaps greater for RIQs than for RQQs, meaning RIQs are still X-ray bright relative to RQQs (as is also suggested by the first column in Table 5), but the uncertainty on the best-fit RIQ intercept exceeds the degree to which it differs from that for RQQs. Figure 11 plots ℓ_x versus $\ell_{uv} + 0.56 \times \ell_r$. This choice of variables is motivated by the coefficients of the $\ell_x(\ell_{uv}, \ell_r)$ model for RLQs, for which c_r is $\approx 0.56 \times b_{uv}$. Collapsing the $\ell_{uv} - \ell_r$ plane to a single joint variable simplifies presentation of the modeling results and enables ready comparison of the properties of subgroups of RLQs to those of RLQs as a whole. It can be seen from (11a) that the *Einstein* sample of RLQs dominates the highest luminosity region of the full sample, which also contains the high-redshift sample objects. Conversely, the lowest luminosity region of the full sample is strongly influenced by the deep-field sample objects, although there are many primary sample photometric quasars in this region as well. In (11b), (11c), and (11d), data for the same subgroups of RLQs as in Figure 8 are shown along with the best-fit $\ell_x(\ell_{uv}, \ell_r)$ model for RLQs for comparison. The subgroups of RLQs do not deviate strongly from the trend for

RLQs in general in these coordinates, although the particularly radio and optically/UV luminous RLQs from the *Einstein* sample (along with a few high-redshift objects) are still excessively X-ray bright.

Joint 90% confidence ellipses (calculated after collapsing the third dimension for ease of viewing) for the various fits to this model are plotted in Figure 12. The full, primary, and *Einstein* samples are plotted in (12a) and (12b), as are the subgroups of RLQs with $R^* < 3$ and $R^* > 3$. The parameters for the primary sample of SDSS RIQs and RLQs are consistent with those of the full sample (not unexpected, since the primary sample makes up a majority of the full sample). There is no evidence of a statistically significant difference in the X-ray luminosity dependence of these subgroups upon optical/UV luminosity, but it appears possible that the $R^* < 3$ objects might have a larger b_{uv} coefficient (and perhaps a smaller c_{r} coefficient); this could be probed with a larger sample. The projected confidence ellipses all overlap in (12b), but it is possible that the *Einstein* RLQs have a stronger dependence of X-ray luminosity upon radio luminosity, as may those RLQs with $R^* > 3$ (a condition satisfied by many *Einstein* RLQs, so again this agreement is not surprising). The joint 90% confidence ellipses for the $\ell_{\text{x}}(\ell_{\text{uv}}, \ell_{\text{r}})$ model applied to subgroups of RLQs divided by radio luminosity and by radio spectral index are plotted in (12c) and (12d), along with the result for RLQs in general provided for comparison. Flat-spectrum RLQs are X-ray brighter than steep-spectrum RLQs due to a larger intercept, but have a consistent dependence of X-ray luminosity upon both optical/UV and radio luminosity. In contrast, RLQs with $\ell_{\text{r}} < 33.3$ and those with $\ell_{\text{r}} > 33.3$ share similar best-fit intercepts, but the more radio-luminous RLQs may have a greater/lesser dependence of X-ray emission upon $\ell_{\text{r}}/\ell_{\text{uv}}$.

4.5.2.2 A “radio-adjusted” $\ell_{\text{x}}(\ell_{\text{uv}})$ RLQ relation

We comment briefly on the possibility of utilizing the fits to X-ray luminosity as a joint function of optical/UV and radio luminosities to investigate whether, after accounting for the influence of jet-linked radio emission, the X-ray luminosity in RLQs is correlated with optical/UV luminosity through a similar relation to that which applies to RQQs (which could imply a consistent disk/coronal structure). This provides a simple test of whether RLQs can be treated as similar to RQQs but with an additional jet contribution to the X-ray luminosity. It seems that the best-fit models of $\ell_{\text{x}}(\ell_{\text{uv}}, \ell_{\text{r}})$ for RIQs do not contradict the possibility that the X-ray luminosity in RIQs is correlated with optical/UV luminosity as for RQQs, and may provide suggestive support for such a scenario (although the uncertainties in the fitted parameters for the RIQ relation are large).

One method of investigating a “radio-adjusted” $\ell_{\text{x}}(\ell_{\text{uv}})$ RLQ relation could be to set the radio luminosity in the best-fit $\ell_{\text{x}}(\ell_{\text{uv}}, \ell_{\text{r}})$ model to a value representative of RQQs (rather than that of the RLQs for which the fit was determined). This requires an accurate parameterization of $\ell_{\text{r}}(\ell_{\text{uv}})$ for RQQs, a difficult function to evaluate given the inherent radio weakness of RQQs. A simple model could have radio luminosity proportional to optical/UV luminosity as $\ell_{\text{r}} = \alpha + \beta \times \ell_{\text{uv}}$; in this case $\ell_{\text{x}}(\ell_{\text{uv}}, \ell_{\text{r}})$ would transform to $\ell_{\text{x}}(\ell_{\text{uv}})$ as (adding in the implicit luminosity normalizations) $\ell_{\text{x}} - 27 = a_0 + c_{\text{r}} \times (\alpha + 30.5\beta - 33.3) + (b_{\text{uv}} + c_{\text{r}}\beta) \times (\ell_{\text{uv}} - 30.5)$. White et al. (2007) present a

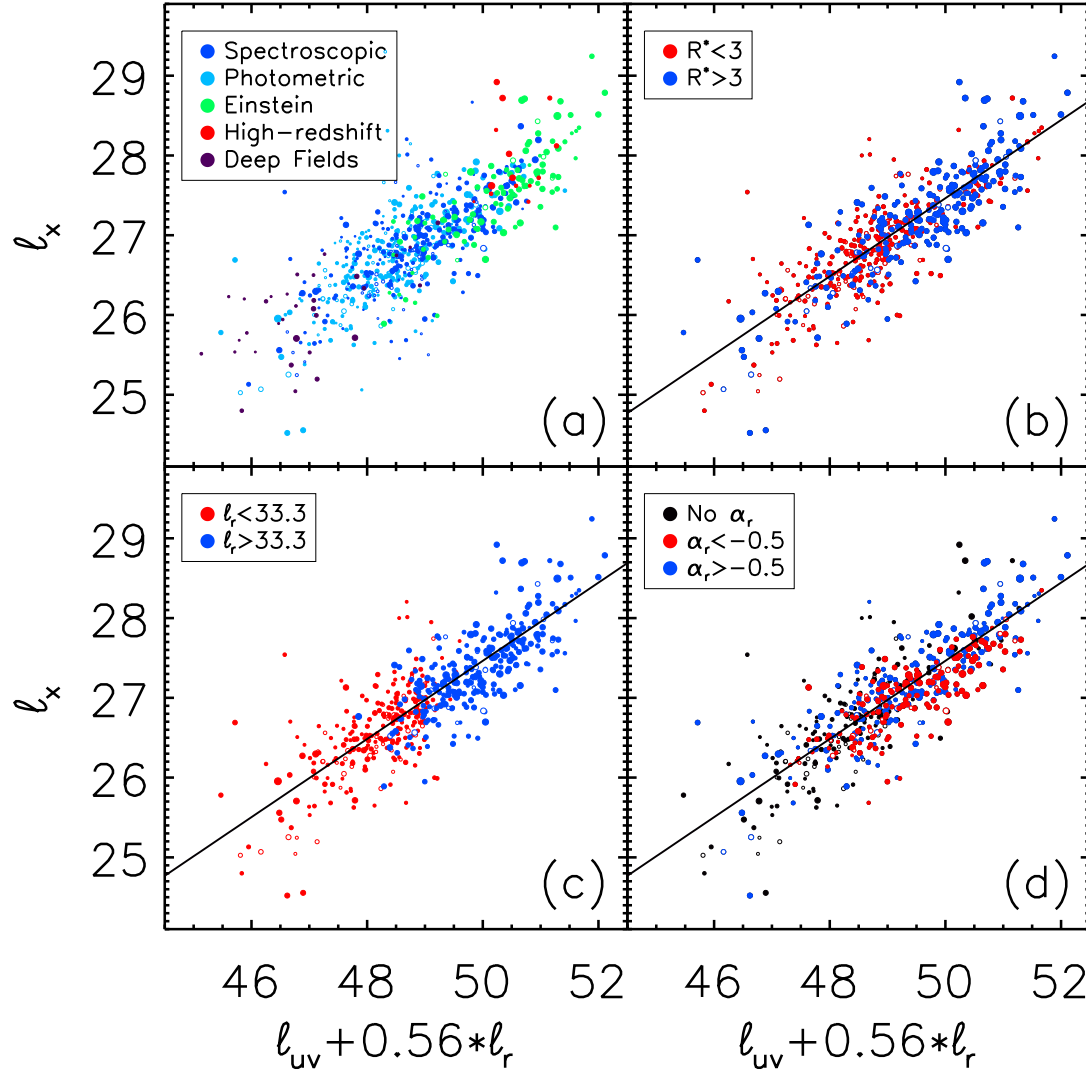


Fig. 4.11 X-ray luminosity as a joint function of optical/UV and radio luminosity for various sub-samples of RLQs. The model considered is $\ell_x = a_0 + b_{uv} \times \ell_{uv} + c_r \times \ell_r$ (where ℓ_x , ℓ_{uv} , and ℓ_r have been normalized prior to fitting as described in §5). Filled symbols are X-ray detections and larger symbols are more radio-loud throughout. The x-axis is based on the best-fit model for RLQs, for which $c_r = 0.56 \times b_{uv}$. The black solid line in panels (b), (c), and (d) is the best-fit model for RLQs.

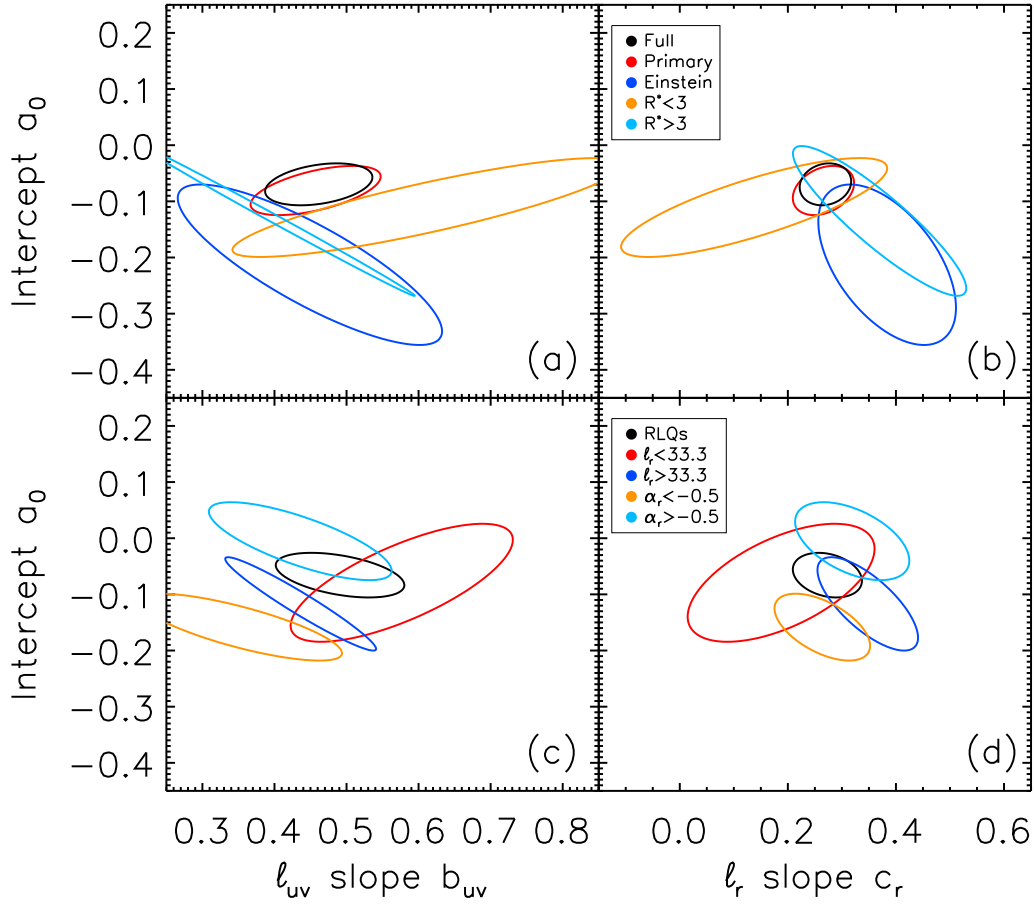


Fig. 4.12 Joint 90% confidence contours for fitting X-ray luminosity as a function of radio and optical/UV luminosity. The model considered is $\ell_x = a_0 + b_{uv} \times \ell_{uv} + c_r \times \ell_r$ (where ℓ_x , ℓ_{uv} , and ℓ_r have been normalized prior to fitting as described in §5). The legend in (b) also applies to (a) and the legend in (d) also applies to (c). See §5.2 for discussion.

correlation (their equation 2) that extends to low ($R^* < 1$) radio-loudness values and is equivalent¹¹ to $\alpha = 4.57$ and $\beta = 0.85$. Adopting these values of α and β , the RLQ fit of $\ell_x = -0.066 + 0.490\ell_{uv} + 0.273\ell_r$ becomes $\ell_x = -0.832 + 0.722\ell_{uv}$; this may be compared with the RQQ relation of $\ell_x = -0.545 + 0.649\ell_{uv}$ (all fitted coefficients from Table 6). The slope for RLQs in this adjusted relation is close to (although outside the 1σ errors) but slightly larger than that for RQQs. The difference in intercepts as compared to the RQQ relation may be reflective of greater beaming in the RLQs (although some RQQs may have a boosted component of radio emission; e.g., Miller et al. 1993; Falcke et al. 1996), in which case the RQQ relation ought to have the radio luminosity similarly enhanced prior to substitution and comparison. For illustrative purposes, accounting for an additional beaming enhancement of a factor of 11.2 (e.g., corresponding to an inclination of $\sim 5^\circ$ with $\gamma = 10.5$; see §6) would change the transformed RLQ intercept to -0.545 , matching the RQQ result. The transformed RLQ equations suggest a stronger dependence of X-ray luminosity on optical/UV luminosity than is observed for RQQs. It might be inferred from this result that the disk/corona in RLQs is more X-ray efficient at high optical/UV luminosities than in RQQs. However, we have not yet taken the likely beaming of some fraction of the X-ray emission in RLQs into account in these comparisons, and this can provide another mechanism for X-ray enhancement relative to RQQs. We demonstrate in §6 that the RLQ $\ell_x(\ell_{uv}, \ell_r)$ fit can be reproduced assuming a disk/coronal scaling as in RQQs plus a jet component; further discussion is deferred to that section.

4.5.3 $\ell_x(\ell_{uv}, \ell_r, z)$

4.5.3.1 Inclusion of redshift as a fit parameter

We now investigate whether there is a dependency upon redshift in addition to the dependencies upon optical/UV and radio luminosity by plotting the residuals for each best-fit model of $\ell_x(\ell_{uv}, \ell_r)$ against $\log(1+z)$ and against the lookback time divided by the total age of the Universe (standard cosmology; see §1). It can be seen in Figure 13 that there is no obvious dependence on either $\log(1+z)$ or lookback fraction. The only potential trend is a possible tendency for RLQs at high redshift to have positive residuals. However, this is not necessarily a redshift effect; in general, RLQs at higher redshifts are more luminous, and since the $\ell_x(\ell_{uv}, \ell_r)$ model appears to underpredict X-ray emission for particularly radio-loud or radio luminous RLQs (which also tend to be flat-spectrum sources), a modest trend toward positive residuals at high redshift does not require explicit redshift dependence. Additionally, recall from §2.2.2 that due to selection methodology several of the high-redshift sources are particularly radio-loud “blazars” (at presumed relatively low line-of-sight inclinations) for which more extreme X-ray luminosities might be expected regardless of redshift, possibly biasing the high-redshift subsample toward X-ray-bright objects.

Although the $\ell_x(\ell_{uv}, \ell_r)$ residuals do not show any obvious redshift dependence, it is in principle possible that some of the apparent luminosity dependence might actually

¹¹Note that their radio-loudness has been slightly adjusted as a function of optical luminosity relative to the definition used here.

be driven by redshift evolution. We test this possibility by including the redshift dependence as a parameter when modeling, by fitting $\ell_x(\ell_{uv}, \ell_r, z)$, where again the luminosities are normalized prior to fitting. The redshift dependence is put in terms of $\log(1+z)$ or lookback fraction. The best-fit model for the full sample is $\ell_x = (-0.125 \pm 0.056) + (0.440 \pm 0.039) \times \ell_{uv} + (0.272 \pm 0.022) \times \ell_r + (0.147 \pm 0.139) \times \log(1+z)$; when RLQs only are considered, the best-fit model is $\ell_x = (-0.148 \pm 0.058) + (0.462 \pm 0.047) \times \ell_{uv} + (0.278 \pm 0.031) \times \ell_r + (0.212 \pm 0.145) \times \log(1+z)$. In both cases the coefficient for the redshift term is only marginally non-zero ($< 1.5\sigma$), and the joint 90% and 68% confidence ellipses with the optical/UV and radio luminosity coefficients include zero (Figure 14). When the redshift dependence is expressed instead in terms of the fractional lookback time τ_z , the best-fit model for the full sample is $\ell_x = (-0.108 \pm 0.078) + (0.451 \pm 0.039) \times \ell_{uv} + (0.271 \pm 0.022) \times \ell_r + (0.060 \pm 0.121) \times \tau_z$; when RLQs only are considered, the best-fit model is $\ell_x = (-0.131 \pm 0.082) + (0.474 \pm 0.046) \times \ell_{uv} + (0.277 \pm 0.030) \times \ell_r + (0.101 \pm 0.124) \times \tau_z$. In both cases the difference between the coefficient for the redshift term and zero is not statistically significant, and the joint 90% and 68% confidence ellipses with the optical/UV and radio luminosity coefficients include zero (Figure 14). It appears that the high-redshift subsample (within which some objects possess extreme radio properties) exercises a strong influence over the best-fit redshift coefficient; when these 15 objects are removed and the remainder of the full sample is re-fit, the coefficients are $(0.001 \pm 0.144) \times \log(1+z)$ and $(-0.009 \pm 0.119) \times \tau_z$. It may also be worth noting that fitting the *Einstein* objects to the $\log(1+z)$ model suggests (1.8σ) non-zero redshift dependence, whereas the τ_z model does not ($< 1\sigma$); Worrall et al. (1987), using a different methodology than we do here, report no evidence for redshift dependence in their sample of *Einstein* RLQs, so perhaps the τ_z model is to be preferred. We mention for completeness that modeling the X-ray luminosity of some subgroups of RLQs as a function of optical/UV luminosity, radio luminosity, and redshift (as parameterized above), does yield non-zero coefficients (at 1σ confidence) for redshift dependence, but as we conduct such fits with several subgroups it is probable that some such results will arise solely from statistical chance.

We do not find support for a non-zero dependence upon redshift for the X-ray emission properties of the full sample or RLQs alone. The degree to which otherwise comparable RIQs or RLQs at different redshifts could differ in X-ray luminosity may be constrained via the value and 1σ errors on the best-fit coefficient to the redshift term. For the full sample, the coefficient of $(0.147 \pm 0.139) \times \log(1+z)$ suggests a maximum evolution (i.e., using $0.147+0.139$ for the coefficient) in X-ray luminosity between redshift $z=0$ and $z=5$ of $\ell_{x,z=0} - \ell_{x,z=5} = 0.223$, or a ratio in linear units of 1.67. This suggests that the X-ray luminosity of otherwise comparable RIQs or RLQs has not changed by more than 70% over $z=0-5$. For RLQs only, the coefficient of $(0.212 \pm 0.145) \times \log(1+z)$ suggests a maximum difference in X-ray luminosity between redshift $z=0$ and $z=5$ of $\ell_{x,z=0} - \ell_{x,z=5} = 0.278$, or a ratio in linear units of 1.90, corresponding to a change of $\lesssim 90\%$. Similarly, the coefficient of $(0.060 \pm 0.121) \times \tau_z$ suggests a maximum difference in X-ray luminosity between redshift $z=0$ and $z=5$ of $\ell_{x,z=0} - \ell_{x,z=5} = 0.166$, or a ratio in linear units of 1.46, corresponding to a change of $\lesssim 50\%$. For RLQs only, the coefficient of $(0.101 \pm 0.124) \times \tau_z$ suggests a maximum difference in X-ray luminosity between redshift $z=0$ and $z=5$ of $\ell_{x,z=0} - \ell_{x,z=5} = 0.206$, or a ratio in linear units

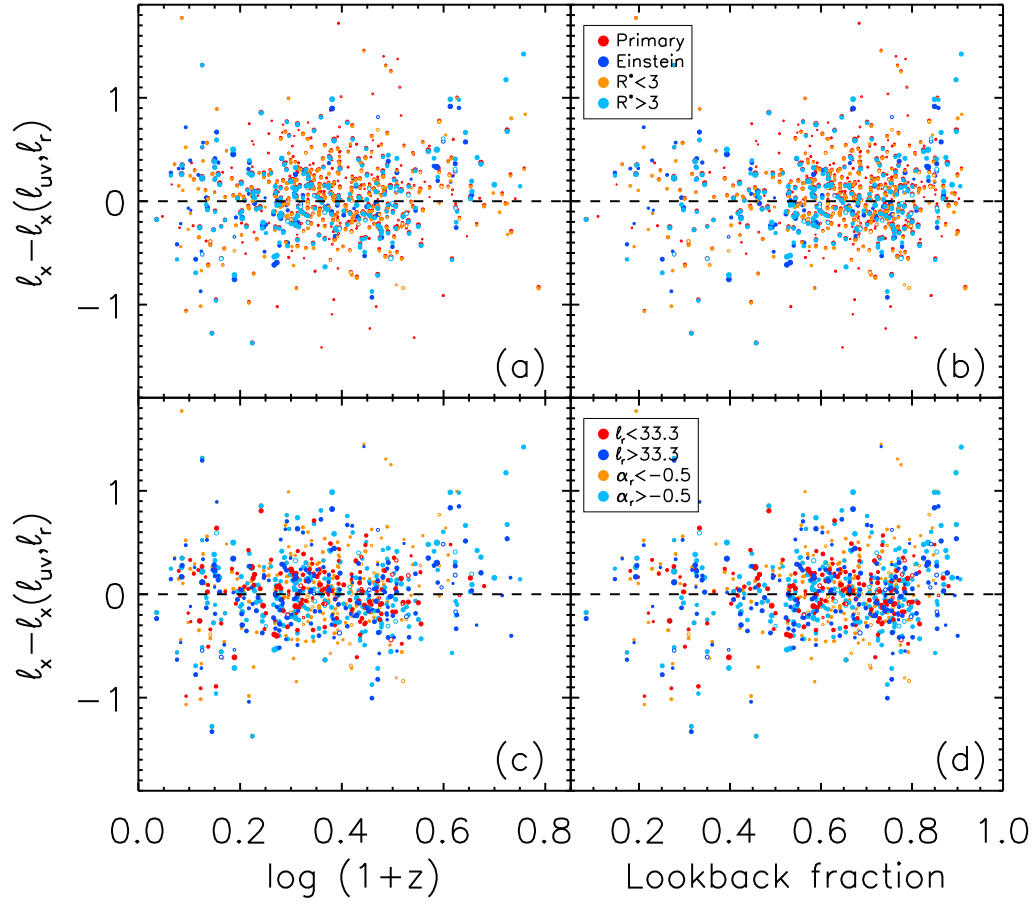


Fig. 4.13 Residuals for best-fit results for X-ray luminosity parameterized by optical/UV and radio luminosity, plotted against redshift and fractional lookback time. The legend in (b) also applies to (a) and the legend in (d) also applies to (c). A single object may be a member of two categories in a given panel, in which case the residual values from the separate fits to each category are each plotted at the redshift of that object. There is no apparent redshift dependence. See §5.3 for discussion.

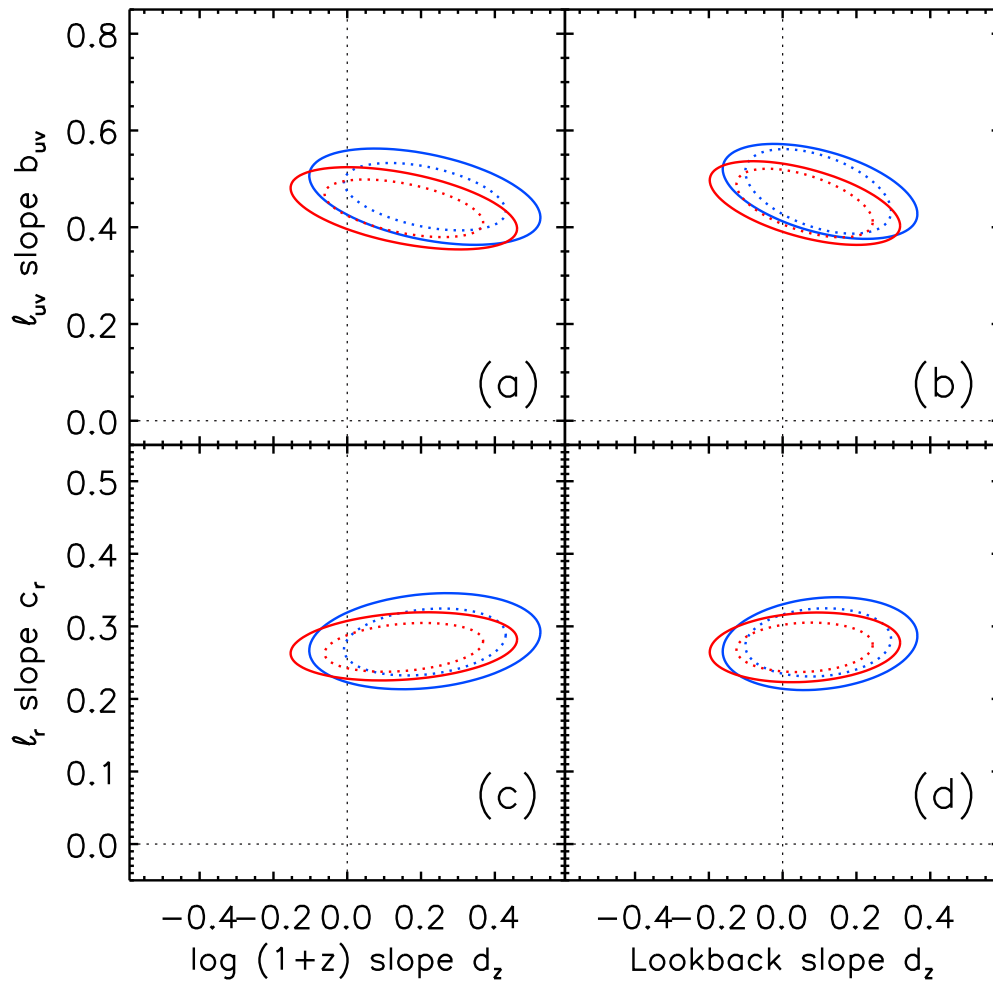


Fig. 4.14 Consideration of redshift dependence. The first model investigated is $\ell_x = a_0 + b_{uv} \times \ell_{uv} + c_r \times \ell_r + d_z \times \log(1+z)$ (where ℓ_x , ℓ_{uv} , and ℓ_r have been normalized prior to fitting as described in §5); the second model investigated replaces $\log(1+z)$ with the fractional lookback time $\tau(z)$. Joint 90% (solid) and 68% (dotted) confidence ellipses are plotted for the full sample (red) and for the sample of RLQs (blue). The difference between the coefficients for redshift dependence and zero is not statistically significant.

of 1.61, corresponding to a change of $\lesssim 60\%$. Although the fraction of quasars that are RLQs is dependent upon redshift (e.g., Jiang et al. 2007), the X-ray properties of individual RIQs and RLQs do not appear to differ strongly when comparing objects at low versus high redshift. Apparently the cosmic evolution in the efficiency of generating RLQs does not substantially impact RLQ structure post-formation.

4.5.3.2 Dependence of relative X-ray brightness on redshift

An alternative manner of visualizing the potential redshift dependence of the X-ray luminosity of RIQs and RLQs is to construct a multiwavelength color-color plot and group objects within separate redshift bins. Figure 15a shows α_{ox} plotted versus R^* for the full sample divided into low, medium, and high redshift ($z < 1$, $1 < z < 2$, and $z > 2$, respectively). Objects become increasingly X-ray bright (with less negative values of α_{ox}) as they become increasing radio-loud, as previously shown in Figure 7, but there is no obvious difference in this trend with redshift. Fitting $\alpha_{\text{ox}}(R^*)$ does suggest that the slope steepens slightly with redshift, but this is offset by a decreased intercept (Figure 15c; see also Figure 5 of Lopez et al. 2006). It is preferable to take the dependence of X-ray luminosity upon optical/UV luminosity into account when constructing the optical/UV-to-X-ray color. We calculate $\Delta\alpha_{\text{ox}}$ as $\alpha_{\text{ox}} - \alpha_{\text{ox}}(\ell_{\text{uv}})$, taking $\alpha_{\text{ox}}(\ell_{\text{uv}})$ from the Just et al. (2007) relation for $\ell_{\text{x}}(\ell_{\text{uv}})$ for RQQs (see also discussion in §4 and §6). Figure 15b shows $\Delta\alpha_{\text{ox}}$ plotted versus R^* for the full sample grouped into low, medium, and high redshift bins. There is no obvious stratification by redshift, but here fitting $\Delta\alpha_{\text{ox}}(R^*)$ suggests that the slight increase in slope with increasing redshift may result in a slight increase in relative X-ray brightness, at least for RLQs with $R^* > 2$ (Figure 15d). The results of this fitting are given in Table 7.

Although we are now explicitly considering radio-loudness as a parameter, there still may be a disproportionate number of objects in the high-redshift bin with low line-of-sight inclinations, preventing the definitive association of a slight increase in relative X-ray brightness with redshift alone. Nevertheless, we can rule out any dramatic change with redshift in the $\Delta\alpha_{\text{ox}}(R^*)$ relation, which is itself useful. For example, it has been suggested that X-ray jets for which inverse Compton scattering of cosmic microwave background photons (IC/CMB; e.g., Tavecchio et al. 2000) provides the dominant emission component should come to dominate over RLQ cores at high redshift (e.g., Rees & Setti 1968; Schwarz 2002). We estimate the enhancement in X-ray luminosity from this process for sources at redshifts of 0.67/1.43/2.49 (the medians within the low/medium/high groupings) and for a jet-linked fraction of the total X-ray emission (prior to accounting for the redshift dependence of IC/CMB X-ray emission) of 1%, 10%, and 99%; the results are plotted (in increasing order of jet dominance) at radio-loudness values¹² of 1.5, 3, and 4.5 in Figure 14d. It can be seen that the $(1+z)^4$ dependence of X-ray jet-linked IC/CMB emission would lead for these parameters to a stronger splitting with redshift than is observed. We find that the X-ray luminosities within our sample of RIQs and RLQs are unlikely to include significant contributions from X-ray IC/CMB

¹²These R^* values increase with increasing jet dominance, as is qualitatively expected, but the precise numerical association between R^* and X-ray jet dominance is model-dependent (as explored in §6.3) and so the chosen R^* values should be regarded as illustrative.

jet emission. In principle it is possible that extremely bright X-ray jet features could be routinely found outside of the extraction regions we use to measure the X-ray luminosity, but to the best of our knowledge such sources are extremely rare. This is consistent with the general lack of observed high-redshift RLQs in which the X-ray jet outshines the core (e.g., Bassett et al. 2004; Lopez et al. 2006).

4.5.4 Additional considerations

We briefly examine four additional topics relevant to the analysis of luminosity correlations: the impact of the selection method, the influence of targeted sources, the normality of the variables, and the potential for spurious or inaccurate results due to luminosity dispersion effects.

4.5.4.1 Optical versus radio selection

As discussed in §2.1.1, the median properties of a quasi-radio-selected sample of RIQs and RLQs (constructed from SDSS spectroscopic quasars by requiring the “FIRST” target flag to be set) are similar to those of “QSO/HIZ” targeted SDSS spectroscopic quasars (with substantial overlap between these samples). The dependence of X-ray luminosity upon optical/UV and radio luminosities is also similar for the “FIRST” and for the “QSO/HIZ” samples, as may be seen from the best-fit relations given in Table 6. Joint 90% and 68% confidence contours from fitting the “FIRST” and the “QSO/HIZ” samples to $\ell_x = a_0 + b_{uv} \times \ell_{uv} + c_r \times \ell_r$ are provided in Figure 16, where it can be seen that the parameter values are consistent. By excluding the small fraction of objects with $\Delta(g - i) > 1$ we omit strongly dust-reddened RLQs, which may be associated with young quasars (e.g., Urrutia et al. 2008, 2009). Within the relative color range we accept, there does not appear to be a difference in the X-ray properties of SDSS RIQs and RLQs selected by color compared to those selected due to radio emission. Presumably the X-ray emission mechanisms are likewise similar, and so the results from §5 and the modeling in §6 are generally applicable.

4.5.4.2 Influence of targeted objects

Only 16% of RIQs and RLQs within the primary sample were targeted for X-ray observations (§3.4) and inclusion of these sources does not bias the results of the luminosity correlation analysis, although there are some minor differences in the properties of targeted and off-axis objects. Compared to those objects observed serendipitously, the targeted RIQs and RLQs are at somewhat lower redshifts (median z of 1.03 versus 1.47) but are also brighter (median m_i of 17.94 versus 19.63) and so have modestly higher optical/UV luminosities (median ℓ_{uv} of 30.67 versus 30.34). The targeted RIQs and RLQs are also somewhat more radio-loud (median R^* of 3.09 versus 2.43) and $\sim 15\%$ X-ray brighter relative to optical/UV luminosity (median $\ell_x - \ell_{x,RQQ}$ of 0.46 versus 0.40, with $\ell_x - \ell_{x,RQQ}$ as defined in §4). The results of fitting off-axis objects are consistent with those obtained for the full and primary samples for both the $\ell_x(\ell_{uv})$ and $\ell_x(\ell_{uv}, \ell_r)$ models. The best-fit parameters for the slopes (b_{uv} , c_r) for the off-axis sample have 1σ intervals that overlap those of the full and primary samples. Fitting the targeted objects

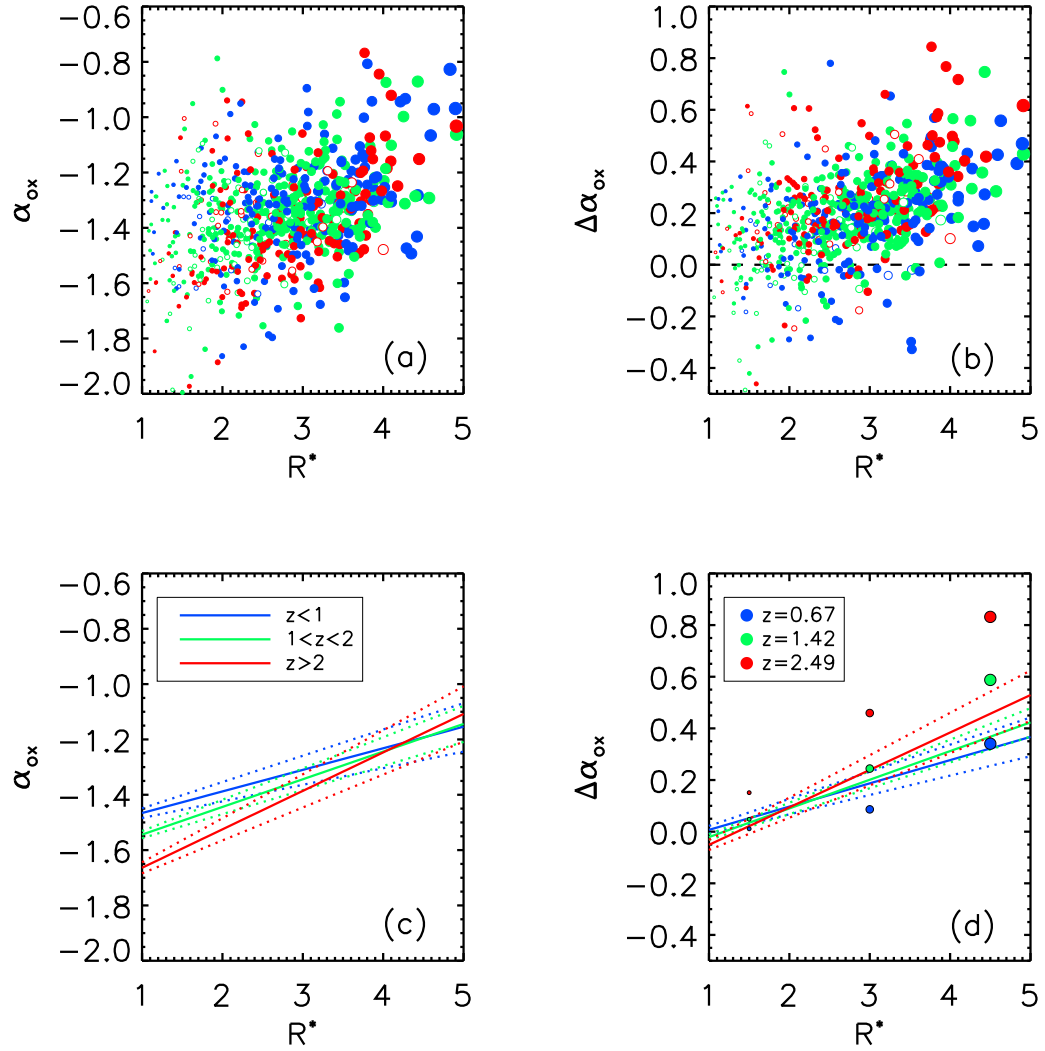


Fig. 4.15 Consideration of relative X-ray brightness as a function of radio-loudness. The full sample of RIQs and RLQs is shown in (a) for $\alpha_{\text{ox}}(R^*)$ and in (b) for $\Delta\alpha_{\text{ox}}(R^*)$, with blue, green, and red colors indicating low, medium, or high redshift ($z < 1$, $1 < z < 2$, and $z > 2$, respectively). Best-fit trend lines are shown in (c) and (d) with the 1σ errors on the slopes indicated by dashed lines. The expected enhancement in X-ray brightness from the $(1+z)^4$ dependence of IC/CMB jet-linked X-ray emission is also plotted in (d) for comparison; the set of points at $R^*=1.5, 3$, and 4.5 correspond to models in which the jet-linked fraction of the X-ray continuum (prior to considering redshift) is 1%, 10%, and 99%, respectively.

separately produces 1σ intervals for b_{uv} that do not overlap those of the full or primary samples; the targeted objects have a weaker dependence of X-ray luminosity upon optical/UV luminosity. The best-fit parameter for c_{r} is consistent with the results for the full and primary samples, indicating the targeted objects have a similar dependence of X-ray luminosity upon radio luminosity.

4.5.4.3 Log-normality of residuals

A presumption that considered variables are normally distributed at a given value is inherent in the chosen method of analysis (and indeed in most parametric modeling), and can be checked by examining the residuals from the best-fit models for X-ray luminosity in our sample of optically-selected RIQs and RLQs. However, it is not clear *a priori* that the RIQs and RLQs considered here ought to show normally-distributed residual X-ray luminosity (in logarithmic units), since there are distinct X-ray emission mechanisms for RIQs and RLQs (disk/corona and jet-linked) as opposed to a single dominant X-ray emission mechanism (disk/corona) in RQQs. Histograms of the residual X-ray luminosity for RIQs and RLQs, RLQs alone, and RQQs are provided in Figure 17, along with best-fit Gaussians computed for detections only and also for limits treated as detections. There is a tail of X-ray weak objects within the RQQ sample (17c), some of which might be low-redshift BAL RQQs. The sample of RIQs and RLQs (17a) also shows an X-ray weak tail, but this tail is less prominent among RLQs (17b). These may again be BAL objects, which decrease in percentage as radio-loudness increases (e.g., Shankar et al. 2008). However, in contrast to the situation for RQQs, there is also an X-ray bright tail for RIQs and RLQs. These X-ray bright objects are generally members of the set of particularly radio-loud or radio-luminous RLQs, and hence may be jet-dominated at X-ray frequencies. Unfortunately the presence of limits in our sample makes it difficult to utilize standard tests for normality. An Anderson-Darling test applied to detected objects suggests that all three distributions are not inconsistent (at the 95% level) with a normal distribution, with the RLQ sample apparently closest to normality (this may be reflective of relatively fewer X-ray weak RLQ outliers); while this is best regarded as suggestive rather than conclusive, it does indicate that our methodology is unlikely to produce biased results due to underlying non-normality.

4.5.4.4 Robustness of luminosity correlations

The degree of inherent scatter in the luminosities can affect the results of correlation studies. For example, Yuan et al. (1998) demonstrated that when the optical/UV luminosity scatter σ_{uv} is significantly larger than the X-ray luminosity scatter σ_{x} , a fit to $\alpha_{\text{ox}}(\ell_{\text{uv}})$ over a limited range of ℓ_{uv} can indicate an anti-correlation where none necessarily exists. Relatedly, $\sigma_{\text{uv}} \gg \sigma_{\text{x}}$ can give a fitted slope for the $\ell_{\text{x}}(\ell_{\text{uv}})$ relation less than unity even if these luminosities are actually proportional (when the considered luminosity ranges are small). Since our sample of RIQs and RLQs has $\sigma_{\text{uv}} \simeq \sigma_{\text{x}}$ (both are 0.59 for the primary sample), this issue is unlikely to skew our best-fit results. In general, examined luminosity correlations are significantly less likely to yield spurious or inaccurate results with a sample spanning a large range in luminosities (e.g., see discussion in §5 of Just et al. 2007) relative to the observed dispersion, as does our sample. For radio,

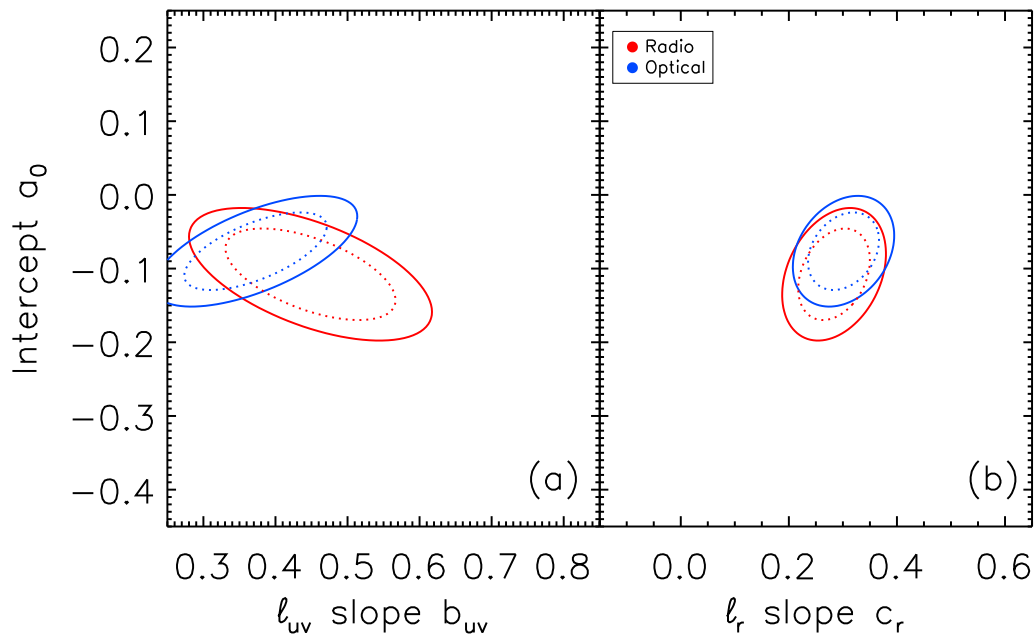


Fig. 4.16 Comparison of a quasi-radio-selected (red ellipses) sample of RIQs and RLQs to an optically-selected (blue ellipses) sample (both drawn from SDSS/FIRST data), illustrated with joint 90% (solid) and 68% (dotted) confidence ellipses for the model $\ell_x = a_0 + b_{uv} \times \ell_{uv} + c_r \times \ell_r$. The axes are scaled to match Figure 12. The RIQs and RLQs targeted by SDSS as FIRST sources do not have properties inconsistent with those targeted due to optical colors, and indeed the overlap between the two subgroups is substantial ($\gtrsim 80\%$).

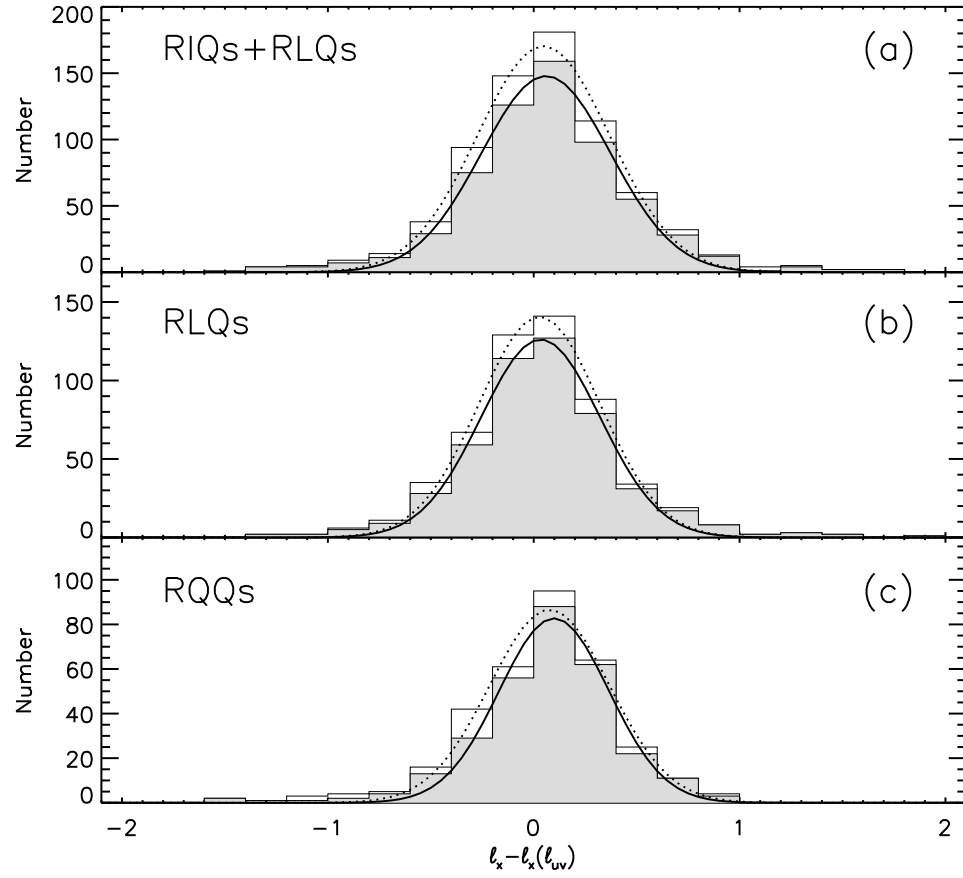


Fig. 4.17 Evaluation of normality for residuals from fitting X-ray luminosity as a joint function of optical/UV and radio luminosity (RIQs and RLQs, top panel; RLQs, middle panel; fits from Table 6) and as a sole function of optical/UV luminosity (RQQs, bottom panel; data from Steffen et al. 2006). The open histograms include limits and are fit with Gaussians as indicated by the dotted curves, while the filled histograms are detections only and are fit with Gaussians as indicated by the solid curves.

optical/UV, and X-ray luminosities, the range from the 5th to the 95th percentiles is greater than three¹³ times larger than the dispersion, for both the full and the primary sample. Additionally, since much of our analysis is concerned with comparing the results of (similarly conducted) fits to different groupings of RIQs and RLQs, any systematic skewing of correlations would not impact our conclusions regarding the relative differences in how X-ray luminosity is dependent on optical/UV and radio luminosities within these subgroups.

4.6 A physical model for X-ray emission in RIQs and RLQs

It is of interest to evaluate the physical basis for the correlations discussed in §5. It is widely theorized that the increasing X-ray brightness of RIQs and RLQs with increasing radio loudness or luminosity is driven by a source of nuclear X-ray emission that is directly or indirectly powered by the radio jet (e.g., see discussion in §1), but the precise nature of this linkage is not clearly understood. We make use of previous results from the literature to simulate a population of RIQs and RLQs with radio and optical properties consistent with observations, and then test competing models for the X-ray emission through comparing the properties of the simulated data sets to observations. The structure and parameters of this modeling are given in Table 8.

We adopt a physical model that contains emission contributions from the core and lobes at radio frequencies (with the core presumed to be dominated by the small-scale radio jet), from the disk and small-scale jet at optical/UV frequencies, and from the disk/corona and an additional “jet-linked” component at X-ray frequencies. Most of the parameters for the radio and optical emission components in this model are fixed by prior work; likely values for a few free parameters were determined through comparison to our sample data. The X-ray disk/corona emission is presumed to scale with the optical/UV disk emission as established for RQQs, as seems reasonable based on the results of §4 and §5.

We consider three possibilities for the X-ray jet-linked emission: in model A, the X-ray jet-linked emission is proportional to the intrinsic radio-jet emission (prior to applying beaming) and is also itself unbeamed; in model B, the X-ray jet-linked emission shares the beaming factor δ that applies to the radio-jet emission; in model C, the X-ray jet-linked emission has a lower bulk Lorentz factor γ_x (and thus a lower beaming factor δ_x at low inclinations) than the radio-jet emission. The models A, B, and C correspond in a general sense to cases in which the jet-linked X-ray emission originates in an additional accretion flow structure, or cospatially with the radio-jet emission, or within the small-scale jet but predominantly in a less-relativistic region, respectively. Note that we are not attempting to “fit” the X-ray emission uniquely (such an approach is unproductive with these data) but are rather concerned with critically examining different plausible and representative physical scenarios and describing the consequent implications including,

¹³Values are $\sigma_r/\sigma_{uv}/\sigma_x = 1.10/0.70/0.69$ and $0.90/0.59/0.59$ for the full and primary samples, with 5th–95th percentiles of 31.38–34.96/29.28–31.60/25.76–27.98 and 31.45–34.57/29.38–31.26/25.79–27.77 for $\ell_r/\ell_{uv}/\ell_x$. These yield ratios of the radio/UV/X-ray luminosity range to the dispersion of 3.25/3.31/3.22 and 3.47/3.19/3.36 for the full and primary samples, respectively.

for example, the implied fraction of RIQs and RLQs for which the X-ray emission is jet-dominated.

In this section, we first describe the various components of the basic model, then match the simulated luminosities to the observed primary sample data, and then consider additional observational constraints upon the models and determine the dominant source of X-ray emission in each case.

4.6.1 The model components

4.6.1.1 Radio emission: core and lobes

We follow the general unification scheme described by Jackson & Wall (1999), in which FR I and low-excitation emission-line FR II radio galaxies are the parent population of BL Lacs, while high-excitation emission-line FR II radio galaxies are the parent population of RLQs, but update the beaming model and luminosity function to reflect more recent consensus. The radio source population is presumed to be described by the luminosity function presented by Willott et al. (2001), which is based on low-frequency (151 MHz and 178 MHz) data and is thus relatively unbiased toward beaming, and is computed at luminosities sufficiently high that contamination from star-forming galaxies is negligible. The simulated objects include radio galaxies and quasars; we select for the latter simply by requiring the inclination to be $\theta < 60^\circ$ (we also require $\theta > 5^\circ$ to remove highly beamed objects, which our sample attempts to exclude). A sample of RIQs and RLQs is synthesized with redshift and luminosity distributions drawn from the luminosity function, and with randomly assigned orientations (uniform in $\sin \theta$). The intrinsic core prominence (the ratio of core-to-lobe radio flux at low frequencies; i.e., unaffected by beaming) is taken from the Bayesian modeling of FR II sources carried out by Mullin & Hardcastle (2009) and is simulated including intrinsic scatter in core power based on their best-fit model; we also take the typical bulk Lorentz factor $\gamma = 10.5$ for core emission from their work. The parameters we adopt are those from Table 5 of Mullin & Hardcastle (2009) for the model excluding low-excitation emission-line objects.

The observed radio characteristics for a given simulated source are calculated for the inclination of that source. The core emission from the small-scale jet is boosted by $\delta^{2-\alpha_r}$ where $\delta = \gamma^{-1}(1 - \beta \cos \theta)^{-1}$ (e.g., Worrall & Birkinshaw 2006). The 1.4 GHz flux densities for the lobes and core of each simulated source are determined assuming $\alpha_r = -1$ for lobe emission and $\alpha_r = -0.5$ for core emission (consistent with the methodology used in §3.2 to calculate ℓ_r for the sample sources from the observed FIRST flux densities). A limit of 1 mJy was imposed to match the FIRST catalog detection limit, and components with simulated flux densities below this limit were dropped from further consideration.

4.6.1.2 Disk-dominated optical/UV emission

Optical emission from RLQs can be generated by quasi-thermal emission from the accretion disk and by nonthermal (e.g., synchrotron) emission from the small-scale jet. In our sample, the equivalent widths of the broad emission lines limit the degree to which a featureless jet-linked component can contribute to the optical/UV emission.

However, it is not possible in practice to determine simply the fraction of optical/UV emission that is disk-linked in individual objects from either the optical/UV spectra¹⁴ or from the radio multifrequency data.¹⁵ The observational indications that disk emission remains dominant in broad-line RIQs and RLQs therefore guide our models but do not provide sufficient motivation to fix simply the fraction of optical/UV emission that is disk-linked.

We estimate the jet-linked optical/UV component from the jet radio emission presuming $\alpha_{\text{ro}} = -0.8$, reflective of the tendency for the synchrotron spectrum of jet emission to steepen at higher frequencies. The disk-linked component is dependent upon physical processes not directly incorporated into our modeling (most notably the accretion rate); fortunately, there are radio characteristics which are thought to be likewise sensitive to such processes, and so it is possible to estimate the optical disk luminosity from the already-modeled radio properties. In particular, Willott et al. (1999) find a correlation between low-frequency radio power and narrow-line emission in radio galaxies which they argue indicates an underlying dependence upon accretion rate (to feed the jet and furnish sufficient ionizing photons incident upon the narrow line region; Willott et al. 1999 also comment that direct illumination from the jet or jet-cloud collisions are generally of secondary importance but are relevant in some individual objects). Motivated by such relationships, we set the disk to have a monochromatic luminosity at rest-frame 2500 Å that is a fixed fraction of the intrinsic (unbeamed) jet monochromatic luminosity at rest-frame 5 GHz (a log offset of -1.7 , or a fraction of 2%, provides a reasonable match to the data). The correlation between low-frequency radio power and narrow-line emission observed by Willott et al. (1999) has a 1σ scatter of 0.5 dex; we introduce into the model a similar spread in disk optical/UV emission at a given intrinsic jet luminosity by adding random normal scatter with $\sigma = 0.5$ dex to the disk optical/UV emission. We emphasize that this methodology is not reflective of a direct physical link between jet and disk emission but rather captures the influence of additional processes, particularly the accretion rate, on both jet and disk emission.

For most of the simulated sources the disk emission dominates over that from the jet at optical/UV wavelengths (by factors of a few to several hundred), and it is only for particularly low-inclination objects that the jet emission contributes significantly to the optical/UV emission. This is consistent with the observed optical/UV spectra for our sample RIQs and RLQs.

4.6.1.3 Dual X-ray emission components

Chandra and *XMM-Newton* observations of FR II radio galaxies show that their X-ray spectra often contain two components, which can be interpreted as emission from

¹⁴Such an approach would have to account for the known trends in emission-line strength with luminosity (Baldwin effects; e.g., Baldwin 1977; Osmer & Shields 1999) that occur even absent optical jet emission, but there is still significant scatter in broad line strength between otherwise similar objects and so the accuracy of this method is fundamentally limited.

¹⁵In principle, the observed radio core flux could be extrapolated to the optical/UV band using the measured radio spectral index. However, even ignoring the uncertainty in the spectral index, any intervening spectral break (which is not uncommon, even in a simple synchrotron context) essentially destroys the accuracy of the extrapolation.

both a disk/corona and a jet-linked component (e.g., Evans et al. 2006). The X-ray spectra of powerful RLQs, on the other hand, can typically be fit with a single power-law model; this suggests they are dominated by jet emission, generally inferred to be inverse Compton radiation (e.g., Belsole et al. 2006). Guided by prior work and the results discussed in §4 and §5, we include in our model X-ray emission from a disk/corona as operates in RQQs, and also from the small-scale jet. Our sample includes objects of modest radio loudness and luminosity; since these observed properties are dependent on intrinsic power but also viewing angle, we expect our sample to include objects at inclinations intermediate between radio galaxies and luminous RLQs, allowing us to investigate in our simulations the increasing jet contribution to the X-ray continuum as inclination decreases (with scatter reflective of intrinsic variance in unbeamed radio core luminosities).

We assume the X-ray emission associated with the disk/corona is related to the optical disk emission in the same manner as for RQQs and can therefore be calculated using the results of Steffen et al. (2006) and the simulated optical/UV disk emission. Random normal scatter with $\sigma = 0.25$ dex is added to the disk/coronal X-ray luminosities to mimic the scatter in the RQQ relation. While the details of the accretion structure in typical RLQs may not precisely match those of RQQs (due to the impact of the jet, and are possibly also affected by the generally greater mass and perhaps spin rate of the central supermassive black hole in RLQs; see discussion in §1), it seems reasonable to postulate that a given optical/UV disk emission should produce roughly comparable X-ray emission in RLQs as in RQQs. In any event, it is not possible to leave both the disk/corona and jet-linked X-ray emission as simultaneously free parameters in the absence of additional observational input (such as high-quality X-ray spectra) that most of our sources lack.

The jet-linked¹⁶ X-ray emission cannot be synchrotron emission from the same population of electrons as generates the radio-jet emission (in contrast to the apparent situation for lower power FR I jets; e.g., Chiaberge et al. 2000), as this process does not generate sufficient X-ray emission to match observations. Inverse Compton processes must be considered; sources of seed photons include emission from the jet (self-Compton, or SSC), radiation from the central engine (external Compton, or EC), and the cosmic microwave background (IC/CMB). The IC/CMB model has a strong dependence upon redshift, which conflicts with the lack of redshift dependence observed in our sample (see §5.3), and in any case is unlikely to produce as many seed photons as can the nucleus on the relevant parsec-scale or smaller distances (e.g., Schwartz 2002). Comparison of the SSC and EC processes suggests the latter dominates this close to the central engine (e.g., Sokolov & Marscher 2005).

The precise physical parameters governing X-ray jet emission (such as the size of the emission region or the magnetic-field strength) likely vary significantly from object to object. Since we are interested in general trends rather than the specific details of a given source, we assume some “standard” intrinsic ratio between radio and X-ray jet-linked

¹⁶The use of the term “jet-linked” with respect to model A should be understood to refer to the correlation between X-ray and intrinsic (unbeamed) radio-jet emission; it is possible but not required that this X-ray component is produced in a jet.

emission, which we set to obtain consistency with the observed primary sample X-ray luminosities. The intrinsic jet-linked X-ray emission is then modified in models B and C for the observer based on the bulk velocity and inclination of the jet, with presumed dominant EC emission boosted by $\delta^{3-2\alpha_x}$ (an additional factor of $1 - \alpha$ beyond the radio synchrotron emission; e.g., Dermer 1995), with $\alpha_x = -0.5$ taken to match the typical energy index of RLQs (e.g., Page et al. 2005). X-ray censoring is added to the simulated sample in quasi-random fashion, with fainter objects more likely to be labeled as upper limits. For simplicity, this is accomplished through randomly selecting 88%/76% of objects with simulated $\ell_x > 26.8 / < 26.8$ as detections; the simulated detection rate matches that of the primary sample overall and within each X-ray luminosity bin.

4.6.2 Comparison to observed luminosities

In principle, this modeling process will produce a simulated population of RIQs and RLQs that can be directly compared to the observed primary sample data. However, the nature of our sample introduces a few complicating effects that need to be considered. One important parameter is the limiting magnitude for inclusion within the primary sample. Since we prefer to retain as many observed objects as possible, we do not impose a magnitude limit on the observed objects. However, only 7.5% of the primary sample RIQs and RLQs have $m_i > 20.7$, and so this is used as an effective magnitude cutoff for the simulations.

The normalization (i.e., number of objects) of the simulated population should be able to be set solely based on the sky coverage fraction of the observed sample, but this is difficult to evaluate for the various X-ray missions and their complex instrumental fields of view. Matched total numbers of simulated and sample objects are not critical for conducting a comparison (it is the distribution of luminosities that is of interest); nonetheless, it is convenient for examining the results of the simulations if the simulated population is of the same size as the observed sample. Since we are interested in how X-ray luminosity is related to radio and optical/UV luminosities and unconcerned with the sky density of (selected) RIQs and RLQs, we simulate a large population and then draw from it to obtain an equal number of simulated and observed objects.

Another relevant effect is the redshift-dependent efficiency of the SDSS color-selection targeting algorithm and of the photometric quasar classification algorithm. The median redshift of the simulated population is 1.80, higher than that of the observed primary sample (for which the median redshift is 1.41). Although the redshift dependencies of quasar color-selection techniques presumably explain most of the discrepancy between the observed and simulated median redshifts, there are a few more factors that could act to decrease the median redshift of the observed primary sample. For example, there is a bias toward lower redshifts for the minority of sources that were X-ray targeted (rather than serendipitous) and a possible bias against spectroscopic identification of fainter objects for which measuring broad emission lines is more difficult. Fortunately, our goal of evaluating X-ray luminosity as a function of radio and optical/UV luminosity does not depend on redshift (e.g., see §5.3), and so it is not necessary to account for all the various selection effects that may influence the difference in redshift distribution. We match in redshift and number simultaneously by drawing from the large simulated

population those objects with redshifts most nearly equal to the observed sample. Note that the underlying basic model could be falsified at this stage were the simulated radio luminosities (specified primarily by the adopted luminosity function, the adopted intrinsic jet/lobe properties, and the random inclination) to disagree with observation. However, a Kolmogorov-Smirnov (KS) test gives a probability of $p = 0.26$, indicating that the simulated and observed samples cannot be considered to differ significantly in their radio luminosity distributions. The median radio luminosity for the primary sample is $\ell_r = 32.81$ with a standard deviation of 0.90, while that of the simulated sample is $\ell_r = 32.84$ with a standard deviation of 0.91. It would also be possible at this stage to falsify the nature of the presumed correlation between intrinsic radio jet power and optical/UV disk luminosity if the distribution of simulated optical/UV luminosities were to disagree with observation (the median can always be made to agree by adjusting the ratio, but the distribution reflects the lack of beaming in the optical/UV luminosities, in contrast to the radio). However, a KS test gives a probability of $p = 0.20$, indicating that the simulated and observed samples cannot be considered to differ significantly in their optical/UV luminosity distributions. The median optical/UV luminosity for the primary sample is $\ell_{uv} = 30.36$ with a standard deviation of 0.59, while that of the simulated sample is $\ell_{uv} = 30.34$ with a standard deviation of 0.66. The radio-loudness distributions are also not inconsistent (KS probability 0.14) with observed/simulated median values of 2.50/2.52 and standard deviations of 0.76/0.75. These radio and optical/UV properties are the same for each of models A, B, and C.

For any of models A, B, or C to constitute viable descriptions of the X-ray emission from RIQs and RLQs, it is necessary (but not sufficient) that the distribution of simulated X-ray luminosities not disagree with observation. The X-ray disk/corona emission is completely specified by the optical/UV disk emission, and so it is the additional “jet-linked” X-ray emission that must be accurately modeled. The median value of the overall simulated X-ray luminosity can always be made to agree with observations by adjusting the ratio between the jet-linked X-ray component and the intrinsic radio-jet luminosity, but the distribution is governed by the degree to which the jet-linked emission is beamed (as well as the scatter in the disk/corona X-ray emission, but this is fixed based on the Steffen et al. 2006 observations of RQQs). The log offsets between intrinsic radio-jet luminosity (prior to applying beaming) and intrinsic X-ray luminosity of the jet-linked component (prior to applying beaming to models B and C) required to match simulated with observed median X-ray luminosities are -5.0 , -7.4 , and -7.2 . The X-ray bulk Lorentz factor in model C is $\gamma_x = 2.5$; for reference, this corresponds to $\delta_x = 4.6$ for an inclination of $\theta = 5^\circ$ (rather than $\delta = 11.4$ as with the $\gamma = 10.5$ that applies to the radio jet). For model C, X-ray bulk Lorentz factors of $\gamma_x = 2 - 3$ can equally well match the primary sample X-ray luminosity distributions, but as shown in §6.3, $\gamma_x = 2.5$ produces the best agreement to the observed $\ell_x(\ell_{uv}, \ell_r)$ relation. KS tests (treating upper limits as detections, but the simulated censoring matches the data) give probabilities of $p = 0.36$ and $p = 0.59$ for models A and C, respectively, indicating that the simulated and observed samples cannot be considered to differ significantly in their X-ray luminosity distribution for these models. However, the KS test probability for model B is $p = 7.5 \times 10^{-5}$; the simulated distribution of X-ray luminosities differs significantly from that observed. In particular, a tail to large X-ray luminosity values in the simulated population for model

B does not agree with the data, which appear to show at most a modest skew toward higher X-ray luminosities (see also §5.4). This tail in the model is more pronounced at X-ray than radio frequencies because the dependence upon the δ beaming factor is greater (by $1 - \alpha$ in the exponent) for the X-ray emission. These results may be seen in the left-hand panels of Figure 18.

All three models obviously produce (by design) enhanced X-ray emission relative to RQQs of comparable optical/UV luminosity, as can be seen in the right-hand panels of Figure 18 and as given in Table 9. However, the manner in which they do so differs. In these figures the simulated objects are color-coded by inclination (blue for $5^\circ < \theta < 10^\circ$, green for $10^\circ < \theta < 20^\circ$, and red for $20^\circ < \theta < 60^\circ$). For model A, there is essentially no inclination dependence to the X-ray excess, since the X-ray luminosity is unbeamed. For model B, there is a strong inclination dependence, with the lowest inclination RLQs being extremely X-ray bright (to a degree that does not match observations). Note that these simulated low-inclination objects are still expected to be disk-dominated at optical/UV frequencies (as also applies to models A and C) and are thus not blazars, so the comparison to the observed primary sample (from which all identified blazars have been removed) is properly matched. For model C, there is a definite but modest dependence upon inclination. Simultaneous consideration of the distribution of radio, optical/UV, and X-ray luminosities, following the analysis performed in §4 and §5 for observed RIQs and RLQs, provides additional insight helpful to evaluating the feasibility of the three models.

4.6.3 Modeling results

We first examine how the “excess” X-ray luminosity (X-ray luminosity less that of a RQQ of matched optical/UV luminosity) for the simulated RIQs and RLQs depends upon radio luminosity for the three models. In Figure 19, left-hand side, the simulated objects are again color-coded by inclination, and the primary sample data are plotted along with the median and interquartile range measurements from Figure 7a. It may be observed that model A does not appear to capture accurately the rise in X-ray brightness with increasing radio luminosity. This is because in model A the X-ray luminosity is unbeamed, whereas the radio luminosity is beamed, and so the most radio-luminous objects tend to have low inclinations (are color-coded blue). Conversely, model B overpredicts the degree to which X-ray brightness depends on increasing radio luminosity, or inclination. It is only for model C that the X-ray brightness compared to RQQs may be seen to increase with radio luminosity in a manner analogous to that observed.

Modeling X-ray luminosity as a joint function of optical/UV and radio luminosity, as done for the observed RIQs and RLQs in §5.2, makes clear the differing manner in which the three models are dependent on optical/UV and radio luminosity (see Table 9). The right-hand side of Figure 19 shows the joint 90% confidence ellipses for the primary (red) and for the full (black) observed sample, along with the calculated result for each model (blue). For model A, the X-ray luminosity is strongly dependent on optical/UV luminosity but does not particularly depend on radio luminosity. The best-fit relation for the population simulated with model A is $\ell_x = (-0.556 \pm 0.047) + (0.646 \pm 0.056) \times \ell_{uv} + (0.070 \pm 0.038) \times \ell_r$. This result reflects the underlying dependence of both the optical

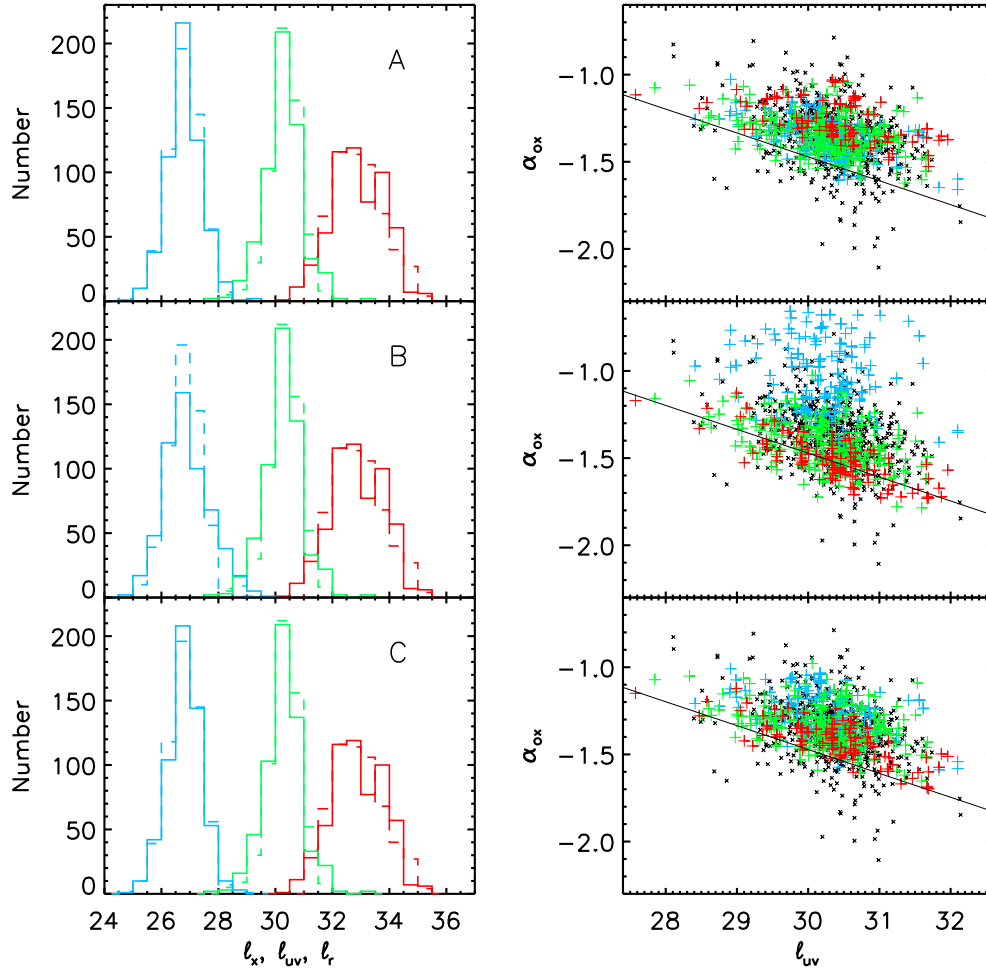


Fig. 4.18 Simulated populations of RIQs and RLQs compared with an observed sample. The models differ principally in the degree of beaming of the jet-linked X-ray emission: A is unbeamed, B is beamed with δ as for the radio jet, and C is beamed to a lesser degree. The left-hand side shows histograms of radio (red), optical/UV (green), and X-ray (blue) luminosity, for observations (dashed) and simulation (solid). The right-hand side shows the $\alpha_{\text{ox}} - \ell_{\text{uv}}$ relation for the primary sample (black crosses) and for the simulation, with objects color-coded by inclination (blue is $5^\circ < \theta < 10^\circ$, green is $10^\circ < \theta < 20^\circ$, and red is $20^\circ < \theta < 60^\circ$). The solid line is the RQQ relation. See §6 for discussion.

disk emission (and thereby the disk/corona X-ray component) and the “jet-linked” X-ray component on the intrinsic (unbeamed) radio-jet luminosity. The weak dependence of X-ray luminosity upon radio luminosity in model A is inconsistent with the results from fitting the primary and full sample. For model B, the X-ray luminosity is strongly dependent upon radio luminosity and does not significantly depend upon optical/UV luminosity. This result is due to the increased dominance of the X-ray continuum by jet-linked emission for a large fraction of the simulated sources, particularly those at low inclinations. The best-fit relation for the population simulated with model B is $\ell_x = (-0.301 \pm 0.044) + (0.008 \pm 0.056) \times \ell_{uv} + (0.726 \pm 0.043) \times \ell_r$. This reflects the mutual beaming of the radio and X-ray jets, but these parameters are also inconsistent with observations. For model C, the X-ray luminosity is dependent upon both optical/UV and radio luminosities in a manner similar to that observed, as illustrated by the overlapping confidence ellipses. The best-fit relation for the population simulated with model C is $\ell_x = (-0.325 \pm 0.034) + (0.509 \pm 0.034) \times \ell_{uv} + (0.280 \pm 0.026) \times \ell_r$. This result reflects the milder beaming with $\gamma_x = 2.5$ that places model C in some sense intermediate between model A and model B. For comparison, model C with $\gamma_x = 2.0$ (model C2) has a best-fit relation $\ell_x = (-0.360 \pm 0.035) + (0.578 \pm 0.041) \times \ell_{uv} + (0.207 \pm 0.029) \times \ell_r$ and with $\gamma_x = 3.0$ (model C3) a best-fit relation $\ell_x = (-0.265 \pm 0.031) + (0.468 \pm 0.037) \times \ell_{uv} + (0.364 \pm 0.028) \times \ell_r$ (shown as dotted blue ellipses in Figure 19), bracketing the $\gamma_x = 2.5$ result but not providing as close a match to observations.

The simulated populations may be utilized to evaluate the dominant emission component at each frequency, and in particular to examine the degree to which X-ray luminosity is dominated by the jet-linked component, as a function of inclination, for the different models (see Figure 20). In nearly all cases, the optical/UV luminosity is disk-dominated. For most sources, and for all the low-inclination sources, the radio luminosity is jet-dominated. These simulations actually slightly overpredict the fraction of lobe-dominated objects, a result that is perhaps related to the simplistic treatment within the model of lobes as point sources for the purposes of evaluating FIRST detection, when in reality the diffuse emission can be more difficult to measure. In each of models A, B, and C, the X-ray luminosity is dominated by disk/corona emission for a sizeable fraction of objects; there is agreement that despite the greater median X-ray luminosities of RIQs and RLQs relative to RQQs, there are many individual objects for which a disk/corona analogous to that in RQQs is sufficient to produce the majority of observed X-ray emission. For models B and C, the degree to which the X-ray emission is jet-dominated is correlated with the degree to which the radio emission is jet-dominated (to a lesser degree in model C, for which the beaming factor is lower). For the preferred model C, the majority of objects with inclinations less than 20° have X-ray luminosities dominated by jet-linked emission.

Despite the general nature of the scenarios considered under models A, B, and C, these simulations provide insight into the degree to which the “excess” X-ray luminosity in RIQs and RLQs is jet-linked and beamed. It seems likely that some beaming must be present (model A does not satisfactorily match observations), but to a lesser degree than affects the radio jet (model B does not satisfactorily match observations). This suggests that the majority of the jet-linked X-ray emission is not produced copatially with the radio jet emission, but likely primarily originates in a somewhat slower

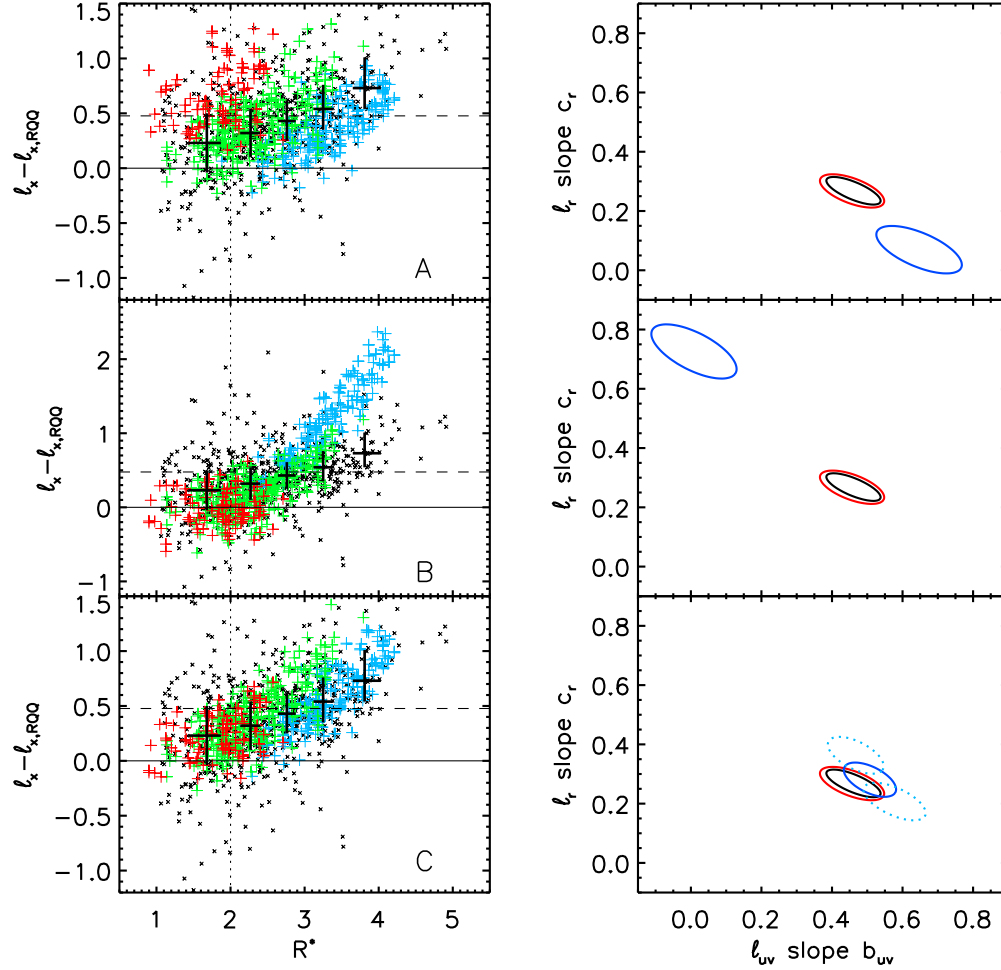


Fig. 4.19 Simulated populations of RIQs and RLQs compared with an observed sample. The models differ principally in the degree of beaming of the jet-linked X-ray emission: A is unbeamed, B is beamed with $\gamma_x = 10.5$ as for the radio jet, and C is beamed to a lesser degree with $\gamma_x = 2.5$. The left-hand side shows “excess” X-ray luminosity relative to comparable RQQs (see Figure 7a) for the observed sample (small black crosses) and for the simulation, with objects color-coded by inclination (blue is $5^\circ < \theta < 10^\circ$, green is $10^\circ < \theta < 20^\circ$, and red is $20^\circ < \theta < 60^\circ$). The large black crosses give the median and interquartile range for the primary sample. The right-hand side shows joint 90% confidence ellipses for X-ray luminosity fit as a joint function of optical/UV and radio luminosity, for the primary sample (red), the full sample (black), and each model (blue). The dotted blue ellipses are for models C2 and C3 with $\gamma_x = 2$ and 3 . See §6 for discussion.

jet region. The preferred model C implies that high signal-to-noise X-ray spectroscopy of RIQs or RLQs established (e.g., from radio properties) as possessing intermediate inclinations should result in some such objects showing X-ray spectra in which an unabsorbed disk/corona-linked component and a jet-linked component are simultaneously apparent (e.g., through differing power-law slopes). Future work with significantly larger samples could potentially investigate whether the small-scale jet has velocity structure (as in a fast spine/slow sheath model; see, e.g., Jester et al. 2006b), most simply through considering two X-ray jet components with differing bulk Lorentz factors. Modeling deficiencies that are unlikely to impact these results but could be addressed to improve the precision of comparison to data include limited consideration of selection effects and ad-hoc normalization of simulated sample size.

4.6.4 Alternative model parameters

Although we have not conducted an exhaustive search of the multidimensional parameter space, the presented models (A, B, C, C2, and C3) together cover a large range of plausible possibilities, and from this set model C best matches observations. It is of interest to evaluate whether a modified set of models would still yield qualitatively similar results. Here, we briefly describe the effects of altering selected model parameters in a reasonable fashion.

The credible interval for γ from the adopted Mullin & Hardcastle (2009) model ranges from 3.20 to 14.05. The higher γ produces an acceptable match to the primary sample radio and optical/UV luminosities without changing any other model parameters (KS probabilities of 0.14/0.45 for ℓ_r/ℓ_{uv}) and can match the X-ray luminosity of models A and C but not B (KS probabilities of 0.10/5.7 $\times 10^{-5}$ /0.12 for A/B/C). The lower γ does not easily give a good match to both the radio and optical/UV luminosities. For a simulated cutoff magnitude of $m_i = 20.3$ and a ratio of optical/UV disk emission to unbeamed radio emission of -1.9 (logarithmic units), the KS probabilities are 0.034/0.066 for ℓ_r/ℓ_{uv} . The simulated median X-ray luminosities may be matched to observations with resulting KS probabilities of 0.034/0.23/0.33 for models A/B/C. In this scenario model A is not a good match to the data (the simulated scatter is lower than observed), but because γ is close to γ_x models B and C are similar. However, the increase in “excess” X-ray luminosity with increasing radio-loudness for models B and C is more rapid than observed.

Willott et al. (2001) consider two additional models for their radio luminosity function in addition to the version we use (see their §3.2). If instead a population of RIQs and RLQs is simulated based on their model which contains a steeper high-redshift decay (their Equation 11), then an inferior but acceptable match to the primary sample radio and optical/UV luminosities (KS probabilities of 0.076/0.066 for ℓ_r/ℓ_{uv}) may be obtained by adjusting the limiting magnitude to $m_i = 20.55$. The X-ray jet offset for model A must also be slightly altered to -5.2 ; then the KS probabilities for matching simulated versus observed X-ray luminosity are 0.49/0.01/0.26 for models A/B/C. Model B is again not a good match. If instead the Willott et al. (2001) model which becomes constant at high redshift (their Equation 12) is used to simulate a population of RIQs and RLQs, an acceptable match to the radio and optical/UV luminosity distributions of the

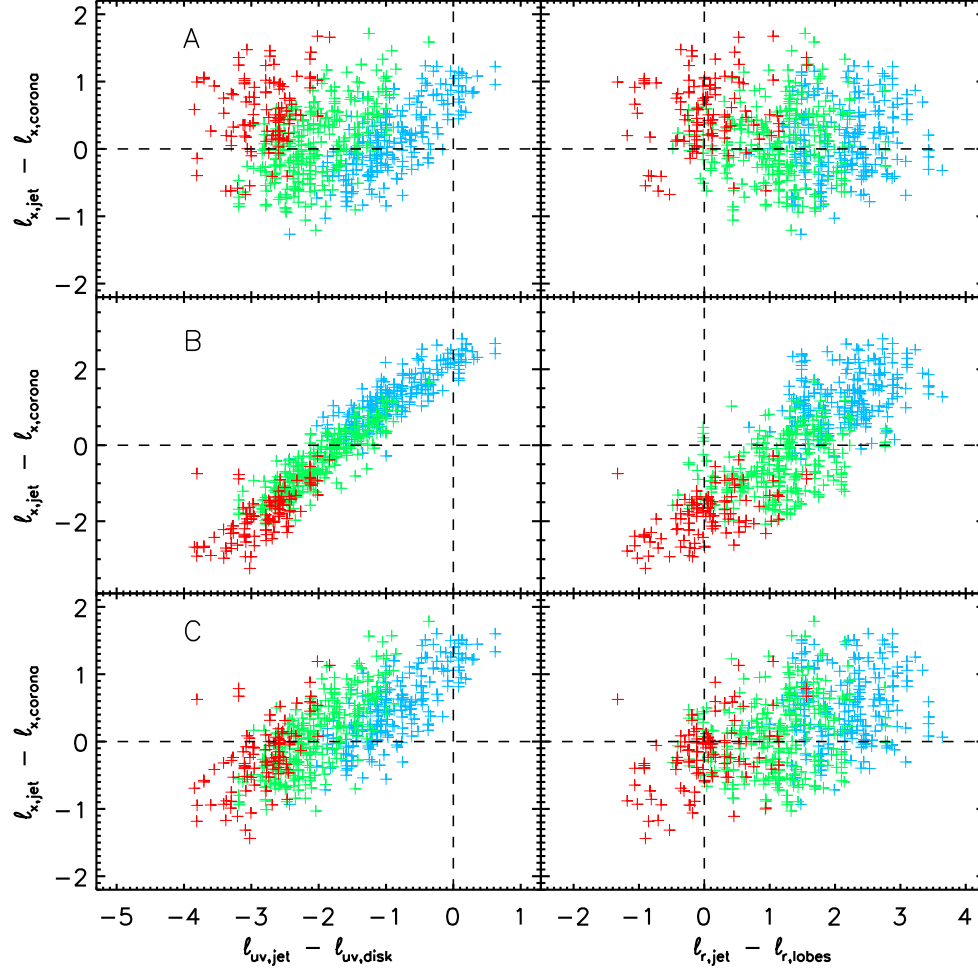


Fig. 4.20 Simulated populations of RIQs and RLQs. The models differ principally in the degree of beaming of the jet-linked X-ray emission: A is unbeamed, B is beamed with δ as for the radio jet, and C is beamed to a lesser degree. In all panels objects are color-coded by inclination (blue is $5^\circ < \theta < 10^\circ$, green is $10^\circ < \theta < 20^\circ$, and red is $20^\circ < \theta < 60^\circ$). The left-hand side shows X-ray luminosity components versus optical/UV luminosity components, while the right-hand side shows X-ray luminosity components versus radio luminosity components. See §6 for discussion.

primary sample is obtained (KS probabilities of 0.089/0.26 for ℓ_r/ℓ_{uv}). With the X-ray jet offset for model A again set to -5.2 , the KS probabilities for matching simulated versus observed X-ray luminosity are $0.54/9.7 \times 10^{-5}/0.18$ for models A/B/C. Model B remains a poor match. Additionally, the median simulated redshift (prior to matching redshifts to the primary sample) is 2.10, higher than that of the primary sample (1.41) and also higher than that simulated with the version of the Willott et al. (2001) model we use (1.80).

We also consider a scenario in which the X-ray jet emission is beamed as $\delta^{2-\alpha_x}$ (as is the radio jet emission) rather than as $\delta^{3-2\alpha_x}$. This might apply if, for example, the X-ray jet emission were to be dominated by synchrotron emission from a secondary population of high-energy electrons. This change only affects models B and C. It is necessary to adjust the X-ray jet offsets to $-6.5/-6.3$ to match the median X-ray luminosity, after which the KS probabilities are 0.18/0.33 for models B/C. With less extreme X-ray beaming model B can match the observed distribution of X-ray luminosities. However, model B still predicts a greater fraction of X-ray-bright objects than is observed, and the increase in “excess” X-ray luminosity with increasing radio-loudness is also more rapid than observed. Model C remains a superior explanation of the data.

4.7 Conclusions

The primary results of our analysis of the properties of RIQs and RLQs are the following:

1. Sample: We have compiled a sample of 177 RIQs and 550 RLQs (primarily by matching optically selected SDSS quasars to the FIRST survey, taking into account extended radio emission) with high-quality archival X-ray coverage by *Chandra*, *XMM-Newton*, or *ROSAT*. The full sample is almost unbiased with respect to X-ray properties, has a high (85%) detection rate, and can be utilized to investigate the nature and origin of X-ray emission in RLQs. The sample size is significantly larger than earlier studies of RLQs and provides superior coverage of the luminosity-redshift plane.

2. Trends: We calculate the ratio of X-ray luminosity in RLQs relative to that of comparable RQQs and determine how this ratio increases with both radio loudness and luminosity. This ratio of “excess” X-ray luminosity ranges from ~ 1 – 2 for RIQs through the canonical ~ 3 for RLQs to $\gtrsim 10$ for strongly radio-loud ($R^* > 4$) or luminous ($\ell_r > 35$) objects. We also present fits to the X-ray luminosity calculated as a function of both optical and radio luminosity, useful for determining the “typical” X-ray luminosity for any given RLQ. We find that RIQs are similar to RQQs, and quantify the manner in which RLQs become more X-ray luminous for large R^* or ℓ_r or for flat radio spectra. Finally, we do not find any significant redshift dependence in the properties of RIQs and RLQs, implying IC/CMB jet-linked emission does not contribute substantially to the X-ray continuum.

3. Models: We conduct Monte Carlo simulations based on a low-frequency radio luminosity function to which we add a randomly inclined relativistic jet. The optical disk emission is successfully modeled as correlated with the intrinsic (unbeamed) radio-jet luminosity, and the X-ray emission contains both disk/corona and jet-linked components. We consider three models for the non-coronal core X-ray luminosity component, and

conclude that the jet-linked X-ray emission is likely beamed but with a lesser bulk Lorentz factor than applies to the radio-jet emission. The alternative possibilities of unbeamed X-ray emission and of X-ray emission with $\gamma \sim 10.5$ as for the radio jet do not appear to match adequately the observed data. For the preferred model, the radio emission is mostly jet dominated, the optical/UV emission is almost exclusively disk dominated, and the X-ray emission is split between disk/corona and jet-linked components with the jet becoming increasingly dominant at low inclinations.

4.8 Acknowledgments

We thank B. Luo, Y. Xue, and D. A. Rafferty for assistance with photometric redshifts and for making their catalogs available prior to publication. We thank M. Eracleous for useful conversations. BPM, WNB, and DPS thank NASA ADP grant NNX10AC99G for support; DPS also thanks NSF grant AST06-07634. Funding for the SDSS and SDSS-II has been provided by the Alfred P. Sloan Foundation, the Participating Institutions, the National Science Foundation, the U.S. Department of Energy, the National Aeronautics and Space Administration, the Japanese Monbukagakusho, the Max Planck Society, and the Higher Education Funding Council for England. The SDSS Web Site is <http://www.sdss.org/>.

4.9 Appendix A: Using GALEX data to improve photometric redshifts

Out of the 346 photometric RIQs and RLQs under consideration prior to incorporation of GALEX photometry, 127 (37%) have $z_{\text{phot}} > 1.9$ ¹⁷, of which 107 have GALEX coverage. The color-color index $(m_{\text{NUV}} - m_r) - 2.5(m_g - m_r)$ cleanly separates $z_{\text{spec}} \leq 1$ from $z_{\text{spec}} \geq 1.9$ objects (D. W. Hogg 2009, personal communication). We flag the 30 objects with photometric redshifts $z_{\text{phot}} \geq 1.9$ but $(m_{\text{NUV}} - m_r) - 2.5(m_g - m_r) < 1.5$, of which we estimate ~ 25 are actually low-redshift quasars. From the catalog of SDSS DR3 quasars matched to GALEX data provided by Trammell et al. (2007), of the quasars with both FUV and NUV detections the fraction with $z_{\text{spec}} > 1.9$ is 6.9% (or 7.7%/8.6% for objects with $m_i > 19/20$; the median m_i for the photometric sample is 20.0). The photometric sample of quasars contains 103 objects detected in both the FUV and NUV, of which 24 (23%) have estimated redshifts $z > 1.9$; it seems likely that $\sim 15 (= 24 - 103 \times 0.086)$ of these objects have incorrect photometric redshifts. Most (19/24) of the objects with both FUV and NUV detections are already flagged for rejection by the color-color cut. After combining methods we generate a rejection list of 35 objects with photometric redshifts $z \geq 1.9$ but GALEX properties more characteristic of low-redshift quasars; we estimate $\sim 28/35$ are indeed low-redshift, so only $\leq 10\%$ of genuine $z \geq 1.9$ quasars are lost through these cuts. The GALEX detection rate of low-redshift SDSS quasars is sufficiently high (Trammell et al. 2007) that virtually all interlopers with GALEX coverage are expected to be identifiable through this process.

¹⁷It is not necessary that the redshift distributions of the photometric and spectroscopic samples precisely match, but the fact that the percentage of spectroscopic RIQs and RLQs with $z_{\text{spec}} > 1.9$ is 34% for objects with $m_i > 19$ may provide additional confirmation that most of the photometric redshifts are accurate.

We checked the rejection list of 35 objects (with photometric redshifts $z \geq 1.9$ but GALEX properties more characteristic of low-redshift quasars) for SDSS DR6 spectroscopic coverage, finding 8 objects with spectroscopic redshifts available for comparison. From these, 6 objects have incorrect photometric redshifts $z \geq 1.9$ but spectroscopic redshifts $z \leq 1$ (of which 4 objects were flagged for rejection by both the color-color and the joint-detection cuts and 2 identified by only one method each). The other 2 objects also have (less dramatically) incorrect photometric redshifts, with spectroscopic redshifts ~ 0.5 below the photometric estimate. No objects with spectroscopically confirmed photometric redshifts of $z > 1.9$ are on this rejection list. We correct the redshifts (and luminosities) of these 8 objects with spectroscopic coverage and then remove them from the rejection list, which therefore consists of 27 objects. Of the 20 objects with photometric redshifts $z \geq 1.9$ that lack GALEX coverage, 5 also have spectroscopic redshifts and are retained, while the remaining 15 (of which ~ 4 are likely actually low-redshift) are conservatively added to the rejection list. After discarding objects on the rejection list, the updated candidate list of photometric RIQs and RLQs contains 304 ($= 346 - 27 - 15$) objects, within which the remaining fraction with this type of redshift misidentification is only $\sim 1.5\%$.

4.10 Appendix B: Notes on individual deep-field objects

Here we present brief commentary on selected RIQs and RLQs from the CDF-N and the E-CDF-S; the interested reader is referred to the provided references for additional detail.

123538.51+621643.0 is included in the *XMM-Newton* Bright Serendipitous Survey (Della Ceca et al. 2004). Galbiati et al. (2005) describe it as a non-blazar AGN (with $R^* = 1.22$ and $\alpha_r = 2.5$ calculated from 1.4 to 8.5 GHz) and find that the X-ray spectrum can be adequately fit by a power-law model with $\Gamma = 1.96^{+0.08}_{-0.05}$ and no intrinsic absorption.

123649.62+620737.8 is near the borderline of our X-ray hardness-ratio cut and may be mildly obscured, although it is nevertheless relatively X-ray bright. It is classified as a type-2 AGN by, e.g., Padovani et al. (2004), using the definition of Szokoly et al. (2004). Trouille et al. (2008) characterize the optical spectrum as showing high excitation lines (i.e., not an obvious broad-line object), but its $\Delta(g-i)$ value is -0.17 , bluer than the typical quasar at that redshift.

123746.63+621739.0 is listed in the radio catalog of Richards et al. (1998) as having a radio flux density of $11.1 \mu\text{Jy}$ at 8.5 GHz, and is also in the radio catalog of Richards et al. (1999) with a flux density of $998 \mu\text{Jy}$ at 1.4 GHz, in agreement with the flux density from Biggs & Ivison (2006). The optical counterpart has quasar-like colors but lacks an optical spectrum that would permit definitive classification.

033115.03-275518.5 has a lobe-dominated radio morphology and shows double-peaked optical broad-line emission structure. Details may be found in Luo et al. (2009).

033124.86-275207.1 has two other optical objects within $2.5''$ but the selected counterpart is secure. It is described in Rovilos et al. (2007) as a type-1 AGN based on its soft X-ray spectrum.

033139.49–274119.6 is listed in the ACTA radio catalog of Norris et al. (2006) as having a 1.4 GHz flux density of 0.2 mJy, in agreement with the flux density of 206 μ Jy from Miller et al. (2008). This object is detected in the *Spitzer* Wide-Area Infrared Extragalactic Survey (Lonsdale et al. 2003) and has optical quasar-like colors but lacks an optical spectrum that would permit definitive classification.

033208.66–274734.4 is a bright RIQ with a broad-line optical spectrum (e.g., Tozzi et al. 2009). Lehmer et al. (2005) describe the X-ray spectrum (containing ~ 20000 counts) as having an effective photon index of $\Gamma = 1.73$ (calculated from the hardness ratio) and Steffen et al. (2006) quote a radio-loudness of $R^* = 1.14$.

033210.91–274414.9 is a RLQ with a broad-line optical spectrum (e.g., Tozzi et al. 2009). Wang et al. (2007) find that the X-ray spectrum (containing ~ 1000 counts) can be well-fit by a power-law model with $\Gamma = 1.88 \pm 0.09$ and no intrinsic absorption.

033211.63–273725.9 has COMBO-17 colors consistent with those of a template quasar spectrum. Lehmer et al. (2005) describe the X-ray spectrum as having an effective photon index of $\Gamma = 1.44$ (calculated from the hardness ratio) and Steffen et al. (2006) quote a radio-loudness of $R^* = 1.29$. This source is detected in the *Spitzer* Wide-Area Infrared Extragalactic Survey.

033227.01–274105.0 is a broad-line quasar (e.g., Tozzi et al. 2009). Galbiati et al. (2005) quote $R^* = 2.05$ and $\alpha_r = -0.53$ and fit the X-ray spectrum with a power-law plus blackbody model ($\Gamma = 2.04 \pm 0.15$ and $kT = 0.15 \pm 0.06$) with no intrinsic absorption.

4.11 Appendix C: Verification of fitting methodology

We fit X-ray luminosity as a function of various parameters using the IDL code of Kelly (2007), which takes into account censoring of the dependent variable and uncertainties in all variables. This is an advance over methods that consider either censoring (e.g., ASURV) or errors (e.g., the IDL program fitexy) but not both simultaneously. Here, we illustrate the fitting technique through application to the RQQ sample of Steffen et al. (2006), for which results using an alternative method (ASURV) have already been reported.

In this sample of RQQs the uncertainties are dominated by intrinsic variability (see, e.g., §3.5 of Gibson et al. 2008), as is also the case for the RIQs and RLQs that form the primary focus of this work. The uncertainties we use throughout are based on observed data, but we investigate here the degree to which the fitting results are sensitive to alternative values for the uncertainties. Figure 21a shows $\ell_x(\ell_{uv})$ computed for RQQs for our standard errors (solid line), for a fit resulting from doubling the standard errors (dashed line), and for a fit resulting from halving the standard errors (dotted line). The coefficients for the standard error fit are $\ell_x = (-0.545 \pm 0.023) + (0.649 \pm 0.021) \times \ell_{uv}$; for the double errors fit they are $\ell_x = (-0.540 \pm 0.023) + (0.673 \pm 0.022) \times \ell_{uv}$; for the half errors fit they are $\ell_x = (-0.546 \pm 0.023) + (0.644 \pm 0.021) \times \ell_{uv}$. When comparing the coefficient values it must be kept in mind that these coefficients are probabilistically derived, so a large number of fits would be required to quantify most accurately the impact of using different error values. However, it is clear that varying the uncertainties

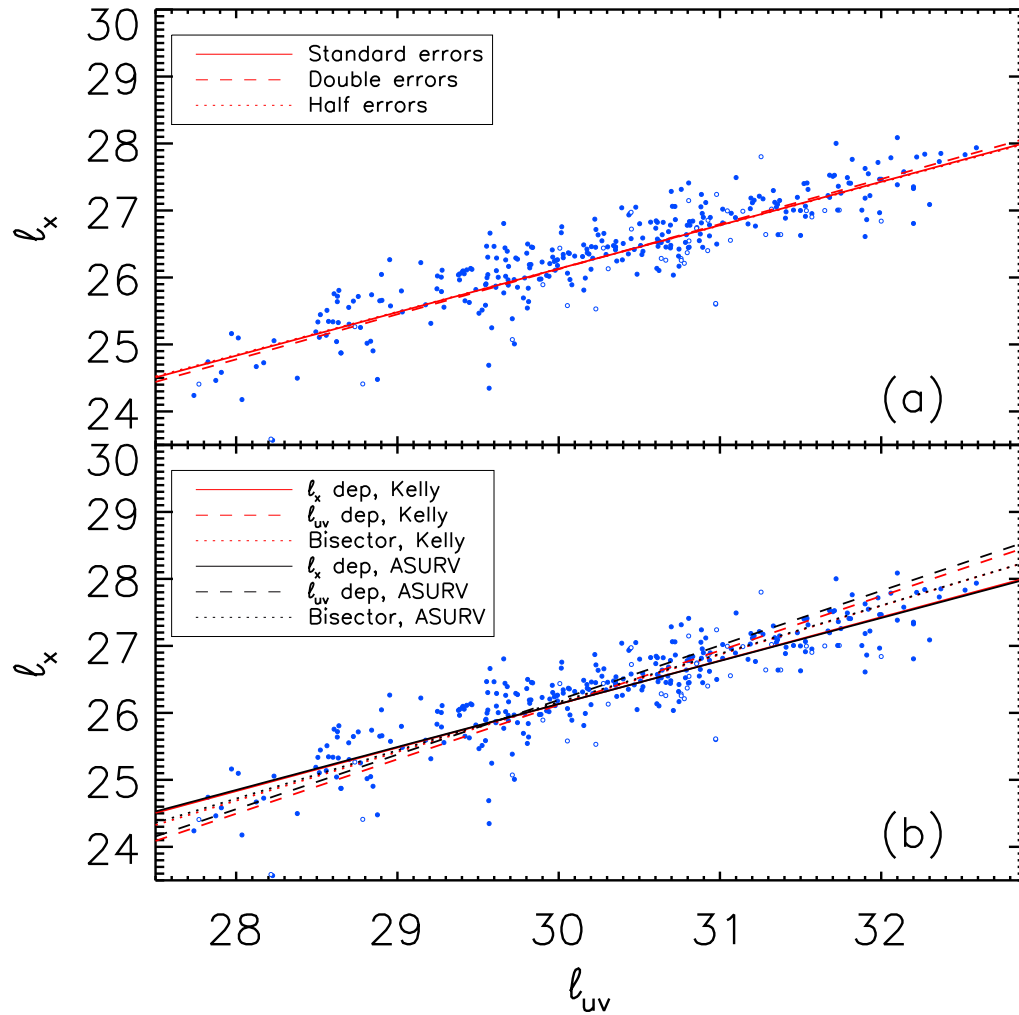


Fig. 4.21 Demonstration of fitting methodology for $\ell_x(\ell_{uv})$ applied to RQQs. The top panel illustrates that varying the uncertainties in the variables within a reasonable range has only a minimal impact upon the best-fit correlation. The bottom panel shows that using the code of Kelly (2007) provides results consistent with those given by ASURV, and illustrates the effect of considering ℓ_{uv} rather than ℓ_x as the dependent variable, or of using the bisector line. See Appendix C for details.

within reasonable bounds does not dramatically alter the parameters of the best-fit line (i.e., the credible intervals of the parameters overlap).

The best-fit model obtained through using the Kelly (2007) code agrees with that calculated by Steffen et al. (2006) using ASURV and treating ℓ_x as the dependent variable (their Equation 1a), which is $\ell_x = -0.546 + (0.642 \pm 0.021) \times \ell_{uv}$ using our normalization convention. As described in §5.1, it seems reasonable on both practical and statistical grounds to consider ℓ_x as the dependent variable throughout. However, other approaches are possible; we investigate the effect of considering ℓ_{uv} as the dependent variable and of using the bisector best-fit line. When fitting $\ell_{uv}(\ell_x)$ and inverting the results, the slope will generally be steeper than for the fit conducted with ℓ_x as the dependent variable. A complicating factor is that it is no longer possible to consider the censoring in ℓ_x . However, treating all upper limits as X-ray detections, we find $\ell_x = -0.475 + 0.812 \times \ell_{uv}$, which may be compared with the Steffen et al. (2006) result (their Equation 1b) of $\ell_x = -0.400 + 0.815 \times \ell_{uv}$. For reference, the best-fit lines calculated using the IDL program fitexy are $\ell_x = -0.500 + 0.695 \times \ell_{uv}$ and $\ell_x = -0.491 + 0.736 \times \ell_{uv}$ treating ℓ_x and ℓ_{uv} in turn as the dependent variable. Calculating the bisector using Table 1 of Isobe et al. (1990) gives $\ell_x = -0.493 + 0.727 \times \ell_{uv}$ for our fits, or $\ell_x = -0.478 + 0.721 \times \ell_{uv}$ from Steffen et al. (2006; their Equation 1c). The bisector slope is slightly higher, but it may be seen in Figure 21b that the change in the distance from the best-fit line for any given point is at most ~ 0.2 over the span of the variables. When we discuss “outliers” or “positive residuals” we are referring to greater distances from the best-fit line.

Finally, we note that the best-fit lines may not always appear to run through the highest density of points. This can result from the presence of upper limits; for example, the RIQ fit in Figure 9a (for which the ASURV-computed coefficients are virtually identical) may appear different than would be the case were all the upper limits detections.

Table 4.1. Primary sample RIQs and RLQs

Name ^a	z	m_i	$\Delta(g-i)$	ℓ_r	ℓ_{uv}	ℓ_x	Det ^b	R^*	α_{ox}	α_r	$\ell_{r,core}$	SDSS ^c	X-ray ^d
000442.18+000023.3	1.008	19.02	-0.02	31.92	30.28	26.99	1	1.64	-1.27	0.00	31.92	S	X
000622.60-000424.4	1.038	19.49	0.21	34.97	30.05	27.29	1	4.91	-1.06	-0.72	34.97	S	C
001130.40+005751.8	1.492	20.08	-0.05	33.96	30.13	27.25	1	3.84	-1.10	-0.22	33.96	S	X
004413.72+005141.0	0.941	18.45	0.06	32.64	30.42	26.69	1	2.23	-1.43	0.00	0.00	S	X
005009.81-003900.6	0.728	19.89	0.63	31.68	29.37	26.25	1	2.32	-1.20	0.00	31.68	S	C
005905.50+000651.6	0.719	17.46	-0.07	34.42	30.62	27.37	1	3.80	-1.24	-0.40	34.42	S	C
012401.76+003500.9	1.850	20.23	0.26	34.13	30.26	26.90	1	3.86	-1.29	-0.70	34.13	S	C
012517.14-001828.8	2.278	18.27	0.06	34.80	31.29	27.67	1	3.51	-1.39	-0.82	34.80	S	R
012528.84-000555.9	1.077	16.47	-0.09	34.59	31.36	27.81	1	3.23	-1.36	0.22	34.59	S	R
012734.57-000523.8	1.598	20.37	0.14	33.32	30.04	26.74	1	3.28	-1.27	0.00	33.32	S	R

Note. — Table 1 is provided in its entirety in the online edition of the journal. A portion is shown here for guidance as to its form and content.

^aName is J2000 from optical RA/Dec and is SDSS DR5 for spectroscopic quasars or SDSS DR6 for photometric quasars.

^b1 = X-ray detection; 0 = X-ray upper limit.

^cS = spectroscopic, from the DR5 quasar catalog of Schneider et al. (2007); P = photometric, from the DR6 quasar catalog of Richards et al. (2009).

^dC = *Chandra*; X = *XMM-Newton*; R = *ROSAT*.

Table 4.2. RIQs and RLQs selected from deep surveys

Name ^a	z	m_i	ℓ_r	ℓ_{uv}	ℓ_x^b	R^*	α_{ox}	Ref ^c
Color selected								
033115.03–275518.5	1.369	21.43	32.71	29.60	26.48	3.10	–1.19	1
033124.86–275207.1	1.328	21.09	33.17	29.30	25.71	3.87	–1.37	
033139.49–274119.6	2.215	23.12	31.35	29.29	<25.04	2.06	< –1.63	
033208.66–274734.4	0.543	18.77	31.02	29.26	25.94	1.76	–1.27	2
033210.91–274414.9	1.605	22.95	32.26	29.10	26.07	3.15	–1.16	3
033211.63–273725.9	1.636	18.99	32.36	30.71	26.84	1.64	–1.48	
033227.01–274105.0	0.737	19.08	32.31	29.94	26.33	2.36	–1.38	3
033302.67–274823.1	3.021	23.96	31.37	29.31	26.50	2.06	–1.07	
033310.20–274841.9	1.034	22.66	32.67	28.57	25.70	4.10	–1.10	3
123529.38+621256.4	2.413	23.20	31.24	29.36	26.11	1.87	–1.24	5
123538.51+621643.0	0.712	19.70	31.49	29.52	26.50	1.96	–1.16	5
123649.62+620737.8	1.610	23.51	31.24	28.84	26.17	2.40	–1.02	6
123746.63+621739.0	2.316	23.35	32.11	29.24	<25.19	2.86	< –1.55	
095958.54+015254.6	1.019	21.86	31.01	28.55	24.80	2.46	–1.44	
100046.92+020726.6	1.210	21.69	31.81	28.96	25.37	2.84	–1.38	
100114.86+020208.9	0.969	20.63	31.97	29.31	25.99	2.65	–1.27	8
Broad-line selected								
033225.17–274218.8	1.617	23.36	30.69	28.82	25.77	1.87	–1.16	4
123704.11+620755.4	1.253	22.07	30.43	29.11	25.53	1.32	–1.37	7
123707.51+622148.0	1.451	23.03	30.44	28.91	26.20	1.52	–1.04	7
095821.65+024628.2	1.403	19.05	32.36	30.48	26.74	1.87	–1.43	8
095835.06+022316.9	1.845	22.43	30.94	29.38	26.26	1.55	–1.19	8
095838.47+022439.3	1.161	21.86	30.33	28.70	26.23	1.62	–0.95	8
095908.32+024309.6	1.317	18.43	33.32	30.66	27.15	2.66	–1.34	8
095921.31+024412.4	1.004	20.46	31.57	29.42	25.53	2.15	–1.49	8
100114.86+020208.8	0.969	21.00	31.97	29.26	26.18	2.70	–1.18	8
100129.83+023239.0	0.826	20.54	30.35	28.80	25.53	1.55	–1.25	8
100205.03+023731.5	0.519	19.05	30.67	29.25	26.23	1.42	–1.15	8
100213.42+023351.7	1.143	21.76	30.25	28.93	25.68	1.31	–1.24	8
100228.82+024016.9	3.144	21.27	31.55	29.68	26.76	1.87	–1.12	8
100230.06+014810.4	0.626	19.65	30.22	28.30	25.51	1.92	–1.06	8
100240.93+023448.4	1.677	21.98	30.74	29.34	25.89	1.39	–1.32	8
100249.33+023746.5	2.124	19.75	32.83	30.62	26.37	2.21	–1.63	8

^aName is J2000 from optical RA/dec.

^bX-ray luminosities are from *Chandra* observations except for the broad-line selected COSMOS objects, for which the X-ray luminosities are from *XMM-Newton* observations. See §2.2.3 for details.

^cReferences for spectroscopic redshifts: 1 = Luo et al. (2009); 2 = Mignoli et al. (2005); 3 = Silverman et al., in prep; 4 = Szokoly et al. (2004); 5 = Barger et al. (2003); 6 = Barger et al. (2008); 7 = Trouille et al. (2008); 8 = Trump et al. (2009). Other redshift values are photometric from Luo et al. (2010; CDF-S X-ray detections); Rafferty et al. (2010; X-ray limits and E-CDF-S detections); Xue et al. (2010; CDF-N); and COSMOS.

Table 4.3. Sample characteristics

Sample	X-ray sources			Median properties					
	N	N_{det}	$100\frac{N_{\text{det}}}{N}$	z	ℓ_{r}	ℓ_{uv}	ℓ_{x}	R^*	α_{ox}
Full, primary, and supplemental samples									
Full	727	617	85	1.40	32.99	30.43	26.89	2.62	−1.35
Primary	575	475	83	1.41	32.81	30.36	26.82	2.50	−1.35
Spectroscopic	274	238	87	1.30	33.02	30.48	26.89	2.46	−1.38
QSO/HIZ	178	159	89	1.19	33.15	30.66	26.99	2.50	−1.40
FIRST	155	134	86	1.25	33.15	30.73	27.01	2.39	−1.42
Photometric	301	237	79	1.47	32.68	30.25	26.75	2.51	−1.33
Off-axis	483	384	80	1.45	32.68	30.33	26.79	2.43	−1.35
Targeted	92	91	99	1.04	33.65	30.67	27.05	3.10	−1.35
Supplemental	152	142	93	1.36	34.30	30.96	27.42	3.10	−1.36
<i>Einstein</i>	105	97	92	1.04	34.53	31.14	27.56	3.42	−1.38
High- z	15	15	100	4.31	34.38	31.52	27.72	2.56	−1.42
Deep fields	32	30	94	1.33	31.50	29.29	26.11	2.06	−1.25
RIQs and RLQs									
RIQs	177	128	72	1.45	32.05	30.40	26.69	1.68	−1.42
RLQs	550	489	89	1.37	33.33	30.45	26.99	2.89	−1.34
Groupings of RLQs									
$R^* < 3$	309	266	86	1.42	32.90	30.37	26.82	2.50	−1.38
$R^* \geq 3$	241	223	93	1.28	34.18	30.62	27.21	3.47	−1.30
$\ell_{\text{r}} < 33.3$	268	225	84	1.26	32.70	30.11	26.59	2.51	−1.32
$\ell_{\text{r}} \geq 33.3$	282	264	94	1.61	34.15	30.86	27.36	3.31	−1.35
$\alpha_{\text{r}} < -0.5$	168	152	90	1.25	33.65	30.48	27.03	3.19	−1.37
$\alpha_{\text{r}} \geq -0.5$	206	193	94	1.26	33.70	30.62	27.18	3.10	−1.31

Note. — The columns N , N_{det} , and $100\frac{N_{\text{det}}}{N}$ give the number of sources, the number of X-ray detected sources, and the percentage of sources with X-ray detections, respectively. Radio, optical/UV, and X-ray monochromatic luminosities ℓ_{r} , ℓ_{uv} , and ℓ_{x} have units of $\log \text{ ergs s}^{-1} \text{ Hz}^{-1}$ at rest-frame frequencies of 5 GHz, 2500 Å, and 2 keV, respectively. The radio loudness is $R^* = \ell_{\text{r}} - \ell_{\text{uv}}$ and the optical/UV-to-X-ray spectral slope is $\alpha_{\text{ox}} = 0.384 \times (\ell_{\text{x}} - \ell_{\text{uv}})$. RIQs have $1 \leq R^* < 2$ and RLQs have $R^* \geq 2$. Details regarding the various samples may be found in Section 2.

Table 4.4. RIQ and RLQ properties as a function of ℓ_{uv}

Statistic	ℓ_{uv} bin range					
	<29.5	29.5–30	30–30.5	30.5–31	31–31.5	≥ 31.5
X-ray sources						
N	68	108	230	187	87	47
N_{det}	56	91	193	153	81	43
$100 \frac{N_{\text{det}}}{N}$	82	84	84	82	93	91
Redshift						
Mean	0.89	1.04	1.38	1.71	2.06	2.74
25th %	0.43	0.72	1.05	1.03	1.15	1.88
50th %	0.71	1.03	1.40	1.67	1.93	2.44
75th %	1.15	1.33	1.73	2.22	2.90	3.62
ℓ_{x}						
Mean	25.91	26.44	26.78	27.08	27.61	27.87
25th %	25.54	26.20	26.50	26.82	27.36	27.58
50th %	26.00	26.47	26.80	27.08	27.60	27.76
75th %	26.26	26.65	27.02	27.35	27.81	28.17
α_{ox}						
Mean	−1.22	−1.29	−1.35	−1.40	−1.39	−1.51
25th %	−1.34	−1.37	−1.43	−1.49	−1.46	−1.61
50th %	−1.23	−1.29	−1.34	−1.41	−1.40	−1.53
75th %	−1.08	−1.20	−1.25	−1.30	−1.30	−1.43
R^*						
Mean	2.64	2.53	2.51	2.68	3.01	2.67
25th %	1.92	2.02	1.93	2.00	2.35	2.13
50th %	2.62	2.43	2.49	2.66	3.16	2.69
75th %	3.27	3.03	2.98	3.39	3.71	3.24

Note. — Properties here are for the full sample of RIQs and RLQs. Quantities and units are as defined in Table 3. The ℓ_{uv} bins are plotted in Figure 3.

Table 4.5. Excess X-ray luminosity as a function of R^* and ℓ_r

Statistic	R^* bin range					ℓ_r bin range				
	<2.0	2.0–2.5	2.5–3.0	3.0–3.5	≥ 3.5	< 32.2	32.2–32.9	32.9–33.6	33.6–34.3	≥ 34.3
X-ray sources										
N	177	154	155	129	112	163	176	168	99	121
N_{det}	128	127	139	116	107	127	133	149	94	114
$100 \frac{N_{\text{det}}}{N}$	72	82	90	90	96	78	76	89	95	94
$\ell_x - \ell_{x,\text{RQQ}}$										
Mean	0.23	0.32	0.42	0.56	0.74	0.29	0.32	0.44	0.49	0.70
25th %	−0.04	0.10	0.25	0.35	0.54	−0.04	0.07	0.23	0.30	0.44
50th %	0.23	0.32	0.43	0.54	0.73	0.33	0.31	0.44	0.47	0.65
75th %	0.50	0.54	0.61	0.76	1.01	0.58	0.59	0.65	0.71	0.89
R^*										
Mean	1.63	2.26	2.76	3.25	3.89	1.88	2.26	2.80	3.09	3.63
25th %	1.43	2.13	2.64	3.12	3.65	1.51	1.87	2.52	2.75	3.35
50th %	1.68	2.27	2.76	3.25	3.81	1.87	2.24	2.80	3.13	3.65
75th %	1.87	2.40	2.88	3.39	4.03	2.14	2.58	3.07	3.45	3.90
ℓ_r										
Mean	31.99	32.64	33.17	33.75	34.42	31.67	32.54	33.23	33.92	34.80
25th %	31.56	32.17	32.83	33.33	34.01	31.40	32.36	33.07	33.73	34.51
50th %	32.05	32.63	33.19	33.72	34.65	31.79	32.54	33.23	33.92	34.75
75th %	32.36	32.99	33.53	34.26	35.00	32.01	32.71	33.39	34.08	35.00

Note. — The “excess” X-ray luminosity is defined as $\ell_x - \ell_{x,\text{RQQ}}$, where $\ell_{x,\text{RQQ}} = 0.721\ell_{\text{uv}} + 4.531$ from Steffen et al. (2006). Other quantities and units are as defined in Table 3. Note that the first R^* bin is the sample of RIQs. The inner bins in R^* increase by linear factors of ~ 3 ; the inner bins in ℓ_r increase by linear factors of ~ 5 . The excess X-ray luminosity as a function of R^* and ℓ_r is plotted in Figure 7.

Table 4.6. Correlations with X-ray luminosity

Sample	$\ell_x = a_0 + b_{uv} \times \ell_{uv}$ a_0	b_{uv}	$\ell_x = a_0 + b_{uv} \times \ell_{uv} + c_r \times \ell_r$ a_0	b_{uv}	c_r
Full, primary, and supplemental samples					
Full	$-0.110^{+0.019}_{-0.019}$	$0.748^{+0.027}_{-0.026}$	$-0.070^{+0.017}_{-0.017}$	$0.460^{+0.035}_{-0.034}$	$0.269^{+0.022}_{-0.022}$
Primary	$-0.154^{+0.021}_{-0.022}$	$0.694^{+0.036}_{-0.036}$	$-0.080^{+0.021}_{-0.021}$	$0.457^{+0.041}_{-0.040}$	$0.267^{+0.026}_{-0.025}$
Spectroscopic	$-0.144^{+0.031}_{-0.031}$	$0.611^{+0.055}_{-0.053}$	$-0.060^{+0.029}_{-0.030}$	$0.354^{+0.057}_{-0.056}$	$0.298^{+0.034}_{-0.035}$
QSO/HIZ	$-0.148^{+0.038}_{-0.040}$	$0.623^{+0.061}_{-0.059}$	$-0.076^{+0.036}_{-0.035}$	$0.371^{+0.064}_{-0.064}$	$0.302^{+0.042}_{-0.042}$
FIRST	$-0.192^{+0.044}_{-0.044}$	$0.674^{+0.077}_{-0.077}$	$-0.107^{+0.040}_{-0.041}$	$0.448^{+0.077}_{-0.077}$	$0.283^{+0.044}_{-0.045}$
Photometric	$-0.143^{+0.031}_{-0.032}$	$0.769^{+0.055}_{-0.050}$	$-0.084^{+0.030}_{-0.031}$	$0.564^{+0.061}_{-0.061}$	$0.225^{+0.039}_{-0.038}$
Off-axis	$-0.171^{+0.025}_{-0.025}$	$0.743^{+0.045}_{-0.045}$	$-0.076^{+0.026}_{-0.026}$	$0.516^{+0.050}_{-0.049}$	$0.257^{+0.031}_{-0.030}$
Targeted	$-0.016^{+0.048}_{-0.045}$	$0.499^{+0.065}_{-0.066}$	$-0.069^{+0.041}_{-0.041}$	$0.314^{+0.066}_{-0.066}$	$0.279^{+0.051}_{-0.051}$
Supplemental	$+0.006^{+0.041}_{-0.042}$	$0.795^{+0.043}_{-0.042}$	$-0.030^{+0.037}_{-0.039}$	$0.473^{+0.073}_{-0.072}$	$0.252^{+0.047}_{-0.047}$
<i>Einstein</i>	$+0.019^{+0.065}_{-0.067}$	$0.771^{+0.078}_{-0.081}$	$-0.212^{+0.067}_{-0.064}$	$0.452^{+0.081}_{-0.087}$	$0.382^{+0.061}_{-0.059}$
RQQs, RIQs, and RLQs					
RQQs	$-0.545^{+0.023}_{-0.023}$	$0.649^{+0.021}_{-0.021}$
RIQs	$-0.429^{+0.044}_{-0.044}$	$0.577^{+0.064}_{-0.066}$	$-0.492^{+0.264}_{-0.268}$	$0.629^{+0.232}_{-0.228}$	$-0.055^{+0.222}_{-0.224}$
RLQs	$-0.020^{+0.019}_{-0.019}$	$0.789^{+0.028}_{-0.028}$	$-0.066^{+0.019}_{-0.018}$	$0.490^{+0.042}_{-0.041}$	$0.273^{+0.031}_{-0.030}$
Groupings of RLQs					
$R^* < 3$	$-0.149^{+0.024}_{-0.025}$	$0.760^{+0.037}_{-0.037}$	$-0.112^{+0.039}_{-0.040}$	$0.614^{+0.121}_{-0.127}$	$0.133^{+0.114}_{-0.109}$
$R^* \geq 3$	$+0.143^{+0.028}_{-0.027}$	$0.782^{+0.037}_{-0.037}$	$-0.132^{+0.061}_{-0.061}$	$0.406^{+0.085}_{-0.083}$	$0.367^{+0.074}_{-0.072}$
$\ell_r < 33.3$	$-0.156^{+0.040}_{-0.039}$	$0.688^{+0.054}_{-0.052}$	$-0.080^{+0.050}_{-0.048}$	$0.575^{+0.073}_{-0.073}$	$0.188^{+0.081}_{-0.080}$
$\ell_r \geq 33.3$	$+0.105^{+0.031}_{-0.030}$	$0.659^{+0.045}_{-0.046}$	$-0.117^{+0.038}_{-0.038}$	$0.436^{+0.049}_{-0.050}$	$0.348^{+0.043}_{-0.043}$
$\alpha_r < -0.5$	$-0.067^{+0.027}_{-0.028}$	$0.653^{+0.050}_{-0.052}$	$-0.158^{+0.026}_{-0.028}$	$0.354^{+0.066}_{-0.065}$	$0.265^{+0.040}_{-0.041}$
$\alpha_r \geq -0.5$	$+0.098^{+0.031}_{-0.031}$	$0.734^{+0.040}_{-0.039}$	$-0.006^{+0.032}_{-0.033}$	$0.435^{+0.057}_{-0.057}$	$0.322^{+0.047}_{-0.047}$

Note. — All fitting is done with the IDL code of Kelly (2007), which utilizes Bayesian techniques that incorporate both errors and upper limits. Errors are assumed to be dominated by intrinsic random flux variability; see, e.g., §3.5 of Gibson et al. (2008). The luminosities are normalized prior to fitting as $\ell_r - 33.3, \ell_{uv} - 30.5, \ell_x - 27.0$. For any given model fit the quoted parameter values are the median of draws from the posterior distribution and the errors are 1σ . These results are plotted in Figures 9–13.

Table 4.7. α_{ox} and $\Delta\alpha_{\text{ox}}$ as functions of R^*

Sample	N	z^{a}	$R^{*\text{a}}$	$\alpha_{\text{ox}}/\Delta\alpha_{\text{ox}}^{\text{a}}$	Intercept a	Slope b
$\alpha_{\text{ox}} = a + b \times R^*$						
$z < 1$	203	0.67	2.70	-1.31	$-1.544^{+0.052}_{-0.050}$	$0.078^{+0.017}_{-0.018}$
$1 < z < 2$	356	1.43	2.52	-1.36	$-1.644^{+0.035}_{-0.035}$	$0.100^{+0.013}_{-0.013}$
$z > 2$	168	2.49	2.58	-1.41	$-1.803^{+0.058}_{-0.058}$	$0.078^{+0.017}_{-0.018}$
$\Delta\alpha_{\text{ox}} = a + b \times R^*$						
$z < 1$	203	0.67	2.70	0.18	$-0.083^{+0.044}_{-0.045}$	$0.090^{+0.015}_{-0.015}$
$1 < z < 2$	356	1.43	2.52	0.18	$-0.132^{+0.030}_{-0.030}$	$0.111^{+0.011}_{-0.011}$
$z > 2$	168	2.49	2.58	0.21	$-0.196^{+0.054}_{-0.056}$	$0.145^{+0.020}_{-0.019}$

^aMedian values from within the subsample. The first three rows give α_{ox} values and the last three rows give $\Delta\alpha_{\text{ox}}$ values, where $\Delta\alpha_{\text{ox}}$ corresponds to $\alpha_{\text{ox}} - \alpha_{\text{ox,RQQ}}$ with $\alpha_{\text{ox,RQQ}}$ computed from the $\ell_{\text{x}}(\ell_{\text{uv}})$ correlation (see also §4).

Note. — Fitting as described for Table 6. Errors are propagated from those assumed for luminosities.

Table 4.8. Description of model components

Parameter	Value	Comment ^a
z	Random	From W01 RLF, then use closest to primary sample to account for redshift selection effects. Drawn from uniform distribution in $\sin \theta$
θ	Random	
Radio		
$\rho, \sigma_\rho, \gamma$	−5.61, 1.38, 10.49	From Table 5 of MH09. Both ρ and σ_ρ are expressed as natural logs.
$\ell_{r,lobes}$	Random	From W01 RLF, then shifted to 5 GHz using $\alpha_r = -1$
$\ell_{r,jet0}$	Calculated	$\ell_{r,jet0}$ from $\ell_{r,lobes}$ and ρ with scatter from σ_ρ
$\ell_{r,jet}$	Calculated	$\ell_{r,jet} = \ell_{r,jet0} \times \delta^{2-\alpha_r}$, $\delta = \gamma^{-1}(1 - \beta \cos \theta)^{-1}$, $\alpha_r = -0.5$
$f_{r,min}$	1 mJy	Flux density limit (5σ at 1.4 GHz) of FIRST survey
Optical		
ρ_{dj0}, σ_{dj0}	−1.7, 0.5	Logarithmic ratio of disk to intrinsic (unbeamed) radio jet; correlation motivated by W99 results.
$\ell_{uv,disk}$	Calculated	$\ell_{uv,disk} = \ell_{r,jet0} + \rho_{dj0}$ with scatter from σ_{dj0}
$\ell_{uv,jet}$	Calculated	Extrapolated from $\ell_{r,jet}$ using $\alpha_{ro} = -0.8$. Observations restrict optical jet flux.
$m_{i,max}$	20.7	Cutoff magnitude based on depth of primary sample.
X-ray		
$\ell_{x,corona}$	Calculated	Determined from $\ell_{uv,disk}$ following the RQQ relation of S06.
$\rho_{j,A}, \rho_{j,B}, \rho_{j,C}$	−5.0, −7.4, −7.2	Logarithmic ratio of X-ray jet-linked emission to intrinsic radio jet for models A, B, and C.
$\gamma_{x,A}, \gamma_{x,B}, \gamma_{x,C}$	1.0, 10.5, 2.5	Bulk Lorentz factor governing beaming of X-ray jet-linked emission for models A, B, and C.
$\ell_{x,jet}$	Calculated	Determined from $\ell_{r,jet0}$ and ρ_j , with boosting of $\delta_x^{3-2\alpha_x}$, $\alpha_x = -0.5$

^aReferences in the comments are W01: Willott et al. (2001); MH09: Mullin & Hardcastle 2009; W99: Willott et al. (1999); S06: Steffen et al. (2006).

Note. — See §6 for modeling details.

Table 4.9. Model X-ray luminosities and $\ell_x(\ell_{\text{uv}}, \ell_r)$

Sample	X-ray luminosities			$\ell_x = a_0 + b_{\text{uv}} \times \ell_{\text{uv}} + c_r \times \ell_r$		
	ℓ_x	σ	KS p^a	a_0	b_{uv}	c_r
Primary	26.82	0.59	...	$-0.080^{+0.021}_{-0.021}$	$0.457^{+0.041}_{-0.040}$	$0.267^{+0.026}_{-0.025}$
Model A	26.77	0.61	0.36	$-0.556^{+0.043}_{-0.047}$	$0.646^{+0.056}_{-0.056}$	$0.070^{+0.038}_{-0.038}$
Model B	26.79	0.81	< 0.01	$-0.301^{+0.040}_{-0.044}$	$0.008^{+0.055}_{-0.056}$	$0.726^{+0.043}_{-0.043}$
Model C	26.80	0.59	0.59	$-0.325^{+0.029}_{-0.034}$	$0.509^{+0.034}_{-0.034}$	$0.280^{+0.026}_{-0.026}$
Model C2	26.82	0.59	0.49	$-0.360^{+0.031}_{-0.035}$	$0.578^{+0.039}_{-0.041}$	$0.207^{+0.029}_{-0.029}$
Model C3	26.83	0.62	0.20	$-0.265^{+0.031}_{-0.029}$	$0.468^{+0.035}_{-0.037}$	$0.364^{+0.028}_{-0.028}$

^aKolmogorov-Smirnov test comparing distribution of model ℓ_x values to that of the primary sample (computed treating observed and simulated upper limits as detections). The probability p -values given indicate that for all but Model B the simulated X-ray luminosities are not inconsistent with the observed X-ray luminosities.

Note. — Models are described in §6. Fitting as described in Table 6. Upper limits are included in the simulated sample at a rate consistent with those observed in the primary sample.

Chapter 5

Chandra observations of the hybrid morphology radio sources 3C 433 and 4C 65.15: FR IIs with asymmetric environments

5.1 Introduction

Radio-loud active galactic nuclei (AGNs) with extended radio emission may be broadly classified as either edge-darkened or edge-brightened. As defined following Fanaroff & Riley (1974), FR I sources show initially prominent jets tapering off into dim and diffuse plumes, whereas FR II sources show tightly collimated jets terminating in luminous hotspots and complex lobes. FR I sources are typically less radio luminous than are FR IIs (Fanaroff & Riley 1974), with the dividing luminosity being an increasing function of host-galaxy optical luminosity (Owen & Ledlow 1994). At low redshift FR Is tend to inhabit richer groups than do FR IIs (e.g., Zirbel 1997) although this trend seems to vanish at moderate redshift ($z \gtrsim 0.3$; e.g., Auger et al. 2008). Less than 1% of radio sources possess both an FR I jet and an FR II lobe on the opposite side of the core (Gawroński et al. 2006). Gopal-Krishna & Wiita (2000) argue that the structure of such hybrid morphology radio sources (HYMORS) is most plausibly due to the propagation of twin jets into an asymmetric medium. Despite their rarity, such mixed sources are of significant general interest to understanding the degree to which the surrounding environment influences morphology and FR type.

X-ray observations provide a productive approach toward understanding the nature of hybrid morphology sources, since the X-ray properties of the nucleus and jets in FR IIs are broadly distinct from those of FR Is. FR Is show correlations between radio, optical, and X-ray nuclear luminosity (extending to beamed sources), suggesting that the majority of the core emission in FR Is, from radio to X-ray wavelengths, is produced in an unresolved synchrotron-emitting jet (e.g., Chiaberge et al. 2000; Evans et al. 2006). The X-ray spectra of FR I sources typically do not show significant intrinsic absorption, and it is unlikely that apparently unabsorbed FR Is harbor a luminous accretion disk hidden by heavy absorption, as they are not particularly bright at IR wavelengths (e.g., Müller et al. 2004); this implies that most FR Is are likely inefficient accretors (e.g., Chiaberge et al. 2000; Evans et al. 2006). FR IIs display a wider range of observed properties, presumably related to their inclination to the line of sight. Some unification models (e.g., Urry & Padovani 1995) for radio-loud FR II sources connect narrow-line radio galaxies (NLRGs), broad-line radio galaxies (BLRGs), and radio-loud quasars (RLQs) based on viewing angle in a manner similar to radio-quiet unification schemes: NLRGs are thought to be shrouded by a dusty torus, BLRGs allow a clear view of the central engine, and RLQs are seen closer to the axis of the jet. Indeed,

BLRGs show optical emission well in excess of that predicted by the FR I radio-optical correlation, presumably from the accretion disk (e.g., Varano et al. 2004). X-ray studies also offer broad support for unification models, as NLRGs generally show significant ($N_{\text{H}} > 5 \times 10^{22} \text{ cm}^{-2}$) intrinsic absorption (e.g., Evans et al. 2006) but RLQs typically do not (e.g., Belsole et al. 2006);¹ the X-ray spectrum of RLQs flattens as inclination to the line of sight decreases, consistent with increasing dominance from a beamed jet (e.g., Belsole et al. 2006).

X-ray observations also show clear differences between the properties of the kpc-scale jets in FR Is and FR IIs. FR I jets have flat or convex spectral energy distributions (SEDs), with $\alpha_{\text{ro}}/\alpha_{\text{ox}} \lesssim 1$, and steep X-ray power-law spectra ($\Gamma \gtrsim 2$), consistent with a common synchrotron origin for the radio-to-X-ray jet emission (e.g., Worrall & Birkinshaw 2006). However, the concave SEDs and flatter X-ray spectra seen in FR II quasar jets require a distinct origin for the X-ray jet emission. One commonly discussed model is Compton upscattering of cosmic microwave background photons (IC/CMB; e.g., Tavecchio et al. 2000), a particularly efficient method of X-ray production at small inclination angles and large redshifts; however, the predicted dominance of X-ray jets over core emission at high redshifts (Schwartz 2002) has not yet been observed (e.g., Bassett et al. 2004; Lopez et al. 2006), and there are additional complications to the IC/CMB model (e.g., Hardcastle 2006). An appealing alternative is that the X-ray jet emission in RLQs with concave SEDs may arise from a second population of highly energetic synchrotron-emitting electrons (e.g., Atoyan & Dermer 2004).

We report here on recent *Chandra* observations of the hybrid radio sources 3C 433 and 4C 65.15. 3C 433 is a low-redshift ($z = 0.102$) NLRG with highly unusual extended radio emission (e.g., van Breugel et al. 1983), giving it an ambiguous FR I/II morphological classification (Wills et al. 2002). There is a luminous southern FR II lobe that includes a primary hotspot and bright outer ridges and a knotty northern FR I jet ending in a diffuse plume that stretches perpendicularly to the east.² The complex southern lobe contains considerable cold gas, as indicated by HI measurements (Mirabel 1989; Morganti et al. 2003). Black et al. (1992) resolve the core into two components (C2 and C1) separated by only ~ 1 kpc; the northern core component (C1) is most likely an inner jet knot. 4C 65.15 ($z = 1.625$) was noted as a possible hybrid object by Gopal-Krishna & Wiita (2000); the radio image shows a southern jet lacking a primary hotspot (Lonsdale et al. 1993) that peaks in brightness as it abruptly bends at a right angle and then gradually expands and fades away to the west, somewhat similar to the striking structure of the FR I jet of 3C 433. The (strongly polarized) northern FR II hotspot is much brighter than the nucleus at 8.5 GHz. The Sloan Digital Sky Survey (SDSS; York et al. 2000) spectrum of 4C 65.15 shows typical quasar C IV, C III, and Mg II broad emission lines; 4C 65.15 also has associated narrow absorption blueward of the C IV emission line (Vestergaard 2003). Both objects have radio luminosities consistent with those of comparable FR II sources. Both also are lobe-dominated; while the RLQ

¹Some high-redshift RLQs display significant intrinsic X-ray absorption (e.g., Yuan et al. 2006 and references therein).

²For simplicity we will refer throughout to the “FR II lobe” and “FR I jet” in each object; these classifications should be understood to refer to the dominant type of structure on a given side.

4C 65.15 is presumably inclined closer to the line of sight than the NLRG 3C 433, beaming or projection effects alone cannot explain the hybrid structure in either case. The primary scientific goal for this project is to determine the fundamental nature of these objects through categorizing their nuclear and jet X-ray properties as either FR I, FR II, or mixed.

This paper is organized as follows: §2 presents the X-ray observations and relevant images, §3 describes analysis of the 3C 433 data, §4 describes analysis of the 4C 65.15 data, §5 discusses the results in the context of known properties of FR Is and FR IIs, and §6 summarizes the main conclusions of this work. A standard cosmology with $H_0 = 71 \text{ km s}^{-1} \text{ Mpc}^{-1}$, $\Omega_M = 0.27$, and $\Omega_\Lambda = 0.73$ is assumed throughout. This choice results in luminosity distances of 465 and 12160 Mpc and angular-distance scales of 1.86 and 8.56 kpc arcsec $^{-1}$ for 3C 433 and 4C 65.15, respectively. The Galactic column density toward 3C 433 ($\alpha_{2000} = 21 \text{ } 23 \text{ } 44.5$, $\delta_{2000} = +25 \text{ } 04 \text{ } 27$) is $1.19 \times 10^{21} \text{ cm}^{-2}$; toward 4C 65.15 ($\alpha_{2000} = 13 \text{ } 25 \text{ } 29.7$, $\delta_{2000} = +65 \text{ } 15 \text{ } 13$) it is $1.95 \times 10^{20} \text{ cm}^{-2}$. Unless otherwise noted, errors are given as 90% confidence intervals for one parameter of interest ($\Delta\chi^2 = 2.71$).

5.2 Observations

3C 433 was observed by *Chandra* on 2007 Aug 28 using ACIS-S3 in a standard 1/2 subarray. After Good Time Interval (GTI) filtering the exposure time was 37.2 ks, and the count rate from the core was 0.076 counts s $^{-1}$; there are ~ 2800 total counts in the core. The source light curve does not show significant variability. Radio and optical data help place the *Chandra* results in context. We make use of high-resolution radio maps of 3C 433 created from archival Very Large Array (VLA) data at two frequencies: a 1.5 GHz image with a resolution of 1.0'' (from observations conducted on 1986 Apr 25) illustrates the large-scale radio structure, while a 8.3 GHz image with a resolution of 0.25'' based on data presented in Black et al. (1992) reveals the structure of the inner jet. A *Hubble Space Telescope* (*HST*) WFPC2 image was retrieved from the MAST archives³; these data were previously discussed by de Koff et al. (1996), who noted the large-scale dust absorption features in the host galaxy. An adaptively smoothed 0.5–2 keV image is shown in Figure 1a, overlaid with 1.5 GHz radio contours. The smoothed image was generated using the CIAO task *csmooth* with a minimum significance (signal-to-noise ratio) of 2 and a maximum significance of 5. There is extended X-ray emission within the southern lobe and to the north on either side of the radio jet; these structures are also apparent in unsmoothed images. Closer investigation reveals that the X-ray nucleus is resolved by *Chandra* (see §3).

4C 65.15 was observed by *Chandra* on 2007 Jul 20 using ACIS-S3 in full-frame mode. After GTI filtering the effective exposure time was 35.8 ks and the count rate in the core was 0.044 counts s $^{-1}$; there are ~ 1600 total counts in the core. The source light curve shows mild ($\sim 20\%$) variability on ks timescales. Analysis of the jet and environment of 4C 65.15 was aided by 8.5 GHz radio data with a resolution of 0.25'' (from observations conducted on 1999 Aug 9), 4.9 GHz data with a beamsize of $0.47'' \times 0.31''$ at

³Multimission Archive at STScI: <http://archive.stsci.edu/index.html>

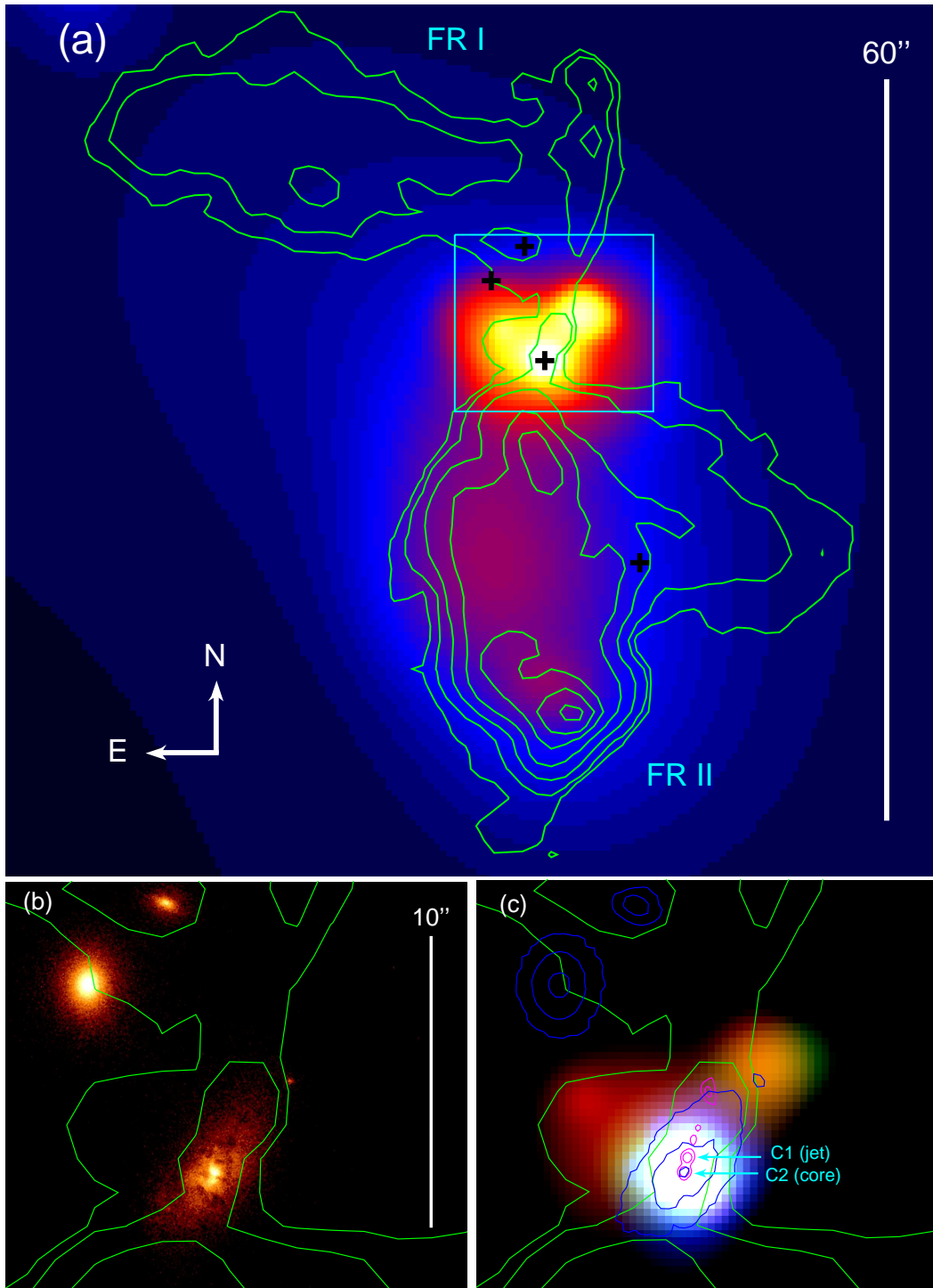


Fig. 5.1 (a) Adaptively smoothed 0.5–2 keV *Chandra* image of 3C 433 overlaid with 1.5 GHz radio contours at levels of 0.7, 2, 7, 20, 40, 55, and 70 mJy beam⁻¹. Galaxies are marked with crosses. The square region shows the coverage of the lower panels in this figure. (b) *HST* WFPC2 image of 3C 433; note the dust in the host galaxy. (c) Smoothed X-ray image color coded by energy band (red is 0.3–1 keV, green is 1–2 keV, and blue is 2–8 keV) with radio and optical contours overlaid. The magenta contours are high-resolution 8.3 GHz VLA data.

position angle 13° (from observations conducted on 1983 Sep 19), and optical data in the form of an *r*-band SDSS image. An adaptively smoothed 0.5–8 keV image is shown in Figure 2, overlaid with radio contours. The smoothed image was created from an image rebinned to $0.25''$ pixels from which the pipeline pixel randomization had been removed, and was generated using the CIAO task *csmooth* with a minimum significance of 1.5, a maximum significance of 5, and an initial minimum smoothing scale of 1.3 pixels. The X-ray core is unresolved. X-ray jet emission is detected at the location of the bend on the FR I side of the nucleus and appears to extend along the jet. There appears to be X-ray emission near the tail⁴ of the FR I jet and near the FR II lobe, ~ 5 counts in both cases; the local background in comparable-sized regions a similar distance from the core is ~ 1.5 counts, so these are only marginal detections.

X-ray spectra were extracted from the nuclear region and from other areas of interest for both sources, and models were fit using XSPEC 12 (Arnaud 1996). After examining the spectra, we preferred to fit the ungrouped spectrum for 3C 433 (using the *C*-statistic; Cash 1979) to model the low-count region below 2 keV better. Such considerations do not apply to 4C 65.15, so this spectrum was grouped to contain 15 counts per bin and fit using the χ^2 statistic. All fits were conducted over the 0.3–8 keV energy band, and all models include fixed Galactic absorption.

5.3 3C 433

The nuclear X-ray spectrum of 3C 433 was extracted from a circular region with a radius of 5 pixels ($\simeq 2.5''$), centered on the peak flux. The spectrum (Figure 3a) shows the intrinsic X-ray absorption expected in a NLRG. A simple power-law model with intrinsic neutral absorption has best-fit parameters for the column density of $N_{\text{H}} = 7.17 \times 10^{22} \text{ cm}^{-2}$ and for the photon index of $\Gamma = 1.27$ but does not provide a satisfactory fit, as indicated by the large positive residuals below 2 keV and the high *C*-statistic value [691 for 523 degrees of freedom (dof); 99.97% of Monte Carlo simulations conducted using the XSPEC *goodness* command have lower *C*-statistic values, indicating the fit is poor]. The spectrum can be satisfactorily fit with a partial-covering model with a covering fraction of 0.993 ($N_{\text{H}} = 8.64 \times 10^{22} \text{ cm}^{-2}$, $\Gamma = 1.44$, *C*-statistic/dof = 596/522, 50.10% of simulations have lower *C*-statistic values, indicating an acceptable fit). Table 1 lists parameters and errors for this and the following models. The excess soft emission can also be accommodated through an additional emission component, either a power law ($\Gamma_{\text{unabs}} = 2.2 \pm 0.8$) or thermal bremsstrahlung ($kT = 1.2^{+14.2}_{-0.6}$ keV; note the upper limit for the temperature is poorly constrained); this unabsorbed component would contain ~ 80 counts, primarily in the soft band. The total 0.5–8 keV model flux, dominated by the absorbed component, is $1.84 \times 10^{-12} \text{ erg cm}^{-2} \text{ s}^{-1}$. There is a 34 ks *ASCA* SIS spectrum obtained on 1997 May 28 (PI Yamashita) with a 0.5–8 keV model flux of $2.75^{+1.92}_{-1.33} \times 10^{-12} \text{ erg cm}^{-2} \text{ s}^{-1}$, consistent with this *Chandra* observation.

There is diffuse soft X-ray emission surrounding the nucleus and extending particularly toward the northeast and northwest (see Figure 1c) out to ~ 5 – $6''$ (~ 9 – 11 projected

⁴Lower frequency maps (e.g., Reid et al. 1995) show diffuse emission to the northwest of the nucleus, suggesting it is possible that the jet continues to curve and fan out.

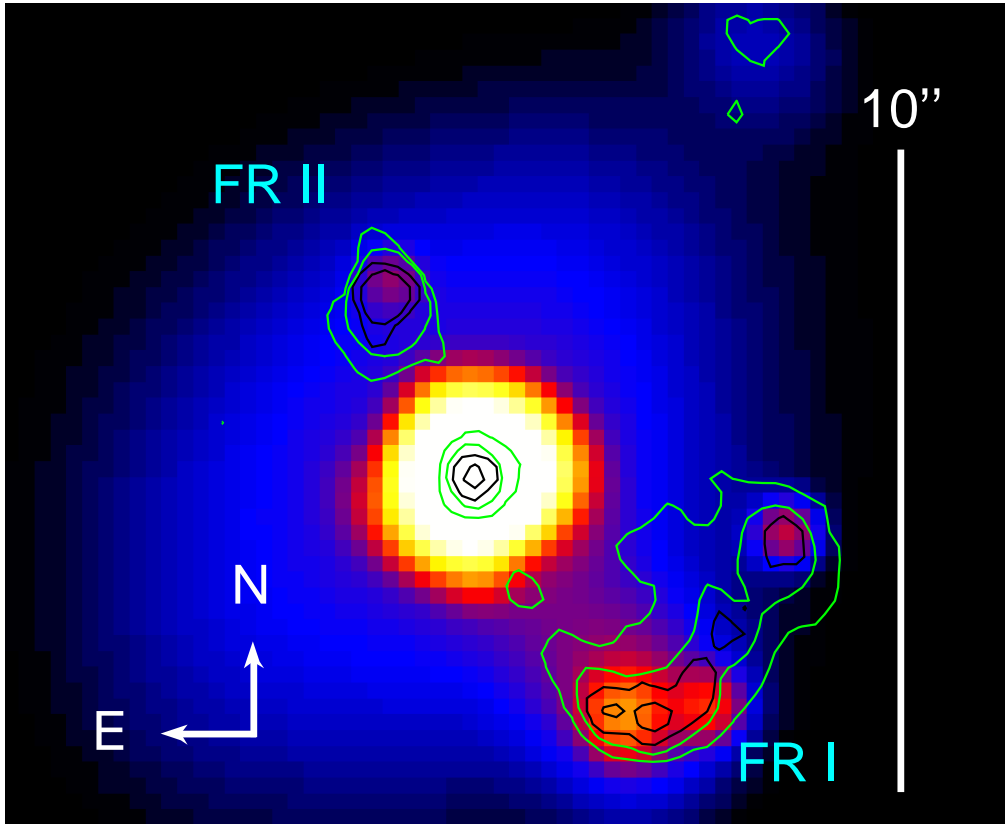


Fig. 5.2 Adaptively smoothed 0.5–8 keV *Chandra* image of 4C 65.15 overlaid with 4.9 GHz radio contours (green) at levels of 0.2 and 1 mJy beam⁻¹ and 8.5 GHz contours (black) at levels of 0.5 and 2 mJy beam⁻¹. The 4.9 GHz contours (from an image with lower resolution than that at 8.5 GHz) illustrate the curvature and low surface brightness expansion of the jet, while the higher frequency radio data show the knot structure at the bend. There are ~ 1600 counts in the core and ~ 30 counts in the extended X-ray feature at the bend in the FR I jet. There are ~ 5 counts near both the tail of the FR I jet and the FR II lobe.

kpc). It appears most likely that this soft X-ray flux is associated with hot gas such as is often observed around FR II radio sources. The gas is not distributed in a symmetric halo, but nonspherical distributions have been found in *Chandra* observations of other radio galaxies (e.g., Kraft et al. 2005). The *HST* image (Figure 1b) shows a faint point source northwest of the host galaxy; were this the source of the X-rays to the northwest, the X-ray/optical flux ratio would be consistent with the object being a background AGN (Maccacaro et al. 1988), although an optical spectrum is necessary for conclusive classification. Despite the sparse counts the soft X-ray emission in this northwestern area appears extended, leading us to favor hot gas as the emission source. The best-fit temperature for a thermal bremsstrahlung model applied to the northwest diffuse X-ray emission is $kT = 1.37^{+1.66}_{-0.59}$ keV. The volume corresponding to the X-ray emission is difficult to measure accurately but may be approximated as a sphere with a radius of $2.5''$ (4.7 kpc). Neglecting line emission (which contributes significantly to the soft X-ray emission below 1 keV), a gas cloud with approximately solar abundances would be required to have a density of $n \sim 0.06 \text{ cm}^{-3}$ to account for the observed X-ray flux, corresponding to a total mass of $6.6 \times 10^8 M_\odot$ and an ideal-gas pressure of $1.5 \times 10^{-10} \text{ dynes cm}^{-2}$. The northeastern diffuse X-ray emission appears to occupy a slightly smaller volume, and could have similar density and pressure with about half the total mass as the gas to the northwest. The hot gas would be overpressured with respect to typical intergalactic medium (IGM) temperatures and densities, suggesting either that we are observing it at a favorable time before it disperses (see also §5.2) or else there is a quasi-continuous source of heating, perhaps related to the northern jet.

We can utilize spatial analysis of the soft X-ray emission in the vicinity of the core to determine whether the low-energy X-ray spectrum originates primarily in the core or is dominated by the diffuse emission. A 0.3–1 keV image was constructed with the pipeline pixel randomization removed and with $0.1''$ pixel binning. Figure 3b shows a radial profile extracted from this image using circular annuli compared with a 1 keV point spread function (PSF) calculated with MARX.⁵ The 0.3–1 keV emission within the spectral-extraction region contains contributions from both nuclear and diffuse emission; from the PSF normalization, $\sim 50\%$ of the counts to $\simeq 2.5''$ are from the core and $\sim 50\%$ from the diffuse emission. For the double power-law model, $\sim 80\%$ of the 0.3–1 keV counts are from the unabsorbed component (with similar results when the low-energy emission is modeled as thermal bremsstrahlung), with the absorbed component only contributing $\sim 20\%$ of the counts over this energy range. This suggests $\sim 30\%$ of the 0.3–1 keV counts originate in the core and are not associated with the absorbed spectral component; this may be soft X-ray emission from an unresolved small-scale jet. Separate consideration of the soft X-ray emission to the north and south of the nucleus indicates the soft emission does not skew strongly to the north, implying the C1 inner jet knot contributes only a small fraction of the soft emission within the spectral extraction region; however, the uncertainties with so few counts are large.

There are sufficient counts over the entire *Chandra* spectrum to resolve the core region on subarcsecond scales and to determine directly whether the inner jet knot C1 is detected in X-rays. We performed a maximum-likelihood reconstruction (see §2

⁵MARX is a *Chandra* ray-trace simulator; see <http://space.mit.edu/ASC/MARX/>

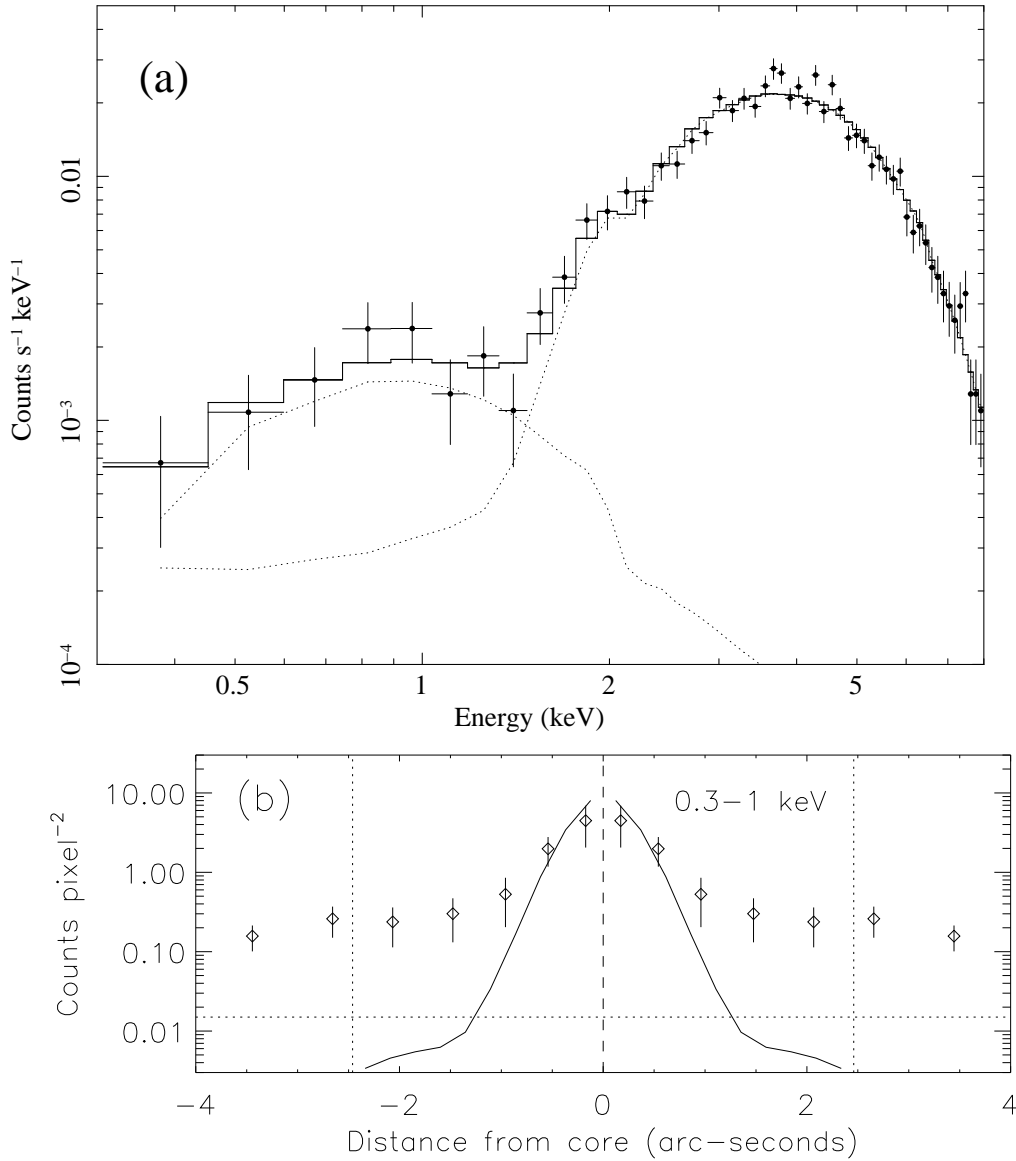


Fig. 5.3 (a) *Chandra* 0.3–8 keV spectrum of 3C 433, showing substantial absorption below 2 keV. For plotting purposes the data were rebinned to have a minimum significance of 10σ , with a maximum of 10 bins combined. The model shown is a double power-law fit with one component possessing no intrinsic absorption (with $\Gamma = 2.2$) and the other absorbed by a neutral column of $N_{\text{H}} \simeq 8.3 \times 10^{22} \text{ cm}^{-2}$ (with $\Gamma = 1.4$); this is the second model in Table 1. The unabsorbed component can be equally well fit with a thermal bremsstrahlung model with $kT = 1.2 \text{ keV}$. (b) 0.3–1 keV radial profile of the 3C 433 core region, constructed from circular annuli and plotted with a mirrored negative axis for ease of viewing. The solid line shows a scaled 1 keV PSF generated with MARX. The spectrum shown in (a) was extracted from a circular region $\simeq 2.5''$ in radius (denoted with vertical dotted lines); the soft unabsorbed spectral component contains roughly equal contributions from the diffuse emission and the core. The diffuse emission persists to $\sim 5''$ – $6''$; the background level is indicated with a horizontal dotted line.

of Townsley et al. 2006) on images from which the pipeline pixel randomization had been removed and that were binned to $0.1''$ pixels. These spanned several different energy ranges, using appropriate PSFs calculated with MARX. The X-ray core is indeed extended toward the north, with emission in excess of that expected from a point source observed at approximately the same position angle and distance as C1 is relative to C2 (see Figures 4a and 4b). The C1-linked X-ray emission is most apparent in hard-band images and is therefore not directly related to the diffuse soft X-ray emission. The observed extension in the X-ray core is not an artifact of the mirror pair 6 misalignment (see §4.2.3 of The *Chandra* Proposers' Observatory Guide), as it persists at energies below ~ 4 keV. It is unlikely that the core, observed on-axis and consisting of ~ 2800 counts, would be significantly distorted in one direction due solely to statistical noise; even were such to occur, it is further unlikely that the angle and position would randomly align so closely with C1. The 2–6 keV radial profile also shows a statistically significant excess of X-ray emission beyond that expected from a point source to the north of the X-ray core (Figure 4c). Adding an additional point source $0.6''$ from the core provides a much improved (but not exact) match to the overall profile. The normalization is $\simeq 10\%$ that of the core, suggesting that C1-linked X-ray emission contributes a few hundred counts to the overall X-ray spectrum. There is no indication that the hard X-ray component in the overall spectrum itself requires multiple power laws for an acceptable fit, so the C1-linked X-ray spectrum appears to be broadly similar to that of the core.

No Fe $K\alpha$ emission line is detected in the X-ray spectrum of 3C 433. The fit is not significantly improved by adding a Gaussian with fixed rest-frame energy 6.4 keV and fixed width 0.1 keV; the rest-frame upper limit to the equivalent width of any Fe $K\alpha$ emission is 85 eV. Permitting the line energy to vary does not suggest any emission from ionized iron. Inspection of the spectrum reveals a marginal feature at rest frame 8.2 keV (equivalent width $\simeq 150$ eV), but the model fit is not significantly improved after adding this component and in any event there is no obvious physical origin for such emission here. The lack of iron emission is somewhat atypical for X-ray spectra of heavily absorbed (FR II) radio galaxies, which often show Fe $K\alpha$ line emission of ~ 100 –300 eV equivalent width (e.g., Evans et al. 2006); perhaps the somewhat lower intrinsic absorption in 3C 433 results in emission from a narrow Fe $K\alpha$ line being diluted below detectability.

The southern lobe of 3C 433 contains diffuse X-ray emission that is easily seen in the soft-band unsmoothed image and appears as a curving band along the east side of the southern lobe in the 0.5–2 keV smoothed image. There are $\sim 120 \pm 14$ counts (1σ errors) above background in the 0.3–8 keV band, with a 0.5–8 keV model flux of 2.3×10^{-14} erg cm $^{-2}$ s $^{-1}$. Similarly sized regions extracted from east, south, and west of the lobe do not contain a statistically significant excess of counts above background. The extent of lobe emission above 2 keV is unclear; smoothed hard-band images suggest extended emission preferentially located southwest of the nucleus, but this cannot be confirmed in unsmoothed images.

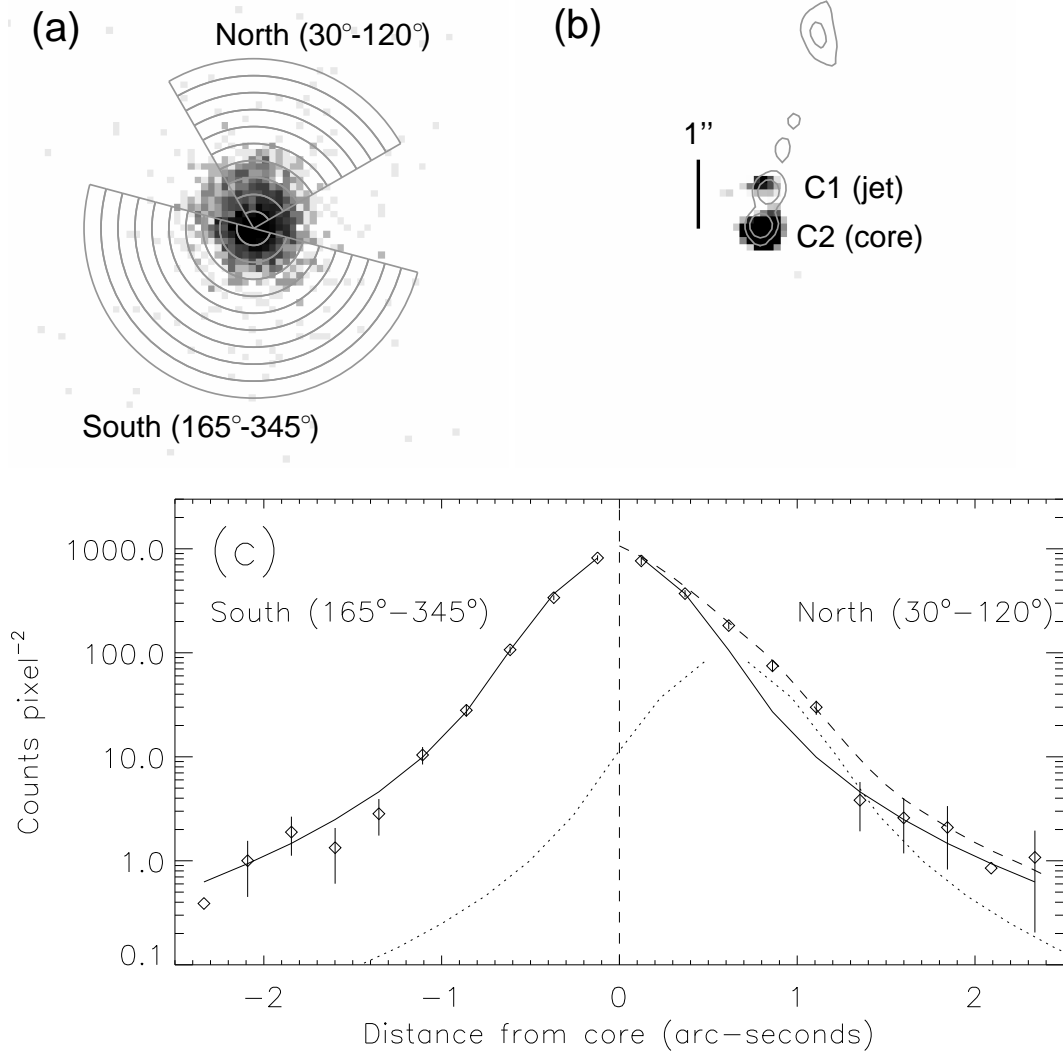


Fig. 5.4 (a) *Chandra* 2–6 keV image of the 3C 433 core with pipeline pixel randomization removed and rebinned to 0.1'' pixels. The extraction regions used to produce the bottom panel in the figure are shown. (b) A maximum-likelihood reconstruction of the 2–6 keV image overlaid with 8.3 GHz VLA contours. (c) A radial profile of the 3C 433 core. The solid line shows a scaled 4 keV PSF generated with MARX. There is excess X-ray emission to the north, presumably associated with the northern component of the radio “double core” noted by Black et al. (1992). The dotted line shows a 4 keV PSF scaled to 10% of the core and offset by 0.6'', and the dashed line shows the superposition of the two PSFs.

5.4 4C 65.15

There are no bright inner radio-jet knots in 4C 65.15 and no indication that the X-ray nucleus of 4C 65.15 is extended. The nuclear X-ray spectrum was extracted from a circular region with a radius of $2.4''$; the X-ray jet emission is located outside this area. The initial model for 4C 65.15 consisted of an unabsorbed power law. The best-fit photon index is $\Gamma = 1.89 \pm 0.07$ and the fit is acceptable, with $\chi^2 = 55.75$ for 82 dof. The 0.5–8 keV model flux is 2.55×10^{-13} erg cm $^{-2}$ s $^{-1}$. There is a 6 ks *ROSAT* PSPC observation obtained on 1992 Nov 30 (PI Laor) with a count rate implying an extrapolated 0.5–8 keV flux of $2.38 \pm 0.36 \times 10^{-13}$ erg cm $^{-2}$ s $^{-1}$, consistent with this *Chandra* observation. The model was slightly improved by adding intrinsic absorption with a best-fit neutral column density of $N_{\text{H}} = 1.31^{+1.43}_{-1.25} \times 10^{21}$ cm $^{-2}$, with the photon index adjusting to $\Gamma = 1.97^{+0.11}_{-0.05}$. Note that the 90% confidence region for the column density is barely above zero. The χ^2/dof for this model is 52.75/81, a decrease with an *F*-test probability of occurring by chance of 3.5%. This fit is shown in Figure 5. Some X-ray absorption is perhaps plausible in light of the associated narrow C IV absorption in 4C 65.15 and the general tendency for X-ray and UV absorption to be linked (e.g., Brandt et al. 2000; Gallagher et al. 2001).

Adding an Fe K α emission line with a fixed rest-frame energy of 6.4 keV and a fixed width of 0.1 keV did not improve the fit, and the spectrum shows no noticeable excess emission at that energy (the rest-frame upper limit to the equivalent width is 101 eV). Permitting the energy of the line to vary gives a best-fit value of rest frame 7.10 keV; fitting to the ungrouped spectrum (using the *C*-statistic) also gives an energy of 7.06 keV for a 34 eV (rest frame) equivalent width line, but the 90% confidence interval for the line normalization includes zero. We conclude there is no significant iron emission detected in this spectrum.

The X-ray emission in the FR I jet in 4C 65.15 contains sufficient photons for basic spectral modeling (31 counts in the 0.3–8 keV band) using the *C*-statistic and permitting only one spectral-shape free parameter. A power-law model (plus fixed Galactic absorption) gives $\Gamma = 1.17^{+0.41}_{-0.49}$ and a 0.5–8 keV model flux of 7.9×10^{-15} erg cm $^{-2}$ s $^{-1}$. A thermal model is not a very good fit for reasonable temperatures (the best-fit is $kT \sim 200$ keV) and is physically unlikely for jet-related X-ray emission.

There is apparent excess X-ray emission to the northeast of the core of 4C 65.15 located near the northern FR II radio lobe, but the paucity of counts above background (~ 3.5 net counts over 0.5–8 keV) makes this only a marginal detection. X-ray emission from hotspots in FR II sources can often be successfully explained with synchrotron self-Compton models, although low-luminosity cases may be simple synchrotron. We can estimate the expected X-ray emission from the FR II lobe of 4C 65.15 using a radio-to-X-ray flux ratio typical for other FR II hotspots (see Table 3 from Hardcastle et al. 2004) and obtain a predicted 0.5–8 keV X-ray count rate of $\sim (4\text{--}80) \times 10^{-5}$ counts s $^{-1}$, or $\sim 1.5\text{--}30$ counts in 35.8 ks. The lower end of this range is more representative of luminous hotspots, such as that of 4C 65.15, and is broadly consistent with the observed counts.

There is also apparent excess X-ray emission within the tail of the southwest jet (again ~ 3.5 net counts over 0.5–8 keV, a marginal detection). It is not immediately clear whether such emission, if genuine, is associated with a terminal hotspot or an

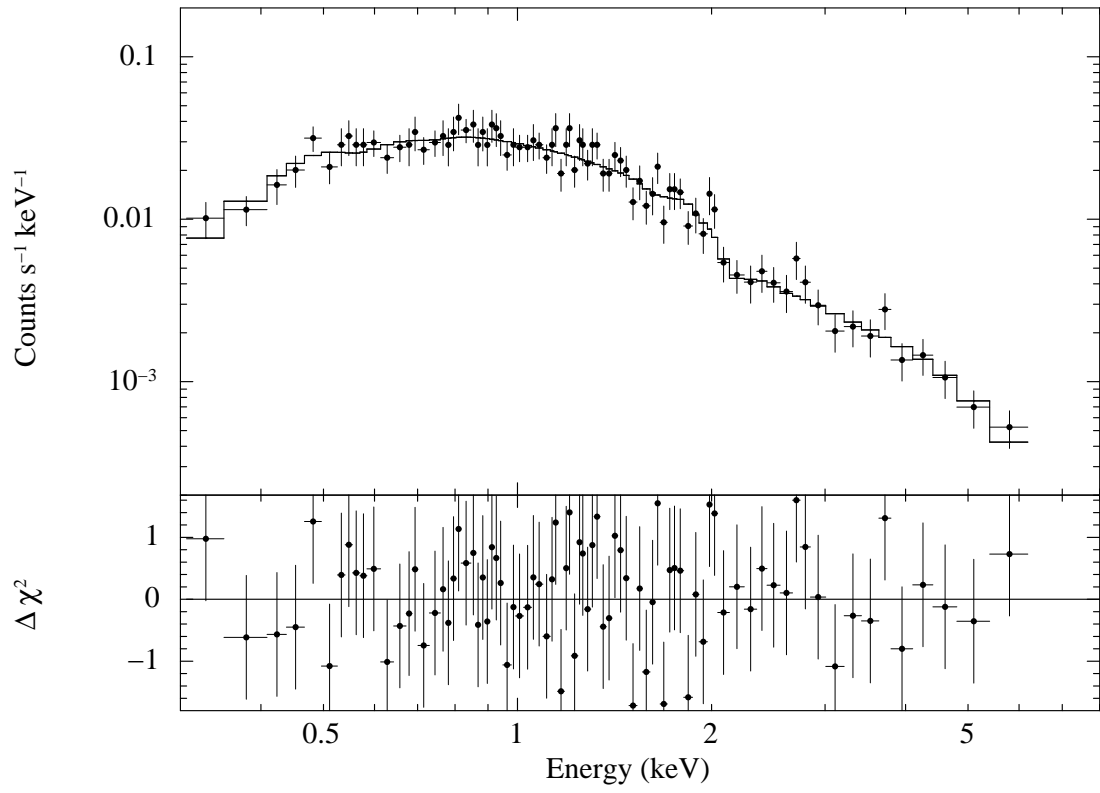


Fig. 5.5 *Chandra* 0.3–8 keV spectrum of 4C 65.15, fit with a power-law model with $\Gamma = 2.0$ and mild intrinsic absorption of $N_{\text{H}} = 1.3 \times 10^{21} \text{ cm}^{-2}$. No significant iron emission is detected. The residuals in the bottom panel are in units of sigma with error bars of size unity.

outer jet knot. In the context of an hotspot interpretation, the low radio flux of this feature suggests an expected 0.5–8 keV X-ray count rate of $\sim(3\text{--}50)\times 10^{-6}$ counts s $^{-1}$, or $\sim 0.1 - 1.8$ counts in 35.8 ks (calculated as above). Here the higher end of this range is more representative for hotspots of lower luminosities, but even so this would be a somewhat X-ray bright hotspot. If instead the X-ray emission arises in a jet feature, the ratio of X-ray-to-radio flux is perhaps somewhat less than in the bend, plausibly decreasing along the jet such as is often observed. Deeper X-ray observations would be required to conduct more quantitative analysis.

Table 5.1 X-ray spectral fitting

3C 433 model	Γ	N_{H} (10^{22} cm $^{-2}$)	Comments	cstat/dof
Single-component power law with partial-covering absorption	$1.44^{+0.13}_{-0.12}$	$8.64^{+0.75}_{-0.64}$	$f_{\text{c}} = 0.993^{+0.003}_{-0.002}$	596/522
Absorbed power law with unabsorbed power law	$1.39^{+0.22}_{-0.21}$	$8.25^{+1.09}_{-0.93}$	$\Gamma_{\text{unabs}} = 2.18^{+0.80}_{-0.83}$	594/521
Absorbed power law with unabsorbed thermal	$1.41^{+0.19}_{-0.24}$	$8.26^{+0.94}_{-1.04}$	$kT = 1.17^{+14.22}_{-0.62}$	594/521
4C 65.15 model	Γ	N_{H} (10^{21} cm $^{-2}$)	Comments	χ^2/dof
Unabsorbed power law	$1.89^{+0.07}_{-0.07}$			56/82
Absorbed power law	$1.97^{+0.11}_{-0.05}$	$1.31^{+1.43}_{-1.25}$	$F\text{-test } p=0.035$	53/81

5.5 Discussion

5.5.1 Jet emission

The inner jet in 3C 433 (C1) is detected in X-rays, but it is difficult to be quantitative about its characteristics due to its close proximity to the nucleus. The jet/core flux ratio for C1 of $\sim 10\%$ is somewhat larger than for typical FR II quasar jet knots, which generally have values of 1%–8% (e.g., Marshall et al. 2005). The radio-to-X-ray spectral slope of $\alpha_{\text{rx}} \sim 0.8$ is also flatter than the $\alpha_{\text{rx}} \sim 0.9\text{--}1.0$ that is typical for FR II quasar knots (e.g., Marshall et al. 2005). The inner knot C1 appears to be relatively X-ray luminous (note the comparisons do not take into account the distance of knots from the core). At the large inclinations indicated for this NLRG, the IC/CMB process should not contribute significantly to jet X-ray emission, and instead the X-ray jet emission may be synchrotron dominated. The data do not permit differentiation between simple synchrotron and multiple component models.

The X-ray spectrum of the inner jet appears to be dominated by hard-band emission, perhaps suggesting that C1 is absorbed ($N_{\text{H}} > 1.7 \times 10^{22}$ cm $^{-2}$) even at ~ 1 kpc

distance from the core. The “torus” of absorbing material presumably responsible for obscuring the core typically is believed not to extend to such distances (e.g., Maiolino & Risaliti 2007). However, this location is well within the scale of the dust structures seen in the host galaxy, so C1 may happen to lie along a line of sight that passes through a dense dust cloud or lane; Figure 1b provides tentative support for this hypothesis. de Koff et al. (2000) estimate the mass of dust in 3C 433 as $10^{5.7} M_{\odot}$ based on absorption maps and $10^8 M_{\odot}$ based on emission measured by *IRAS*, so there may be sufficient material to account for the inferred absorption if a clump covers the X-ray emitting region of the inner jet.

The nuclear soft X-ray emission might itself contain a contribution from an unresolved small-scale jet, as discussed in §3. Some support for this idea is provided by the agreement of the core radio/X-ray luminosity ratio with those of unabsorbed “jet-related” components in the FR IIs studied by Evans et al. (2006). The 3C 433 X-ray spectrum suggests that such nuclear jet-related emission is not strongly absorbed, contrasting with the C1 jet knot; indeed, strong absorption of the nuclear jet-related emission would render detection as a distinct spectral component difficult. Further, if the unabsorbed luminosity for this nuclear jet-related component were calculated from the observed nuclear soft-band flux but assuming the C1 column density, then the X-ray luminosity would exceed the expected FR II trend based on the radio core luminosity (although there are substantial uncertainties in the measurements as well as scatter in the correlation). Since the dust in the host galaxy of 3C 433 appears to be distributed in a patchy manner, the column densities associated with this dust may well vary on scales $\lesssim 1$ kpc.

The jet in 4C 65.15 has a clear detection in X-rays and radio flux measurements at several frequencies. The X-ray photon index of $\Gamma = 1.17^{+0.41}_{-0.49}$ from the power-law model is consistent with the $\Gamma \sim 1.1$ – 1.7 found by Sambruna et al. (2004) for the brightest X-ray knots in their *Chandra* and *HST* survey of core-dominated FR II quasars with known radio jets. It does not match the X-ray spectra of prominent knots in FR I jets, which are generally significantly steeper with $\Gamma \gtrsim 2$ (e.g., 3C 66B: Hardcastle et al. 2001; 3C 31: Hardcastle et al. 2002; M 87: Marshall et al. 2002; Cen A: Hardcastle et al. 2003; B2 0755+37: Parma et al. 2003). The SED of the X-ray-emitting jet region is plotted in Figure 6. The radio points are summed over the resolved features at the jet bend. The radio-to-X-ray spectral slope is $\alpha_{\text{rx}} = 0.96$; unfortunately, the SDSS upper limit does not impose useful constraints upon α_{ro} or α_{ox} . The high-frequency radio spectral slope is steeper; between 5 and 15 GHz, $\alpha_{\text{r}} = 1.08$. Consequently, the high-frequency radio spectral slope predicts synchrotron X-ray emission (for simple models, assuming the population of electrons extends to sufficiently high energies) with a flux lower than the X-ray jet emission that is actually detected. Moreover, the measured X-ray spectral index is much flatter than α_{rx} ; the 90% confidence upper limit from spectral fitting for α_{x} is 0.6. It appears most likely that the jet X-ray emission is not an extension of the synchrotron component responsible for the radio emission, although deeper optical observations would be helpful for better understanding the shape of the jet SED.

The X-ray and radio surface-brightness profiles within the 4C 65.15 jet bend do not appear to align; Figure 2 suggests the X-ray emission peaks slightly upstream of the maximum radio brightness. (The paucity of counts as well as the limited angular size

of the region of interest in the jet bend restrict the usefulness of more detailed spatial analysis.) Such an offset would make it less likely that the IC/CMB process dominates the jet X-ray emission, since the low-energy electrons involved should not congregate upstream of the peak radio synchrotron emission. This conclusion might be reached independently through consideration of the lobe-dominated nature of 4C 65.15, which constrains the inclination and hence limits the efficiency of IC/CMB emission. A model involving a second high-energy population of X-ray synchrotron emitting electrons could accommodate both any offset and a concave jet SED. The high radio luminosity, broad-line quasar classification, and apparently concave jet SED of 4C 65.15 are similar to the properties of typical FR II quasars, suggesting that the distorted southern radio structure in 4C 65.15 reflects an external influence, most likely a dense surrounding environment disrupting the outer jet.

5.5.2 Environment

3C 433 appears to reside in a group environment. Zirbel (1997) found a background-corrected group richness of 12.6 ± 4.4 for 3C 433; the mean richness among low-redshift FR IIs in that study was 5.8 (scatter 5.6), and 76% had a richness of <10 . There is a close companion ~ 14 projected kpc to the northeast; although the redshift of this nearby galaxy is unknown, its angular size is consistent with being at the same distance as 3C 433. There is another galaxy ~ 17 projected kpc to the north and an additional galaxy ~ 34 projected kpc to the southwest, as well as an optical point source $\sim 4''$ northwest of the optical nucleus of 3C 433 whose nature is unclear. There is evidence that 3C 433 is either experiencing tidal forces driving star formation or else has undergone a recent minor merger: Wills et al. (2002) identify a young stellar population in 3C 433 from UV/optical spectral analysis, and the dust structure suggests 3C 433 has been disturbed (de Koff et al. 2000) in some manner. Such activity could plausibly generate asymmetries in the surrounding IGM.

The SDSS image of 4C 65.15 shows a handful of nearby optical sources, but they are too faint to have SDSS spectral coverage and so their redshifts are uncertain. There is no overdensity of nearby sources (with $m_r < 23$) in the vicinity of 4C 65.15 on scales of $90''$, $60''$, or $30''$, nor are there more galaxies (resolved sources: type=3) near 4C 65.15 on these same scales.

Both 3C 433 and 4C 65.15 display bends in the jet on the FR I side of the nucleus. While bends in radio jets are not uncommon, the change in direction is particularly abrupt ($\sim 90^\circ$) for both 3C 433 and 4C 65.15. 3C 433 likely lies with its jet axis nearly in the plane of the sky, as indicated by its large lobe-to-core flux ratio and NLRG status, and so the observed bend should closely correspond to the physical change in direction. The bend in 4C 65.15 may be exaggerated due to an orientation closer to the line of sight. Judging from the core-to-lobe flux ratio and from the core radio-to-optical luminosity ratio (e.g., Wills & Brotherton 1995), 4C 65.15 is inclined at $\sim 35^\circ \pm 10^\circ$ to the line of sight; this is the lower limit for the deprojected bending angle (e.g., see §3 of Jorstad & Marscher 2004). The jet structure in 3C 433 and 4C 65.15 is suggestive of an environmental interaction redirecting the jet, consistent with a dense clumpy medium on the FR I side such as might also produce the hybrid structure through decelerating

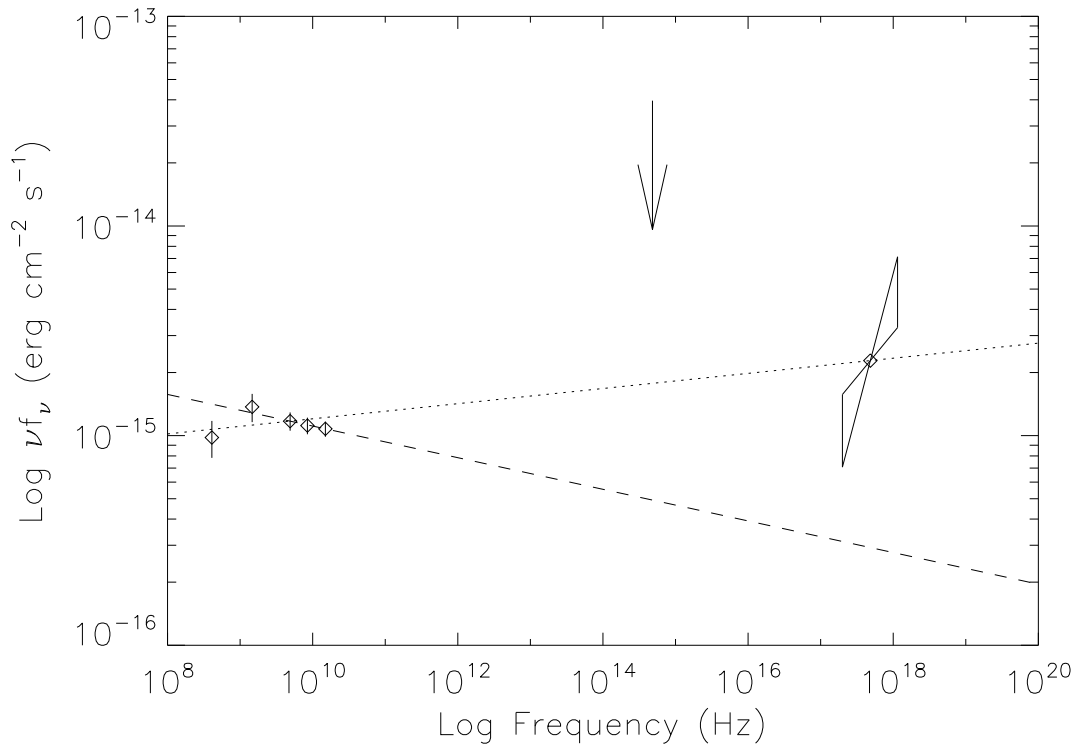


Fig. 5.6 Spectral energy distribution for the jet in 4C 65.15. The radio fluxes are for the resolved feature at the bend of the jet (see Figure 2), the optical limit is from the SDSS *r*-band image, and the X-ray flux and spectral index confidence range are from fitting the *Chandra* data. The dotted line indicates the α_{rx} power law calculated between 5 GHz and 2 keV and the dashed line indicates α_{r} calculated between 5 GHz and 15 GHz. It appears likely that the X-ray data cannot be explained as arising from the same synchrotron component which generates the radio flux; deeper optical imaging could confirm this hypothesis.

the jet closer to the core. An interesting possibility for producing X-ray emission at the site of an abrupt jet bend (such as is observed in 4C 65.15) is suggested by Worrall & Birkinshaw (2005) for 3C 346: interaction between the jet and a wake created by a companion galaxy moving through the IGM generates an oblique shock, redirecting the jet and powering X-ray synchrotron emission. It is perhaps noteworthy that 3C 433 has been included in lists of “X-shaped” radio sources; while there have been suggestions that such morphologies arise from the merger of supermassive black holes (e.g., Merritt & Ekers 2002), it has been convincingly argued (e.g., Worrall et al. 1995; Kraft et al. 2005; Cheung 2007) that hydrodynamic backflows from the jet within an asymmetric medium can naturally produce “X-shaped” structure.

5.5.3 Comparison to other radio sources

There is a correlation between core radio and X-ray luminosity for FR I sources, presumably reflecting jet dominance of the nuclear emission from radio through X-ray frequencies. FR II sources tend to have higher (unabsorbed) X-ray luminosities at a given core radio luminosity, perhaps because their X-ray emission includes a contribution from Compton upscattering of disk photons in a hot corona (e.g., Evans et al. 2006). Both 3C 433 and 4C 65.15 have nuclear (unabsorbed) X-ray luminosities that lie above the FR I correlation, consistent with other FR II sources (Figure 7). The nuclear X-ray spectra are also FR II in nature (intrinsic absorption for the NLRG 3C 433, a power law for the RLQ 4C 65.15), and the jet SED of 4C 65.15 is consistent with those of other FR II quasar jets. We conclude that the hybrid sources 3C 433 and 4C 65.15 should be regarded as FR II objects in which a particularly dense environment has induced FR-I-like jet structure.

There are only a handful of known hybrid morphology sources possessing high-resolution X-ray data. Gopal-Krishna & Wiita (2000) list six HYMORS, from which three (PKS 0521–365, PG 1004+130, and S5 2007+777) have *Chandra* coverage. Birkinshaw et al. (2002) detected X-ray emission from the FR I jet of the BL Lac PKS 0521–365 which could be satisfactorily interpreted with a synchrotron model, and also detected the FR II hotspot in X-rays with a flux similar to that expected from previous observations of hotspots in FR IIs. Miller et al. (2006) found an X-ray counterpart slightly upstream of the radio FR I jet in the broad absorption line RLQ PG 1004+130, with a flat photon index and a concave SED more typical of FR II quasar jets than FR I jets. Sambruna et al. (2008) presented *Chandra* observations of the BL Lac S5 2007+777; the FR I jet is detected in X-rays and displays properties similar to those of other FR II quasar jets. Another possible hybrid source with *Chandra* coverage is the BLRG 3C 17, which displays an edge-brightened northern lobe and a curving jet to the southeast that features a bright inner knot, an abrupt bend, and then an expanding tail (Morganti et al. 1999). Two X-ray emitting features in the jet were discovered by Massaro et al. (2008). X-ray emission in the inner knot is consistent with a single-component synchrotron spectrum, although an IC/CMB interpretation is also possible. The outer X-ray knot, located at the bend, appears to have a hard X-ray spectrum, and a synchrotron model following the suggested UV cutoff predicts lower X-ray flux than is observed, indicating the SED is likely concave. Both PG 1004+130 and 3C 17 would be classified as FR II sources

based on their radio luminosities and optical broad line emission, and their jet SEDs match more closely to FR II quasar jets than to typical FR I sources. The radio/optical properties of the BL Lac objects PKS 0521–365 and S5 2007+777 are intermediate between FR I and FR II, and for these sources the prominence of the FR I jet may reflect their low inclination to the line of sight.

5.6 Conclusions

Chandra observations of the hybrid morphology radio sources 3C 433 and 4C 65.15 reveal that they have X-ray properties consistent with those of comparable FR II sources, supporting the hypothesis that the apparent FR I structure in the jet arises from environmental interactions. In particular, we find the following:

1. The NLRG 3C 433 displays nuclear X-ray absorption with a column density of $N_{\text{H}} = 8.3 \times 10^{22} \text{ cm}^{-2}$, similar to other NLRGs and in agreement with predictions for high-inclination FR II sources from some unification models. The broad-line RLQ 4C 65.15 shows at most mild intrinsic absorption, similar to other RLQs and in agreement with predictions for intermediate-inclination FR II sources from some unification models.

2. The unabsorbed nuclear X-ray luminosities for both 3C 433 and 4C 65.15 lie along the track populated by FR II sources when plotted against core radio luminosity and do not fall along the radio/X-ray luminosity correlation followed by FR Is (Evans et al. 2006).

3. The knot/core and X-ray/radio luminosity ratio of the inner jet in 3C 433 (the C1 component) are rather high, but the close proximity to the core makes it difficult to assess the full SED. The X-ray jet in the RLQ 4C 65.15 has a flat photon index ($\Gamma \sim 1.2$) that is flatter than the radio-to-X-ray spectral slope, suggesting the SED is concave. Flat X-ray spectral slopes and concave SEDs are characteristic of FR II quasar jets and distinguish them from FR I jets.

Chandra observations of additional hybrid morphology objects would be useful in clarifying whether most such sources can be characterized as intrinsically FR IIs with a one-sided FR I jet structure generated through environmental interactions. If so, it might be expected that FR IIs residing within a particularly dense but symmetric environment could display FR-I-like jet structure on both sides of the core. Perhaps the few known broad-line FR Is such as 2114+820 (Lara et al. 1999) are such objects; 2114+820 has radio-core/X-ray luminosity properties consistent with FR II sources (Figure 7). Deep radio observations sensitive to extended emission are necessary to detect FR I jets beyond the local universe; Heywood et al. (2007) carried out a VLA survey of 18 radio-luminous broad-line quasars with extended structure and moderate redshifts ($z = 0.36\text{--}2.5$) and discovered that 4–6 (22%–33%) showed apparent FR I morphologies. There should also be varying degrees of hybridization if this interpretation is correct. 3C 433 itself could be considered somewhat of an intermediate case between a source with a two-sided FR I structure and one with an FR I jet opposing an FR II lobe, since its extended and complex southern lobe is suggestive of jet disruption prior to the outer hotspot.

It would also be interesting to examine hybrid morphology RLQs known to be inclined with the FR I side pointed toward the observer. Such objects should be intrinsically unabsorbed, so if the density of the hypothesized “frustrating” medium matches

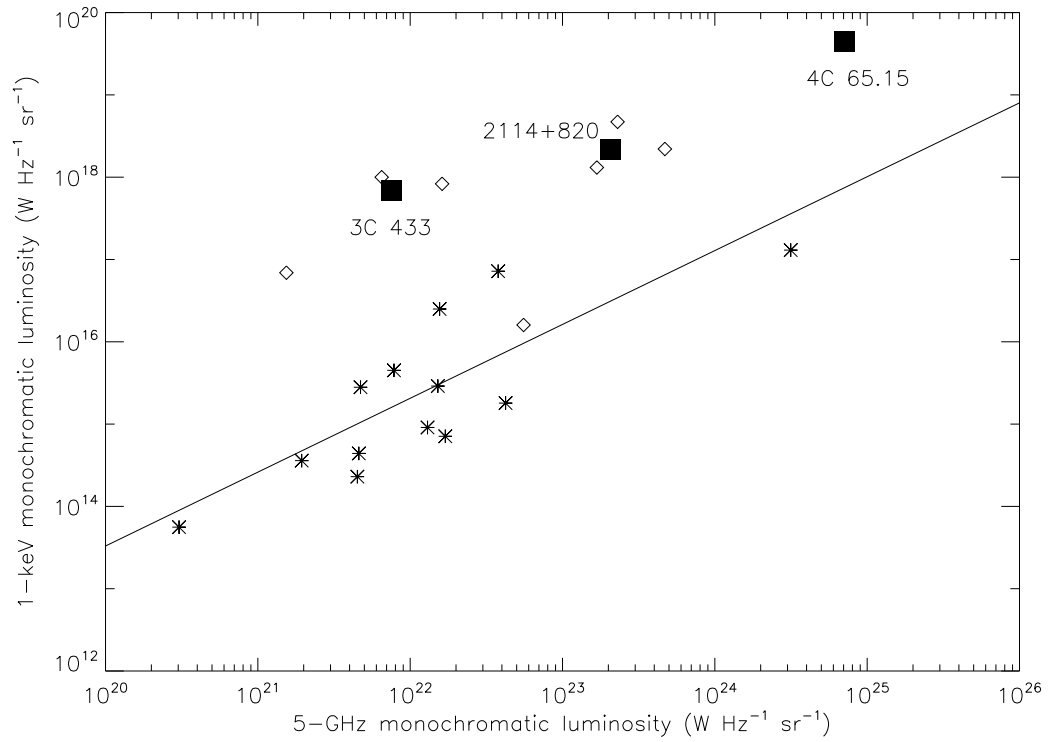


Fig. 5.7 Plot of (unabsorbed) X-ray luminosity versus core radio luminosity with data from Evans et al. (2006). Asterisks denote FR I sources, diamonds are FR II sources, and the solid line shows the best fit to the FR I luminosity correlation. The low-excitation FR II 3C 388 and the absorbed FR I Cen A have been omitted. 3C 433 and 4C 65.15 are plotted as squares; their X-ray/radio properties match those of the FR IIs. Also shown is 2114+820, a broad-line object with an FR I morphology.

that suggested as necessary for jet confinement or disruption (e.g., De Young 1993; Carvalho 1998) it might be directly detectable as absorption against the bright nucleus.

5.7 Acknowledgments

We thank the anonymous referee for constructive suggestions that improved the paper. We thank Leisa Townsley and Pat Broos for assistance with maximum-likelihood image reconstruction, Doug Gobeille for reducing and analyzing archival L-band VLA data of 3C 433, Ed Fomalont and the NRAO VLA Archive Survey⁶ team for reducing and analyzing C-band and X-band observations of 3C 433 and 4C 65.15, and Dan Harris and Gordon Garmire for productive conversations. We acknowledge support for this work under *Chandra* X-ray Center grant GO7-8118X (BPM, WNB) and NASA LTSA grant NAG5-13035 (WNB).

⁶The NVAS can currently be browsed through <http://www.aoc.nrao.edu/~vlbacald/>

Chapter 6

Conclusions and Future Work

6.1 Summary of Results

6.1.1 X-ray Absorption and an X-ray Jet in the Radio-Loud Broad Absorption Line Quasar PG 1004+130

We investigated the X-ray properties of PG 1004+130, a BAL RLQ with a hybrid FR I/FR II radio morphology. This optically bright, low-redshift quasar was undetected by *Einstein*, marking it as anomalously X-ray weak relative to other radio-loud quasars. The 22.2 ks *XMM-Newton* and 41.6 ks *Chandra* observations presented here are the first X-ray detections of PG 1004+130 and constitute the highest spectral quality X-ray observations of a radio-loud BAL quasar available to date. The *Chandra* ACIS-S spectrum shows evidence for complex soft X-ray absorption not detected in the data obtained 1.7 yr previously with *XMM-Newton*, with a best-fit intrinsic column density of $N_{\text{H}} = 1.2 \times 10^{22} \text{ cm}^{-2}$ for the preferred partial-covering model. There is no significant difference in the hard-band power-law photon index of $\Gamma \approx 1.5$ between the two observations. The *Chandra* image also reveals extended X-ray emission $\approx 8''$ (30 kpc) south-east of the nucleus, aligned with the FR I jet but upstream of the 1.4 GHz radio-brightness peak. The jet is not detected by *HST*, and the optical upper limit rules out a simple single-component synchrotron interpretation of the radio-to-X-ray emission. The multiwavelength characteristics of the PG 1004+130 jet, including its relatively flat X-ray power law and concave spectral energy distribution, are similar to those of powerful FR II jets. The lack of strong beaming in PG 1004+130 limits the efficiency of inverse Compton upscattering, and we consider the X-ray emission to most likely arise from a second synchrotron component generated by highly energetic electrons.

6.1.2 A *Chandra* Survey of the X-ray Properties of Broad Absorption Line Radio-Loud Quasars

This work presented the results of a *Chandra* study of 21 BAL RLQs. We conducted a *Chandra* snapshot survey of 12 bright BAL RLQs selected from SDSS/FIRST data and possessing a wide range of radio and C IV absorption properties. Optical spectra were obtained nearly contemporaneously with the Hobby-Eberly Telescope; no strong flux or BAL variability was seen between epochs. In addition to the snapshot targets, we include in our sample 9 additional BAL RLQs possessing archival *Chandra* coverage. We compare the properties of (predominantly high-ionization) BAL RLQs to those of non-BAL RLQs as well as to BAL RQQs and non-BAL RQQs for context.

All 12 snapshot and 8/9 archival BAL RLQs are detected, with observed X-ray luminosities less than those of non-BAL RLQs having comparable optical/UV luminosities by typical factors of 4.1–8.5. (BAL RLQs are also X-ray weak by typical factors of 2.0–4.5 relative to non-BAL RLQs having both comparable optical/UV and radio luminosities.) However, BAL RLQs are not as X-ray weak relative to non-BAL RLQs as are BAL RQQs relative to non-BAL RQQs. While some BAL RLQs have harder X-ray spectra than typical non-BAL RLQs, some have hardness ratios consistent with those of non-BAL RLQs, and there does not appear to be a correlation between X-ray weakness and spectral hardness, in contrast to the situation for BAL RQQs. RLQs are expected to have X-ray continuum contributions from both disk-corona and small-scale jet emission. While the entire X-ray continuum in BAL RLQs cannot be obscured to the same degree as in BAL RQQs, we calculate that the jet is likely partially covered in many BAL RLQs. We comment briefly on implications for geometries and source ages in BAL RLQs.

6.1.3 X-ray Emission from Optically Selected Radio-Intermediate and Radio-Loud Quasars

We presented the results of an investigation into the X-ray properties of radio-intermediate and radio-loud quasars (RIQs and RLQs, respectively). We combine large, modern optical (SDSS) and radio (FIRST) surveys with archival X-ray data from *Chandra*, *XMM-Newton*, and *ROSAT* to generate an optically selected sample that includes 177 RIQs and 550 RLQs. This sample is constructed independently of X-ray properties but has a high X-ray detection rate (85%), and it extends to high redshifts (23% of objects have $z = 2 - 5$) and high radio-loudness values (33% of objects have $R^* = 3 - 5$, using logarithmic units). We measure the “excess” X-ray luminosity of RIQs and RLQs relative to radio-quiet quasars (RQQs) as a function of radio loudness and luminosity, and parameterize the X-ray luminosity of RIQs and RLQs both as a function of optical/UV luminosity and also as a joint function of optical/UV and radio luminosity. The X-ray properties of RIQs are generally similar to those of RQQs, and it is only at high values of radio-loudness ($R^* \gtrsim 3.5$) and radio luminosity that RLQs become strongly X-ray bright. We find no evidence for evolution in the properties of individual RIQs and RLQs with redshift, implying jet-linked IC/CMB emission does not contribute substantially to the X-ray continuum. Finally, we consider a model in which the nuclear X-ray emission contains both disk/corona-linked and jet-linked components and demonstrate that the X-ray jet-linked emission is likely beamed but to a lesser degree than applies to the radio jet; the alternatives of no X-ray beaming or strong X-ray beaming are not able to replicate the properties of the observed sample. This model is used to quantify the increasing dominance of jet-linked X-ray emission at low inclinations.

6.1.4 *Chandra* observations of the hybrid morphology radio sources 3C 433 and 4C 65.15: FR IIs with asymmetric environments

We presented *Chandra* observations of the hybrid morphology radio sources 3C 433 and 4C 65.15, two members of the rare class of objects possessing an FR I jet on one side of the core and an FR II lobe on the other. The X-ray spectrum of 3C 433 shows

intrinsic absorption (with a column density of $N_{\text{H}} \simeq 8 \times 10^{22} \text{ cm}^{-2}$), such as is typical of FR II narrow-line radio galaxies. There is excess X-ray emission below 2 keV containing contributions from diffuse soft X-ray emission (likely hot gas with $kT \sim 1.2 \text{ keV}$) as well as from the nucleus. The core of 3C 433 is extended in hard X-rays, presumably due to X-ray emission from the inner-jet knot on the FR I side that is apparent in the radio map. It is possible that the X-ray emission from this inner-jet knot is absorbed by the dust known to be present in the host galaxy. The spectrum of 4C 65.15 can be modeled with a simple power law with perhaps mild intrinsic absorption ($N_{\text{H}} \simeq 1.3 \times 10^{21} \text{ cm}^{-2}$). X-ray emission is detected at the bend in the FR I jet. This X-ray jet emission lies above the extrapolation from the high-frequency radio synchrotron emission and has a spectral slope flatter than α_{rx} , indicating that the jet spectral energy distribution is concave as with other FR II quasar jets. Both 3C 433 and 4C 65.15 have unabsorbed X-ray luminosities, radio luminosities, and optical spectra typically seen in comparable sources with FR II morphologies. Presumably the FR I structure seen on one side in these hybrid sources is generated by a powerful jet interacting with a relatively dense environment.

6.2 Future Work

These results indicate several promising directions to extend and build upon our X-ray investigations into jets and outflows in RLQs. I briefly describe some ongoing, planned, and desired future work related to the topics covered in this thesis.

The exciting discoveries of variable X-ray absorption and an X-ray jet in the hybrid morphology BAL RLQ PG 1004+130 motivate follow-up X-ray observations to monitor the changing absorption and to simultaneously investigate the X-ray spectrum and extended emission in greater detail. Desired future work could involve joint *Chandra* (60 ks) and *XMM-Newton* (60 ks) observations of PG 1004+130 (separated by 1–9 months) which, in conjunction with our previous X-ray coverage, would yield: (1) One of the most comprehensive X-ray spectral monitoring campaigns of a variable BAL quasar undertaken to date, probing the range of absorption properties on both multi-year and multi-month timescales, thus illuminating variability tendencies in BAL-linked X-ray absorbers and also constraining their location and dynamics. (2) The highest signal-to-noise X-ray spectra of a radio-loud BAL quasar currently available, enabling modeling of the soft X-ray absorption as well as investigation of any high-energy spectral flattening from an otherwise obscured nucleus, hence permitting comparison of absorber characteristics to those for the best-studied radio-quiet BAL quasars. (3) The deepest *Chandra* coverage ever obtained of a disrupting jet in a hybrid morphology radio source (the stacked observations will total 100 ks, $2.5\times$ more sensitive than the existing data), allowing measurement of the spatial extent and spectral characteristics of the X-ray emission, thereby providing useful insight into the shock-complex energetics. We hope to obtain such observations in the future.

We are currently conducting a study of BAL variability in RLQs, and have obtained HET/LRS spectra of 16 RLQs to compare with prior-epoch SDSS observations. Similar studies have been done for RQQs and have found that mild variability in the depth of BAL features is not uncommon, particularly within narrow velocity ranges, but strong velocity shifts are rare (e.g., Gibson et al. 2008); there further seems to be

a tendency for BALs in RQQs to vary in the range associated with disk-wind outflow velocities (e.g., Lundgren et al. 2007). Our new observations of BAL RLQs will enable us to accomplish the following: (1) Provide the first-ever systematic study of BAL variability in RLQs. (2) Allow statistically meaningful comparison to the variability properties of BALs in RQQs. (3) Determine whether the BALs in RLQs have variability tendencies correlated with radio characteristics. (4) Better constrain the density and structure of those BALs observed to vary in depth. (5) Measure the acceleration and evaluate whether radiative pressure is the primary driver in those BALs observed to vary in velocity. The BAL RLQs in our sample have a variety of radio luminosities, morphologies, and radio spectral indices. This study will help determine whether BALs in RLQs are predominantly associated with disk-wind outflows, as appears likely for RQQs, or whether a significant subset of BAL RLQs contain polar winds, as suggested by radio data.

Several new HYMORS have recently been discovered (Gawroński et al. 2006; 2010, in prep) through searches of the FIRST survey followed up with high-resolution *VLA* imaging. Many of these newly identified HYMORS lack optical spectra, and the lack of a secure redshift and knowledge of the optical emission line type complicates interpretation of the radio properties. For example, broad-line objects with high radio luminosities can be reasonably categorized as intrinsically FR II sources, but without optical data no such determination is possible. We are pursuing NOAO and HET time to obtain optical spectra of some of these new HYMORS. We have also identified promising scientific projects that could be undertaken with new *Chandra* X-ray observations of select HYMORS that would complement and extend our current work. X-ray observations of HYMORS provide an important opportunity to study the disruption (without termination) of a powerful jet, an ongoing point of theoretical and numerical discussion (e.g., Meliani et al. 2008), and to study whether the downstream flow takes on FR I-type characteristics. In certain cases there is also the possibility to directly measure or constrain the density and size-scale of the obstructing medium through X-ray spectral fitting of the nucleus, searching for low-energy absorption that is not expected to be intrinsically present in such sources and can therefore be associated with the near-side large-scale environment.

The past decade has seen noteworthy advances in our understanding of RLQs. Much of the success of the scientific community in explaining the properties of jets and outflows in RLQs has come through X-ray observations carried out by modern telescopes such as *XMM-Newton* and *Chandra*. Several significant remaining questions regarding how jets and outflows are launched, how they interact with and impact their host galaxy and surrounding environment, and how they fit into an evolutionary understanding of quasars, are presently being profitably addressed (for example, through deep X-ray surveys, or supercomputer simulations). Some additional puzzles are ideally suited for investigation using the capabilities of the planned *International X-ray Observatory*. The next 10–20 years promise to provide new insights into RLQs, along with the new mysteries that inevitably come coupled with scientific discovery.

Bibliography

- Adelman-McCarthy, J. K., et al. 2007, *ApJS*, 172, 634
- Alexander, D. M., et al. 2003, *AJ*, 126, 539
- Anderson, S. F., Weymann, R. J., Foltz, C. B., & Chaffee, F. H., Jr. 1987, *AJ*, 94, 278
- Anderson, S. F., et al. 2007, *AJ*, 133, 313
- Arav, N., Kaastra, J., Steenbrugge, K., Brinkman, B., Edelson, R., Korista, K. T., & de Kool, M. 2003, *ApJ*, 590, 174
- Arnaud, K. A. 1996, *ASP Conf. Ser. 101: Astronomical Data Analysis Software and Systems V*, ed. G. H. Jacoby & J. Barnes (San Francisco: ASP), 17
- Atoyan, A., & Dermer, C. D. 2004, *ApJ*, 613, 151
- Auger, M. W., Becker, R. H., & Fassnacht, C. D. 2008, *AJ*, 135, 1311
- Avni, Y., & Tananbaum, H. 1986, *ApJ*, 305, 83
- Bahcall, J. N., Kirhakos, S., Saxe, D. H., & Schneider, D. P. 1997, *ApJ*, 479, 642
- Baldwin, J. A. 1977, *ApJ*, 214, 679
- Barger, A. J., et al. 2003, *AJ*, 126, 632
- Barger, A. J., Cowie, L. L., & Wang, W.-H. 2007, *ApJ*, 654, 764
- Barger, A. J., Cowie, L. L., & Wang, W.-H. 2007, *ApJ*, 654, 764
- Bassett, L. C., Brandt, W. N., Schneider, D. P., Vignali, C., Chartas, G., & Garmire, G. P. 2004, *AJ*, 128, 523
- Bauer, F. E., Alexander, D. M., Brandt, W. N., Hornschemeier, A. E., Vignali, C., Garmire, G. P., & Schneider, D. P. 2002, *AJ*, 124, 2351
- Bauer, F. E., Alexander, D. M., Brandt, W. N., Schneider, D. P., Treister, E., Hornschemeier, A. E., & Garmire, G. P. 2004, *AJ*, 128, 2048
- Becker, R. H., White, R. L., & Helfand, D. J. 1995, *ApJ*, 450, 559
- Becker, R. H., Gregg, M. D., Hook, I. M., McMahon, R. G., White, R. L., & Helfand, D. J. 1997, *ApJ*, 479, L93
- Becker, R. H., White, R. L., Gregg, M. D., Brotherton, M. S., Laurent-Muehleisen, S. A., & Arav, N. 2000, *ApJ*, 538, 72
- Becker, R. H., et al. 2001, *ApJS*, 135, 227
- Belsole, E., Worrall, D. M., & Hardcastle, M. J. 2006, *MNRAS*, 366, 339
- Benn, C. R., Carballo, R., Holt, J., Vigotti, M., González-Serrano, J. I., Mack, K.-H., & Perley, R. A. 2005, *MNRAS*, 360, 1455

- Best, P. N., Kauffmann, G., Heckman, T. M., & Ivezić, Ž. 2005, *MNRAS*, 362, 9
- Biggs, A. D., & Ivison, R. J. 2006, *MNRAS*, 371, 963
- Birkinshaw, M., Worrall, D. M., & Hardcastle, M. J. 2002, *MNRAS*, 335, 142
- Black, A. R. S., Baum, S. A., Leahy, J. P., Perley, R. A., Riley, J. M., & Scheuer, P. A. G. 1992, *MNRAS*, 256, 186
- Blandford, R. D., & Payne, D. G. 1982, *MNRAS*, 199, 883
- Blandford, R. D., & Znajek, R. L. 1977, *MNRAS*, 179, 433
- Blundell, K. M., & Kuncic, Z. 2007, *ApJ*, 668, L103
- Brandt, W. N., Laor, A., & Wills, B. J. 2000, *ApJ*, 528, 637
- Brandt, W. N., & Alexander, D. M. 2010, *Proceedings of the National Academy of Sciences*, arXiv:1001.5054
- Brocksopp, C., Starling, R. L. C., Schady, P., Mason, K. O., Romero-Colmenero, E., Puchnarewicz, E. M. 2006, *MNRAS*, 366, 953
- Brinkmann, W., Yuan, W., & Siebert, J. 1997, *A&A*, 319, 413
- Brotherton, M. S., van Breugel, W., Smith, R. J., Boyle, B. J., Shanks, T., Croom, S. M., Miller, L., & Becker, R. H. 1998, *ApJ*, 505, L7
- Brotherton, M. S., Laurent-Muehleisen, S. A., Becker, R. H., Gregg, M. D., Telis, G., White, R. L., & Shang, Z. 2005, *AJ*, 130, 2006
- Brotherton, M. S., De Breuck, C., & Schaefer, J. J. 2006, *MNRAS*, 372, L58
- Capak, P., et al. 2007, *ApJS*, 172, 99
- Cappelluti, N., et al. 2009, *A&A*, 497, 635
- Cardelli, J. A., Clayton, G. C., & Mathis, J. S. 1989, *ApJ*, 345, 245
- Carilli, C. L., Perley, R. A., Dreher, J. W., & Leahy, J. P. 1991, *ApJ*, 383, 554
- Carvalho, J. C. 1998, *A&A*, 329, 845
- Cash, W. 1979, *ApJ*, 228, 939
- Celotti, A., Ghisellini, G., & Chiaberge, M. 2001, *MNRAS*, 321, L1
- Cheung, C. C. 2007, *AJ*, 133, 2097
- Chiaberge, M., Capetti, A., & Celotti, A. 2000, *A&A*, 355, 873
- Cirasuolo, M., Celotti, A., Magliocchetti, M., & Danese, L. 2003, *MNRAS*, 346, 447
- Coleman, G. D., Wu, C.-C., & Weedman, D. W. 1980, *ApJS*, 43, 393
- Condon, J. J., Cotton, W. D., Greisen, E. W., Yin, Q. F., Perley, R. A., Taylor, G. B., & Broderick, J. J. 1998, *AJ*, 115, 1693

- Croston, J. H., Birkinshaw, M., Hardcastle, M. J., & Worrall, D. M. 2004, *MNRAS*, 353, 879
- de Koff, S., Baum, S. A., Sparks, W. B., Biretta, J., Golombek, D., Macchetto, F., McCarthy, P., & Miley, G. K. 1996, *ApJS*, 107, 621
- de Koff, S., et al. 2000, *ApJS*, 129, 33
- de Vries, W. H., Becker, R. H., & White, R. L. 2006, *AJ*, 131, 666
- De Young, D. S. 1993, *ApJ*, 402, 95
- Dermer, C. D. 1995, *ApJ*, 446, L63
- Douglas, J. N., Bash, F. N., Bozayan, F. A., Torrence, G. W., & Wolfe, C. 1996, *AJ*, 111, 1945
- Elvis, M., & Fabbiano, G. 1984, *ApJ*, 280, 91
- Elvis, M., et al. 1994, *ApJS*, 95, 1
- Elvis, M., et al. 2009, *ApJS*, 184, 158
- Eracleous, M., & Halpern, J. P. 2004, *ApJS*, 150, 181
- Evans, D. A., Worrall, D. M., Hardcastle, M. J., Kraft, R. P., & Birkinshaw, M. 2006, *ApJ*, 642, 96
- Evans, I. N., Evans, J. D., Fabbiano, G., Glotfelty, K. J., McCollough, M. L., McDowell, J. C., Primini, F. A., & Rots, A. H. 2008, *Proc. SPIE*, 7016,
- Falcke, H., Sherwood, W., & Patnaik, A. R. 1996, *ApJ*, 471, 106
- Falomo, R., Carangelo, N., & Treves, A. 2003, *MNRAS*, 343, 505
- Fanaroff, B. L., & Riley, J. M. 1974, *MNRAS*, 167, 31P
- Foltz, C. B., Chaffee, F. H., Jr., Hewett, P. C., MacAlpine, G. M., Turnshek, D. A., Weymann, R. J., & Anderson, S. F. 1987, *AJ*, 94, 1423
- Fomalont, E.B., in *Origin of Cosmic Rays*, IAU Symp. 94, eds. Setti, G., Spada, G., & Wolfendale, A. W., Reidel, Dordrecht, Holland
- Galbiati, E., et al. 2005, *A&A*, 430, 927
- Gallagher, S. C., Brandt, W. N., Chartas, G., & Garmire, G. P. 2002, *ApJ*, 567, 37
- Gallagher, S. C., Brandt, W. N., Wills, B. J., Charlton, J. C., Chartas, G., & Laor, A. 2004, *ApJ*, 603, 425
- Gallagher, S. C., Brandt, W. N., Chartas, G., Priddey, R., Garmire, G. P., & Sambruna, R. M. 2006, *ApJ*, 644, 709
- Gallagher, S. C., Hines, D. C., Blaylock, M., Priddey, R. S., Brandt, W. N., & Egami, E. E. 2007, *ApJ*, 665, 157
- Garcia, A., Sodr , L., Jablonski, F. J., & Terlevich, R. J. 1999, *MNRAS*, 309, 803
- Garmire, G. P., Bautz, M. W., Ford, P. G., Nousek, J. A., & Ricker, G. R. 2003, *Proc. SPIE*, 4851, 28

- Gawiser, E., et al. 2006, *ApJS*, 162, 1
- Gawroński, M. P., Marecki, A., Kunert-Bajraszewska, M., & Kus, A. J. 2006, *A&A*, 447, 63
- Gehrels, N. 1986, *ApJ*, 303, 336
- Georganopoulos, M., & Kazanas, D. 2004, *ApJ*, 604, L81
- Chiaberge, M., Capetti, A., & Celotti, A. 2000, *A&A*, 355, 873
- Giacconi, R., et al. 2002, *ApJS*, 139, 369
- Gibson, R. R., Brandt, W. N., & Schneider, D. P. 2008, *ApJ*, 685, 773
- Gibson, R. R., Brandt, W. N., Schneider, D. P., & Gallagher, S. C. 2008, *ApJ*, 675, 985
- Gibson, R. R., et al. 2009, *ApJ*, 692, 758
- Gopal-Krishna, & Wiita, P. J. 2000, *A&A*, 363, 507
- Green, P. J., Aldcroft, T. L., Mathur, S., Wilkes, B. J., & Elvis, M. 2001, *ApJ*, 558, 109
- Green, P. J., et al. 2009, *ApJ*, 690, 644
- Gregg, M. D., Becker, R. H., Brotherton, M. S., Laurent-Muehleisen, S. A., Lacy, M., & White, R. L. 2000, *ApJ*, 544, 142
- Gregg, M. D., Becker, R. H., & de Vries, W. 2006, *ApJ*, 641, 210
- Gregory, P. C., Scott, W. K., Douglas, K., & Condon, J. J. 1996, *ApJS*, 103, 427
- Hall, P. B., et al. 2002, *ApJS*, 141, 267
- Hall, P. B., Gallagher, S. C., Richards, G. T., Alexander, D. M., Anderson, S. F., Bauer, F., Brandt, W. N., & Schneider, D. P. 2006, *AJ*, 132, 1977
- Hardcastle, M. J., Birkinshaw, M., & Worrall, D. M. 2001, *MNRAS*, 326, 1499
- Hardcastle, M. J., Worrall, D. M., Birkinshaw, M., Laing, R. A., & Bridle, A. H. 2002, *MNRAS*, 334, 182
- Hardcastle, M. J., Worrall, D. M., Kraft, R. P., Forman, W. R., Jones, C., & Murray, S. S. 2003, *ApJ*, 593, 169
- Hardcastle, M. J., Harris, D. E., Worrall, D. M., & Birkinshaw, M. 2004, *ApJ*, 612, 729
- Hardcastle, M. J. 2006, *MNRAS*, 370, 134
- Hardcastle, M. J., Evans, D. A., & Croston, J. H. 2009, *MNRAS*, 396, 1929
- Harris, D. E., Cheung, C. C., Biretta, J. A., Sparks, W. B., Junor, W., Perlman, E. S., & Wilson, A. S. 2006, *ApJ*, 640, 211
- Harris, D. E., & Krawczynski, H. 2002, *ApJ*, 565, 244
- Hasinger, G. 2008, *A&A*, 490, 905
- Hewett, P. C., & Foltz, C. B. 2003, *AJ*, 125, 1784

- Hill, G. J., Nicklas, H. E., MacQueen, P. J., Tejada, C., Cobos Duenas, F. J., & Mitsch, W. 1998, *Proc. SPIE*, 3355, 375
- Ilbert, O., et al. 2008, *Astronomical Society of the Pacific Conference Series*, 399, 169
- Ivezić, Ž., et al. 2002, *AJ*, 124, 2364
- Ivezić, Z., et al. 2004, *Astronomical Society of the Pacific Conference Series*, 311, 347
- Jackson, C. A., & Wall, J. V. 1999, *MNRAS*, 304, 160
- Jaffe, W. J., & Perola, G. C. 1973, *A&A*, 26, 423
- Jansen, F., et al. 2001, *A&A*, 365, L1
- Jester, S., et al. 2005, *AJ*, 130, 873
- Jester, S., K rding, E., & Fender, R. 2006a, VI Microquasar Workshop: Microquasars and Beyond
- Jester, S., Harris, D. E., Marshall, H. L., & Meisenheimer, K. 2006b, *ApJ*, 648, 900
- Jiang, D. R., & Wang, T. G. 2003, *A&A*, 397, L13
- Jiang, L., Fan, X., Ivezić, Ž., Richards, G. T., Schneider, D. P., Strauss, M. A., & Kelly, B. C. 2007, *ApJ*, 656, 680
- Jin, Y. K., Zhang, S. N., & Wu, J. F. 2006, *ApJ*, 653, 1566
- Jorstad, S. G., & Marscher, A. P. 2004, *ApJ*, 614, 615
- Just, D. W., Brandt, W. N., Shemmer, O., Steffen, A. T., Schneider, D. P., Chartas, G., & Garmire, G. P. 2007, *ApJ*, 665, 1004
- Kardashev, N. S. 1962, *Soviet Astronomy*, 6, 317
- Kaspi, S., Brandt, W. N., Maoz, D., Netzer, H., Schneider, D. P., & Shemmer, O. 2007, *ApJ*, 659, 997
- Kellermann, K. I., Sramek, R., Schmidt, M., Shaffer, D. B., & Green, R. 1989, *AJ*, 98, 1195
- Kellermann, K. I., Fomalont, E. B., Mainieri, V., Padovani, P., Rosati, P., Shaver, P., Tozzi, P., & Miller, N. 2008, *ApJS*, 179, 71
- Kelly, B. C. 2007, *ApJ*, 665, 1489
- Kelly, B. C., Bechtold, J., Siemiginowska, A., Aldcroft, T., & Sobolewska, M. 2007, *ApJ*, 657, 116
- Kraft, R. P., Burrows, D. N., & Nousek, J. A. 1991, *ApJ*, 374, 344
- Kraft, R. P., Hardcastle, M. J., Worrall, D. M., & Murray, S. S. 2005, *ApJ*, 622, 149
- Krolik, J. H., & Kallman, T. R. 1987, *ApJ*, 320, L5
- Kunert-Bajraszewska, M., & Marecki, A. 2007, *A&A*, 469, 437

- Lacy, M., Gregg, M., Becker, R. H., White, R. L., Glikman, E., Helfand, D., & Winn, J. N. 2002, *AJ*, 123, 2925
- Laor, A. 2000, *ApJ*, 543, L111
- Laor, A., & Brandt, W. N. 2002, *ApJ*, 569, 641
- Laor, A., & Behar, E. 2008, *MNRAS*, 390, 847
- Lara, L., Márquez, I., Cotton, W. D., Feretti, L., Giovannini, G., Marcaide, J. M., & Venturi, T. 1999, *New Astronomy Review*, 43, 643
- Ledlow, M. J., & Owen, F. N. 1996, *AJ*, 112, 9
- Lehmer, B. D., et al. 2005, *ApJS*, 161, 21
- Lehmer, B. D., Brandt, W. N., Hornschemeier, A. E., Alexander, D. M., Bauer, F. E., Koekemoer, A. M., Schneider, D. P., & Steffen, A. T. 2006, *AJ*, 131, 2394
- Lewis, G. F., Chapman, S. C., & Kuncic, Z. 2003, *ApJ*, 596, L35
- Liu, Y., Jiang, D. R., Wang, T. G., & Xie, F. G. 2008, *MNRAS*, 391, 246
- Lonsdale, C. J., Barthel, P. D., & Miley, G. K. 1993, *ApJS*, 87, 63
- Lonsdale, C. J., et al. 2003, *PASP*, 115, 897
- Lopez, L. A., Brandt, W. N., Vignali, C., Schneider, D. P., Chartas, G., Garmire, G. P. 2006, *AJ*, 131, 1914
- Lu, Y., Wang, T., Zhou, H., & Wu, J. 2007, *AJ*, 133, 1615
- Luo, B., et al. 2008, *ApJS*, 179, 19
- Luo, B., et al. 2009, *ApJ*, 695, 1227
- Luo, B., et al. 2010, *ApJS*, 187, 560
- Lynden-Bell, D. 1969, *Nature*, 223, 690
- Ma, F. 2002, *MNRAS*, 335, L99
- Maccacaro, T., Gioia, I. M., Wolter, A., Zamorani, G., & Stocke, J. T. 1988, *ApJ*, 326, 680
- Mackay, C. D. 1971, *MNRAS*, 154, 209
- Maiolino, R., & Risaliti, G. 2007, *The Central Engine of Active Galactic Nuclei*, 373, 447
- Maoz, D. 2007, *MNRAS*, 377, 1696
- Marshall, H. L., Miller, B. P., Davis, D. S., Perlman, E. S., Wise, M., Canizares, C. R., & Harris, D. E. 2002, *ApJ*, 564, 683
- Marshall, H. L., et al. 2005, *ApJS*, 156, 13
- Martin, D. C., et al. 2005, *ApJ*, 619, L1

- Massaro, F., Harris, D. E., Chiaberge, M., Grandi, P., Macchetto, F. D., Baum, S. A., O'Dea, C. P., & Capetti, A. 2009, *ApJ*, 696, 980
- Matt, G. 2002, *Royal Society of London Philosophical Transactions Series A*, 360, 2045
- McLure, R. J., & Dunlop, J. S. 2001, *MNRAS*, 321, 515
- Meier, D. L. 2001, *ApJ*, 548, L9
- Menou, K., et al. 2001, *ApJ*, 561, 645
- Merritt, D., & Ekers, R. D. 2002, *Science*, 297, 1310
- Metcalfe, R. B., & Magliocchetti, M. 2006, *MNRAS*, 365, 101
- Miller, B. P., Brandt, W. N., Gallagher, S. C., Laor, A., Wills, B. J., Garmire, G. P., & Schneider, D. P. 2006, *ApJ*, 652, 163
- Miller, B. P., & Brandt, W. N. 2009, *ApJ*, 695, 755
- Miller, B. P., Brandt, W. N., Gibson, R. R., Garmire, G. P., & Shemmer, O. 2009, *ApJ*, 702, 911
- Miller, N. A., Fomalont, E. B., Kellermann, K. I., Mainieri, V., Norman, C., Padovani, P., Rosati, P., & Tozzi, P. 2008, *ApJS*, 179, 114
- Miller, P., Rawlings, S., & Saunders, R. 1993, *MNRAS*, 263, 425
- Mirabel, I. F. 1989, *ApJ*, 340, L13
- Montenegro-Montes, F. M., Mack, K.-H., Vigotti, M., Benn, C. R., Carballo, R., González-Serrano, J. I., Holt, J., & Jiménez-Luján, F. 2008, *MNRAS*, 388, 1853
- Montenegro-Montes, F. M., Mack, K. -, Benn, C. R., Carballo, R., Dallacasa, D., González-Serrano, J. I., Holt, J., & Jiménez-Luján, F. 2009, *arXiv:0903.5119*
- Morganti, R., Oosterloo, T., Tadhunter, C. N., Aiudi, R., Jones, P., & Villar-Martin, M. 1999, *A&AS*, 140, 355
- Morganti, R., Oosterloo, T., Tadhunter, C., & Emonts, B. 2003, *New Astronomy Review*, 47, 273
- Müller, S. A. H., Haas, M., Siebenmorgen, R., Klaas, U., Meisenheimer, K., Chini, R., & Albrecht, M. 2004, *A&A*, 426, L29
- Mullin, L. M., & Hardcastle, M. J. 2009, *MNRAS*, 398, 1989
- Murphy, E. M., Lockman, F. J., Laor, A., & Elvis, M. 1996, *ApJS*, 105, 369
- Murray, N., Chiang, J., Grossman, S. A., & Voit, G. M. 1995, *ApJ*, 451, 498
- Neilsen, J., & Lee, J. C. 2009, *Nature*, 458, 481
- Norris, R. P., et al. 2006, *AJ*, 132, 2409
- O'Dea, C. P. 1998, *PASP*, 110, 493
- Ogle, P. M., Cohen, M. H., Miller, J. S., Tran, H. D., Goodrich, R. W., & Martel, A. R. 1999, *ApJS*, 125, 1

- Osmer, P. S., & Shields, J. C. 1999, *Quasars and Cosmology*, 162, 235
- Owen, F. N., & Ledlow, M. J. 1994, *The Physics of Active Galaxies*, 54, 319
- Pacholczyk, A. G. 1970, *Series of Books in Astronomy and Astrophysics*, San Francisco: Freeman, 1970
- Padovani, P., Allen, M. G., Rosati, P., & Walton, N. A. 2004, *A&A*, 424, 545
- Page, K. L., Reeves, J. N., O'Brien, P. T., & Turner, M. J. L. 2005, *MNRAS*, 364, 195
- Parma, P., de Ruiter, H. R., Capetti, A., Fanti, R., Morganti, R., Bondi, M., Laing, R. A., & Canvin, J. R. 2003, *A&A*, 397, 127
- Perley, R. A., Condon, J. J., Cotton, W. D., Cohen, A. S., Lane, W. M., Kassim, N. E., Lazio, T. J. W., & Erickson, W. C. 2006, *VizieR Online Data Catalog*, 8079, 0
- Plotkin, R. M., Anderson, S. F., Hall, P. B., Margon, B., Voges, W., Schneider, D. P., Stinson, G., & York, D. G. 2008, *AJ*, 135, 2453
- Plotkin, R. M., et al. 2010, *AJ*, 139, 390
- Rafferty, D. A., Brandt, W. N., Alexander, D.M. , Xue, Y. Q., Bauer, F. E., Lehmer, B. D., Luo, B., & Papovich, C. 2010, *ApJ*, submitted
- Porquet, D., Reeves, J. N., O'Brien, P., & Brinkmann, W. 2004, *A&A*, 422, 85
- Proga, D., Stone, J. M., & Kallman, T. R. 2000, *ApJ*, 543, 686
- Ramsey, L. W., et al. 1998, *Proc. SPIE*, 3352, 34
- Rawlings, S., & Saunders, R. 1991, *Nature*, 349, 138
- Rees, M. J., & Setti, G. 1968, *Nature*, 219, 127
- Reeves, J. N., & Turner, M. J. L. 2000, *MNRAS*, 316, 234
- Reichard, T. A., et al. 2003, *AJ*, 126, 2594
- Reid, A., Shone, D. L., Akujor, C. E., Browne, I. W. A., Murphy, D. W., Pedelty, J., Rudnick, L., & Walsh, D. 1995, *A&AS*, 110, 213
- Rengelink, R. B., Tang, Y., de Bruyn, A. G., Miley, G. K., Bremer, M. N., Roettgering, H. J. A., & Bremer, M. A. R. 1997, *A&AS*, 124, 259
- Richards, E. A., Kellermann, K. I., Fomalont, E. B., Windhorst, R. A., & Partridge, R. B. 1998, *AJ*, 116, 1039
- Richards, E. A., Fomalont, E. B., Kellermann, K. I., Windhorst, R. A., Partridge, R. B., Cowie, L. L., & Barger, A. J. 1999, *ApJ*, 526, L73
- Richards, G. T., et al. 2001, *AJ*, 121, 2308
- Richards, G. T., et al. 2002, *AJ*, 123, 2945
- Richards, G. T., et al. 2009, *ApJS*, 180, 67

- Rovilos, E., Georgakakis, A., Georgantopoulos, I., Afonso, J., Koekemoer, A. M., Mobasher, B., & Goudis, C. 2007, *A&A*, 466, 119
- Sambruna, R. M., Gambill, J. K., Maraschi, L., Tavecchio, F., Cerutti, R., Cheung, C. C., Urry, C. M., & Chartas, G. 2004, *ApJ*, 608, 698
- Sambruna, R. M., Donato, D., Cheung, C. C., Tavecchio, F., & Maraschi, L. 2008, *ApJ*, 684, 862
- Scarpa, R., & Urry, C. M. 2001, *ApJ*, 556, 749
- Schaefer, J. J., Brotherton, M. S., Shang, Z., Gregg, M. D., Becker, R. H., Laurent-Muehleisen, S. A., Lacy, M., & White, R. L. 2006, *AJ*, 132, 1464
- Scheuer, P. A. G. 1995, *MNRAS*, 277, 331
- Schinnerer, E., et al. 2007, *ApJS*, 172, 46
- Schlegel, D. J., Finkbeiner, D. P., & Davis, M. 1998, *ApJ*, 500, 525
- Schmidt, M. 1963, *Nature*, 197, 1040
- Schmidt, M., & Green, R. F. 1983, *ApJ*, 269, 352
- Schneider, D. P., et al. 2007, *AJ*, 134, 102
- Schwartz, D. A., Marshall, H. L., Gelbord, J. M., et al. 2005, in 'The X-ray Universe 2005', ESA Press, Noordwijk
- Schwartz, D. A. 2002, *ApJ*, 569, L23
- Shakura, N. I., & Syunyaev, R. A. 1973, *A&A*, 24, 337
- Shankar, F., Dai, X., & Sivakoff, G. R. 2008, *ApJ*, 687, 859
- Shastri, P., Wilkes, B. J., Elvis, M., & McDowell, J. 1993, *ApJ*, 410, 29
- Siemiginowska, A., Bechtold, J., Aldcroft, T. L., Elvis, M., Harris, D. E., & Dobrzycki, A. 2002, *ApJ*, 570, 543
- Siemiginowska, A., Smith, R. K., Aldcroft, T. L., Schwartz, D. A., Paerels, F., & Petric, A. O. 2003, *ApJ*, 598, L15
- Siemiginowska, A., LaMassa, S., Aldcroft, T. L., Bechtold, J., & Elvis, M. 2008, *ApJ*, 684, 811
- Sokolov, A., & Marscher, A. P. 2005, *ApJ*, 629, 52
- Spergel, D. N., et al. 2003, *ApJS*, 148, 175
- Spergel, D. N., et al. 2007, *ApJS*, 170, 377
- Sprayberry, D., & Foltz, C. B. 1992, *ApJ*, 390, 39
- Sramek, R. A., & Weedman, D. W. 1980, *ApJ*, 238, 435
- Stalin, C. S., Gopal-Krishna, Sagar, R., & Wiita, P. J. 2004, *MNRAS*, 350, 175
- Stawarz, L., Sikora, M., Ostrowski, M., & Begelman, M. C. 2004, *ApJ*, 608, 95

- Stawarz, L., Ostorero, L., Begelman, M. C., Moderski, R., Kataoka, J., & Wagner, S. 2008, *ApJ*, 680, 911
- Steffen, A. T., Strateva, I., Brandt, W. N., Alexander, D. M., Koekemoer, A. M., Lehmer, B. D., Schneider, D. P., & Vignali, C. 2006, *AJ*, 131, 2826
- Stoeckle, J. T., Morris, S. L., Weymann, R. J., & Foltz, C. B. 1992, *ApJ*, 396, 487
- Stockton, A. 1978, *ApJ*, 223, 747
- Strateva, I. V., Brandt, W. N., Schneider, D. P., Vanden Berk, D. G., & Vignali, C. 2005, *AJ*, 130, 387
- Suchkov, A. A., Hanisch, R. J., Voges, W., & Heckman, T. M. 2006, *AJ*, 132, 1475
- Szokoly, G. P., et al. 2004, *ApJS*, 155, 271
- Tavecchio, F., Maraschi, L., Sambruna, R. M., & Urry, C. M. 2000, *ApJ*, 544, L23
- Tavecchio, F., Ghisellini, G., & Celotti, A. 2003, *A&A*, 403, 83
- Townsley, L. K., Broos, P. S., Feigelson, E. D., Garmire, G. P., & Getman, K. V. 2006, *AJ*, 131, 2164
- Tozzi, P., et al. 2009, *ApJ*, 698, 740
- Trammell, G. B., Vanden Berk, D. E., Schneider, D. P., Richards, G. T., Hall, P. B., Anderson, S. F., & Brinkmann, J. 2007, *AJ*, 133, 1780
- Trouille, L., Barger, A. J., Cowie, L. L., Yang, Y., & Mushotzky, R. F. 2008, *ApJS*, 179, 1
- Trump, J. R., et al. 2006, *ApJS*, 165, 1
- Trump, J. R., et al. 2009, *ApJ*, 696, 1195
- Turner, T. J., George, I. M., Nandra, K., & Mushotzky, R. F. 1997, *ApJ*, 488, 164
- Urrutia, T., Lacy, M., Gregg, M. D., & Becker, R. H. 2005, *ApJ*, 627, 75
- Urrutia, T., Lacy, M., & Becker, R. H. 2008, *ApJ*, 674, 80
- Urrutia, T., Becker, R. H., White, R. L., Glikman, E., Lacy, M., Hodge, J., & Gregg, M. D. 2009, *ApJ*, 698, 1095
- Urry, C. M., & Padovani, P. 1995, *PASP*, 107, 803
- van Breugel, W., Helfand, D., Balick, B., Heckman, T., & Miley, G. 1983, *AJ*, 88, 40
- Vanden Berk, D. E., Stoughton, C., Crotts, A. P. S., Tytler, D., & Kirkman, D. 2000, *AJ*, 119, 2571
- Vanden Berk, D. E., et al. 2001, *AJ*, 122, 549
- Vanden Berk, D. E., et al. 2004, *ApJ*, 601, 692
- Vanden Berk, D. E., et al. 2005, *AJ*, 129, 2047
- Varano, S., Chiaberge, M., Macchetto, F. D., & Capetti, A. 2004, *A&A*, 428, 401

- Vestergaard, M. 2003, *ApJ*, 599, 116
- Vestergaard, M., Peterson, B. M. 2006, *ApJ*, 641, 689
- Wang, J. X., et al. 2007, *ApJ*, 657, 95
- Wang, J., Jiang, P., Zhou, H., Wang, T., Dong, X., & Wang, H. 2008, *ApJ*, 676, L97
- Watson, M. G., et al. 2009, *A&A*, 493, 339
- Weymann, R. J., Morris, S. L., Foltz, C. B., & Hewett, P. C. 1991, *ApJ*, 373, 23
- White, R. L., Becker, R. H., Helfand, D. J., & Gregg, M. D. 1997, *ApJ*, 475, 479
- White, R. L., et al. 2000, *ApJS*, 126, 133
- White, R. L., Helfand, D. J., Becker, R. H., Glikman, E., & de Vries, W. 2007, *ApJ*, 654, 99
- Wilkes, B. J., & Elvis, M. 1987, *ApJ*, 323, 243
- Willott, C. J., Rawlings, S., Blundell, K. M., & Lacy, M. 1999, *MNRAS*, 309, 1017
- Willott, C. J., Rawlings, S., Blundell, K. M., Lacy, M., & Eales, S. A. 2001, *MNRAS*, 322, 536
- Willott, C. J., Rawlings, S., Archibald, E. N., & Dunlop, J. S. 2002, *MNRAS*, 331, 435
- Willott, C. J., Rawlings, S., & Grimes, J. A. 2003, *ApJ*, 598, 909
- Wills, B. J., & Brotherton, M. S. 1995, *ApJ*, 448, L81
- Wills, B. J., Brandt, W. N., & Laor, A. 1999, *ApJ*, 520, L91
- Wills, K. A., Tadhunter, C. N., Robinson, T. G., & Morganti, R. 2002, *MNRAS*, 333, 211
- Wilson, A. S., & Colbert, E. J. M. 1995, *ApJ*, 438, 62
- Windhorst, R. A., Miley, G. K., Owen, F. N., Kron, R. G., & Koo, D. C. 1985, *ApJ*, 289, 494
- Wolf, C., et al. 2004, *A&A*, 421, 913
- Worrall, D. M., Tananbaum, H., Giommi, P., & Zamorani, G. 1987, *ApJ*, 313, 596
- Worrall, D. M., Birkinshaw, M., & Cameron, R. A. 1995, *ApJ*, 449, 93
- Worrall, D. M., & Birkinshaw, M. 2005, *MNRAS*, 360, 926
- Worrall, D. M., & Birkinshaw, M. 2006, *Physics of Active Galactic Nuclei at all Scales*, 693, 39
- Worrall, D. M. 2009, *A&A Rev.*, 17, 1
- Wright, A., & Otrupcek, R. 1990, *PKS Catalog (1990)*, 0
- Wu, J. F., Zhang, S. N., Lu, F. J., & Jin, Y. K. 2007, *Chinese Journal of Astronomy and Astrophysics*, 7, 81
- Xue, Y. Q., Brandt, W. N., Luo, B., Rafferty, D. A., Alexander, D. M., Bauer, F. E., Lehmer, B. D., Schneider, D. P., & Silverman, J. D. 2010, *ApJ*, submitted
- York, D. G., et al. 2000, *AJ*, 120, 1579

- Young, M., Elvis, M., & Risaliti, G. 2009, *ApJS*, 183, 17
- Yuan, W., Siebert, J., & Brinkmann, W. 1998, *A&A*, 334, 498
- Yuan, W., Fabian, A. C., Worsley, M. A., & McMahon, R. G. 2006, *MNRAS*, 368, 985
- Zamfir, S., Sulentic, J. W., & Marziani, P. 2008, *MNRAS*, 387, 856
- Zamorani, G., et al. 1981, *ApJ*, 245, 357
- Zhou, H., Wang, T., Wang, H., Wang, J., Yuan, W., & Lu, Y. 2006, *ApJ*, 639, 716
- Zirbel, E. L. 1997, *ApJ*, 476, 489

Curriculum Vitae for Brendan P. Miller

Education

The Pennsylvania State University University Park, PA 2003–Present
Ph.D. in Astronomy and Astrophysics expected 5/2010
Massachusetts Institute of Technology Cambridge, MA 1998–2002
B.S. Physics; B.S. Earth, Atmospheric, and Planetary Science

Fellowships and Awards

Pennsylvania Space Grant Consortium Fellowship, NASA 2005–2007
Zaccheus Daniel Trust Award, PSU Department of Astronomy & Astrophysics 2007
Brumbach Fellowship, PSU Department of Astronomy & Astrophysics 2005
Braddock/Roberts Fellowship, PSU Eberly College of Science 2003–2005
University Graduate Fellowship, Pennsylvania State University 2003–2004

Research Experience

Thesis Research The Pennsylvania State University 2005–Present
Advisor: Dr. Niel Brandt
Currently investigating accretion structure, jets, and outflows in radio-loud quasars, particularly through analysis of X-ray observations.

Graduate Research The Pennsylvania State University 2004–2006
Advisor: Dr. Mercedes Richards
Completed a study of accretion structures around Algol binaries involving the reduction, analysis, and modeling of optical and UV spectra.

Undergraduate Research The Massachusetts Institute of Technology 2000–2002
Advisor: Dr. Herman Marshall
Characterized the structure and spectral energy distribution of quasar jets to determine the dominant X-ray emission mechanism within jet knots.

Teaching Experience

Visiting Instructor of Physics The College of Wooster 2009–Present
Developed and taught wide range of courses including Astronomy of the Solar System (intended for non-majors) and Modern Physics (required for majors).

Instructor, Astro 1 The Pennsylvania State University Summer 2008
Responsible for all aspects of introductory astronomy course. Created and presented lectures, homework, and exams; designed in-class hands-on activities.

Science and math teacher DeNovo Academy 2002–2003
Developed and implemented curricula within Minnesota state standards for alternative high school. Taught subjects including physics, chemistry, and math.